Title

Electrochemical Advanced Oxidation Processes for Distributed Water Treatment

Author

Duan, Yanghua

Publication Date

2022

Electrochemical Advanced Oxidation Processes for Distributed Water Treatment

By

Yanghua Duan

A dissertation submitted in partial satisfaction of the

requirements for the degree of

Doctor of Philosophy

in

Engineering - Civil and Environmental Engineering

in the

Graduate Division

of the

University of California, Berkeley

Committee in charge:

Professor David L. Sedlak, Chair
Professor Baoxia Mi
Professor Bryan D. McCloskey

Summer 2022

Electrochemical Advanced Oxidation Processes for Distributed Water Treatment

Abstract

Electrochemical Advanced Oxidation Processes for Distributed Water Treatment

by

Yanghua Duan

Doctor of Philosophy in Engineering - Civil and Environmental Engineering

University of California, Berkeley

Professor David L. Sedlak, Chair

Distributed water treatment has emerged as an alternative to centralized water systems as a means of providing drinking water in locations where population density is too low to support the distribution networks needed to move treated water to places where it will be used. By exploitation of non-traditional water sources, distributed water treatment also has the potential to address the problem of water scarcity. Electrochemical advanced oxidation processes are promising techniques for distributed water treatment because of their small footprint, flexible operation and ability to remove contaminants without any chemical input. However, their adaptation has been hampered by challenges including the high cost of electrodes, slow mass transport of contaminants, high energy consumption, and difficulties in scaling up treatment processes. This research attempts to develop new electrochemical advanced oxidation processes for distributed water treatment by providing both a mechanistic understanding of the chemical reactions taking place and a better understanding of practical engineering considerations needed to deploy the technologies.

Urban stormwater is one of the non-traditional water sources that is attractive to water-stressed cities because it is available in large quantities and does not require large investments in conveyance systems. To provide a means of removing chemical contaminants in distributed water systems, an electrochemical advanced oxidation process that is compatible with high-capacity stormwater recharge systems (e.g., drywells) was developed. The treatment system consisted of an electrochemical module for H_2O_2 production and an ultraviolent (UV) reactor for converting hydrogen peroxide (H_2O_2) into hydroxyl radical ($^\bullet$OH). To minimize the energy consumption and system footprint, production of a concentrated H_2O_2 stock solution prior to the storm event was evaluated. The H_2O_2 generation was optimized in terms of its energy efficiency and oxidant production rate. The solution pH was identified as the main factor affecting the H_2O_2 stability, with basic conditions leading to greater loss through dismutation. Using this information, the stability was enhanced by mixing the basic H_2O_2-containing catholyte with the acidic anolyte. The proposed advanced oxidation process demonstrated effective removal of trace organic contaminants in full-scale stormwater treatment system. However, the energy efficiency was limited by the inefficient UV light

utilization, due to light reflection and backscattering at the water-air interface in the UV reactor as well as competition for UV light absorption with H_2O_2.

In response to the inefficient light utilization by the UV/H_2O_2 process, an alternative approach for converting H_2O_2 to $^{\bullet}OH$ was developed. In Chapter 3, the reaction mechanism and reactive oxidant yields produced by activation of H_2O_2 on an inexpensive stainless-steel electrode was investigated. The stainless-steel electrode was investigated at different pH values and applied potentials using probe compounds to differentiate the production of different reactive oxidants ($^{\bullet}OH$ versus Fe[IV]) from H_2O_2 activation. The stainless-steel electrode demonstrated high yields for converting H_2O_2 into $^{\bullet}OH$ at circumneutral pH conditions. In the presence of H_2O_2 concentrations comparable to those that might be generated by electrochemical reduction of O_2, the stainless-steel electrode removed trace organic contaminants from an authentic water sample. However, loss of $^{\bullet}OH$ on or near the electrode surface decreased the utilization efficiency of $^{\bullet}OH$.

Finally, a reagent-free dual-cathode treatment process was evaluated. The system coupled the air-diffusion electrode with the stainless-steel electrode. The performance of the system was optimized separately for H_2O_2 generation and H_2O_2 activation. The optimal potential for H_2O_2 production on the air-diffusion electrode was identified as -0.04 V and the optimal potential for trace organic contaminant transformation on the stainless-steel electrode was identified as +0.02 V. The different optimal potential for each process suggests that the treatment could overcome the imbalance between H_2O_2 generation and H_2O_2 activation encountered in previously described composite electrodes. In tests of the combined electrochemical treatment system, the dual-cathode treatment process oxidized uncharged compounds (e.g., atrazine) but was unable to oxidize negatively charged benzoate. The efficiency of the system was also much less susceptible to competition for oxidants from negatively charged macromolecules (e.g., humic substances). These findings suggest that electrostatic repulsion minimizes the scavenging effect of negatively charged oxidant scavengers. The dual-cathode treatment system consumed about 10 kWh/m^3, which is comparable to that of anodic oxidation and point-of-use UV/H_2O_2 process.

Collectively, results of the experiments described in this dissertation indicate that electrochemical advanced oxidation processes hold promise as distributed drinking water treatment systems. The air-diffusion electrode can produce concentrated H_2O_2 stock solutions in an off-line reactor or lower levels of H_2O_2 can be produced in situ. Two H_2O_2 activation techniques, UV light and a stainless-steel electrode, converted H_2O_2 into reactive oxidant species that are capable of removing trace organic contaminants. Additional research is needed to scale up the lab scale systems, understand long-term performance of the electrodes, and develop strategies for treatment automation.

Table of contents

Table of contents ... i

List of figures ... iv

List of tables ... xi

Acknowledgments ... xii

CHAPTER 1. Introduction ... 1

1.1 Distributed water treatment as a solution for the global water challenges ... 2

1.2 Treatment technologies for distributed water treatment ... 3

1.2.1 Ultraviolet (UV)/H_2O_2 ... *3*

1.2.2 Anodic processes for contaminants oxidation ... *4*

1.2.3 Reduction of H_2O_2 for $^{\bullet}OH$ production ... *5*

1.3 Electrochemical generation of chemical reagents for distributed water treatment 6

1.4 Dissertation Outline ... 8

CHAPTER 2. An Electrochemical Advanced Oxidation Process for the Treatment of Urban Stormwater ... 10

2.1 Introduction ... 11

2.2 Materials and Methods ... 12

2.2.1 Materials ... *12*

2.2.2 Electrochemical cell and UV reactor ... *13*

2.2.3 H_2O_2 generation and energy consumption ... *14*

2.2.4 H_2O_2 stability ... *14*

2.2.5 Advanced oxidation process ... *14*

2.2.6 Analytical methods ... *17*

2.2.7 Kinetic model for the UV/H_2O_2 treatment ... *17*

2.3 Results and Discussion ... 19

2.3.1 H_2O_2 generation as a function of current density ... *19*

2.3.2 Energy consumption during H_2O_2 generation ... *23*

2.3.3 H_2O_2 stability during storage ... *27*

2.3.4 Trace organic contaminant removal by advanced oxidation ... *31*

2.3.5 Full-scale treatment system design and considerations ... *35*

2.4 Conclusions 38

CHAPTER 3. Factors Affecting the Yield of Hydroxyl Radical by Electrochemical Activation of H_2O_2 on Stainless-Steel Electrodes 40

3.1 Introduction 41

3.2 Materials and Methods 42

3.2.1 Materials *42*

3.2.2 Electrolysis in Na_2SO_4 electrolyte *42*

3.2.3 Electrolysis in authentic surface water *44*

3.2.4 Analytical methods *47*

3.3 Results and Discussion 48

3.3.1 Pre-conditioning of stainless-steel electrodes *48*

3.3.2 Effects of pH and applied potential on H_2O_2 transformation rates *49*

3.3.3 Reactive oxidant production *54*

3.3.4 Metals release from stainless-steel electrode *56*

3.3.5 Surface scavenging of $^{\bullet}OH$ *63*

3.3.6 Possible mechanisms of H_2O_2 activation *66*

3.3.7 Oxidation of trace organic contaminants in authentic surface water *68*

3.4 Environmental Implications 70

CHAPTER 4. Reagent-Free Electrochemical Advanced Oxidation for Distributed Water Treatment Enabled by Air-Diffusion and Stainless-Steel Electrodes 72

4.1 Introduction 73

4.2 Materials and Methods 74

4.2.1 Materials *74*

4.2.2 Electrolysis *75*

4.2.3 Trace organic contaminants removal pathways *76*

4.2.4 Analytical methods *77*

4.3 Results and Discussion 78

4.3.1 Air-diffusion electrode for H_2O_2 production *78*

4.3.2 Trace organic contaminant removal by the dual-cathode treatment process 83

4.3.3 Trace organic contaminants removal pathways *86*

4.3.4 Performance in the presence of $^{\bullet}OH$ scavengers *88*

4.3.5 Removal of trace organic contaminants from authentic surface water *90*

4.3.6 Energy consumption ... 92
4.4 Environmental implications ... 93
CHAPTER 5. Conclusions ... 96
5.1 Summary ... 97
5.1.1 An electrochemical advanced oxidation process for the treatment of urban stormwater ... 97
5.1.2 Factors affecting the yield of hydroxyl radical by electrochemical activation of H_2O_2 on stainless-steel electrodes ... 97
5.1.3 Reagent-free electrochemical advanced oxidation for distributed water treatment enabled by air-diffusion and stainless-steel electrodes ... 98
5.2 Future research ... 98
References ... 101
Appendix ... 129
A.1 An electrochemical advanced oxidation process for the treatment of urban stormwater ... 129
A.1.1 Determination of the photon fluence rate ... 129
A.2 Factors affecting the yield of hydroxyl radical by electrochemical activation of H_2O_2 on stainless-steel electrodes ... 132
A.2.1 Reaction rate constants for $^{\bullet}OH$ with organic buffer compounds ... 132
A.2.2 Analytical methods for detection of MES and PIPES ... 133
A.2.3 Prediction of reaction rate between H_2O_2 and Fe(II) ... 134
A.3 Factors affecting the yield of hydroxyl radical by electrochemical activation of H_2O_2 on stainless-steel electrodes ... 135
A.3.1 Detection of $^{\bullet}OH$ scavengers and the associated oxidation products ... 135
A.3.2 Estimation of the diffusion distance of $^{\bullet}OH$ ... 136
A.3.3 Energy consumption of point-of-use UV/H_2O_2 process ... 138

List of figures

Figure 1.1 Distributed treatment systems have strong potential to address the water challenges associated with climate change, chemical contaminants, and uneven urbanization.......... 3

Figure 1.2 Electrochemical reactor operation in (a) flow-by mode operation and (b) flow-through mode operation. Adapted from (Chaplin 2019). 5

Figure 1.3 Schematic of an electrochemical reactor that contains an air-diffusion electrode as the working electrode for H_2O_2 production. 7

Figure 1.4 Schematic of the proposed stormwater treatment system combining an electrochemical reactor for H_2O_2 production and a UV reactor for H_2O_2 activation. 8

Figure 2.1 Schematic of the reactor setup for UV/H_2O_2 process.......... 15

Figure 2.2 Catholyte pH change during H_2O_2 generation. Error bars represent one standard deviation; error bars not shown are smaller than symbols. 20

Figure 2.3 Production of H_2O_2 during electrolysis in 0.2 M Na_2SO_4-amended stormwater and 0.2 M Na_2SO_4 electrolyte at varying current densities. Error bars represent one standard deviation. 21

Figure 2.4 Faraday efficiency during electrolysis in 0.2 M Na_2SO_4-amended simulated stormwater and 0.2 M Na_2SO_4 electrolyte. Error bars represent one standard deviation. 23

Figure 2.5 Cell voltage as a function of time during electrolysis in 0.2 M Na_2SO_4-amended simulated stormwater and 0.2 M Na_2SO_4 electrolyte. Error bars represent one standard deviation. 24

Figure 2.6 Effect of Na_2SO_4 amendment concentrations in simulated stormwater and applied current densities on energy consumption for H_2O_2 generation. 25

Figure 2.7 Estimated salt amendment cost, electricity cost and overall cost for H_2O_2 generation at various Na_2SO_4 amendment concentrations and current densities; $[H_2O_2]$ = 450 mM. 26

Figure 2.8 Energy consumption of H_2O_2 generation under different applied current densities for 0.2 M Na_2SO_4-amended stormwater and 0.2 M Na_2SO_4 electrolyte. Error bars not shown are smaller than symbols. 27

Figure 2.9 Solution pH during H_2O_2 storage. Error bars represent one standard deviation; error bars not shown are smaller than symbols.......... 28

Figure 2.10 Hydrogen peroxide stability in catholyte and catholyte mixed with anolyte. 29

Figure 2.11 Predicted cumulative loss of H_2O_2 during storage of stock solutions prepared in advance of a storm event. 30

Figure 2.12 Effect of humic acid concentrations on $[H_2O_2]$ and [CBZ] in the AOP. (A) CBZ concentration and (B) H_2O_2 concentration. $[H_2O_2]_{\text{initial}}$ = 1 mM; $[\text{CBZ}]_{\text{initial}}$ = 10 μg/L. Symbols and lines are assigned to experimental data and model predictions, respectively. Error bars represent one standard deviation; error bars not shown are smaller than symbols.. 32

Figure 2.13 Schematic of light field in the UV reactor.. 33

Figure 2.14 Effect of humic acid concentrations on UV light loss by reflection and backscattering and through absorption by chromophores. $[H_2O_2]_{initial}$ = 1 mM; $[CBZ]_{initial}$ = 10 μg/L; P_{lamp} = 60 W.. 34

Figure 2.15 Effect of humic acid concentrations on estimated steady-state $^{\bullet}OH$ concentration and $^{\bullet}OH$ scavenging by scavengers and contaminants (Radicals: $O_2^{-}\cdot$, $HO_2\cdot$). The height indicates steady state $^{\bullet}OH$ concentration and the patterns within indicate the portion of the $^{\bullet}OH$ consumed by each species. $[H_2O_2]_{initial}$ = 1 mM; $[CBZ]_{initial}$ = 10 μg/L; P_{lamp} = 60 W. 35

Figure 2.16 Predicted CBZ removal for operation of the full-scale system under different conditions including: initial $[H_2O_2]$, number of 500-W UV lamps, and stormwater containing different concentrations of humic acid (A) 0.13 mg-C/L, (B) 1.25 mg-C/L, (C) 2.5 mg-C/L, and (D) 5.0 mg-C/L.. 36

Figure 2.17 Predicted E_{EO} for operating the full-scale system under different initial $[H_2O_2]$, number of UV lamps with stormwater containing different concentrations of humic acid (A) 0.13 mg-C/L, (B) 1.25 mg-C/L, (C) 2.5 mg-C/L, and (D) 5.0 mg-C/L. The power consumption associated with H_2O_2 generation was set as 1.9×10^{-5} kWh/mg-H_2O_2 to represent the average consumption for all current densities. 37

Figure 3.1 Schematic configuration of the electrochemical reactor. The system was operated with a constant potential by a potentiostat... 42

Figure 3.2 H_2O_2 concentrations in the presence of 100 mM of (A) methanol, (B) 2-propanol in buffer-containing Na_2SO_4 electrolyte. The experiments were conducted in the absence of stainless-steel electrodes. No formation of formaldehyde or acetone was observed. Error bars represent one standard deviation... 43

Figure 3.3 Schematic configuration of the undivided electrochemical reactor. 45

Figure 3.4 Concentrations of (A) H_2O_2 and (B) trace organic contaminants in Na_2SO_4-amended surface water in the absence of stainless-steel electrode. $[H_2O_2]_0$ = 1.25 mg/L. Error bars represent one standard deviation; error bars not shown are smaller than symbols. 46

Figure 3.5 Concentrations of trace organic contaminants in Na_2SO_4-amended surface water in the absence of H_2O_2. Potential = +0.020 V. Error bars represent one standard deviation; error bars not shown are smaller than symbols... 47

Figure 3.6 (A) H_2O_2 transformation, (B) formaldehyde formation, (C-E) metal leaching, and (F) current density during the pre-conditioning process. Potential = +0.020 V when not specified. Error bars and confidence band represent one standard deviation............ 49

Figure 3.7 (A) Rate constants for hydrogen peroxide decomposition, (B) current densities at different pH values and applied potentials. $[H_2O_2]_0$ = 1.25 mg/L, [Probe compound] = 100 mM. Error bars represent one standard deviation. 50

Figure 3.8 H_2O_2 concentrations in the cathode chamber at (A) pH 6 and (B) pH 7 with various concentrations of methanol in electrolyte. (C) Current density as a function of methanol concentration. Potential = +0.020V, $[H_2O_2]_0$ = 1.25 mg/L. Error bars represent one standard deviation; error bars not shown are smaller than symbols. 51

Figure 3.9 Pourbaix diagram for H_2O_2, $[H_2O_2]$ = 37 μM and $[^{\bullet}OH]_{SS} = 3.6 \times 10^{-11}$ M. The $[^{\bullet}OH]_{SS}$ was estimated based on a previously reported 1,4-dioxane degradation kinetics under similar operating conditions (Weng et al. 2020). Symbols represent experimental conditions tested in this study. 52

Figure 3.10 H_2O_2 transformation in the cathode chamber at varying initial H_2O_2 concentration. Applied potential = +0.020V, pH = 6. 53

Figure 3.11 Relationship between the observed current densities and initial H_2O_2 concentration. Applied potential = +0.020V, pH = 6. 54

Figure 3.12 Yield of oxidants as a function of pH and applied potential. $[H_2O_2]_0$ = 1.25 mg/L, [Probe compound] = 100 mM. Error bars represent one standard deviation; error bars not shown are smaller than symbols. 55

Figure 3.13 Electron utilization efficiency for (A) producing reactive oxidants and (B) for activating H_2O_2 as a function of pH and applied potential. $[H_2O_2]_0$ = 1.25 mg/L, [Probe compound] = 100 mM. Error bars represent one standard deviation; error bars not shown are smaller than symbols. 56

Figure 3.14 Concentrations of iron and chromium after five minutes of electrolysis at a potential of +0.020 V. *represents experiments conducted at potentials lower than +0.020 V (i.e., -0.039 V at pH 8 and -0.098 V at pH9). Error bars represent one standard deviation.. 57

Figure 3.15 Pourbaix diagram for (A) Fe, $[Fe]_{tot}$ = 1 mg/L, (B) Cr, $[Cr]_{tot}$ = 10 μg/L. Symbols represent experimental conditions tested in this study. 58

Figure 3.16 Atomic concentration of Fe in different oxidation states. Potential = +0.020 V, *represents experiments conducted at potentials lower than +0.020 V (i.e., -0.039 V at pH 8 and -0.098 V at pH9). Error bars represent one standard deviation........................ 60

Figure 3.17 Comparison of XPS measurements at different water vapor pressure. No apparent change was observed except for O1s. The additional peaks at 537 and 540 eV for O1s were associated with water vapor and potentially physically adsorbed water, respectively. 61

Figure 3.18 Metal concentrations after five minutes of electrolysis under various experimental conditions. Potential = +0.020 V, pH = 6. Error bars represent one standard deviation. For experiments conducted under anerobic conditions, the solution was purged with N_2 for at least 20 minutes before the experiment and was continuously purged with N_2 throughout the experiments in the sealed H-cell reactor. The flow rate of the N_2 stream was maintained at 0.5 L/min. Error bars represent one standard deviation. 62

Figure 3.19 Metal concentrations after five minutes of electrolysis of electrolyte containing varying concentrations of methanol. Error bars represent one standard deviation. Potential = +0.020 V. 63

Figure 3.20 Observed •OH yield as a function of methanol concentration. Potential = +0.020 V; $[H_2O_2]_0$ = 1.25 mg/L. Dashed lines represent the predicted stoichiometric efficiency based on eq 3.5. Error bars represent one standard deviation; error bars not shown are smaller than symbols. 64

Figure 3.21 Linear relationship between inverse of observed •OH yield and inverse of concentration of methanol. Error bars represent one standard deviation........ 65

Figure 3.22 Predicted •OH branching ratios for the treatment of 20 μg/L of carbamazepine with 4.5 g of stainless-steel electrode in the presence of 1.25 mg/L of H_2O_2 and various concentrations of competing organic compounds. Carbamazepine and H_2O_2 are also shown on the right axis. 66

Figure 3.23 Possible mechanisms for H_2O_2 transformation. 67

Figure 3.24 H_2O_2 decomposition and formaldehyde formation at open circuit potential and +0.020 V. Experiments conducted in buffered Na_2SO_4 electrolyte, pH = 6. $[H_2O_2]_0$ = 1.25 mg/L. Error bars represent one standard deviation. 68

Figure 3.25 (A) concentrations of representative trace organic contaminants and (B) released Fe and Cr during the treatment of an authentic water sample. Potential = +0.020 V, 1.25 mg/L of H_2O_2 was dosed every 20 minutes. Error bars represent one standard deviation. 69

Figure 4.1 Electrochemical cell configurations for H_2O_2 generation: (A) undivided cell configuration, (B) divided cell configuration. ADE represents air-diffusion electrode. .. 75

Figure 4.2 Photo of the stainless-steel electrode reactor. 76

Figure 4.3 Tafel plot of the relationship between current density (i) and overpotential for O_2 reduction for the formation of H_2O_2. 79

Figure 4.4 (A) Linear sweep voltammetry curves of the air-diffusion electrode and P75T carbon fiber paper substrate in 250 mM Na_2SO_4 (pH buffered at 7.0 by 50 mM phosphate buffer), potential scan rate: 2 mV s^{-1}. The inset shows the average current density observed through multiple trials using a 5 min chronoamperometry at the specified potentials in the presence of 10 mM H_2O_2. The dashed line indicates the equilibrium potential for the H_2O_2 generation reaction in the presence of 10 mM H_2O_2 at pH 7 (E = +0.32 V). (B) H_2O_2 production rate and Faraday efficiency obtained at the specified potentials with different cell configurations. Experiments conducted in real surface water amended with 250 mM of Na_2SO_4 or in 250 mM of Na_2SO_4 electrolyte. 80

Figure 4.5 (A) Anodic decomposition of H_2O_2. Experiment was conducted in 250 mM of Na_2SO_4 electrolyte using a divided cell configuration. $[H_2O_2]_0$ = 5 mM, applied current = 20 mA. (B) Observed Faraday efficiency in Na_2SO_4-amended surface water and predicted Faraday efficiency loss due to direct anodic oxidation of H_2O_2. Applied potential = -0.07 V, average observed current = 19 ± 1 mA for the undivided cell configuration. 82

Figure 4.6 pH values observed under various applied potentials on the air-diffusion electrode with different electrochemical cell configurations. Experiment was conducted in Na_2SO_4-amended surface water. 82

Figure 4.7 Schematic illustration of the dual-cathode treatment process. The air-diffusion electrode was separated from the Pt/Ti counter electrode by a cation exchange membrane. The stainless-steel electrode was coupled with a Pt electrode as the counter electrode in the flow-through reactor. 83

Figure 4.8 Control for TrOC sorption by the dual-cathode treatment system without any applied potential. Experimental conditions: 250 mM Na_2SO_4 buffered with 1 mM of PIPES buffer (pH 7), $[TrOCs]_0$ = 20 μg/L, recirculation rate = 70 mL/min.................... 84

Figure 4.9 Effect of applied potential on the air-diffusion electrode on (A) rate of removal of TrOCs and (B) observed current and steady-state H_2O_2 concentration in 250 mM Na_2SO_4 buffered with 5 mM of PIPES buffer (pH 7), recirculation rate = 35 mL/min. Effect of recirculation rate on (C) rate of removal of TrOCs and (D) observed current and H_2O_2 consumption rate in 250 mM Na_2SO_4 buffered with 1 mM of PIPES buffer (pH 7), applied current on air-diffusion electrode = 16 mA, applied potential on stainless-steel electrode (SSE) = +0.02 V. $[TrOCs]_0$ = 20 μg/L for all experiments. 85

Figure 4.10 Removal pathways of carbamazepine and atrazine in the dual-cathode treatment process. Conditions: $[TrOCs]_0$ = 20 μg/L, applied current on air-diffusion electrode = 16 mA, applied potential on stainless-steel electrode = +0.02 V, recirculation rate = 70 mL/min. SSE represents stainless-steel electrode; ADE represents air-diffusion electrode; DET represents direct electron transfer... 86

Figure 4.11 Comparison of the rate of TrOC oxidation by $^{\bullet}OH$ calculated based on the subtraction method versus inhibited TrOC removal rate upon addition of 200 mM of 2-propanol and allyl alcohol.. 87

Figure 4.12 Removal of benzoic acid and production of oxidation products of 2-propanol or benzoic acid. Conditions: $[TrOC]_0$ = 20 μg/L in 250 mM Na_2SO_4 buffered with 1 mM of PIPES buffer (pH 7), $[^{\bullet}OH\ scavenger]_0$ = 10 mM, applied current on air-diffusion electrode = 16 mA, applied potential on stainless-steel electrode = +0.02 V, recirculation rate = 70 mL/min. 88

Figure 4.13 Comparison of observed versus predicted scavenging effect of 2-propanol on TrOC removal. 89

Figure 4.14 H_2O_2 concentrations and consumption rates observed when authentic water was treated. Conditions: $[TrOC]_0$ = 20 μg/L, $[TOC]_0$ = 5.1 mg-C/L, applied current on air-diffusion electrode = 16 mA, applied potential on stainless-steel electrode = +0.02 V, recirculation rate = 70 mL/min. SSE represents stainless-steel electrode. 90

Figure 4.15 Concentrations of TrOCs and TOC observed when authentic water was treated. Conditions: $[TrOC]_0$ = 20 μg/L, $[TOC]_0$ = 5.1 mg-C/L, applied current on air-diffusion electrode = 16 mA, applied potential on stainless-steel electrode = +0.02 V, recirculation rate = 70 mL/min. 91

Figure 4.16 Metal released from the stainless-steel electrode when authentic water was treated. Conditions: $[TrOC]_0$ = 20 μg/L, $[TOC]_0$ = 5.1 mg-C/L, applied current on air-diffusion electrode = 16 mA, applied potential on stainless-steel electrode = +0.02 V, recirculation rate = 70 mL/min. 91

Figure 4.17 Comparison of energy consumption by the dual-cathode treatment process to other treatment technologies. The energy consumption corresponds to 90% reduction of the initial concentration of TrOCs contaminants (i.e., electrical energy per order) except for seawater RO. 92

Figure 4.18 Schematic of a dual-cathode treatment system with multiple points for dosing H_2O_2. 93

Figure 4.19 H_2O_2 generation in 250 mM Na_2SO_4 buffered with 1 mM of PIPES buffer (pH 7), $[TrOCs]_0$ = 20 μg/L using the divided cell configuration. Applied current on air-diffusion electrode = 16 mA, recirculation rate = 70 mL/min. The air-diffusion electrode had been operated for about 70 hours at 16 mA prior to the test. 94

Figure 4.20 Degradation of TrOCs over three cycles of operation. Applied current on air-diffusion electrode = 16 mA, applied potential on stainless-steel electrode = 0.02 V. Experiments conducted in real surface water, $[TrOCs]_0$ = 20 μg/L, recirculation rate = 70 mL/min. 95

Figure 5.1 Schematic of a spiral reactor for scaling up the H_2O_2 production. Image modified from (Arun et al. 2019). 99

Figure 5.2 (A) Long-term performance of the air-diffusion electrode operated in a flow-through mode. The stormwater contained 10 mg-C/L of humic acid. Current density = 200 A/cm^2, applied charge density = 125 kC/L. (B) Image of the liquid-facing side of the air-diffusion electrode after operation in Na_2SO_4-amended stormwater for 100 hours.... 99

Figure 5.3 Schematic of an automated stormwater advanced oxidation process enabled by wireless controllers and sensors. 100

Figure A.1 Natural logarithm of normalized atrazine concentration versus time. $[Atrazine]_0$ = 100 μg/L in simulated stormwater with 5 mM phosphate buffer (pH = 7) amended with different concentrations of humic acid. 130

Figure A.2 Graphically determination of k_{real} value from the actinometry experiments. Symbols and lines are assigned to results calculated based on $k_{observed}$ and k_{real}, respectively. 132

Figure A.3 Natural logarithm of normalized concentration versus time for carbamazepine and (A) MES in the presence of H_2O_2 at pH 6, (B) PIPES in the presence of H_2O_2 at pH 7, (C) MES in the absence of H_2O_2 at pH 6, and (D) PIPES in the absence of H_2O_2 at pH 7. $[\text{Test compound}]_{init.}$ = 1.0 μM, $[CBZ]_{init.}$ = 0.5 μM, $[H_2O_2]_{init.}$ = 10 μM, [Phosphate buffer] = 100 μM. Error bars represent one standard deviation. 134

Figure A.4 Example chromatogram of (A) DNPH method for acetone detection, (B) 10×diluted sample for the treatment of electrolyte containing 10 mM of 2-propanol at 120 min, (C) 10×diluted sample for the treatment of 250 mM Na_2SO_4 electrolyte containing 10 mM of acetone at 120 min, the electrolyte was buffered by 1 mM of PIPES buffer (pH 7). Applied current on air-diffusion electrode = 16 mA, applied potential on stainless-steel electrode = 0.02 V, recirculation rate = 70 mL/min. 135

Figure A.5 (A) Linear relation between the peak area of the acetone transformation product and the concentration of acetone that was transformed. Experimental condition:

250 mM Na_2SO_4 buffered with 1 mM of PIPES buffer (pH 7), $[acetone]_0 = 10$ mM. Applied current on air-diffusion electrode = 16 mA, applied potential on stainless-steel electrode = 0.02 V, recirculation rate = 70 mL/min. (B) Evaporation control for acetone in water, $[acetone]_0 = 10$ mM. 136

List of tables

Table 2.1 Simulated stormwater matrix composition. Suwannee River natural organic matter (concentration: 10 mg-C/L) or Sigma humic acid (concentration: 0-5 mg-C/L) was also added to the simulated stormwater matrix in some experiments to examine the effect of dissolved organic carbon on reaction efficiency. 13

Table 2.2 Properties of compounds that commonly detected in stormwater. 16

Table 2.3 Reactions relevant to the H_2O_2/UV process.. 18

Table 2.4 UV absorbance at 254 nm wavelength for chromophores. 19

Table 2.5 Performance metrics of different H_2O_2 generation methods............................ 22

Table 2.6 Concentrations of transition metals measured in the waters. 30

Table 3.1 Water quality parameters of the surface water.. 45

Table 3.2 Reactions considered for construction of Pourbaix diagrams. 59

Table A.1 Atrazine photolysis rate constants.. 132

Table A.2 Photon fluence rates for simulated stormwater amended with different concentrations of humic acid (0-5 mg-C/L)... 132

Table A.3 Compound-specific mass spectroscopy parameters. 133

Table A.4 E_{EO} values for UV/H_2O_2 processes at household scales. 138

Acknowledgments

I wish to convey heartfelt gratitude to those who have supported me during my journey through graduate school. My doctorate is the culmination of the tremendous efforts of a host of people.

I would like to express my deepest gratitude to my adviser, Prof. David Sedlak, who has been a role model as a researcher, educator, and mentor for me. His broad expertise and interests in water has trained me to think about water challenges and solutions beyond the scope of my dissertation. His persistence on quality over quantity has motivated me to be the best of myself. He has provided me enormous opportunities and freedom to explore new fields and ideas. His generous guidance was essential to the completion of my doctoral research.

I would like to acknowledge Prof. Baoxia Mi and Prof. Bryan McCloskey for their thoughtful review of this dissertation and for serving on my Qualifying Exam committee. I would also like to thank Prof. Kara Nelson and Prof. Laura Lammers for serving on my Qualifying Exam committee. I wish to thank all my committee members as well as Prof. Lisa Alvarez-Cohen and Prof Ashok Gadgil for offering advice along the way and broadening my horizons beyond environmental chemistry.

I would like to extend my sincere thanks to Joseph Charbonnet, who was a former doctoral student of the Sedlak Lab, and who is my mentor and close friend. His mentorship in the laboratory during my first year and his support along the way were essential to my overall wonderful experience in the graduate school.

I would also like to thank my fellow graduate students, post-doctoral researchers, and research scientists: Wenli Jiang, Jiancong Chen, Siva Rama Satyam Bandaru, Rachel Scholes, Emily Marron, Angela Stiegler, Tae-Kyoung Kim, Daniel Ocasio, Emily Kraemer Sheeleigh, Scarlet-Marie Kilpatrick, Griffin Walsh, Jean Van Buren, Marc Teixido Planes, Amy Cuthbertson, Katerina Tsou, Christopher I Olivares, Emily Cook, Mohan Sun, Ned Antell, Hannah Greenwald, Soliver Fusi, Sunxiang Zheng, Zhongying Wang, Sidney Poon, Casey Finnerty, Monong Wang for providing support and friendship during my time at Berkeley.

Finally, I would like to thank my parents, Wanxiang Duan and Xiaoling Xu, and friend, Menglian Xia, for always supporting me every step of the way. They have always been my source of inspiration and motivation. Without their support, I would not decide to pursue a doctoral degree as an international student. I could not be more thankful for the enormous support they have given me and amazing opportunities they have allowed me to explore.

CHAPTER 1. Introduction

1.1 Distributed water treatment as a solution for the global water challenges

Globally, nearly 2.2 billion people still lack access to safely managed water services, with the majority of these populations located in low-income countries and rural areas where the centralized water infrastructure is often infeasible (Unicef 2017). This lack of safely managed water is estimated to cause 1.2 million deaths and accounts for 2.2% of global deaths (Ritchie and Roser 2021). The social and environmental injustice associated with this situation has motovated efforts to development more effective approaches for providing safe drinking water in these locations.

Despite the significant improvement in public health associated with the extensive network of centralized water system that have been built in middle- and high-income countries, much of the world's water infrastructures has outlived its design lifetime and requires major investments in maintenance or replacement to ensure water quality (Hering et al. 2013). For example, in United States, 6 billion gallons of clean, safe drinking water are lost every day throughly leaky pipes and nearly 240 thousand water main breaks every year (American Society of Civil Engineers 2021).

In addition, climate change, urbanization, and chemical contaminants are posing new challenges for exisiting centralized water infrastructure (National Academies of Sciences, Engineering, and Medicine 2019). For example, climate change is expected to intensify regional contrasts in precipitation that already exist, which will further exacebate water scarcity in dry areas such as southwestern United States (Masson-Delmotte et al. 2021). Furthermore, continued population growth in urban areas will further compound the current water challenges. By 2050, 2 billion more people will live in urban areas but majority of them will be in low-income countries that contain large informal settlements (World Bank Group 2017). With many cities unable to provide adaquate water and sanitation for these areas, residents will face significant risks of water-borne diseases, such as diarrhoea, cholera, and typhoid (Ezeh et al. 2017). Finally, the widely presence of trace organic contaminants such as pesticides, industrial chemicals, and detergent metabolites are challenging for the conventional water systems as many of these organic contaminants are not removed during water treatment (Luo et al. 2014).

To create drinking water systems that are more equitable, affordable and resilient, researchers have proposed the development and deployment of distributed water treatment that rely on non-traditional water sources (Larsen et al. 2016). Non-traditional water sources (i.e., stormwater, roof water, municipal wastewater and groundwater from shallow aquifers), after proper treatment, can be used to agument drinking water supplies. It also can be used for industrial and agricultural purposes. Because of the dispersed nature of these water sources, distributed treatment systems have significant advantages over conventional centralized systems. Advantages of distributed systems include flexibility (i.e., they can be installed quickly and tailored to meet the needs of a wide range of users) and their ability to functions without extensive water distribution infrastrcuture (Leigh and Lee 2019). As a result, distributed water treatment has the potential to reduce energy consumption and lower the cost of infrastructure replacement and construction (Hering et al. 2013).

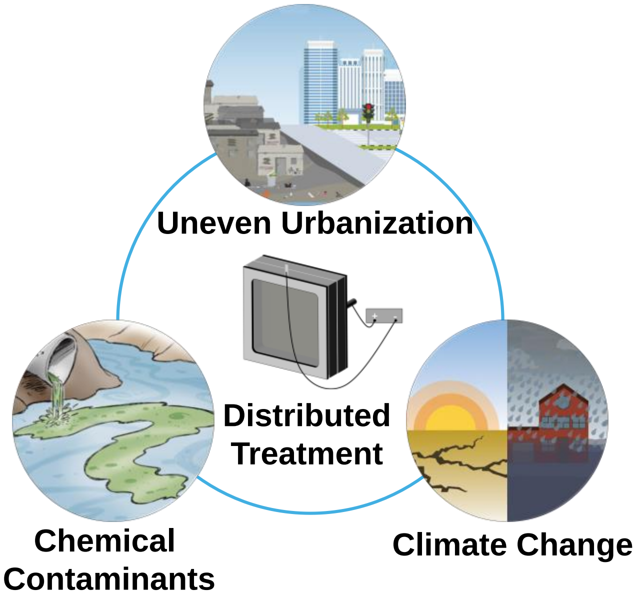

Figure 1.1 Distributed treatment systems have strong potential to address the water challenges associated with climate change, chemical contaminants, and uneven urbanization.

1.2 Treatment technologies for distributed water treatment

Due to economies of scale in manufacturing and their ease of operation, household reverse osmosis (RO) and water filters equipped with sorbents are among the most common distributed water treatment systems installed at household scale, especially when the water source is relatively clean (e.g., tap water or groundwater that contains unsafe levels of contaminants). Despite their relatively low costs, household RO systems are often limited by low water recovery (~50%) and challenges associated with concentrate management (Peter-Varbanets et al. 2009). Sorbents (e.g., activated carbon) produce waste that can be challenging to manage in distributed treatment systems (Baskar et al. 2022, Kah et al. 2021, Trellu et al. 2018). In addition, sorbents also tend to be less effective in the removal of polar, low molecular weight contaminants (e.g., 1,4-dioxane, 1,2,3-trichloropropane) that frequently contaminate water supplies (McElroy et al. 2019, U.S. Environmental Protection Agency 2017). Finally, the operation of those point-of-use water treatment often fail because customers usually do not replace their filter cartridge at the frequency suggested by manufacturers (Wu et al. 2021a).

As an alternative to household RO and sorbents, advanced oxidation processes may be more suitable because they can avoid some of the challenges associated with the waste management and frequent maintenance of system components.

1.2.1 Ultraviolet (UV)/H_2O_2

The UV/H_2O_2 process is the most popular advanced oxidation process for water recycling, groundwater remediation and industrial wastewater treatment because it does not produce toxic byproducts or otherwise diminish water quality (von Gunten 2018).

$$H_2O_2 \xrightarrow{UV} 2\ {}^{\bullet}OH \tag{1.1}$$

The ${}^{\bullet}OH$ produced in eq 1.1 reacts with most organic contaminants at near diffusion-controlled rates. These reactions typically result in oxidation of contaminants to products that are more susceptible to microbial oxidation or other oxidation processes such as by dissolved oxygen or naturally occurring minerals (Cuerda-Correa et al. 2020, Nidheesh et al. 2022).

Despite their simplicity and efficacy, commercially available UV/H_2O_2 systems are often difficult to employ in distributed water treatment systems because submerged UV lamps are prone to fouling and require frequent cleaning and maintenance (Fast et al. 2017). Recently, a low-cost UV reactor was developed for drinking water disinfection in resource limited communities (Gadgil 2008). By suspending the UV lamp above water, this type of UV reactor avoids fouling of the surface. However, this improvement is accompanied by a tradeoff; due to reflection and light scattering, much of the UV light never makes it into the water.

In addition to the fouling on the UV lamps, the UV/H_2O_2 process also exhibits other drawbacks associated with the low molar absorption coefficient of H_2O_2 at 254 nm. For a typical drinking water source containing about 5 mg-C/L of natural organic matter, more than 95% of the UV light will be absorbed by natural organic matter (Duan and Sedlak 2021). As a result, high fluence and high concentrations of H_2O_2 are often applied, resulting in high energy consumption and waste of H_2O_2 (e.g., only ~10% of the H_2O_2 applied is consumed) (Chuang et al. 2017, Zhang et al. 2019).

1.2.2 Anodic processes for contaminants oxidation

Electrochemical anodic oxidation has been studied extensively for removal of trace organic contaminants because of their potential advantages over established water treatment technologies, including: (1) the ability to treat multiple classes of contaminants; (2) in-situ production of chemicals; and (3) modular cell configurations (Barazesh et al. 2015, Barazesh et al. 2016, Radjenovic and Sedlak 2015). Inactive electrodes (e.g., boron-doped diamond, SnO_2, PbO_2, and sub-stoichiometric titanium-oxide) are often used because of their high production of ${}^{\bullet}OH$. These electrodes usually have a high overpotential for O_2 evolution (e.g., $E_H > +2.0$ V vs SHE), which enables the partial oxidation of water to form ${}^{\bullet}OH$ prior to the recombination of O atom to produce O_2 (eq 1.2). The ${}^{\bullet}OH$ is produced at the electrode surface and could either react with contaminants at the surface or diffuse into solution (Xie et al. 2022).

$$H_2O \rightarrow {}^{\bullet}OH + H^+ + e^- \tag{1.2}$$

Due to the diffusion distance of ${}^{\bullet}OH$ is limited to about 1 μm (Kapałka et al. 2009), diffusive transport of contaminant through the boundary at the electrode surface is often the rate-limiting step for contaminant removal, especially when plate electrode reactors are operated in a flow-by mode (Figure 1.2A), which often results in the formation of a thick diffusional boundary layer (e,g, ~100 μm) (Chaplin 2019, Radjenovic and Sedlak 2015). As an alternative, porous three-dimensional electrodes in flow-through mode (Figure 1.2B) can overcome the mass-transfer limitation as the convective transport of water through the small pores of the electrode decreases the diffusional boundary layer thickness. However, fabrication of porous three-dimensional electrodes is limited by their fabrication processes (e.g., boron-doped diamond electrodes are typically synthesized using chemical vapor deposition methods).

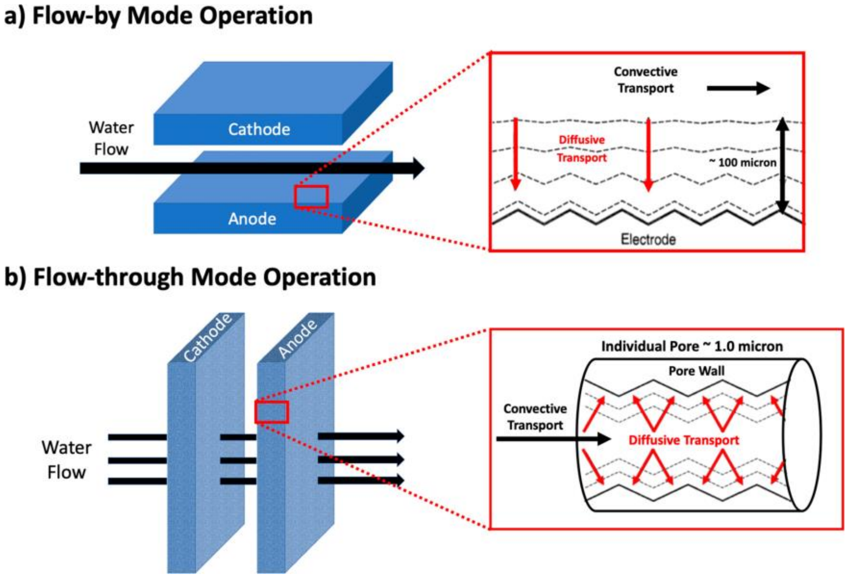

Figure 1.2 Electrochemical reactor operation in (a) flow-by mode operation and (b) flow-through mode operation. Adapted from (Chaplin 2019).

Although the high overpotential increases the activity of the electrode and is also conducive to other contaminant transformation pathway (i.e., direct electron transfer) (Chaplin 2014), it results in high energy consumption. For example, boron-doped diamond electrodes consume about 50 kWh of electricity to achieve 90% removal of organic contaminants (e.g., *p*-chlorobenzoic acid) from 1 m^3 of water, which is over an order of magnitude higher than the energy consumed by seawater desalination (Miklos et al. 2018). In addition to the high energy consumption, the capital cost of the electrodes also limits their application. For example, boron-doped diamond electrodes costs over \$7000 per m^2 (Chaplin 2019). Although other materials (e.g., SnO_2) may have lower cost than the boron-doped diamond electrode, their performance is often limited by their short service lives (Chaplin 2014). Finally, the formation of toxic organic and inorganic products from the electrochemical oxidation process poses additional concerns. For example, the formation of ClO_3^- and ClO_4^- has been observed in the presence of halide ions at concentrations comparable to those expected in drinking water sources (Azizi et al. 2011, Bergmann and Rollin 2007). Therefore, successful implementation of the anodic processes for distributed water treatment requires strategies to lower the energy consumption and fabrication cost as well as to minimize the formation of toxic byproducts.

1.2.3 Reduction of H_2O_2 for $^\bullet OH$ production

As an alternative to producing $^\bullet OH$ by using electrodes to oxidize water, H_2O_2 can be reduced by a one-electron process that forms $^\bullet OH$.

$$H_2O_2 + e^- \rightarrow OH^- + {}^{\bullet}OH \qquad (1.3)$$

The one-electron reduction of H_2O_2 is the basis for using Fenton's reagent (eq 1.3) to treat water that contains high concentrations of organic compounds, such as agricultural and food processing waste, industrial wastewaters, and landfill leachates.

$$Fe^{2+} + H_2O_2 \rightarrow Fe^{3+} + OH^- + {}^{\bullet}OH \qquad (1.4)$$

The Fenton reaction offers several advantages over other advanced oxidation processes as it does not require an external energy input (e.g., UV lamps) and ${}^{\bullet}OH$ production occurs in the bulk aqueous phase where it is not affected by the high concentrations of suspended solids and surface-active organic contaminants (Pignatello et al. 2006). However, the Fenton reaction only produces a high yield of ${}^{\bullet}OH$ over a relatively narrow pH range (i.e., pH 2-4) due to a shift in the reaction mechanism that occurs as Fe(II) hydrolyzes (Bossmann et al. 1998, Hug and Leupin 2003, Jacobsen et al. 1998, Keenan and Sedlak 2008). The narrow pH range limits its application for drinking water treatment or requires expensive acidification and neutralization steps.

Heterogeneous Fenton catalysts (e.g., Fe(III)-oxides) have been used to convert H_2O_2 to ${}^{\bullet}OH$ at circumneutral pH conditions. However, the stoichiometric yield for production of oxidants that are capable of transforming contaminants is typically very low (i.e., < 5%) (Chou et al. 2001, Huang et al. 2001, Huling et al. 1998, Kanel et al. 2004, Lee and Sedlak 2009, Seo et al. 2015, Valentine and Wang 1998, Xue et al. 2009). In these systems, the majority of H_2O_2 is transformed through a non-radical mechanism that converts H_2O_2 directly to O_2 and H_2O (Kwan and Voelker 2002, Petigara et al. 2002, Vafaei Molamahmood et al. 2022).

Custom-made electrodes composed of carbonaceous materials and metals (Hu et al. 2021, Peng et al. 2015, Zeng et al. 2020, Zhao et al. 2016, Zhao et al. 2012) have been proposed as alternatives to heterogeneous catalysts for producing ${}^{\bullet}OH$ from H_2O_2. However, many of these electrodes are fabricated as flat plate reactors that are operated in the flow-by mode and the contaminant transformation is limited by mass transfer of contaminant to the electrode surface (Figure 1.2A).

Recently, a low-cost stainless-steel electrode has been investigated as a means of converting H_2O_2 to ${}^{\bullet}OH$ for contaminant oxidation in RO permeate (Weng et al. 2020). The porous structure of the stainless-steel electrode has a strong potential to improve the treatment performance when operating in a flow-through mode (Figure 1.2B), where convective transport of water can significantly decrease the boundary layer thickness (Chaplin 2019). The high specific surface area of the stainless-steel electrode offers additional advantage to develop compact treatment technologies for distributed treatment system.

1.3 Electrochemical generation of chemical reagents for distributed water treatment

The use of electricity to produce chemical reagents employed in water treatment has strong potential to enable distributed water treatment because the delivery of chemicals (e.g., acids, bases, oxidants, and disinfectants) needed for treatment of drinking water and the provision of sanitation is a major challenge, especially for distributed systems. In addition, from a life cycle analysis perspective, chemical reagents contribute a significant fraction of the total operational cost and greenhouse gas emissions associated with water treatment processes (Mousset et al. 2021).

Recent developments in air-diffusion electrodes have enabled in-situ generation of H_2O_2 (Figure 1.3). The air-diffusion electrode can reduce the complexity of device by eliminating the need to bubble air or pure oxygen into a solution (Barazesh et al. 2015). Additionally, by relying on the O_2 that diffuses into the electrode from the atmosphere, the air-diffusion electrodes overcomes the slow mass transport of dissolved O_2, which often limits the H_2O_2 generation in systems relying on submerged electrodes.(Valim et al. 2013, Zhang et al. 2020b) Finally, a high Faraday efficiency (> 90%) has been achieved in a previous study that used carbon black as the catalyst (Barazesh et al. 2015).

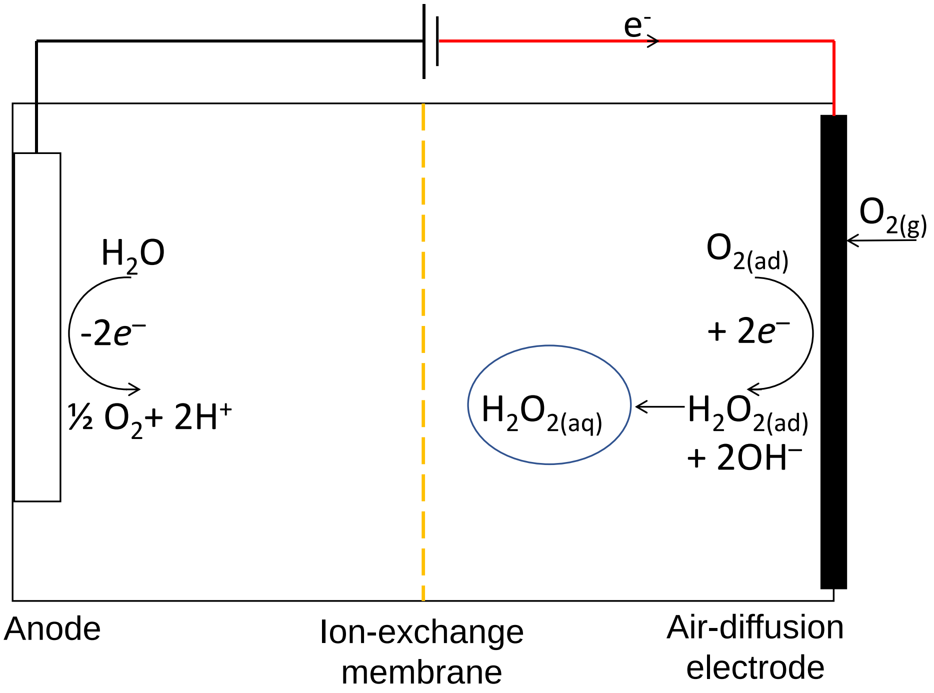

Figure 1.3 Schematic of an electrochemical reactor that contains an air-diffusion electrode as the working electrode for H_2O_2 production.

Despite the potential for deployment of the air-diffusion electrode to generate H_2O_2 for point-of-use UV/H_2O_2 processes, its application for distributed water systems at a larger scale still merits further investigation. For example, distributed stormwater treatment often requires treatment capacity of hundreds of liters per minute for applications such as the treatment of stormwater runoff as it flows into drywells. Scaling up the UV/H_2O_2 prototype by simply increasing the electrode area would require several square meters of the electrodes to generate sufficient concentrations of H_2O_2. Additionally, because of the low conductivity of stormwater runoff, scaling up the reactor by applying a high current density significantly increases the energy consumption due to the ohmic loss in the solution. Therefore, better strategies for H_2O_2 production are needed to for the large-scale distributed water treatment.

In addition to challenges associated with scaling up laboratory-scale treatment systems, precise control of the rate of H_2O_2 production may pose additional challenge for distributed water treatment. For example, insufficient H_2O_2 production could decrease the treatment performance (Wang et al. 2021). Excess amount of H_2O_2 could results in inefficient use of energy and may requires additional post-treatment to remove the residual H_2O_2 (Watts et al. 2012). Thus, research that improves our understanding of reaction mechanisms and processes affecting system performance are critical to future deployment of small-scale electrochemical water treatment systems.

1.4 Dissertation Outline

The rest of dissertation is organized into the following chapters.

Chapter 2 focuses on developing and assessing the feasibility of an electrochemical advanced oxidation process for distributed treatment of stormwater prior to its infiltration into drinking water aquifers. The proposed treatment system consisted of an electrochemical module for H_2O_2 production and a UV reactor that is resistant to fouling (Figure 1.4). The performance of the H_2O_2 production system was evaluated under different current densities and electrolyte compositions in terms of H_2O_2 production rate, Faraday efficiency as well as maximum H_2O_2 concentration that can be generated and stored. Finally, the performance of the electrochemical advanced oxidation process was assessed in lab scale and modeled in full scale (i.e., 400 L/min) to assess its technical and economic feasibility.

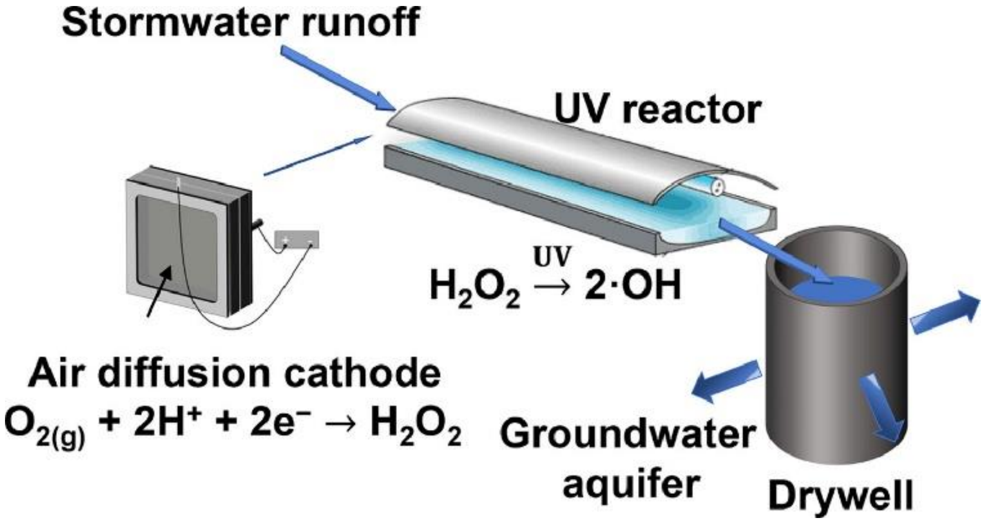

Figure 1.4 Schematic of the proposed stormwater treatment system combining an electrochemical reactor for H_2O_2 production and a UV reactor for H_2O_2 activation.

Chapter 3 focuses on the performance of a stainless-steel electrode that activates H_2O_2 to produce reactive oxidant species. The rate of H_2O_2 activation on the stainless-steel electrode was evaluated under different solution pH and applied potentials. The reactive oxidant species (e.g., Fe[IV] or $^{\bullet}OH$) were identified and their yields were quantified by adding different probe compounds that are known to react preferentially with different oxidants. Metal leaching from stainless-steel electrode was assessed under different operating conditions. Chemical thermodynamics and surface characterization techniques were used to gain insight into the mechanisms of metal leaching. Because the electrode surface may act as a scavenger for the reactive oxidant species, the scavenging capacity of the surface were assessed using competition kinetics. Finally, possible reaction mechanisms for producing the reactive oxidant species on the electrode surface were proposed.

Chapter 4 focuses on the performance of a reagent-free electrochemical treatment process consisted of the air-diffusion electrode and the stainless-steel electrode. The reactor configuration of the air-diffusion electrode was varied to minimize H_2O_2 loss and maintain circumneutral pH condition (H_2O_2 activation on stainless-steel electrode is most effective at circumneutral pH) during H_2O_2 production. The H_2O_2 production process and H_2O_2 activation process were optimized separately in terms of applied potentials. The mass transport of contaminants was assessed by operating under different recirculation rates. The potential benefit of repulsion of negatively charged compounds capable of reacting with $^{\bullet}OH$ by the cathode surface was investigated in the presence of compounds with different charges that are known to react with $^{\bullet}OH$ in the bulk solution. Finally, the removal of trace organic contaminants was tested in an authentic surface water sample and energy consumption was compared with other technologies for distributed water treatment.

Chapter 5 concludes this dissertation by summarizing the key findings from each chapter. This chapter also outlines future research to adapt electrochemical advanced oxidation for distributed water treatment.

CHAPTER 2. An Electrochemical Advanced Oxidation Process for the Treatment of Urban Stormwater

Reproduced with permission from Duan, Y., Sedlak, D. L., An Electrochemical Advanced Oxidation Process for the Treatment of Urban Stormwater. *Water Research X* 2021, 13, 100127.

2.1 Introduction

Climate change and rapid population growth are exacerbating water scarcity in cities around the world (Flörke et al. 2018). The capture and use of urban stormwater are attractive to water-stressed cities because this underutilized water source is available in large quantities and does not require large investments in environmentally damaging, long-distance conveyance systems. Due to limited opportunities for water storage within cities, captured urban runoff might best be used for aquifer recharge in cities that rely upon groundwater (Luthy et al. 2019). However, stormwater contains contaminants including pesticides, compounds released by vehicles and waterborne pathogens, all of which can pose risks to drinking water supplies (Grebel et al. 2013, Rippy et al. 2017, Spahr et al. 2020). Rather than relying upon natural attenuation or treatment after extraction to remove trace organic contaminants, some form of treatment may be appropriate prior to recharge (Zhang et al. 2020a).

Researchers have studied the use of engineered geomedia, such as manganese oxide-coated sands (Charbonnet et al. 2020, Grebel et al. 2016), woodchips (Ashoori et al. 2019), functionalized clays (Ray et al. 2019) and biochar (Ashoori et al. 2019, Boehm et al. 2020, Ulrich et al. 2015) as a passive means of stormwater treatment. However, such treatment systems are often limited by the low hydraulic conductivities of geomedia or underlying soils and sediments (Barnes et al. 2014, Minnesota Stormwater Steering Committee 2005, Ray et al. 2019). Infiltration rates are also limited by the need to achieve adequate contact times between the engineered geomedia and the contaminants (Grebel et al. 2016, Shimabuku et al. 2016). In addition, geomedia eventually will clog or be exhausted, which necessitates replacement or regeneration to assure continued operation (Charbonnet et al. 2018, 2021). As a result, infiltration-based techniques that employ geomedia are often unable to treat large volumes of stormwater in urban areas.

In locations where surface infiltration is impractical, drywells offer an attractive alternative due to their high infiltration rates and small footprints (Edwards et al. 2016). For reference, to achieve a recharge rate of 400 L/min, a value typical of drywells, an area of 1.5 m^2 and 1200 m^2 would be required for drywells and rain gardens (maximum infiltration rate = 2 cm h^{-1}), respectively (Hunt et al. 2010, Prince George's County 1999, Torrent Resources). However, it has been difficult to incorporate treatment systems capable of removing trace organic compounds and viruses into drywells because high flow rates during storms often preclude the use of geomedia. As a result, the use of drywells for urban stormwater infiltration without any form of treatment has contaminated groundwater with volatile organic compounds, benzene, and petroleum hydrocarbons (City of Portland Bureau of Environmental Services 2008, Jurgens et al. 2008, Lindemann 1999).

Advanced oxidation processes (AOPs) such as UV/H_2O_2 have been used for over 40 years to oxidize organic contaminants in hazardous waste, drinking water and contaminated groundwater by taking advantage of the high reactivity and low selectivity of hydroxyl radical ($^{\bullet}$OH) (Koubek 1977). Furthermore, the process also controls waterborne pathogens because the fluence of ultraviolet (UV) light used in the process is typically about ten times higher than values used to disinfect drinking water (Sun et al. 2016). Despite its potential applicability, only a few attempts (Bettman 2020, Zheng et al. 2021) have been made to employ AOPs in stormwater treatment systems due to the cost and challenges associated with system maintenance and reagent replenishment, especially when infiltration structures are distributed around a city.

Electrochemical advanced oxidation processes (EAOPs) are promising options for decentralized system because of their modular design, high efficiency, and ease of automation (Feng et al. 2018, Kanakaraju et al. 2018, Miklos et al. 2018, Moreira et al. 2017, Nidheesh et al. 2018, Yang 2020, Yang and Hoffmann 2016). To overcome the difficulties associated with using AOPs for distributed water treatment, we employed an inexpensive, compact system that generates H_2O_2 by electrochemical reduction of O_2 (eq 2.1) with an air-diffusion cathode that uses only electricity and passive diffusion of air.

$$\mathrm{O_2} + 2e^- + 2\mathrm{H^+} \rightarrow \mathrm{H_2O_2} \quad E_H^\circ = +0.70\ \mathrm{V} \qquad (2.1)$$

The H_2O_2 is then converted to $^\bullet$OH by exposure to UV light (eq 2.2) in a low-cost reactor that was originally developed for drinking water disinfection in resource limited communities (Gadgil 2008).

$$\mathrm{H_2O_2} \xrightarrow{\mathrm{UV}} 2 \cdot \mathrm{OH} \qquad (2.2)$$

To employ this approach in a drywell or another type of stormwater infiltration system, a sufficient quantity of H_2O_2 must be generated using inexpensive equipment that can fit into a small area. To accomplish this objective, we formed H_2O_2 generation and storage strategies to produce a H_2O_2 stock solution prior to the storm event (potentially with stormwater captured previously) and then metered the H_2O_2 stock solution into stormwater prior to exposing it to UV light. Using a kinetic model of H_2O_2 activation and contaminant transformation, we assessed the feasibility of employing UV/H_2O_2 to treat urban stormwater under conditions typically encountered in drywells. Finally, by systematic optimization of each process, we demonstrated EAOP is feasible for distributed stormwater treatment.

2.2 Materials and Methods

2.2.1 Materials

All experiments were performed at room temperature (23 ± 2 °C) with chemicals of reagent grade or higher (Sigma-Aldrich, St. Louis, MO). Suwannee River natural organic matter (reverse osmosis isolate) was obtained from the International Humic Substances Society (St. Paul, MN). Ultrapure water from a Milli-Q system (R > 18 MΩ) was used for all experiments except when specifically noted.

Simulated stormwater was made in the manner described by Grebel et al. (2016). The composition of the water (Table 2.1) was chosen to represent the main solutes in urban runoff. In a previous study, this matrix exhibited similar performance to that observed in authentic stormwater (Grebel et al. 2016). In AOP experiments (Section 2.5), a synthetic humic acid sodium salt (Sigma-Aldrich, St. Louis, MO) and deionized water (Culligan, Rosemont, IL) were used rather than Suwanee River natural organic matter and Milli-Q water because of the high cost of preparing the large volumes of water to run the experiments (i.e., about 9 L of synthetic stormwater was needed to assess each configuration of the treatment system). All solutions containing organic carbon (i.e., humic acid or natural organic matter) were prepared from a concentrated organic carbon stock solution (typically around 100 mg of chemicals/L), which was filtered through 0.45-µm glass fiber filters (Tisch Scientific, Cleves, OH) prior to use.

Table 2.1 Simulated stormwater matrix composition. Suwannee River natural organic matter (concentration: 10 mg-C/L) or Sigma humic acid (concentration: 0-5 mg-C/L) was also added to the simulated stormwater matrix in some experiments to examine the effect of dissolved organic carbon on reaction efficiency.

Constituent	Concentration	Unit
Ca^{2+}	0.75	mM
Mg^{2+}	0.075	mM
Na^{+}	1.75	mM
NH_4^{+}	0.072	mM
SO_4^{2-}	0.33	mM
HCO_3^{-}	1.00	mM
Cl^{-}	1.70	mM
NO_3^{-}	0.072	mM
$H_2PO_4^{-}$	0.016	mM
Ionic strength	4.60	mM
pH	7.46 ± 0.20 6.84 ± 0.30	(Natural organic matter amended) (Humic acid amended)

2.2.2 Electrochemical cell and UV reactor

Electrolysis experiments were performed in a two-chambered parallel plate electrochemical cell modified from the device described by Barazesh et al. (2015). Briefly, the electrochemical cell was made of acrylic plastic (McMaster-Carr, Los Angeles, CA) and equipped with a Pt-coated Ti mesh anode (dimensions: 5.1 × 7.6 cm; TWL, USA) and a home-made air-diffusion cathode (dimensions: 4.0 × 4.0 cm) as described by Barazesh et al. (2015). Graphite powder (200 mesh, Alfa Aesar, Ward Hill, MA) and PTFE were coated on the air-facing side of the cathode. Carbon black (Cabot Black Pearls 2000, Cabot, Boston, MA) and PFTE were coated on the liquid-facing side with propanol as solvent. The cathodic chamber and anodic chamber were separated by a cation exchange membrane (Ultrex CMI-7000, Membranes International Inc., Ringwood, NJ). The thickness of each chamber was 1.7 cm. The divided electrochemical cell was chosen to avoid anodic oxidation of H_2O_2, which could limit the generation of high concentration H_2O_2 solutions and lower the Faraday efficiency of the generation process (Abdullah and Xing 2017, Ma et al. 2019, Panizza and Cerisola 2008, Pérez et al. 2017).

After H_2O_2 was generated in the electrochemical cell, the H_2O_2-containing catholyte was mixed with the anolyte to form a H_2O_2 stock solution. The H_2O_2 stock solution was then diluted into simulated stormwater and passed through a UV reactor. The UV reactor used in this study was described by Gadgil and Garud (1998) . Briefly, the reactor had a volume of 5.5 L and included a 60-watt low-pressure UV lamp (Philips, Andover, MA) mounted under an aluminum reflector. The UV lamp was situated approximately 6 cm above the surface of the flowing water.

2.2.3 H_2O_2 generation and energy consumption

Batch experiments to assess H_2O_2 generation were conducted in Na_2SO_4 electrolyte or in simulated stormwater amended with Na_2SO_4. Equal volumes of solution were circulated in the two-cell chambers at a flow rate of 30 mL/min with a peristaltic pump (Masterflex, Vernon Hills, IL). Electrolysis experiments were performed at fixed currents controlled by a direct current power supply (B&K Precision, Yorba Linda, CA). The air-diffusion cathode was tested under different current densities (200 to 1200 A/m^2) and replaced if any leaks were detected or a low initial Faraday efficiency (i.e., below around 70%) was measured. Despite the decreased performance of the electrode over time, the electrode performance was relatively stable for several runs of operation (at least tens of hours). All H_2O_2 generation experiments were conducted at least in triplicate (n = 3-6).

The applied charge density ($\rho_\mathrm{q}, \mathrm{C/L}$) was calculated based on the current density ($i, \mathrm{A/m^2}$), electrode area ($A, \mathrm{m^2}$), electrolysis time (t, s), and catholyte volume (V_ca, L):

$$\rho_q = \int_0^t \frac{i \times A}{V_{ca}} dt = \frac{iAt}{V_{ca}} \tag{2.3}$$

The energy consumed during H_2O_2 generation was calculated based on the measured H_2O_2 concentration ($[H_2O_2]$, M), catholyte volume (V_ca, L), electrolysis time (t, s), current density ($i, \mathrm{A/m^2}$), and cell voltage (V_cell, V):

$$Energy \left(\frac{kWh}{mg\ \mathrm{H_2O_2}}\right) = \frac{\int_0^t iV_{cell}A dt}{[\mathrm{H_2O_2}]V_{ca}} \frac{1\ mol\ \mathrm{H_2O_2}}{34000\ mg\ \mathrm{H_2O_2}} \frac{1\ kWh}{3.6\times10^6\ J} \tag{2.4}$$

2.2.4 H_2O_2 stability

The stability of the H_2O_2 stock solution was assessed before and after mixing the catholyte with the anolyte. The H_2O_2 was generated under 800 A/m^2 of applied current density in batch mode with Na_2SO_4 electrolyte or Na_2SO_4-amended simulated stormwater. For the mixed electrolyte storage, catholyte and anolyte were mixed slowly with a peristaltic pump. To examine the effect of dissolved solids on H_2O_2 stability, 50 mg/L of San Joaquin soil (NIST SRM 2709a, Gaithersburg, MD) was added to the mixed simulated stormwater (Mean TSS in urban stormwater = 58 mg/L as described by Grebel et al., 2013) .

2.2.5 Advanced oxidation process

Experiments to assess the performance of the AOP were conducted in a simulated stormwater solution amended with different concentrations of Sigma humic acid (0-5 mg-C/L). During each experiment, 9 L of simulated stormwater amended with 10 μg/L of carbamazepine (CBZ) was circulated between a HDPE bucket (M&M Industries, Chattanooga, TN) and the UV reactor (V = 5.5 L) with a submersible pump operated at a flow rate of 7.6 L/min (Figure 2.1). By circulating the stormwater, we were able to simulate the performance of an upscaled UV reactor consisting of multiple UV reactors in series without the complexity of operating the large system under laboratory conditions. The H_2O_2 stock solution was diluted from a 0.18 ± 0.03 M (n = 15) stock solution by mixing equal volumes of catholyte and anolyte generated by batch-mode electrolysis of a 0.2 M Na_2SO_4 electrolyte solution.

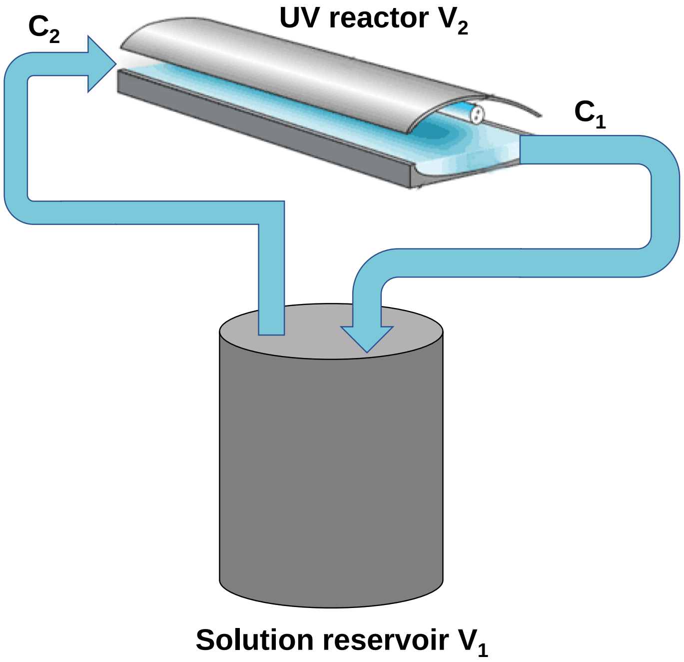

Figure 2.1 Schematic of the reactor setup for UV/H_2O_2 process.

Although CBZ has not been detected frequently in stormwater, it was chosen as a surrogate for trace organic contaminants in stormwater because it is mainly transformed by reactions with $^{\bullet}OH$ radicals; it exhibits a low rate of direct photolysis and does not react with other photo-produced transients produced by UV light (Barazesh et al. 2015). Most stormwater contaminants (e.g., pesticides) exhibit similar rate constants to CBZ for reactions with $^{\bullet}OH$ radical. Some compounds also may be transformed by direct photolysis and/or transient species produced when natural organic matter is exposed to UV light (Table 2.2). For some compounds that react with $^{\bullet}OH$ radicals slower than CBZ (e.g., atrazine), the overall removal rates were observed to be higher than that of CBZ during the UV/H_2O_2 process because the other compounds undergo direct photolysis (Rozas et al. 2016). Therefore, CBZ can be used as a surrogate for most of the trace organic contaminants commonly detected in stormwater.

Table 2.2 Properties of compounds that commonly detected in stormwater.

Contaminant group	Compound	ε_{254} (M^{-1} cm^{-1})	Φ_{254}	$k_{\cdot OH}$ (M^{-1} s^{-1})	Reference
Pharmaceuticals	Carbamazepine	6.0×10^{3}	6.0×10^{-4}	9.1×10^{9}	(Jasper and Sedlak 2013, Pereira et al. 2007b, Vogna et al. 2004)
Biocides	Carbendazim	4.5×10^{3}	2.3×10^{-3}	2.2×10^{9}	(Mazellier et al. 2003, Mazellier et al. 2002)
Insecticides	Dimethoate	0[a]	n.d.[b]	8.5×10^{9}	(Marin et al. 2011, Wu et al. 2021b)
	Diazinon	2.0×10^{3}	8.6×10^{-2}	9.0×10^{9}	(Shemer and Linden 2006)
	Fipronil	n.d.	n.d.	3.9×10^{9}	(King et al. 2020)
	Imidacloprid	1.1×10^{4}	8.5×10^{-3}	1.0×10^{10}	(Aregahegn et al. 2017, Armbrust 2000)
Herbicides	2,4-D	1.5×10^{2}	9.5×10^{-3}	5.1×10^{9}	(Benitez et al. 2004, Feigenbrugel et al. 2006)
	Atrazine	3.9×10^{3}	4.6×10^{-2}	3.0×10^{9}	(Acero et al. 2000, Hessler et al. 1993, Nick et al. 1992)
	Dicamba	4.3×10^{2}	9.5×10^{-2}	1.3×10^{9}	(Armbrust 2000, Wong and Chu 2003)
	Diuron	1.5×10^{4}	2.0×10^{-2}	9.5×10^{9}	(Jirkovský et al. 1997, Olasehinde et al. 2013)
	Isoproturon	5.9×10^{3}	2.0×10^{-3}	5.2×10^{9}	(Benitez et al. 2006, Sanches et al. 2010)
	Mecoprop	2.1×10^{2}	8.8×10^{-1}	2.5×10^{9}	(Armbrust 2000, Semitsoglou-Tsiapou et al. 2016)
	Metolachlor	5.0×10^{2}	3.0×10^{-1}	9.1×10^{9}	(Wu et al. 2007)
Plasticizers	BPA	7.5×10^{2}	4.6×10^{-3}	6.9×10^{9}	(Baeza and Knappe 2011, Peller et al. 2009)

[a] absorption of 254 nm UV is insignificant.

[b] n.d. means no data available.

The light field in the UV reactor was characterized by chemical actinometry using atrazine under the same experimental conditions. The solution was amended with 100 μg/L of atrazine (ε_{254} = 3860 M^{-1} cm^{-1}, Φ_{254} = 0.046 mol Ei^{-1}); the same concentrations of humic acid was used (0-5 mg-C/L). The solution was buffered at pH = 7 using a 5 mM phosphate buffer (Bolton and Linden 2003, Canonica et al. 2008). The light fluence, which was measured before and after the advanced oxidation experiments, varied by less than 5%. Details of the calculation of light fluence are included in Section A.1.1 of the Appendix.

2.2.6 Analytical methods

H_2O_2 was measured with a titanium (IV) sulfate method modified from Eisenberg (1943) with a Shimadzu UV-2600 spectrophotometer at 420 nm. H_2O_2 was measured within 5 minutes of sampling to minimize artifacts caused by H_2O_2 decomposition. Total organic carbon (TOC) was measured using a Shimadzu TOC-V analyzer. CBZ-containing samples were filtered through 0.22-μm glass fiber filters prior to adding isotopically labeled internal standard and 100 μL of methanol to quench any possible $^{\bullet}OH$ reactions that could consume CBZ. CBZ was quantified in multiple reaction monitoring (MRM) mode with an Agilent 1200 series HPLC system coupled to a 6460 triple quadrupole tandem mass spectrometer (HPLC-MS/MS) within 24 hours after sampling (Jasper et al. 2014). Metal ions were quantified in triplicate on an Agilent 7700 Series Inductively Coupled Plasma-Mass Spectrometer (ICPMS).

2.2.7 Kinetic model for the UV/H_2O_2 treatment

A kinetic model was employed based on reaction schemes developed in previously published studies (Crittenden et al. 1999, Glaze et al. 1995, Song et al. 2008) using Kintecus version 6.80 (Ianni 2003).

Previously published studies have described the reaction mechanisms in the UV/H_2O_2 process and measurement of rate constants for the reactions involved in the transformation of trace organic compounds (Baxendale and Wilson 1957, Crittenden et al. 1999, Glaze et al. 1995). Under UV irradiation, each molecule of H_2O_2/ HO_2^- is cleaved to form two $^{\bullet}OH$ or one $^{\bullet}OH$ and one $^{\bullet}O^-$, which react with H_2O to produce $^{\bullet}OH$. A substantial fraction of $^{\bullet}OH$ radicals react with H_2O_2/ HO_2^- to initiate a chain reaction that results in further decomposition of H_2O_2 (Table 2.3 reaction 4, 5, 8, 9, 11, 13, 14). Some of the $^{\bullet}OH$ also react with the trace organic compound, humic substances or HCO_3^-.

The photolysis rate of H_2O_2 is governed by the rate of reaction 1 (Table 2.3). The quantum yield of the primary process (reaction 1) $\Phi_{H_2O_2,primary}$ at 254 nm is 0.5 (Baxendale and Wilson 1957). However, the overall quantum yield $\Phi_{H_2O_2,overall}$, which describes the overall process including the chain reactions is unity at 254 nm (Baxendale and Wilson 1957).

Table 2.3 Reactions relevant to the H_2O_2/UV process

	Reaction	Reaction rate constant	Reference
1	$H_2O_2 \xrightarrow{hv} 2{\cdot}OH$	$k_1 = \frac{W_\lambda}{Z}(1\text{-}10^{-\alpha_\lambda Z})\frac{\varepsilon_{H_2O_2}\Phi_{H_2O_2}}{\alpha_\lambda}$	
2	$HO_2^- + H_2O \xrightarrow{hv} 2{\cdot}OH + OH^-$	$k_2 = \frac{W_\lambda}{Z}(1\text{-}10^{-\alpha_\lambda Z})\frac{\varepsilon_{HO_2^-}\Phi_{HO_2^-}}{\alpha_\lambda}$	
3	$CBZ \xrightarrow{hv} ?$	$k_3 = \frac{W_\lambda}{Z}(1\text{-}10^{-\alpha_\lambda Z})\frac{\varepsilon_{CBZ}\Phi_{CBZ}}{\alpha_\lambda}$	
4	${\cdot}OH + H_2O_2 \longrightarrow O_2^{\bullet-} + H_2O + H^+$	$k_4 = 2.7 \times 10^7\ M^{-1}\ s^{-1}$	(Buxton et al. 1988)
5	${\cdot}OH + HO_2^- \longrightarrow O_2^{\bullet-} + H_2O$	$k_5 = 7.5 \times 10^9\ M^{-1}\ s^{-1}$	(Buxton et al. 1988)
6	${\cdot}OH + HCO_3^- \longrightarrow H_2O + {\cdot}CO_3^-$	$k_6 = 8.5 \times 10^6\ M^{-1}\ s^{-1}$	(Buxton et al. 1988)
7	${\cdot}OH + CO_3^{2-} \longrightarrow OH^- + {\cdot}CO_3^-$	$k_7 = 3.9 \times 10^8\ M^{-1}\ s^{-1}$	(Buxton et al. 1988)
8	${\cdot}OH + HO_2{\cdot} \longrightarrow H_2O + O_2$	$k_8 = 8.0 \times 10^9\ M^{-1}\ s^{-1}$	(Elliot and Buxton 1992, Sehested et al. 1968)
9	${\cdot}OH + O_2^{\bullet-} \longrightarrow OH^- + O_2$	$k_9 = 6.6 \times 10^9\ M^{-1}\ s^{-1}$	(Sehested et al. 1968)
10	${\cdot}OH + CBZ \longrightarrow ?$	$k_{CBZ,{\cdot}OH} = 9.1 \times 10^9\ M^{-1}\ s^{-1}$	(Jasper and Sedlak 2013)
11	$O_2^{\bullet-} + H_2O_2 \longrightarrow {\cdot}OH + OH^- + O_2$	$k_{11} = 0.13\ M^{-1}\ s^{-1}$	(Weinstein and Bielski 1979)
12	$O_2^{\bullet-} + {\cdot}CO_3^- \longrightarrow O_2 + CO_3^{2-}$	$k_{12} = 6.5 \times 10^8\ M^{-1}\ s^{-1}$	(Eriksen et al. 1985)
13	$O_2^{\bullet-} + HO_2{\cdot} + H_2O \longrightarrow H_2O_2 + OH^- + O_2$	$k_{13} = 9.7 \times 10^7\ M^{-1}\ s^{-1}$	(Buxton et al. 1988)
14	$HO_2{\cdot} + HO_2{\cdot} \longrightarrow H_2O_2 + O_2$	$k_{14} = 8.3 \times 10^5\ M^{-1}\ s^{-1}$	(Buxton et al. 1988)
15	${\cdot}CO_3^- + H_2O_2 \longrightarrow HCO_3^- + O_2^{\bullet-} + H^+$	$k_{15} = 8.0 \times 10^5\ M^{-1}\ s^{-1}$	(Draganić et al. 1991)
16	${\cdot}CO_3^- + HO_2^- \longrightarrow HCO_3^- + O_2^{\bullet-}$	$k_{16} = 3.0 \times 10^7\ M^{-1}\ s^{-1}$	(Draganić et al. 1991)
17	${\cdot}CO_3^- + {\cdot}CO_3^- \longrightarrow ?$	$k_{17} = 3.0 \times 10^7\ M^{-1}\ s^{-1}$	(Huie and Clifton 1990, Mandal et al. 1991)
18	${\cdot}OH + DOC \longrightarrow ?$	$k_{18} = 9.8 \times 10^3\ L\ mgC^{-1}\ s^{-1}$	(Appiani et al. 2014) (Barazesh et al. 2015)
19	${\cdot}OH + Cl^- \longrightarrow HOCl^{\cdot-}$	$k_{19} = 4.3 \times 10^9\ M^{-1}\ s^{-1}$	(Jayson et al. 1973)
20	$HOCl^{\cdot-} \longrightarrow {\cdot}OH + Cl^-$	$k_{20} = 6.1 \times 10^9\ s^{-1}$	(Jayson et al. 1973)
21	$HOCl^{\cdot-} + H^+ \longrightarrow Cl{\cdot} + H_2O$	$k_{21} = 2.1 \times 10^{10}\ M^{-1}\ s^{-1}$	(Jayson et al. 1973)
22	${\cdot}CO_3^- + CBZ \longrightarrow ?$	$k_{22} = 2.3 \times 10^6\ M^{-1}\ s^{-1}$	(Jasper and Sedlak 2013)

The molar absorption coefficients of the major chromophores are summarized in Table 2.4. The molar absorption coefficient for humic acid at 254 nm was experimentally measured using a Shimadzu UV-2600 spectrophotometer and a Shimadzu TOC-V analyzer.

Table 2.4 UV absorbance at 254 nm wavelength for chromophores.

Species	DOC	Carbamazepine	H_2O_2
ε	0.083 ± 0.001 (L mg^{-1} cm^{-1})	6025 (M^{-1} cm^{-1})	18.6 (M^{-1} cm^{-1})
References	This study	(Vogna et al. 2004)	(Morgan et al. 1988)

The observed photon fluences, $W_{254,\text{ observed}}$, were used for model validation. For full-scale performance prediction, the UV fluence rates were calculated with number of UV lamps (N), power of UV lamps (P, W) and volume of the full-scale reactor ($V_{\text{full-scale}}$, L) and lab-scale reactor (V_{UV}, L), and $W_{254,\text{ real}}$:

$$W_{full-scale} = \frac{N \cdot P \cdot W_{254,real} \cdot V_{UV}}{60\text{W}\, V_{full-scale}} \tag{2.5}$$

2.3 Results and Discussion

2.3.1 H_2O_2 generation as a function of current density

The applied current density could affect the H_2O_2 generation performance. For stormwater treatment, an ideal electrode should be able to generate a high concentration of H_2O_2 stock solution with high Faraday efficiency. Comparing to in situ generation of H_2O_2 in a flow-through reactor (Barazesh et al. 2015), generating a high concentration of H_2O_2 before a storm event and storing it could reduce the energy consumption and system footprint by reducing the applied current density and electrode area. It could also minimize the amount of salt added to the treated stormwater (when H_2O_2 is produced in a salt-amended electrolyte solution as described below). However, at very high concentrations, especially under basic pH conditions encountered in the catholyte (pH around 11.5, Figure 2.2), the H_2O_2 is unstable due to self-decomposition and reactions with transition metals and organics (Galbács and Csányi 1983, Petigara et al. 2002). Under applied current, H_2O_2 can also undergo electrochemical reduction to H_2O (Jiang et al. 2018b). Therefore, development of a better understanding of the effect of current density on H_2O_2 production rate, Faraday efficiency and factors affecting the maximum H_2O_2 concentration that can be generated provides a basis for selecting an optimum operational mode.

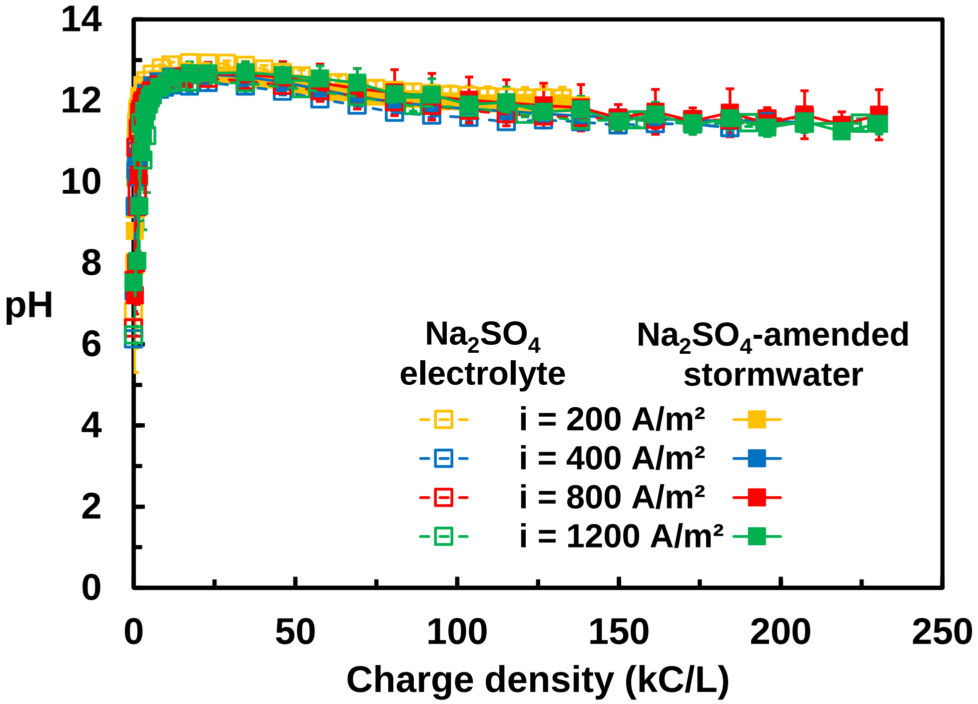

Figure 2.2 Catholyte pH change during H_2O_2 generation. Error bars represent one standard deviation; error bars not shown are smaller than symbols.

Hydrogen peroxide formation in the catholyte (Figure 2.3) exhibited similar behavior in Na_2SO_4 electrolyte and in Na_2SO_4-amended stormwater at current densities ranging from 200 to 1200 A/m^2. The H_2O_2 concentrations increased in approximately a linear fashion with the applied charge density up to about 120 kC/L, at which point a concentration of around 430 mM had been produced. For electrolysis conducted with 200 A/m^2 of current density, the H_2O_2 concentration remained at around 430 mM as the charge density further increased. For electrolysis conducted with higher current densities, after the charge density reaching 120 kC/L, the H_2O_2 generation efficiency decreased until the H_2O_2 concentration in catholyte plateaued at around 600 mM. Because of the similar performance with respect to applied current density, the system design and operation adjustment can be significantly simplified, leading to considerable flexibility in the operation of the treatment system.

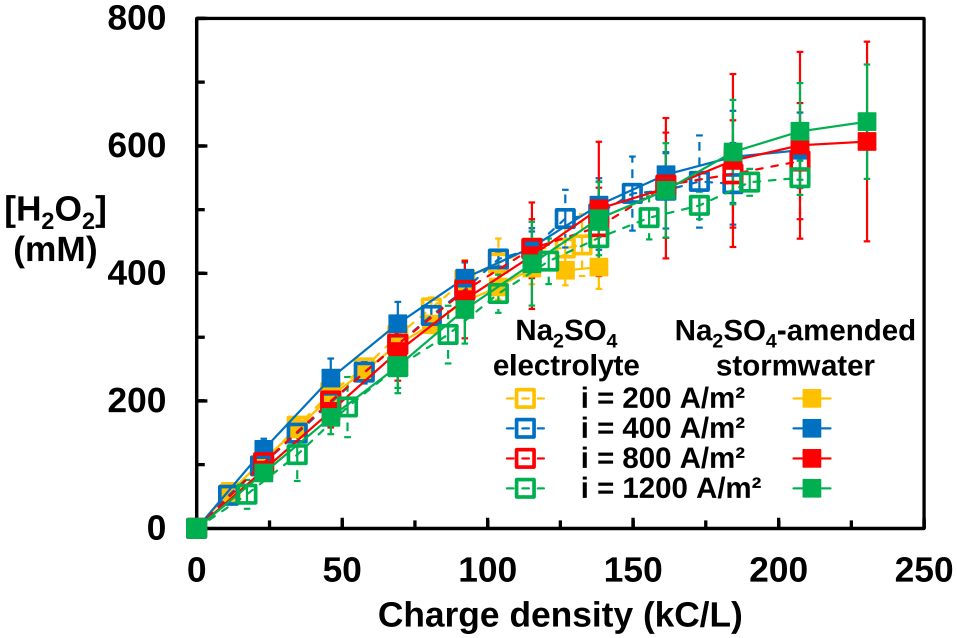

Figure 2.3 Production of H_2O_2 during electrolysis in 0.2 M Na_2SO_4-amended stormwater and 0.2 M Na_2SO_4 electrolyte at varying current densities. Error bars represent one standard deviation.

To assess the performance of this air-diffusion cathode for H_2O_2 generation at high H_2O_2 concentrations, these data were compared with results from previous studies on electrochemical synthesis of H_2O_2 in terms of surface normalized production rate, Faraday efficiency, and maximum H_2O_2 concentration (Table 2.5). The device tested in this study was better suited for producing a concentrated stock solution for use in water treatment than the other 12 systems reported in the literature that also can generate a relatively high concentration of H_2O_2 solution with relative high Faraday efficiency. This may be due to the fact that most previous efforts either focused on achieving the maximum possible H_2O_2 concentration ($[H_2O_2]_{max}$ ranged from 320 to 5500 mM; Faraday efficiency ranged from 12 to 60%) (Iwasaki et al. 2018, Luo et al. 2015, Oloman and Watkinson 1979, Yamanaka et al. 2008, Yamanaka and Murayama 2008, Yamanaka et al. 2006) or high Faraday efficiency (Faraday efficiency ranged from 79 to 99 %; $[H_2O_2]_{max}$ ranged from 24 to 250 mM) (Chen et al. 2017, Li et al. 2013, Sa et al. 2019, Wang et al. 2020b). Li et al. (2020) achieved 980 mM of $[H_2O_2]_{max}$ with a Faraday efficiency of 79%. But their fuel cell reactor inhibits the application of their device in distributed locations because of lack of supply of pure H_2 and O_2 in the actual field condition. In addition, most of those devices were designed to be operated in strongly acidic or alkaline conditions, with deteriorating performances observed at lower acid/base concentrations (Foller et al. 1991, Yamanaka et al. 2008). Among the other approaches, the method of Xia et al. (2019) shows considerable promise due to its high Faraday efficiency (90 to 95 %) and ability to produce a high concentration of H_2O_2 (5900 mM). However, the system requires pumping humidified air as a source of O_2 rather than relying on the passive diffusion of air. The system also requires passage of water through a solid electrolyte. These requirements would likely increase the system cost and increase the risk of system failures, two outcomes that could be problematic in remote operations.

Table 2.5 Performance metrics of different H_2O_2 generation methods.

Cathodic catalyst	Electrolyte	Production rate (mmol cm^{-2} hour^{-1})	Faraday efficiency (%)	$[H_2O_2]_{max}$ (mM)	Reference
Graphite particles	2 M NaOH	N/A	60	800	(Oloman and Watkinson 1979)
Carbon black and PTFE	0.2 M Na_2SO_4	0.6	21	320	(Luo et al. 2015)
Activated carbon, vapor-growing-carbon fiber, and PTFE	1.2 N H_2SO_4	0.14	40	350	(Yamanaka et al. 2008)
Activated carbon, vapor-growing-carbon fiber, and PTFE	Nafion 117	0.04	12	950	(Yamanaka and Murayama 2008)
Heat-treated Mn–porphyrin/Carbon	0.5 M H_2SO_4	0.4	47	1100	(Yamanaka et al. 2006)
CoTPP/Ketjen-Black	Nafion-H	0.9	55	5500	(Iwasaki et al. 2018)
Mesoporous carbon (CMK-3)	0.1 M KOH	N/A	>90	80	(Chen et al. 2017)
Edge site-rich nanocarbon	0.1 M KOH	N/A	99	24	(Sa et al. 2019)
Carbon-supported Ni^{II} single-atom catalysts with a tetradentate Ni-N_2O_2 coordination	0.1 M KOH	1.2	>90	250	(Wang et al. 2020b)
Co–C composite catalyst	Nafion 112	0.2	30	N/A	(Li et al. 2013)
Al_2O_3/platinum diphosphide nanocrystals	Polymer electrolyte	2.3	79	980	(Li et al. 2020)
Functionalized carbon black	Solid electrolyte	3.4	90-95	5900	(Xia et al. 2019)
Black carbon	As described in method	0.3-1.6	60-98*	600	This study

* Faraday efficiency decreased during electrolysis due to H_2O_2 decomposition (Figure 2.4).

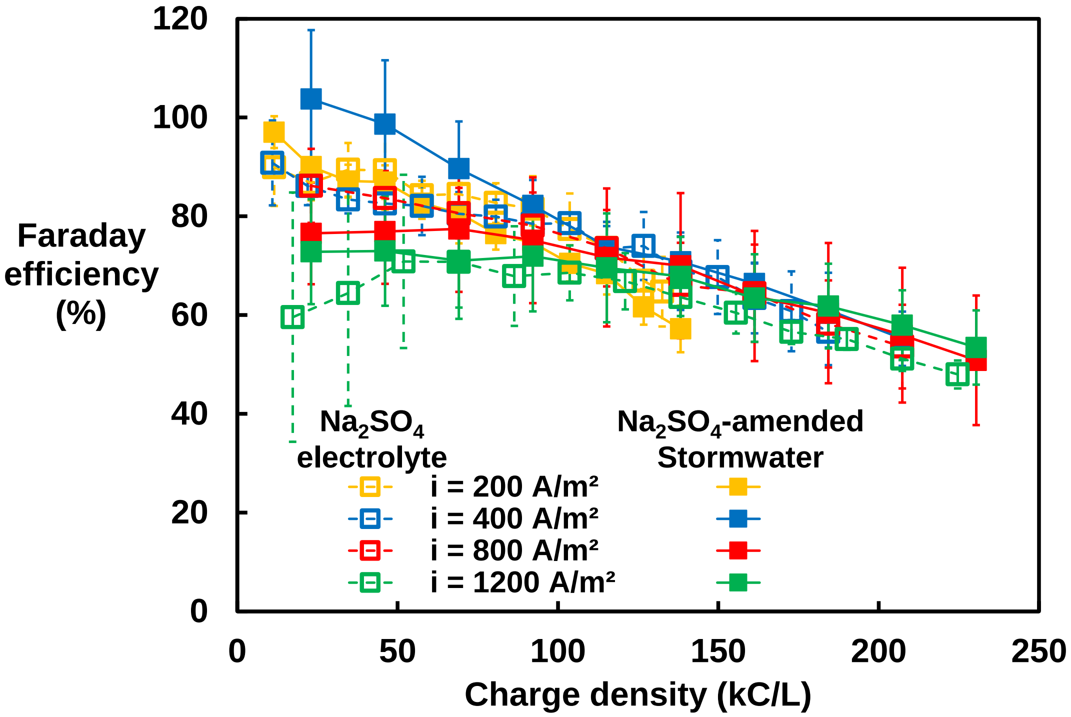

Figure 2.4 Faraday efficiency during electrolysis in 0.2 M Na_2SO_4-amended simulated stormwater and 0.2 M Na_2SO_4 electrolyte. Error bars represent one standard deviation.

2.3.2 Energy consumption during H_2O_2 generation

The energy consumption was dictated by the cell voltage, which was mainly affected by the ohmic loss and the overpotential. The ohmic loss of an electrochemical system depends upon the conductivity of the solution; the overpotential is the driving force of the electrochemical process and was mainly determined by the electrode material and the applied current density.

For low-conductivity solutions (e.g., stormwater), the energy consumption was mainly affected by the low conductivity of the electrolyte. Therefore, it is possible to reduce the energy consumed for H_2O_2 production by adding an inert electrolyte (e.g., Na_2SO_4) to the stormwater. Na_2SO_4 was chosen as the electrolyte amendment because of its relatively low cost (about $100/ton) and the absence of undesirable products (e.g., ClO_3^- from NaCl oxidation) produced when it passes through the anode chamber.

To determine the optimal salt dosage for H_2O_2 generation, electrolysis was performed in simulated stormwater (10 mg-C/L of natural organic matter) amended with varying concentrations of Na_2SO_4 (Figure 2.6). The energy consumption for H_2O_2 generation was estimated assuming a Faraday efficiency η = 65 % and calculated based on the cell voltage recorded after at least one hour of electrolysis (V_{cell}, V), current density (i, A/m^2), cell voltage (V_{cell}, V), electrode area (A, m^2), electrolysis time (t, s), and Faraday constant (F, 96485 C/mol):

$$Energy\ \left(\frac{kWh}{mg\ \mathrm{H_2O_2}}\right) = \frac{iV_{cell}At}{\frac{iAt}{2F}\cdot\eta} = \frac{2FV_{cell}}{\eta}\frac{1\ mol}{34000\ mg\mathrm{H_2O_2}}\frac{1\ kWh}{3.6\times10^6\ J} \tag{2.6}$$

The cell voltage after one hour of electrolysis was used because it can be used as a rough approximation of the averaged cell voltage through the whole H_2O_2 generation process (Figure 2.5).

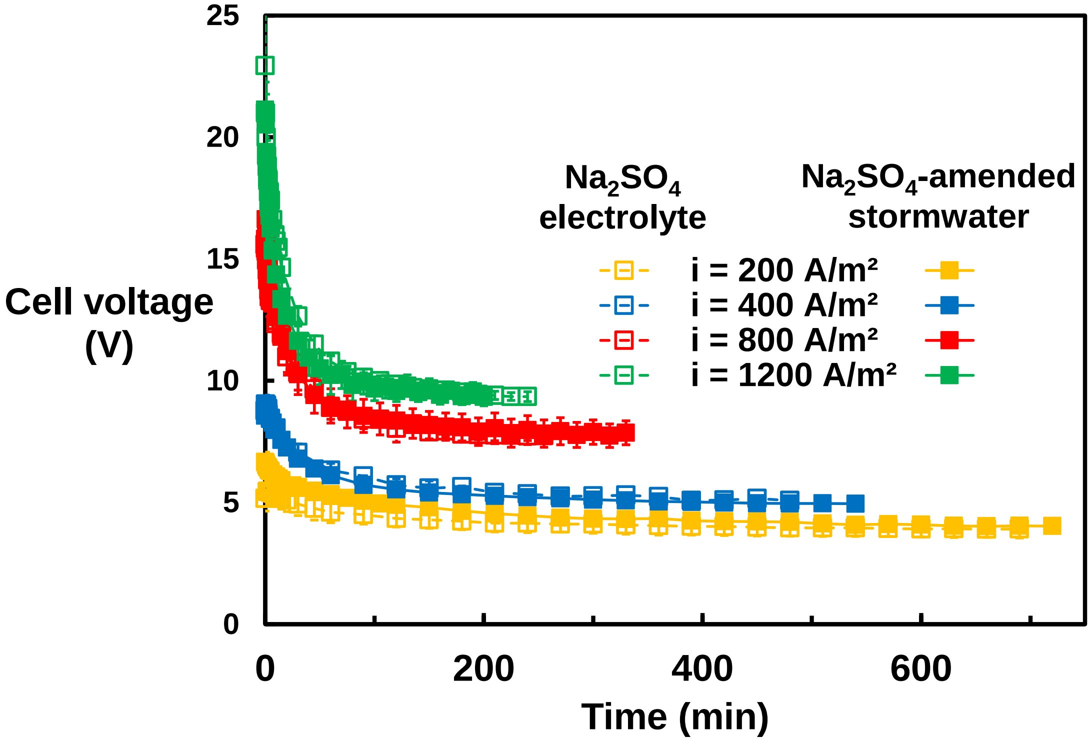

Figure 2.5 Cell voltage as a function of time during electrolysis in 0.2 M Na_2SO_4-amended simulated stormwater and 0.2 M Na_2SO_4 electrolyte. Error bars represent one standard deviation.

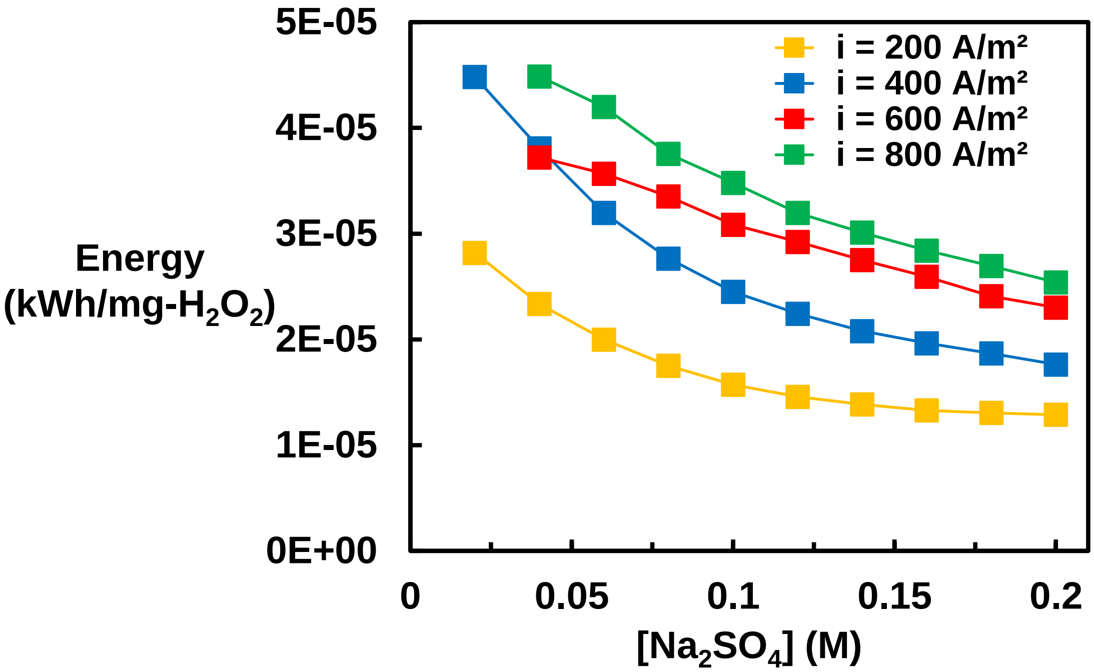

Figure 2.6 Effect of Na_2SO_4 amendment concentrations in simulated stormwater and applied current densities on energy consumption for H_2O_2 generation.

At lower salt concentrations ([Na_2SO_4] < 0.1 M), the energy consumption increased dramatically as the salt concentration decreased. At [Na_2SO_4] > 0.1 M, the addition of salts barely decreased the energy consumption because the overpotential dominated the cell voltage. A Na_2SO_4 concentration of 0.2 M was chosen to strike a balance between energy consumption and the amount of salt added to the stock solution.

The salt amendment cost, electricity cost and overall cost to generate a 450 mM H_2O_2 stock solution were estimated at various Na_2SO_4 amendment concentrations and current densities (Figure 2.7). The cost of Na_2SO_4 was assumed as \$100/ton. The electricity cost was assumed as the average price of electricity in California, \$0.16/kWh (U.S. Energy Information Administration 2020). Given the relatively low cost of the Na_2SO_4 comparing to the cost of electricity, the estimated overall cost of the system was decreased by adding Na_2SO_4 into stormwater used for production of the H_2O_2 stock solution. For realistic operating conditions, the amount of salts can be determined by balancing the energy cost and the cost for delivering and dosing the salts into the solution.

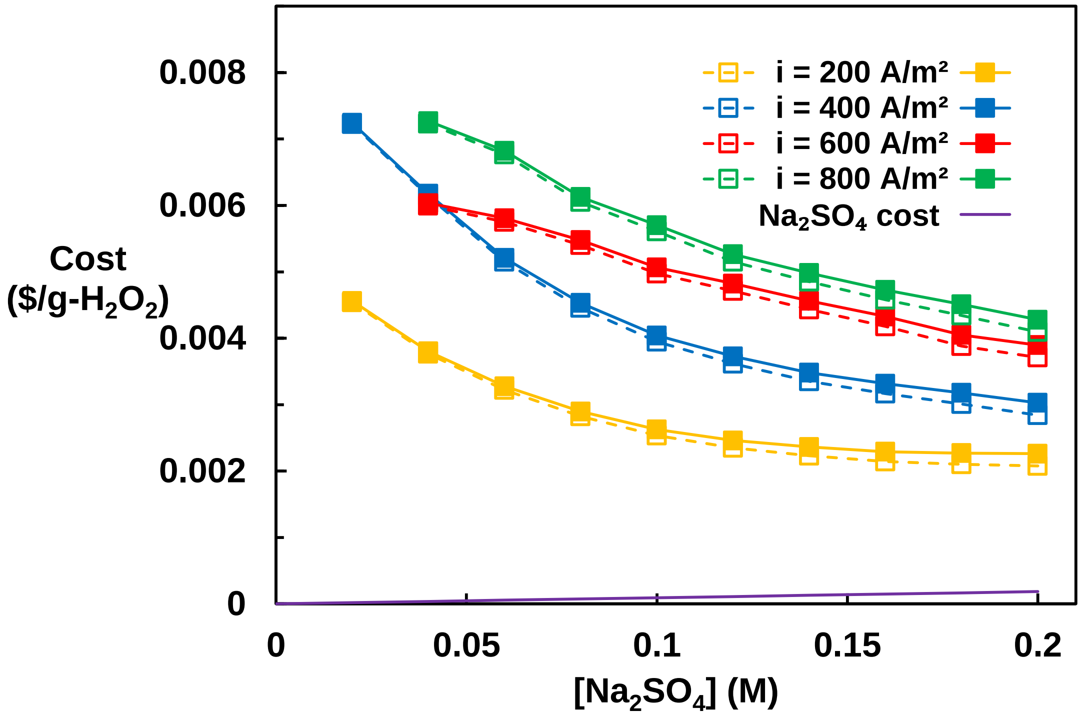

Figure 2.7 Estimated salt amendment cost, electricity cost and overall cost for H_2O_2 generation at various Na_2SO_4 amendment concentrations and current densities; [H_2O_2] = 450 mM.

Adding an electrolyte to a stock solution prior to H_2O_2 generation and then mixing a small volume of concentrated H_2O_2 solution into the stormwater would increase the total dissolved solids (TDS) of the treated stormwater. To avoid adverse impacts on water quality, it is important to assure that the TDS and sulfate concentration of the treated water would not exceed the USEPA secondary maximum contaminant levels (SMCLs) for TDS of 500 mg/L as well as the sulfate concentration limit of 250 mg/L (USEPA 2022b). If the target H_2O_2 concentration in the stock solution was 200 mM and a 0.2 M solution of Na_2SO_4 was used in the stock solution, then addition of H_2O_2 to produce an initial H_2O_2 concentration of 1 mM in the stormwater will increase the TDS by about 140 mg/L and sulfate by around 100 mg/L which would be acceptable for drinking water purposes, provided that the initial stormwater TDS and sulfate concentrations were below 360 mg/L and 150 mg/L, respectively. If this were not the case, a lower concentration of Na_2SO_4 would be necessary.

The energy consumption increased with respect to the applied current density (Figure 2.8). The increasing in energy consumption with increased current density was due to the increased ohmic loss and overpotential. The solution matrix (i.e., the presence or absence of synthetic stormwater constituents) had little effect on the energy consumption because of the similar solution conductivity and H_2O_2 generation performance between Na_2SO_4-amended simulated stormwater and Na_2SO_4 electrolyte. For electrolysis performed with current density of 800 A/m^2 and 1200 A/m^2, the energy consumption increased slightly after the H_2O_2 concentration reaching 450 mM due to decreased H_2O_2 generation efficiency.

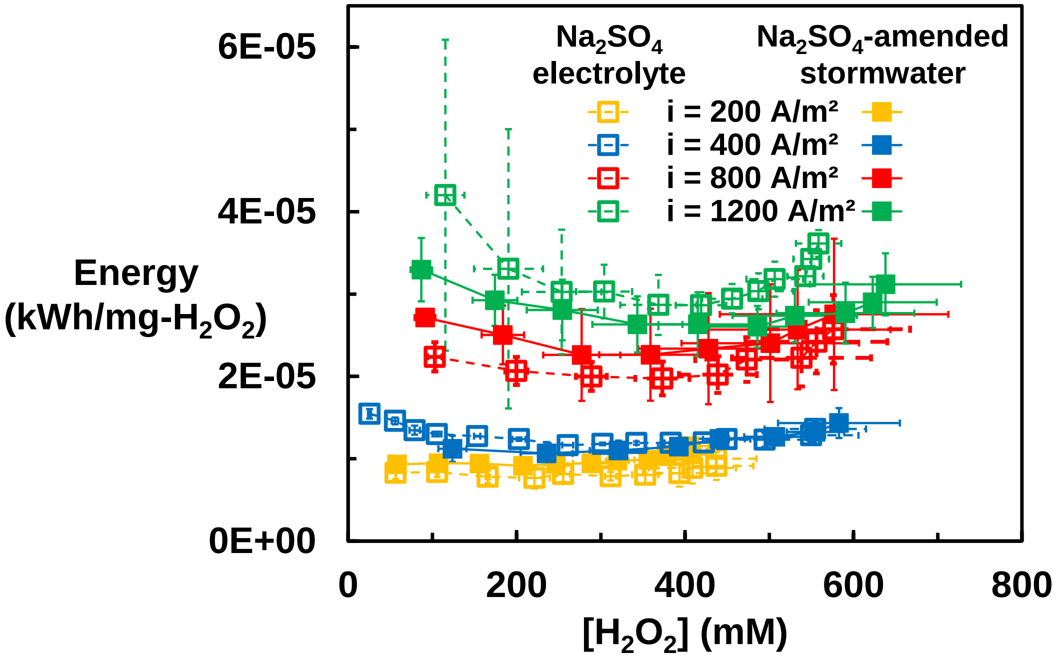

Figure 2.8 Energy consumption of H_2O_2 generation under different applied current densities for 0.2 M Na_2SO_4-amended stormwater and 0.2 M Na_2SO_4 electrolyte. Error bars not shown are smaller than symbols.

Although high current density may reduce the lifetime of the electrode (Carlesi Jara and Fino 2010), it enables H_2O_2 generation with a smaller electrode, which could lower the system capital cost. Use of high current densities could also generate H_2O_2 more quickly, meaning that less time would be needed to generate a sufficient quantity of H_2O_2 to prepare for a storm. Operating at a low current density could lower the energy consumption by over 50% but H_2O_2 loss during storage might become more significant under such conditions (see Section 2.3.3). The current density employed in the system can be adjusted based on uncertainty in the weather forecast, the predicted duration and intensity of the storm and the amount of time that has elapsed since the previous storm, which often affects stormwater quality (Grebel et al. 2013).

Due to the voltage limitation of the power supply used in this research, the energy consumption was evaluated with Na_2SO_4 concentrations above 0.02 M. Given the ionic strength of the simulated stormwater is typically around 0.005 M, use of the air-diffusion cathode to produce a stock solution of H_2O_2 without addition of salts would require a lower applied current density. Further research on electrode performance on H_2O_2 generation under low current density conditions is needed to evaluate the tradeoffs of operating this system without added salts.

2.3.3 H_2O_2 stability during storage

After production, H_2O_2 may need to be stored for periods of several days. The stability of H_2O_2 maybe affected by solution pH (Galbács and Csányi 1983, Watts et al. 1999), transition metals (Haber and Weiss 1934, McKee 1969), organic matter (Petigara et al. 2002, Romero et al. 2009), soil particles (Petigara et al. 2002), and enzymes (Netto et al. 1996). At the high concentration of H_2O_2 employed in this system, microbial activity should be relatively low (Collén and Pedersén 1996). Therefore, the loss caused by peroxidase enzymes should be insignificant in this system.

Previous research has indicated that H_2O_2 is unstable under alkaline pH conditions (Galbács and Csányi 1983, Nicoll and Smith 1955, Špalek et al. 1982). Therefore, the stability of H_2O_2 solution was assessed in the basic catholyte (initial pH around 12) and after the catholyte was mixed with acidic anolyte (which had an initial pH = 0.61 ± 0.04 and 0.78 ± 0.15 for Na_2SO_4 electrolyte and simulated stormwater, respectively) generated during the electrolysis process (referred to as "Na_2SO_4 electrolyte" and "Na_2SO_4-amended stormwater", Figure 2.9).

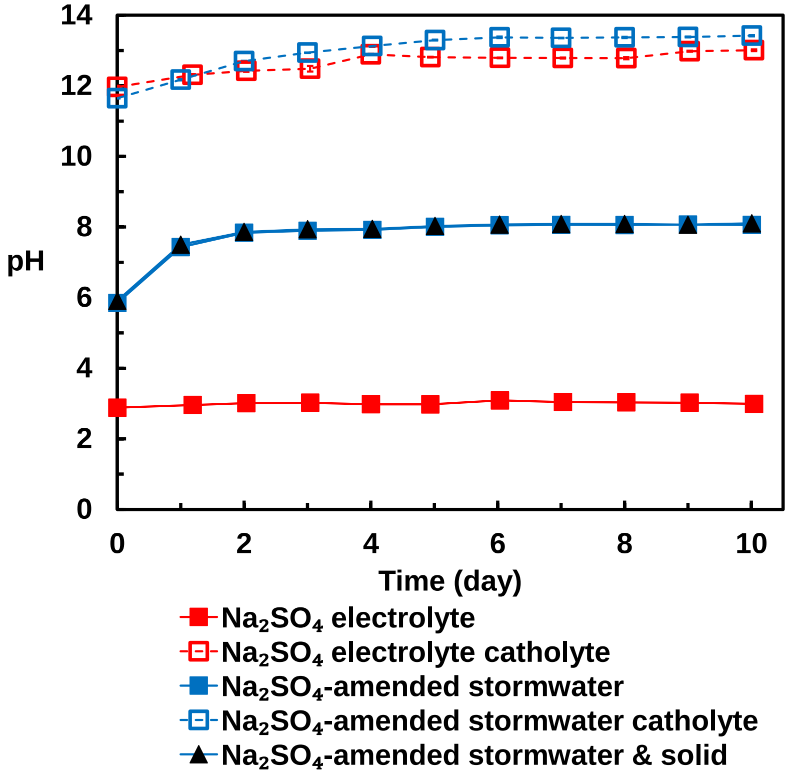

Figure 2.9 Solution pH during H_2O_2 storage. Error bars represent one standard deviation; error bars not shown are smaller than symbols.

The concentration of H_2O_2 decreased by 33% in Na_2SO_4-amended stormwater catholyte and 27% in Na_2SO_4 catholyte within a day. When it was mixed with the anolyte, only 7% and 2% of the H_2O_2 was lost within a day in the mixed Na_2SO_4-amended stormwater and the mixed Na_2SO_4 electrolyte, respectively (Figure 2.10). The enhanced stability was attributed to the reduction in the solution pH (Figure 2.9). Abel (1952) and Duke and Haas (1961) reported the homogeneous, uncatalyzed decomposition rate and reaction mechanism of H_2O_2 in alkaline aqueous solution as described in eq 2.7 and 2.8:

$$H_2O_2 \rightleftharpoons HO_2^- + H^+ \qquad K = 10^{-11.7} \qquad (2.7)$$

$$H_2O_2 + HO_2^- \rightarrow OH^- + O_2 + H_2O \qquad k = 1.61\ M^{-1}\ h^{-1} \qquad (2.8)$$

During the H_2O_2 generation, the high concentration of H_2O_2/HO_2^- in the catholyte buffered the solution pH around the pK_a value of H_2O_2 (eq 2.7). Without further adjusting the pH, the disproportionation reaction (eq 2.8) could be an important loss mechanism.

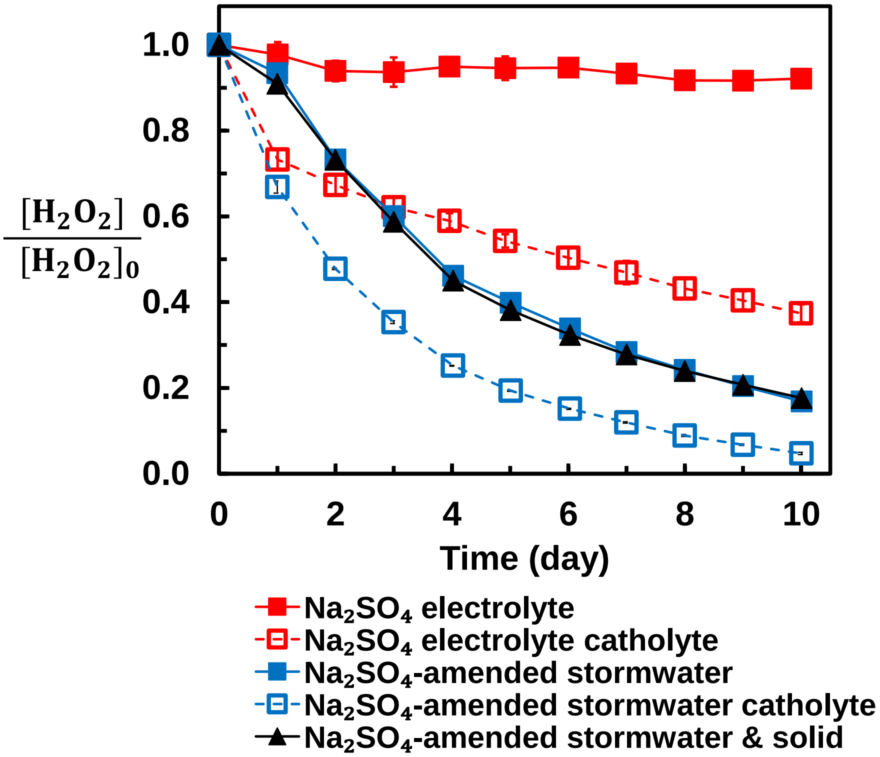

Figure 2.10 Hydrogen peroxide stability in catholyte and catholyte mixed with anolyte.

Although neutralization of the catholyte slowed the rate of H_2O_2 decomposition, rates of H_2O_2 decomposition in the catholyte/anolyte mixture increased substantially after about one day. The most likely explanation for the loss of H_2O_2 was transition metal-catalyzed processes, particularly from Fe and Cu in the Suwannee River natural organic matter (Table 2.6). The reaction mechanisms for H_2O_2 decomposition in simulated stormwater matrix is complicated because of the interactions of H_2O_2 with transition metals (Haber and Weiss 1934, McKee 1969), organic matter (Petigara et al. 2002, Romero et al. 2009, Walling and Goosen 1973) and phosphate (Kakarla and Watts 1997) and is therefore beyond the scope of this study. The measured concentrations of Fe and Cu in Na_2SO_4-amended simulated stormwater were similar to the concentrations observed in stormwater samples collected when suspended particle concentrations were low, as would be expected after stormwater-pretreatment ahead of drywell infiltration (Kabir et al. 2014, Li et al. 2012). Most of the Fe and Cu in stormwater is likely to be associated with natural organic matters or complexed by phosphate (Aiken et al. 2011, Benjamin 2014, Rose and Waite 2003). Therefore, the H_2O_2 stability observed in the Na_2SO_4-amended simulated stormwater should represent its stability under actual field conditions. Addition of 50 mg/L of San Joaquin soil, which is a typical concentration of suspended solids concentrations in stormwater (Mean TSS = 58 mg/L; Grebel et al., 2013), did not affect H_2O_2 stability.

Table 2.6 Concentrations of transition metals measured in the waters.

Concentration (µg/L)	0.2 M Na_2SO_4 electrolyte	0.2 M Na_2SO_4-amended stormwater
Cr	3.2 ± 1.0	3.2 ± 0.04
Mn	1.2 ± 0.51	1.1 ± 0.07
Fe	3.4 ± 2.2	24.1 ± 0.57
Ni	<3.5	<3.5
Cu	0.3 ± 0.06	2.1 ± 0.04
Zn	120 ± 8	150 ± 2

To minimize H_2O_2 loss during storage, the H_2O_2 generation process ideally should be completed immediately before the storm event starts. Assuming the H_2O_2 is generated in a continuous flow-through electrochemical module that has a hydraulic residence time of less than 1 hour, most of the loss of H_2O_2 will occur in the storage tank. The loss will be driven by the H_2O_2 generated at the beginning of the generating process which will be stored for longer time. The cumulative H_2O_2 loss under different operating conditions (Figure 2.11) was calculated based on the results of decomposition experiments (Figure 2.10) and the storage time (T, day):

$$\textit{Cumulative } H_2O_2 \textit{ loss } (\%) = \frac{\int_0^T \left(1-\frac{C}{C_0}\right)dt}{T} \times 100\% \qquad (2.9)$$

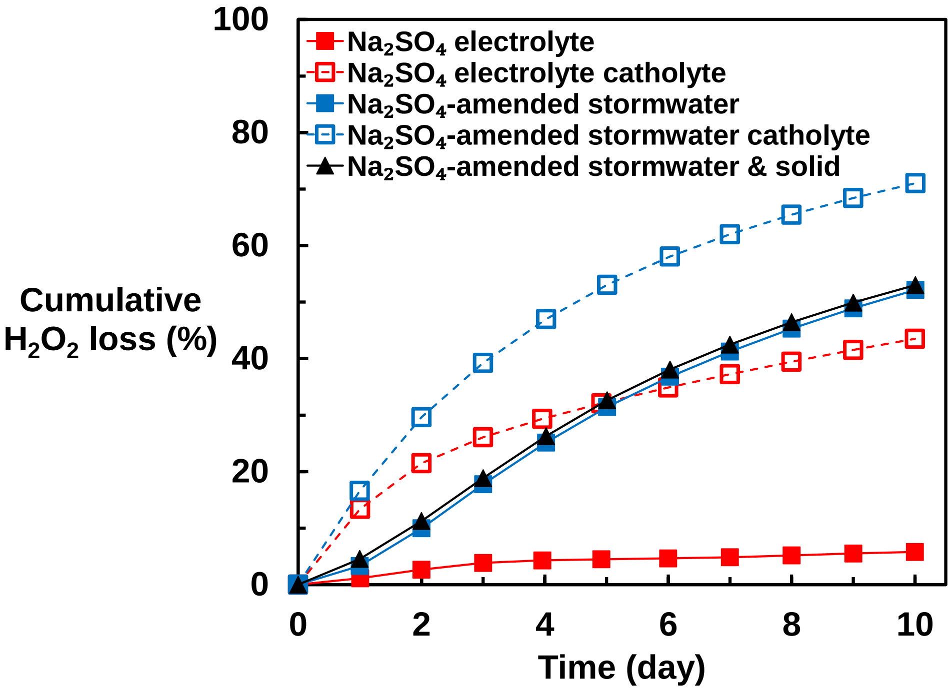

Figure 2.11 Predicted cumulative loss of H_2O_2 during storage of stock solutions prepared in advance of a storm event.

To limit the overall loss of H_2O_2 to less than 20%, several approaches are possible. First, H_2O_2 generated by passage of water through the cathode can be used immediately, if H_2O_2 generation starts less than one day prior to the storm event. Alternatively, stormwater from the cathode chamber can be neutralized by mixing with stormwater that has passed through the anode, in which case the H_2O_2 generation can be started up to three days prior to the storm event. Finally, water with fewer impurities (e.g., tap water), can be used for H_2O_2 generation, in which case, generation of H_2O_2 can take place up to 10 days prior to the storm event.

An effective H_2O_2 generation strategy can be formulated based on the performance of the air-diffusion cathode and the stability of H_2O_2. The required total current was estimated from the stability of H_2O_2, which determines the time available for H_2O_2 generation. To scale up the system for conditions expected in a dry well, the electrode area can be increased by stacking the required number of modular reactors. Finally, a balance between the applied current density, which determines electricity consumption, and the electrode capital cost can be established for each specific application. For example, to treat a typical 8-hour storm event in which water flows at the full infiltration capacity of the drywell (Q = 400 L/min) with an initial H_2O_2 concentration of 1 mM in the stormwater (detailed discussion about $[H_2O_2]_{\text{initial}}$ on the treatment performance is described in section 3.4), the required amount of H_2O_2 stock solution ($[H_2O_2]_{\text{stock}}$ = 200 mM, V = 1 m^3) can be generated with five 40 cm × 40 cm air-diffusion cathodes operating at a current density of 800 A/m^2 for one day prior to the storm event. The 1 m^3 H_2O_2 stock solution reservoir and the electrochemical modules can be deployed within the available service area next to the drywell.

2.3.4 Trace organic contaminant removal by advanced oxidation

To assess the performance of the UV/H_2O_2 AOP, the rate of transformation of a trace organic contaminant that is lost mainly through reactions with $^{\bullet}OH$ (i.e., CBZ) was evaluated in simulated stormwater. Upon exposure to UV light and H_2O_2, most trace organic contaminants in stormwater react with $^{\bullet}OH$ radical at near diffusion-controlled rates (10^9-10^{10} M^{-1} s^{-1}) (Wols and Hofman-Caris 2012).

Some trace organic contaminants may also be transformed by photolysis. The direct photolysis did not contribute significantly to the degradation of carbamazepine during the UV/H_2O_2 process because of its low quantum yield, 6.0×10^{-4} (Pereira et al. 2007b). Based on previously study (Ko et al. 2009), the effect of nitrate on contaminant removal during the UV/H_2O_2 process was negligible at initial H_2O_2 concentration above 20 mg/L. The contribution of indirect photolysis by photo-excited dissolved organic matter (DOC*) for carbamazepine removal was also negligible (Lee et al. 2014). No data is available for the reaction between carbamazepine with $^1O_2$.

The formation rate R_{form} ($M\ s^{-1}$) of $^{\bullet}OH$ from DOM and H_2O_2 were calculated from the rate of H_2O_2 photolysis:

$$R_{\text{form}} = n_{\cdot OH}[\frac{W_\lambda}{Z}(1\text{-}10^{-\alpha_\lambda Z})\frac{\varepsilon_\lambda \Phi_\lambda}{\alpha_\lambda}][C] \qquad (2.10)$$

where, $n_{\cdot\mathrm{OH}}$ = mole of $^{\bullet}OH$ formed per mole of reaction.

With the quantum yield Φ_{DOM} adapted from Jasper and Sedlak (2013), the ratio of $R_{\text{form,DOM}}$ to $R_{\text{form,}H_2O_2}$ in the condition of 5 mg-C/L of humic acid in stormwater can be calculated as 1.7×10^{-4}. Therefore, the contribution of photolysis to the removal of CBZ is expected to be negligible relative to its reactions with $^{\bullet}$OH.

Measured concentrations of H_2O_2 and CBZ were consistent with model predictions (Figure 2.12). The modest overprediction of transformation rates at low humic acid concentrations (i.e., 0 and 0.13 mg-C/L) was likely caused by impurities in the deionized water (i.e., dissolved organic carbon concentrations in deionized water can be as high as 0.5 mg-C/L, given that ion-exchange resins do not remove the organics from the tap water, which had a DOC concentration ranging from 1.5 to 3.0 mg-C/L; East Bay Municipal Utility District, 2019). The small underprediction in CBZ removal rate at the highest humic acid concentration (5.0 mg-C/L) was likely caused by the uncertainty of the rate constant for the reaction between $^{\bullet}$OH and humic acid (typically ± 50%) (Appiani et al. 2014). Under conditions representative of stormwater treatment (i.e., $[H_2O_2]_{\text{initial}}$ and $[\text{CBZ}]_{\text{initial}}$ of 1 mM and 10 μg/L, respectively), the rate of transformation of the trace organic contaminants decreased as the concentration of humic acid increased. At the highest dissolved organic carbon condition tested (5.0 mg-C/L humic acid), the half-life for CBZ removal was around 1.6 min.

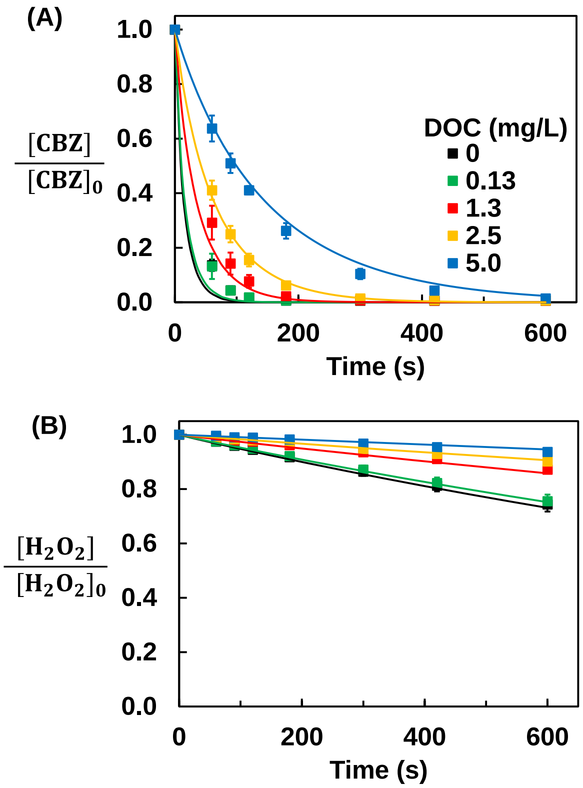

Figure 2.12 Effect of humic acid concentrations on $[H_2O_2]$ and [CBZ] in the AOP. (A) CBZ concentration and (B) H_2O_2 concentration. $[H_2O_2]_{\text{initial}}$ = 1 mM; $[\text{CBZ}]_{\text{initial}}$ = 10 μg/L. Symbols and lines are assigned to experimental data and model predictions, respectively. Error bars represent one standard deviation; error bars not shown are smaller than symbols.

The UV/H_2O_2 process should also result in inactivation of pathogens. The photon fluence rates measured by chemical actinometry indicated that the UV dose delivered to water within 10 minutes of treatment were 2430 mJ/cm^2, 2300 mJ/cm^2, 1700 mJ/cm^2, 1480 mJ/cm^2 and 1360 mJ/cm^2 for humic acid concentration ranging from 0 mg-C/L to 5.0 mg-C/L. For reference, 4-log inactivation of *Cryptosporidium*, *Giardia*, and viruses requires 22 mJ/cm^2, 22 mJ/cm^2, and 186 mJ/cm^2, respectively (USEPA 2003).

To avoid deposition of solutes and minerals on the surface on the UV lamps, the UV reactor was designed with an air gap between the UV lamp and the water surface (Figure 2.13).

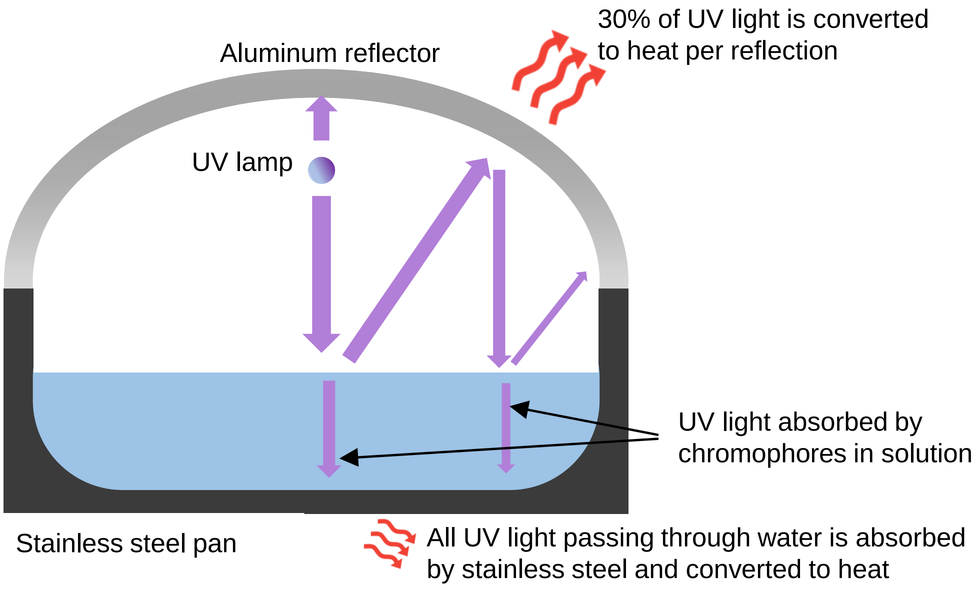

Figure 2.13 Schematic of light field in the UV reactor.

Although this design minimizes complications associated with submerged lamps, it decreases light utilization efficiency, because a substantial fraction of the UV light is reflected and backscattered at the air-water interface and converted into heat. Although the aluminum reflector above the lamp redirects some of the light emitted from the lamp and light reflected from the air-water interface back to the water, it only returns about 70% of UV light per reflection (Li 2000). The percentage of UV light lost as heat was calculated as follows:

$$UV\ light\ lost\ as\ heat\ (\%) = 1 - \frac{W_{254}\, N_A\, h\nu\, A}{P\, \eta} \qquad (2.11)$$

Where: W_{254} = Photon fluence rate at 254 nm (Ei cm^{-2} s^{-1})

$N_A = 6.02\times 10^{23}$ mol^{-1}

$h\nu$ = Energy per photon (J)

A = Air-water interface area (cm^2)

P = Power of UV lamp (W)

η = Electrical to UV conversion efficiency, 35 % (USEPA 2003)

The percentage of UV light lost as heat increased from 17% to 55% as the concentration of humic acid increased from 0 to 5.0 mg-C/L because the humic acid enhanced reflection and backscattering of UV light at the air-water interface (Figure

2.14). The increased light reflection and backscattering with dissolved species agreed with observations from previous research (Clarke et al. 1970, Grüniger et al. 1983, Kozarac et al. 2005, Schwarzenbach et al. 2016). For the light absorbed in the water column, the fraction of light absorbed by each chromophore was calculated based on the concentration and the molar attenuation coefficient. The percentage of UV light absorbed by H_2O_2 decreased from 99% to 4% as the concentration of humic acid increased from 0 to 5.0 mg-C/L. As a result, the $^{\bullet}OH$ production rate decreased and the rate of H_2O_2 loss also decreased.

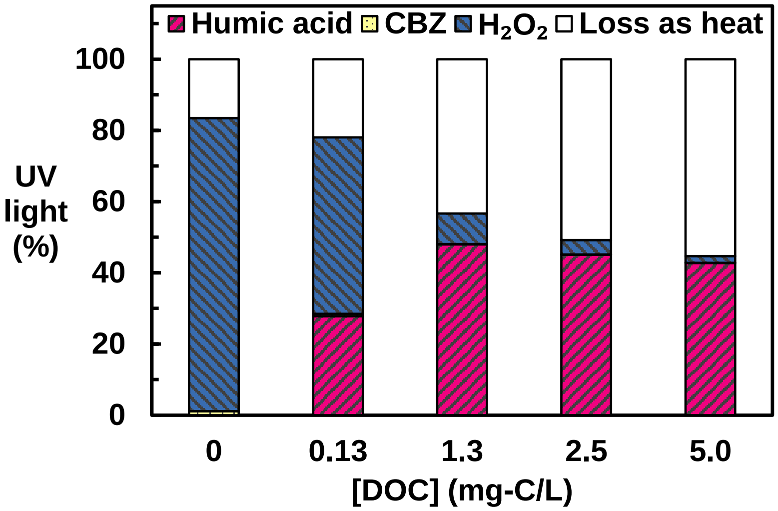

Figure 2.14 Effect of humic acid concentrations on UV light loss by reflection and backscattering and through absorption by chromophores. $[H_2O_2]_{initial}$ = 1 mM; $[CBZ]_{initial}$ = 10 μg/L; P_{lamp} = 60 W.

In addition to slowing the rate of $^{\bullet}OH$ production by competing with H_2O_2 for UV light, humic acid also slowed the CBZ removal by serving as a $^{\bullet}OH$ scavenger (Figure 2.15). The fraction of $^{\bullet}OH$ that reacted with the contaminant or a specific $^{\bullet}OH$ scavenger was estimated based on their reaction rate constants with $^{\bullet}OH$ ($k_{\cdot OH,i}$, M^{-1} s^{-1}) and concentration (C_i). The scavenging effect of Cl^- was neglected because of the fast kinetics of the reverse reaction (Reaction 19 in Table 2.3).

$$Fraction\ of\ {}^{\bullet}OH\ to\ species\ i = \frac{k_{\cdot OH,i}\, C_i}{\sum k_{\cdot OH}\, C} \tag{2.12}$$

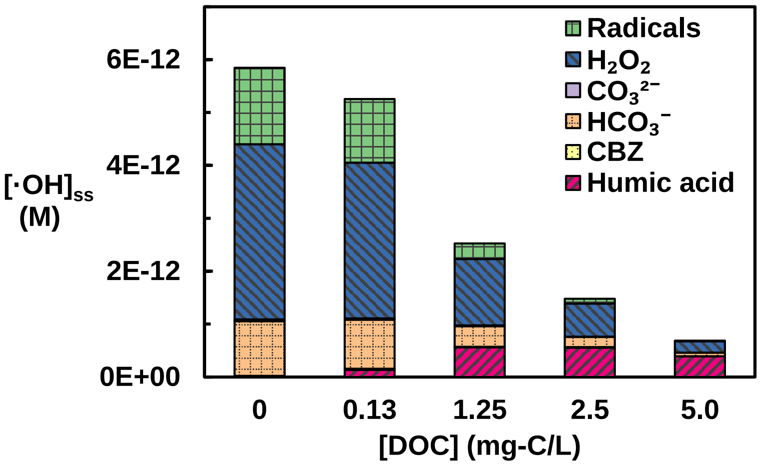

Figure 2.15 Effect of humic acid concentrations on estimated steady-state •OH concentration and •OH scavenging by scavengers and contaminants (Radicals: $O_2^{-}\cdot$, $HO_2\cdot$). The height indicates steady state •OH concentration and the patterns within indicate the portion of the •OH consumed by each species. $[H_2O_2]_{initial}$ = 1 mM; $[CBZ]_{initial}$ = 10 μg/L; P_{lamp} = 60 W.

The concentrations of •OH were obtained from the Kintecus kinetic model over experimental time-scales. The steady-state concentrations of •OH, which were estimated by the average value of the •OH concentrations, decreased by about 90% as the humic acid concentration increased from 0 to 5.0 mg-C/L. As the concentration of humic acid increased, its relative importance as a •OH scavenger also increased. At 5.0 mg-C/L of humic acid, close to half of the •OH produced was scavenged by humic acid. Because the model did not account for the transition metal catalyzed dismutation of $O_2^{-}\cdot$, the steady-state concentration of this species was probably overestimated $O_2^{-}\cdot$. Therefore, the actual scavenging effect of $O_2^{-}\cdot$ (included under "radicals" in Figure 2.15) is probably less important, especially at low humic acid concentrations.

Despite the fact that •OH react quickly with humic acid, CBZ was removed from stormwater in the presence of 5.0 mg-C/L of humic acid because the humic acid only reduced the steady-state •OH concentration by 90%. However, the overall performance of the system is expected to decrease dramatically as the humic acid concentration further increases due to the inefficient UV reactor design and the scavenging effect. Therefore, under conditions likely to be useful in the field, the maximum humic acid concentration in stormwater treated by this system is around 5 mg-C/L.

2.3.5 Full-scale treatment system design and considerations

The kinetic model can provide guidance for the design of full-scale treatment systems and their operation under different conditions. Considering a baseline case with a maximum flow rate of 400 L/min (i.e., 0.067 m^3/s), which is the typical value for drywells (Torrent Resources), along with other design conditions (e.g., system size limited by space available to install a treatment system within a drywell), the UV reactor will need to achieve at least 90% removal of a trace organic contaminant at diffusion-controlled rates, if it is transformed mainly by reactions with •OH. The initial H_2O_2 concentration in stormwater prior to exposure of UV light (hereinafter referred to as "initial H_2O_2 concentration" in this section) would need to be at least 0.1 mM; and between 5 and 25 500-watt low-pressure UV lamps would be needed to achieve the treatment goal if the humic acid concentrations ranged from 0.13 mg-C/L to 5.0 mg-C/L (Figure 2.16). Considering these constraints, the analysis indicated a trade-off between the initial concentration of H_2O_2 and the number of lamps being operated. At a humic acid concentration of 2.5 mg-C/L, 90% of the organic contaminants can be removed with an initial H_2O_2 concentration of 0.6 mM and 15 lamps. For a humic acid concentration of 5 mg-C/L, an initial H_2O_2 concentration of 1 mM and 25 lamps is needed to assure 90% removal of a trace organic contaminant.

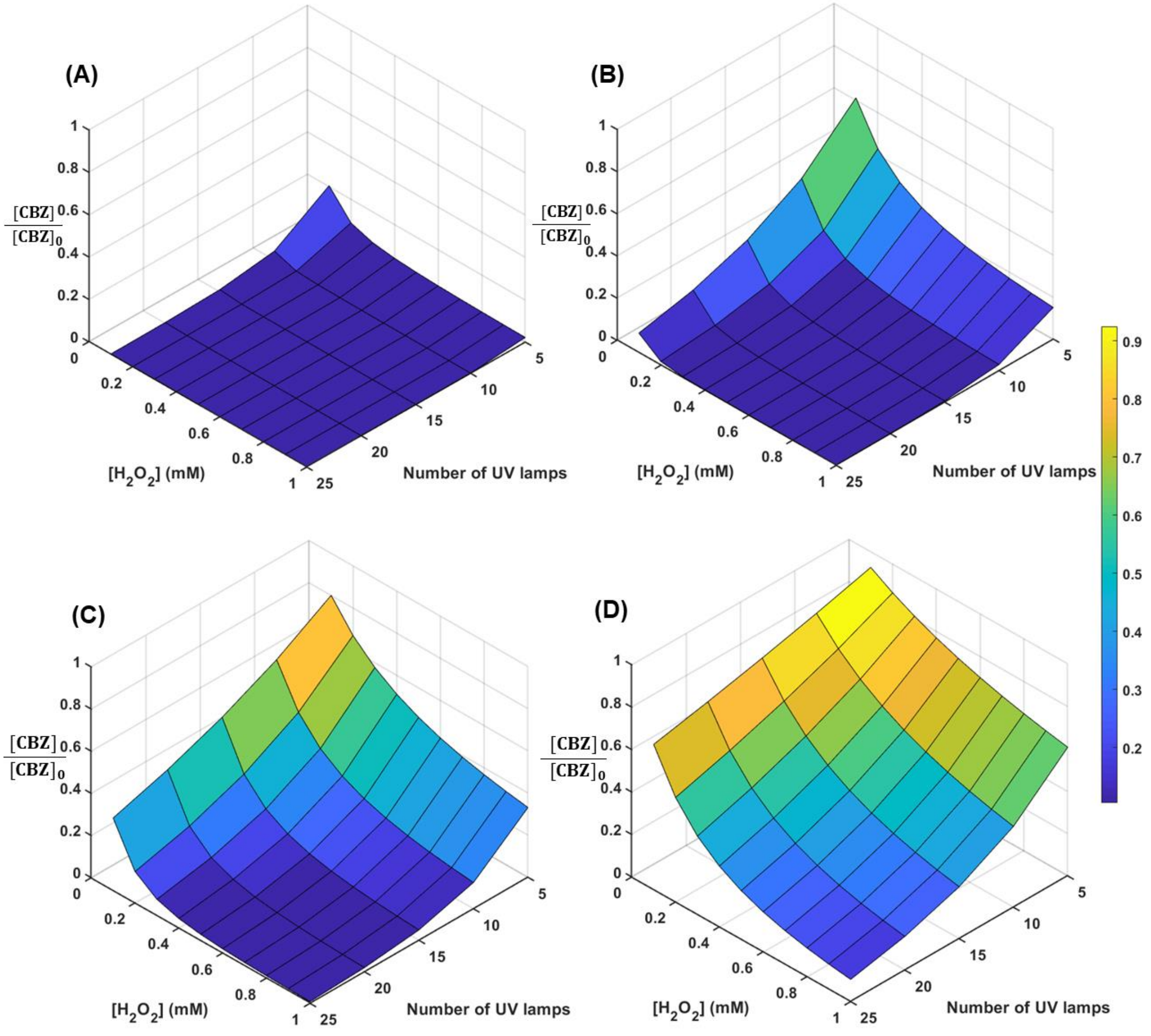

Figure 2.16 Predicted CBZ removal for operation of the full-scale system under different conditions including: initial $[H_2O_2]$, number of 500-W UV lamps, and stormwater containing different concentrations of humic acid (A) 0.13 mg-C/L, (B) 1.25 mg-C/L, (C) 2.5 mg-C/L, and (D) 5.0 mg-C/L.

The initial H_2O_2 concentration in stormwater and the number of lamps being used affect the energy consumption by the full-scale UV/H_2O_2 system. We used the electrical energy per order (E_{EO}) of the system to compare the system performance under different operating conditions (Bolton et al. 2001). Overall, E_{EO} increased with the DOC concentrations because of the light reflection and backscattering at air-water interface, competition for light absorption and $^{\bullet}OH$ scavenging by humic acid (Figure 2.17). We estimated E_{EO} values of approximate were between 0.5 and 2 kWh/m^3 for condition that are likely to be employed in full-scale treatment system. For reference, modern seawater desalination requires about 3 to 5 kWh/m^3 (Kim et al. 2019) and electrochemical oxidation with boron-doped diamond electrodes requires about 40 kWh/m^3 (Lanzarini-Lopes et al. 2017, Vahid and Khataee 2013).

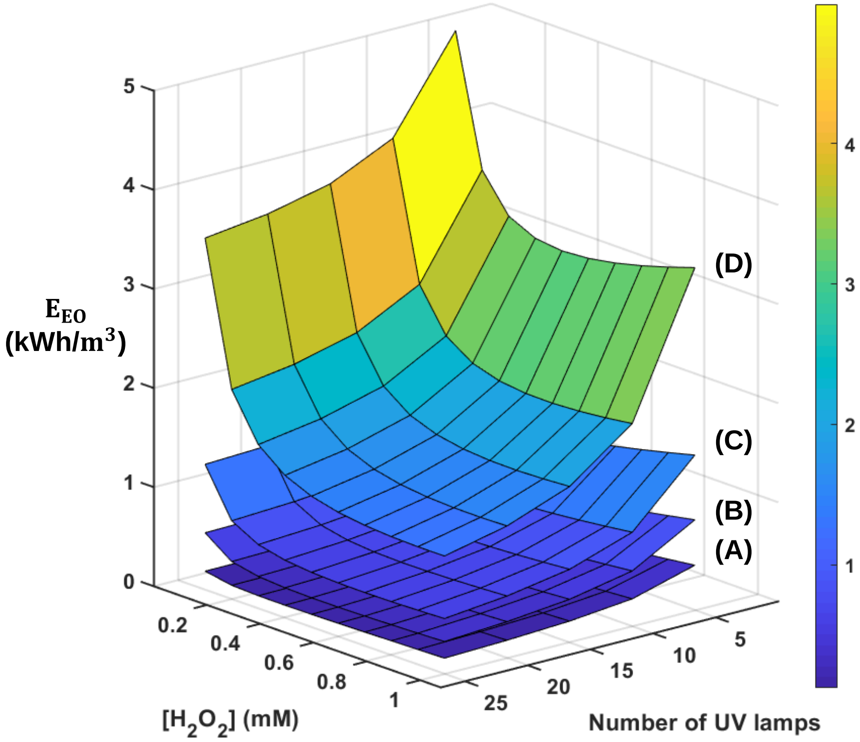

Figure 2.17 Predicted E_{EO} for operating the full-scale system under different initial [H_2O_2], number of UV lamps with stormwater containing different concentrations of humic acid (A) 0.13 mg-C/L, (B) 1.25 mg-C/L, (C) 2.5 mg-C/L, and (D) 5.0 mg-C/L. The power consumption associated with H_2O_2 generation was set as 1.9×10^{-5} kWh/mg-H_2O_2 to represent the average consumption for all current densities.

The specific UV absorbance (SUVA) at 254 nm of humic substances measured in previous study (0.006-0.053 L mg^{-1} cm^{-1}) (Weishaar et al. 2003) were lower than the value measured in this study (0.083 ± 0.001 L mg^{-1} cm^{-1}). If stormwater with a lower SUVA value at 254 nm than the value used in our model is tested, higher removal of contaminants and lower energy consumption may be observed.

Another factor affecting the energy consumption is the applied current density used when preparing the H_2O_2 stock solution. Assuming the power consumption associated with H_2O_2 generation was 1.9×10^{-5} kWh/mg-H_2O_2 ($i = 600$ A/m^2), the H_2O_2 generation process consumed a similar amount of energy as the UV lamp. For example, at 5.0 mg-C/L of humic acid, if the system is operated with an initial H_2O_2 concentration of 0.9 mM and 25 UV lamps (500 W), generating enough H_2O_2 for one hour of continuous dosing into stormwater would consume about 14 kWh of electricity and operating the lamps for one hour would consume about 13 kWh electricity. Generating the same amount of H_2O_2 at current density ranging from 200 A/m^2 to 1200 A/m^2 would consume between 7 kWh and 20 kWh of electricity.

Under the conditions employed in the AOP, less than 30% of the H_2O_2 will be converted into $^{\bullet}OH$ by UV light. Thus, residual H_2O_2 (i.e., up to around 1 mM) remaining after the treatment would be recharged to groundwater. Residual H_2O_2 should decompose in the first several centimeters of subsurface, mainly through reactions catalyzed by transition metal oxides and microbial biomass (Wang et al. 2016). If necessary, iron-containing minerals or manganese-containing minerals can be added to the drywell to enhance the rate of decomposition of H_2O_2 (Pham et al. 2012a). Because O_2 is produced when H_2O_2 decomposes through transition metal-catalyzed reactions, this process increases dissolved oxygen concentrations in the subsurface. This is potentially beneficial because aerobic biodegradation of residual organic contaminants (e.g., transformation products formed by the UV/H_2O_2 process) tends to be more effective than biotransformation that takes place under anoxic or anaerobic conditions (Lhotský et al. 2017, Mikkonen et al. 2018, Regnery et al. 2017, Ying et al. 2008).

Another consideration for successful operation is maintenance. The suspended UV lamp avoids any potential fouling on the lamp sleeve; therefore, the longevity of the UV reactor is only limited by the lifetime of UV lamps (typically >5000 hours). The longevity of the electrochemical reactor is limited by aging of the air-diffusion cathode or the cation exchange membrane. Although additional experiments are needed to further assess the longevity of the air-diffusion cathode, cation exchange membranes have been fabricated to enhance their oxidative stability (they typically operate for >1000 hours) (Park et al. 2018). Because the proposed treatment only operates during the rainy season (a total of several hundred hours of operation per year), it appears likely that the proposed system can be operated with only an annual maintenance, which overlap the annual inspection and maintenance cycle of the drywell (Whatcom County 2021).

2.4 Conclusions

Electrochemical generation of H_2O_2 followed by activation of H_2O_2 with UV light efficiently removed trace organic contaminants from stormwater. H_2O_2 was efficiently generated in stock solutions under different water matrix and applied current densities. The maximum H_2O_2 concentrations achieved in the stock solution were between 400 and 600 mM. Although stormwater composition impacted the H_2O_2 stock solution stability, neutralization of basic pH conditions by mixing the catholyte and anolyte resulted in sufficient stability to enable H_2O_2 generation for up to three days before arrival of a storm and to provide enough H_2O_2 to treat a typical storm lasting as long as eight hours.

These lab-scale tests and model predictions, while indicating the potential for removing trace organic contaminants, did not account for several factors that could be encountered in field-scale applications. For example, during H_2O_2 generation tests, decreased performance of the electrode was observed after extended use, possibly as a result of flooding (i.e., decreased hydrophobicity of the water-facing side of the electrode). Further research should be conducted to investigate the factors that affect the electrode lifetime (e.g., current density, electrolyte conductivity). Due to the variation in stormwater compositions, H_2O_2 decomposition rates in the stock solutions also may merit further assessment. For locations with high concentrations of natural organic matter in stormwater, submerged UV lamps capable of delivering UV light to stormwater more efficiently by avoiding the light reflection and scattering at water/air interface may be needed. However, the tradeoff between lamp fouling and lamp efficiency requires further analysis. UV LED lamps offer promising alternatives because of the minimal heat generation at lamp surface, which reduces the potential for precipitative fouling (Linden et al. 2019). New engineering solutions for fitting the reactors into the drywell may also be advantageous. Low-cost sensors and controllers also may be coupled with operation of this system to maximize water quality benefits and enable remote or automated operations (Kerkez et al. 2016, Mullapudi et al. 2017). Following site-specific optimization, the system should be tested under field conditions.

CHAPTER 3. Factors Affecting the Yield of Hydroxyl Radical by Electrochemical Activation of H_2O_2 on Stainless-Steel Electrodes

Reproduced with permission from Duan, Y., Jiang, W., Sedlak, D. L., Factors Affecting the Yield of Hydroxyl Radical by Electrochemical Activation of H_2O_2 on Stainless Steel Electrodes. In preparation.

3.1 Introduction

Advanced oxidation processes provide a practical option for the treatment of trace organic contaminants (TrOCs) because they are capable of oxidizing contaminants by converting soluble oxidants (e.g., H_2O_2, O_3, HOCl) to highly reactive radicals (e.g., $^{\bullet}OH$, $^{\bullet}Cl$) (Miklos et al. 2018). After the initial oxidation step, many TrOCs undergo further reactions with dissolved oxygen or are transformed to compounds that are more easily degraded by microbes (Cuerda-Correa et al. 2020, Nidheesh et al. 2022). Despite the many advantages of advanced oxidation processes, their applications are limited by the challenges associated with the conversion of oxidants into radicals (Hodges et al. 2018).

Ultraviolet light (i.e., the UV/H_2O_2 process) is one of the most popular advanced oxidation processes employed in water recycling, groundwater remediation and industrial wastewater treatment because it produces fewer toxic byproducts and does not introduce sulfate, iron or other ions that could diminish water quality (Ike et al. 2019, von Gunten 2018). However, the application of UV/H_2O_2 is often limited by competition for photon absorption by other dissolved species. For small-scale systems, deposition of minerals on the surfaces of submerged UV lamps or loss of light emitted by suspended lamps through surface reflection reflects an additional challenge (Duan and Sedlak 2021). As an alternative, the 2-electron reduction of O_2 to H_2O_2 at a cathode, followed by exposure to Fe(II) released from oxidation of an iron anode has been used for industrial wastewater treatment (Brillas et al. 2009). Such electro-Fenton systems only produce high yields of $^{\bullet}OH$ over a relatively narrow pH range (i.e., pH 2-4) due to a shift in the reaction mechanism from $^{\bullet}OH$ to the more selective oxidant (e.g., Fe[IV]) as the pH increases (Bossmann et al. 1998, Hug and Leupin 2003, Jacobsen et al. 1998, Keenan and Sedlak 2008). Electro-Fenton systems also require pumps to avoid O_2 depletion and produce a waste sludge that mainly consists of Fe(III)-oxides (Brillas et al. 2009).

To overcome the challenges associate with sludge management and the need to create acidic pH conditions, numerous heterogeneous catalysts that are capable of converting H_2O_2 to $^{\bullet}OH$ have been investigated. However, the percentage of H_2O_2 that produces oxidants that are capable of transforming contaminants is typically very low (i.e., < 5 %) (Chou et al. 2001, Huang et al. 2001, Huling et al. 1998, Kanel et al. 2004, Lee and Sedlak 2009, Seo et al. 2015, Valentine and Wang 1998, Xue et al. 2009). In these systems, the majority of H_2O_2 is transformed through a non-radical mechanism that converts H_2O_2 directly to O_2 and H_2O (Kwan and Voelker 2002, Petigara et al. 2002, Vafaei Molamahmood et al. 2022). Although heterogeneous Fenton catalysts that contained various additives (e.g., Si, Al) sometimes exhibit higher yields for $^{\bullet}OH$ production (Pham et al. 2009), their applications are still limited by the long-term stability of the catalysts (Pham et al. 2012b). Recently, custom-made electrodes composed of carbonaceous materials and metals have been proposed as alternatives to heterogeneous catalysts (Hu et al. 2021, Peng et al. 2015, Zeng et al. 2020, Zhao et al. 2016, Zhao et al. 2012). However, the electrodes usually require complicated fabrication, resulting in a flat plate reactors that exhibit slow kinetics due to poor mass transfer properties (Chaplin 2019).

Recently, Weng et al. (2020) reported that an inexpensive stainless-steel mesh material was capable of reducing H_2O_2 to $^{\bullet}OH$ in reverse osmosis permeate buffered with phosphate at pH 5.6. This material has the potential to function as a three-dimensional electrode, which could further enhance its performance due to enhanced mass transport (Radjenovic and Sedlak 2015).

In this study, we evaluated the performance of a three dimensional stainless-steel electrode for activating H_2O_2 over environmentally relevant pH conditions (pH 4-9) at different potentials. Specific goals of this study were to: (1) evaluate the effect of pH and potential on H_2O_2 activation; (2) identify the reactive oxidants and quantify their yields; (3) assess the metal leaching tendency of the stainless-steel electrode during H_2O_2 activation; (4) quantify $^{\bullet}OH$ scavenging by the stainless-steel electrodes; and (5) assess the ability of the stainless-steel electrode to remove trace organic contaminants under conditions encountered in drinking water sources.

3.2 Materials and Methods

3.2.1 Materials

All experiments were performed at room temperature (23 ± 2 °C) with chemicals of reagent grade or higher (Sigma-Aldrich, St. Louis, MO, and Fisher Scientific, Pittsburgh, PA). Ultrapure water from a Milli-Q system ($R > 18$ MΩ) was used for all experiments. H_2O_2 (30% v/v) was standardized by the $KMnO_4$ assay (Gill and Zheng 2020) and checked monthly using a Shimadzu UV-2600 UV-vis spectrophotometer at 254 nm ($\varepsilon_{254nm} = 18.6$ M^{-1} cm^{-1}; Morgan et al. 1988).

3.2.2 Electrolysis in Na_2SO_4 electrolyte

Electrolysis experiments were performed at fixed potential versus an Ag/AgCl reference electrode (3M NaCl, BASi, West Lafayette, IN) controlled by a multichannel potentiostat (Gamry Instruments Inc., Warminster, PA). All potentials are reported versus a standard hydrogen electrode (SHE). Electrolysis experiments were performed in a glass H-cell reactor (Figure 3.1) in the batch mode with a platinum electrode as the counter electrode (1.0 × 1.0 cm, 99.99% Pt, TianMeiHeChuang Technology Co., Ltd, Beijing). Both chambers were stirred with Teflon-coated magnetic stir bars at 400 rotations per minute (rpm).

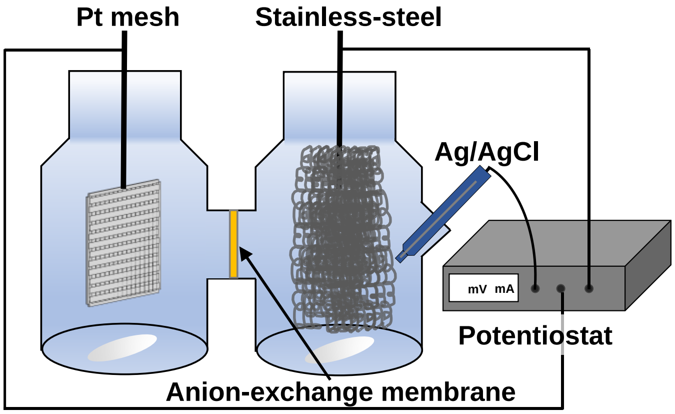

Figure 3.1 Schematic configuration of the electrochemical reactor. The system was operated with a constant potential by a potentiostat.

The cathode chamber and anode chamber each had volumes of 100 mL and were separated by an anion-exchange membrane (Fumasep FAS-PET-130, The Fuel Cell Store, College Station, TX). The anion-exchange membrane was chosen to minimize transport of H_2O_2 and metals between the two chambers. The counter electrode chamber was filled with 200 mM Na_2SO_4, while the working electrode chamber was filled with 200 mM Na_2SO_4 amended with 1 mM of buffer and different concentrations of methanol or 2-propanol to scavenge reactive oxidants produced during H_2O_2 decomposition. The following buffers were used: sodium acetate (pH 4 and 5), 2-(N-morpholino)ethanesulfonic acid (MES; pH 6), piperazine-N,N′-bis(ethanesulfonic acid) (PIPES; pH 7), and sodium borate (pH 8 and 9). MES, PIPES and borate do not form complexes with Fe(II) or Fe(III) (Yu et al. 1997). The initial solution pH was adjusted using H_2SO_4 or NaOH. A lower buffer concentration (i.e., 1 mM) was used during electrolysis to ensure that the majority of the oxidants produced in the process reacted with the probe compounds (i.e., methanol or 2-propanol) and not the buffer. The final pH values for all experiments were observed to vary by less about than about 0.4 pH units and the variation was less than 0.2 pH units for most experimental conditions.

A 200 mM Na_2SO_4 background electrolyte was used to enhance the solution conductivity and avoid overload of the potentiostat and internal resistance compensation. Na_2SO_4 was chosen because of its inert electrochemical behavior (Stang and Harnisch 2016). Additionally, the electrode did not require a stabilization step (Weng et al. 2020) to reach the target potential when elevated background electrolyte concentrations were used. The addition of Na_2SO_4 would not be needed if the system were to be scaled up with a small inter-electrode distance without an ion-exchange membrane.

Methanol was chosen as the probe compound for oxidants because it does not interact with surfaces to an appreciable extent, and it is uncharged over the pH range of interest. Furthermore, the main product of methanol oxidation by $^\bullet$OH and Fe[IV], formaldehyde, can be quantified easily. 2-propanol was chosen as the other oxidant probe because it is only oxidized to acetone by $^\bullet$OH and other strong oxidants (Keenan and Sedlak 2008). Control experiments showed that H_2O_2 did not react with methanol or 2-propanol over the whole pH range tested in this study (Figure 3.2).

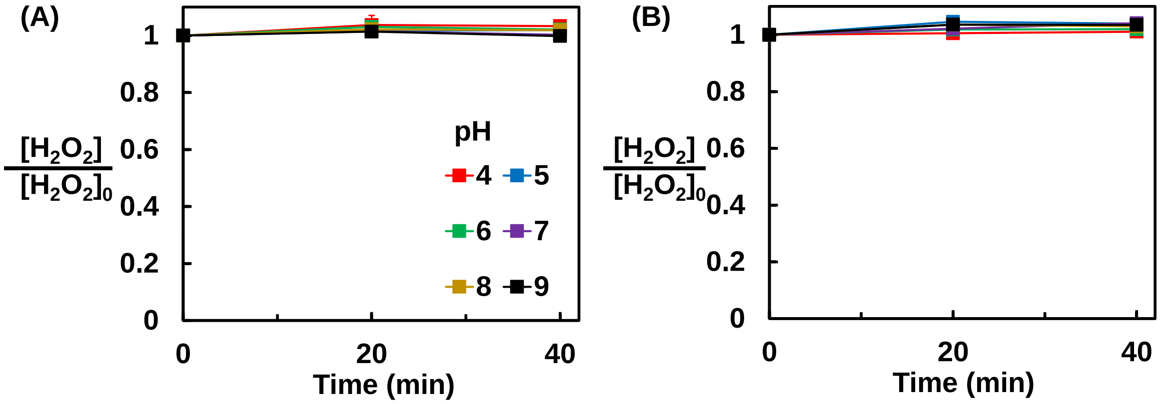

Figure 3.2 H_2O_2 concentrations in the presence of 100 mM of (A) methanol, (B) 2-propanol in buffer-containing Na_2SO_4 electrolyte. The experiments were conducted in the absence of stainless-steel electrodes. No formation of formaldehyde or acetone was observed. Error bars represent one standard deviation.

Unless otherwise specified, a high concentration of probe compounds (i.e., 100 mM) was used to ensure all the produced reactive oxidants were captured by the probe compounds, in which case, the amounts of reactive oxidants generated could be quantified from the formation of the oxidation products (i.e., formaldehyde and acetone, eq 3.1).

$$Oxidant\ yield = \frac{n_{oxidant}}{n_{H_2O_2}} = \frac{n_{oxidation\ product}}{n_{H_2O_2}\ Yield\ of\ product} \tag{3.1}$$

where the yield of product (i.e., formaldehyde and acetone) for the reactions between the probe compounds and $^{\bullet}$OH are 1.000 for methanol and 0.867 for 2-propanol (Asmus et al. 1973).

The activation of H_2O_2 on the electrode surface is expected to produce $^{\bullet}$OH at the surface. Surface-bound $^{\bullet}$OH react with other surface-associated species or it could diffuse into the aqueous phase prior to reacting. The relative reactivity of the surface-bound $^{\bullet}$OH with organic compounds at or near the interface as well as the extent to which the radical diffuses into solution are unknown (Xie et al. 2022). Therefore, we refer to the reactive oxidant that can oxidize both methanol and 2-propanol as $^{\bullet}$OH, without differentiating between $^{\bullet}$OH adsorbed on electrode surface or $^{\bullet}$OH that reacts in the solution phase.

To provide a stable performance, a new Scotch-Brite 20 g stainless-steel scrubber (catalogue number 214C, 3M Company, St. Paul, MN, USA; 80 cm^2/g specific surface area) was cut to around 4.5 g and pre-conditioned. The pre-conditioning process was performed with the working electrode chamber operated in continuous stirred-tank reactor mode to avoid any metal accumulation. The working electrode chamber was fed with a 0.2 M Na_2SO_4 electrolyte that containing methanol (100 mM), buffer and H_2O_2. A total of 5 L of electrolyte was fed into the working electrode chamber over one hour. Hydraulic residence time was maintained at 1.20 ± 0.03 min.

For each operating condition tested (i.e., pH and potential), a new stainless-steel electrode was pre-conditioned. The same electrode was used for all experiments under that operating condition. No significant decrease in the yield of oxidants was observed over time except experiments conducted at pH 6 and +0.020 V. In this experiment, unexpected decreases in performance were observed after pre-conditioning and completion of 15 experiments. After the decreases in performance were observed, another electrode was pre-conditioned following the same protocol and used for the remaining experiments. Before and after each experiment, the stainless-steel electrode was rinsed thoroughly with ultrapure water and air-dried for at least 30 minutes before being reused.

3.2.3 Electrolysis in authentic surface water

To assess the performance of the stainless-steel electrodes under realistic water composition, electrolysis experiments were performed in an undivided reactor (Figure 3.3, V = 125 mL) stirred at 600 rpm. The undivided reactor was used to minimize pH changes during the electrolysis. A fresh stainless-steel electrode (~4.5g) was used for each replicate. Because of the long duration of the electrolysis experiment (i.e., four hours), the pre-conditioning process was included in the experiments.

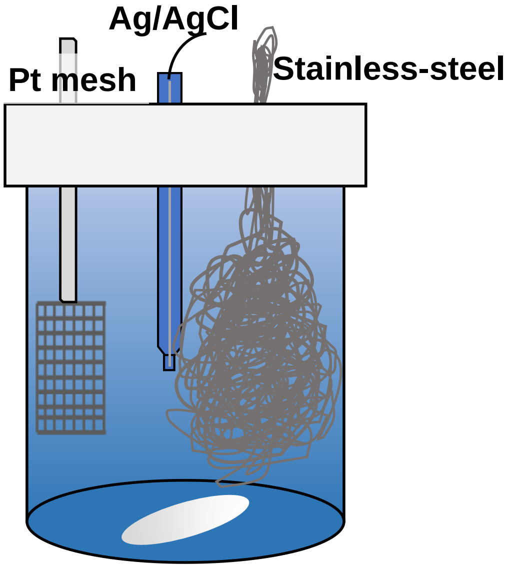

Figure 3.3 Schematic configuration of the undivided electrochemical reactor.

Surface water was collected during a storm event from Strawberry Creek on the University of California, Berkeley campus (37°52'26.9"N 122°15'41.8"W) on December 22, 2021, around 1:30 PM, Pacific Time. The surface water runoff was filtered through 0.7 µm glass fiber filter (MilliporeSigma, Burlington, MA) followed by 0.45 µm Supor® 450 Membrane (Gelman Sciences, Ann Arbor, MI) prior to experiment. A summary of the water quality parameters is provided in Table 3.1.

Table 3.1 Water quality parameters of the surface water.

Parameter	Value
Alkalinity	2.07±0.02 mM
Dissolved organic carbon	5.1±0.1 mg-C/L
$SUVA_{254}$	0.034±0.001 L mg-C^{-1} cm^{-1}
Conductivity	255 µS/cm
pH	7.83±0.04
F^-	0.14 mg/L
Cl^-	10.0 mg/L
Br^-	< 0.58 mg/L
NO_2^-	< 0.78 mg/L
NO_3^-	2.70 mg/L
PO_4^{3-}	< 2.0 mg/L
SO_4^{2-}	16.9 mg/L
Li^+	< 0.14 mg/L
Na^+	15.8 mg/L
K^+	< 1.0 mg/L
NH_4^+	< 2.1 mg/L
Mg^{2+}	8.07 mg/L
Ca^{2+}	21.5 mg/L

The collected surface water was amended with 200 mM of Na_2SO_4 to avoid overloading of the potentiostat. To test the performance of the stainless-steel electrode under circumneutral pH conditions, the initial pH of the surface water was adjusted from 7.8 to 6.0 prior to the electrolysis. (Solution acidification on this magnitude might also occur if the electrode had been part of a three electrode system in which the cathodes for H_2O_2 production and activation were preceded by an anode.) The pH of the solution increased from 6.0 to around 7.3 gradually during electrolysis, potentially caused by CO_2 partitioning between the solution and atmosphere. Based on its alkalinity, the equilibrium pH was estimated to be 8.0 when the water was equilibrated with the atmosphere.

Carbamazepine and atrazine (20 µg/L) were chosen as representative TrOCs because of their high frequencies of detection in surface water and their relative resistance to oxidants other than $^{\bullet}OH$ (de Souza et al. 2020, Spahr et al. 2020, Tixier et al. 2003). H_2O_2 (1.25 mg/L = 37 µM) was dosed every 20 minutes throughout the electrolysis experiments with the surface water sample. Control experiments indicated that H_2O_2 did not react with carbamazepine or atrazine in the absence of stainless-steel electrode (Figure 3.4).

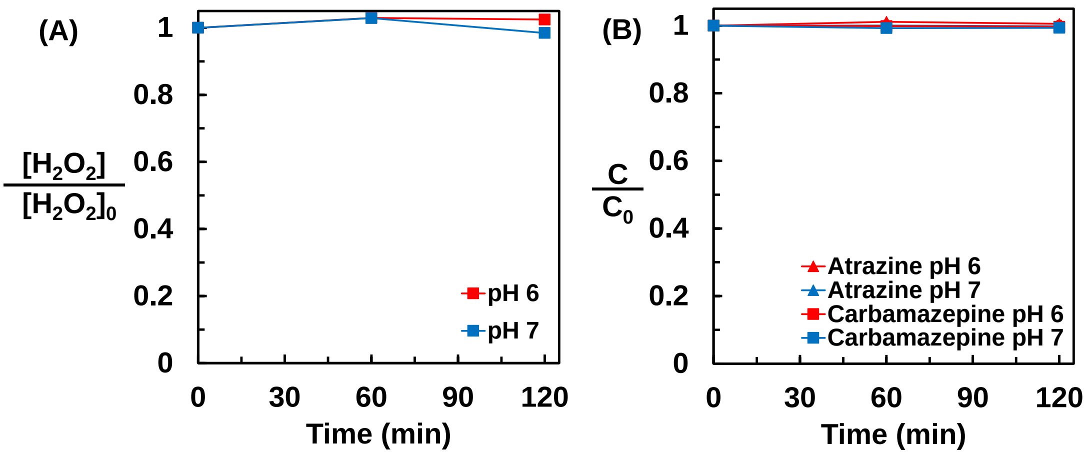

Figure 3.4 Concentrations of (A) H_2O_2 and (B) trace organic contaminants in Na_2SO_4-amended surface water in the absence of stainless-steel electrode. $[H_2O_2]_0$ = 1.25 mg/L. Error bars represent one standard deviation; error bars not shown are smaller than symbols.

Control experiments were also conducted in the absence of H_2O_2 to assess contaminant removal by processes taking place on the electrodes (e.g., direct electron transfer). Results indicated less than 10% loss of atrazine and about 25% loss of carbamazepine over the two-hour experiment (Figure 3.5). This was substantially lower than the removal observed in the presence of H_2O_2 (Figure 3.25A).

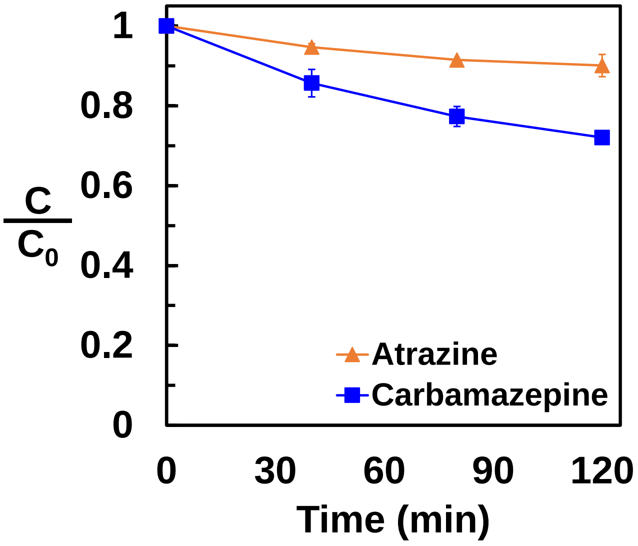

Figure 3.5 Concentrations of trace organic contaminants in Na_2SO_4-amended surface water in the absence of H_2O_2. Potential = +0.020 V. Error bars represent one standard deviation; error bars not shown are smaller than symbols.

3.2.4 Analytical methods

Samples (6 mL aliquots) were periodically collected from the stainless-steel electrode chamber. To prevent continued formation of formaldehyde or acetone from reactions between residual H_2O_2 and Fe(II) remaining at the time of collection, an aliquot of 1,10-phenanthroline (final concentration = 1 mM) was added to the samples (Duesterberg et al. 2005). Formaldehyde and acetone were analyzed using 2,4-dinitrophenylhydrazine (DNPH) derivatization followed by analysis on an Agilent 1260 Infinity high-performance liquid chromatography (HPLC) equipped with diode array detector as described previously (Keenan and Sedlak 2008).

Samples for H_2O_2 and Fe(II) measurement were quenched by mixing with colorimetric reagents immediately after collection. H_2O_2 was measured by a modified version of the peroxidase catalyzed N,N-diethyl-p-phenylenediamine (DPD) oxidation method (Bader et al. 1988). Fe(II) was measured with a modified version of the ferrozine method with addition of an aliquot of ammonia fluoride (final concentration = 7 mM) to prevent the interference by Fe(III) (Keenan and Sedlak 2008, Viollier et al. 2000). Cr(VI) was measured with the diphenylcarbazide method (US Environmental Protection Agency 1992). Aliquots for total metals measurement were acidified immediately after sampling to prevent precipitation and quantified in triplicate on an Agilent 7700 Series Inductively Coupled Plasma-Mass Spectrometer (ICP-MS).

Methanol (10% v/v) was added to carbamazepine- and atrazine-containing samples to quench any possible reactions. Carbamazepine and atrazine were quantified in multiple reaction monitoring (MRM) mode with an Agilent 1260 series HPLC system coupled to a 6460 triple quadrupole tandem mass spectrometer (HPLC-MS/MS) as previously described (Barazesh et al. 2015).

The oxidation state of Fe in the surface of stainless-steel electrodes was characterized by X-ray photoelectron spectroscopy with a K-Alpha XPS spectrometer

(Thermo Scientific Ltd., East Grinstead, UK). Samples were air-dried prior to characterization. The atomic percentage of peaks was determined by a peak-fitting analysis using a nonlinear Shirley-type background. The virgin stainless-steel material was also characterized by ambient-pressure XPS experiments under different water vapor pressure at Beamline 9.3.1 of the Advanced Light Source (Axnanda et al. 2015).

3.3 Results and Discussion

3.3.1 Pre-conditioning of stainless-steel electrodes

Results from preliminary experiments indicated that new stainless-steel electrodes underwent a period of rapid corrosion which was accompanied by the release of metals and variation in performance. After approximately one hour, the leaching of metals substantially decreased and the kinetics of H_2O_2 activation were more reproducible. When operated at pH values below 7 and a potential of +0.020 V in continuous flow mode, elevated metal concentrations were observed within 20 minutes (Figure 3.6C-E). At higher pH values, substantial metal leaching was never observed. Therefore, pre-conditioning (i.e., operating the electrode for one hour) followed by disposal of leached metals may be needed prior to treating water with an initial pH value below 7. Under all tested conditions, the electrode performance stabilized within one hour in terms of H_2O_2 decomposition, reactive oxidant production, metal leaching, and current density (Figure 3.6).

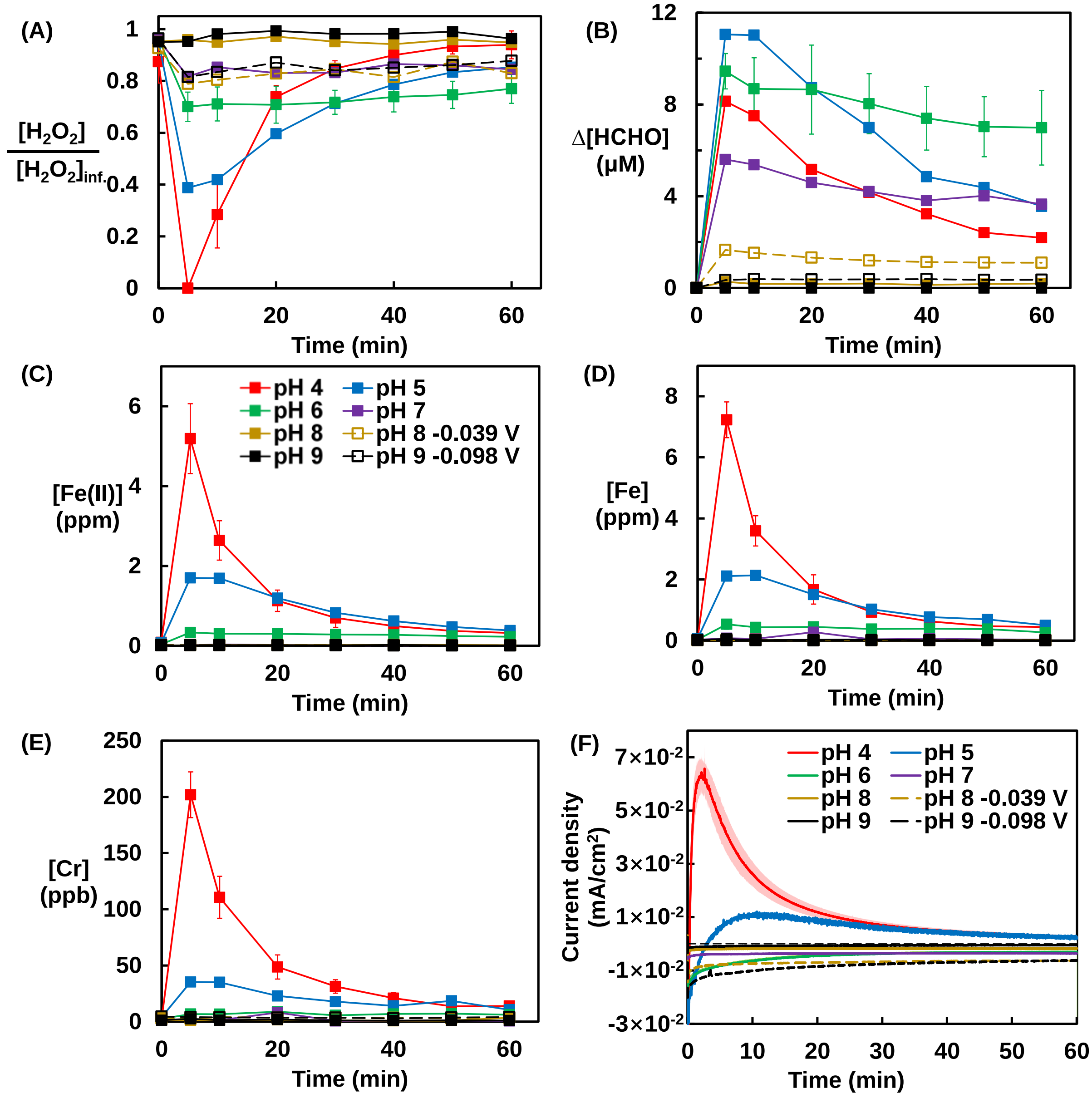

Figure 3.6 (A) H_2O_2 transformation, (B) formaldehyde formation, (C-E) metal leaching, and (F) current density during the pre-conditioning process. Potential = +0.020 V when not specified. Error bars and confidence band represent one standard deviation.

3.3.2 Effects of pH and applied potential on H_2O_2 transformation rates

Experiments were conducted in the pH range of 4-9 with an initial H_2O_2 concentration of 1.25 mg/L (i.e., 37 μM) and applied potential of +0.020 V. These values had been identified previously as the optimal initial H_2O_2 concentration and potential in experiments conducted in phosphate buffered at pH 5.8 (Weng et al. 2020). Assuming first order kinetics, H_2O_2 decomposition rates increased from $4.2\pm2.8 \times 10^{-3}$ s^{-1} to $8.4\pm2.9 \times 10^{-3}$ s^{-1} as the pH increased from 4 to 6. As the pH values increased from 6 to 9, the H_2O_2 decomposition rates decreased to $5.7\pm1.2 \times 10^{-4}$ s^{-1} (Figure 3.7A). Current densities (Figure 3.7B) followed a similar trend as H_2O_2 decomposition, with the highest current density observed at pH 6. The large uncertainty observed for both H_2O_2 decomposition rates and current densities at pH values below 7 were likely associated with the changes in the electrode surface (details described in Section 3.3.4).

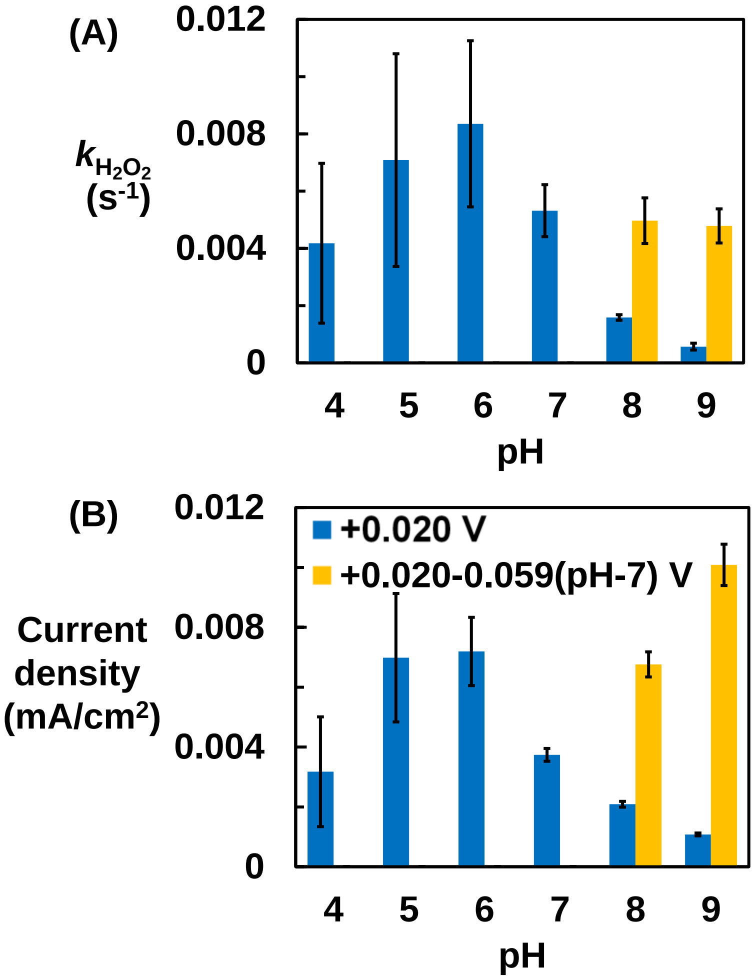

Figure 3.7 (A) Rate constants for hydrogen peroxide decomposition, (B) current densities at different pH values and applied potentials. $[H_2O_2]_0$ = 1.25 mg/L, [Probe compound] = 100 mM. Error bars represent one standard deviation.

The concentrations of probe compounds in electrolyte had no effect on the H_2O_2 decomposition rates and observed current densities (Figure 3.8). The H_2O_2 decomposition rates were consistent with those reported previously for reverse osmosis permeate amended with phosphate buffer and low concentrations of 1,4-dioxane (i.e., 0.2 μM) (Weng et al. 2020).

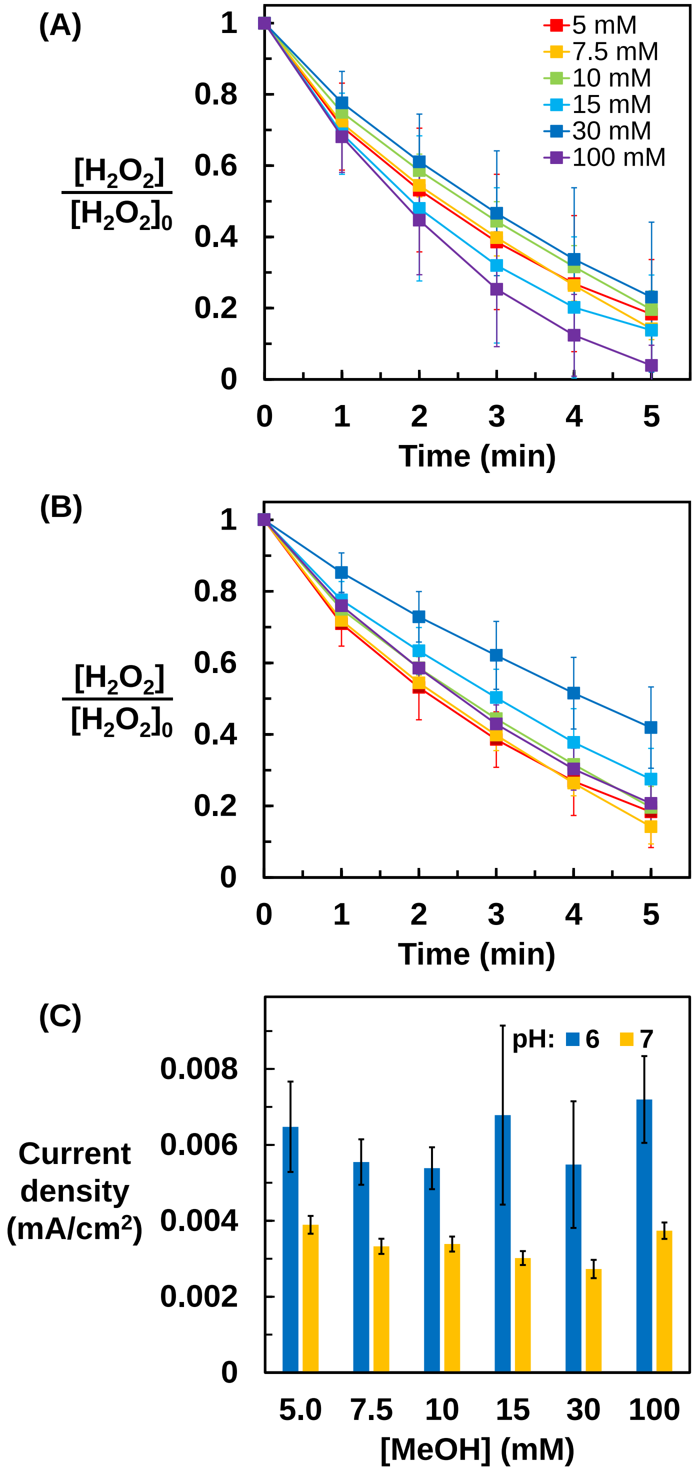

Figure 3.8 H_2O_2 concentrations in the cathode chamber at (A) pH 6 and (B) pH 7 with various concentrations of methanol in electrolyte. (C) Current density as a function of methanol concentration. Potential = +0.020V, $[H_2O_2]_0$ = 1.25 mg/L. Error bars represent one standard deviation; error bars not shown are smaller than symbols.

The applied potentials in all experiments were above the H_2 evolution potential (Figure 3.9), indicating that reduction of water could not explain the observed trend. Because the equilibrium potential of the one-electron reduction of H_2O_2 to ${}^{\bullet}OH$ (eq 3.2) varied with pH with a slope of -0.059 V per unit increase in pH, the overpotential driving this reaction (i.e., difference between the operating potential and the equilibrium potential) also decreased as the pH increased. Therefore, the slow reaction kinetics at pH 8 and 9 could have been due to the smaller driving forces (i.e., overpotentials) for H_2O_2 activation.

$$\mathrm{H_2O_2} + e^- \rightarrow \mathrm{OH^-} + {}^{\bullet}\mathrm{OH} \qquad (3.2)$$

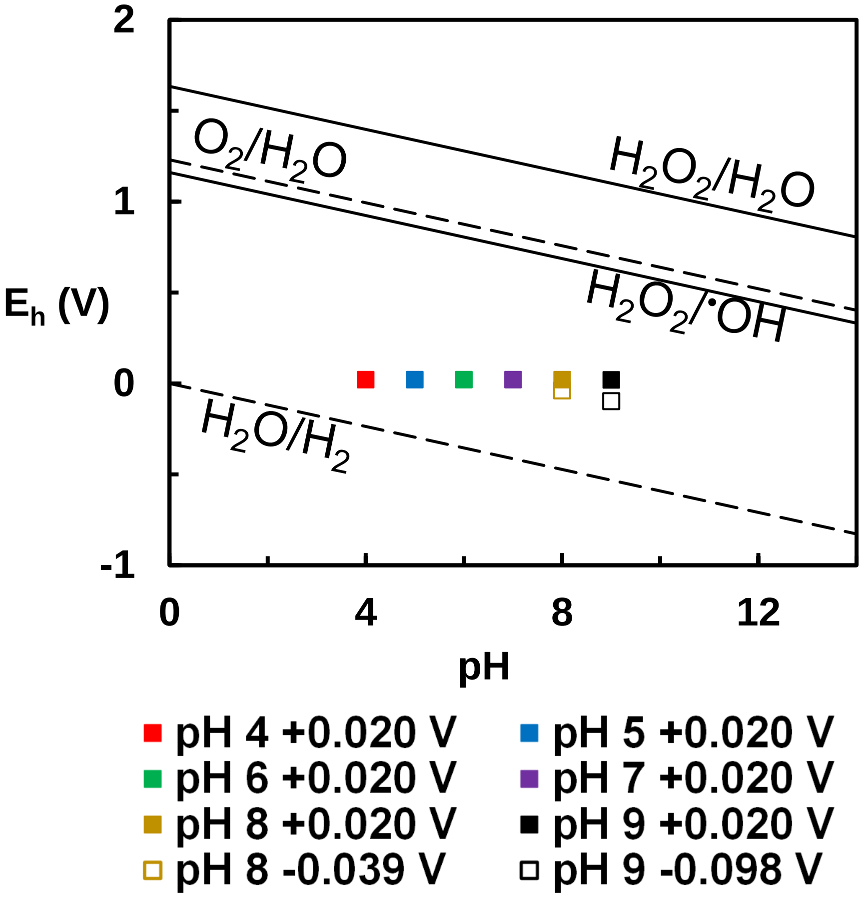

Figure 3.9 Pourbaix diagram for H_2O_2, $[H_2O_2]$ = 37 µM and $[{}^{\bullet}OH]_{SS} = 3.6 \times 10^{-11}$ M. The $[{}^{\bullet}OH]_{SS}$ was estimated based on a previously reported 1,4-dioxane degradation kinetics under similar operating conditions (Weng et al. 2020). Symbols represent experimental conditions tested in this study.

To further investigate the effect of overpotential on the performance of the stainless-steel electrode at high pH values (i.e., 8 and 9), applied potentials were adjusted by -0.059 V per pH increment (i.e., -0.039 V at pH 8 and -0.098 V 9) to maintain the same driving force as values applied at pH 7 and +0.020 V. With the same overpotential, H_2O_2 decomposition rates were almost identical to those observed at pH 7. However, the observed current densities were higher than those observed at pH 7 and +0.02V, indicating that H_2O_2 could have been lost through different pathways.

To gain insight into the rate-limiting step of the H_2O_2 activation process, the experiment was repeated at varying initial H_2O_2 concentrations. In comparison with the experiments conducted with 1.25 mg/L of H_2O_2, increasing the initial H_2O_2 concentration to 2.5 mg/L and 5.0 mg/L resulted in about 10% and 40% reduction in the H_2O_2 loss rates (Figure 3.10). The decrease in the rate of H_2O_2 decomposition was much smaller than values predicted if H_2O_2 activation on the surface was the rate-limiting step (i.e., zero order kinetics).

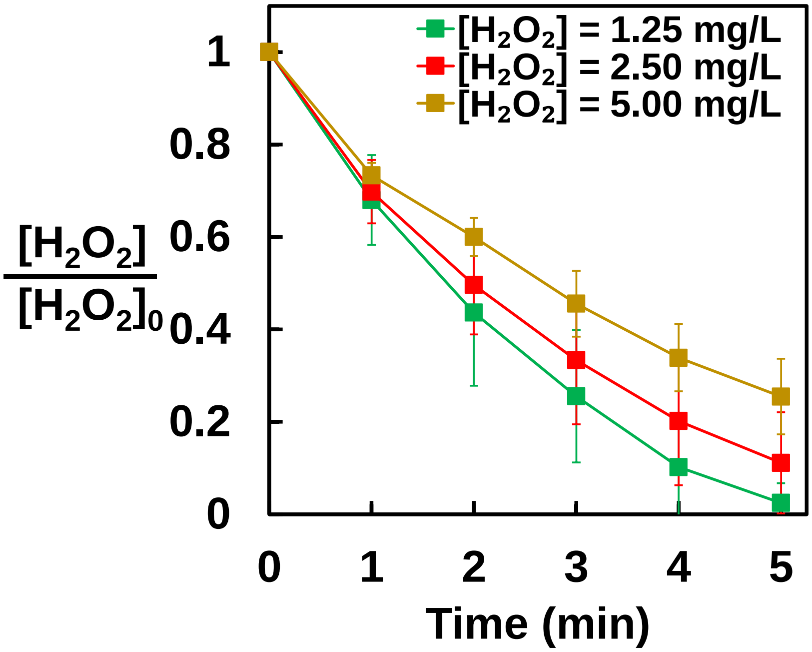

Figure 3.10 H_2O_2 transformation in the cathode chamber at varying initial H_2O_2 concentration. Applied potential = +0.020V, pH = 6.

The mass-transport limiting current density was predicted based on film theory. The mass-transfer coefficient k_m was predicted by:

$$k_m = \frac{D}{L_f} \tag{3.3}$$

where D is the diffusion coefficient of H_2O_2 in water (1.5×10^{-5} cm^2 s^{-1}) (Abdekhodaie et al. 2015, Gros and Bergel 1995), and L_f is the film thickness (about 100 μm) (Chaplin 2014, 2019). The rate constant limited by mass transport, k_{limt}, was predicted by:

$$k_{limt} = k_m a \tag{3.4}$$

where a is the surface area to volume ratio (m^2/m^3). The measured rate constants were comparable with mass-transport limitations (predicted $k_{limt} = 5.4 \times 10^{-3}$ s^{-1}).

Finally, a linear relationship correlation was observed between the observed current densities and the initial H_2O_2 concentration, suggesting the presence of excess available reactive sites on the stainless-steel electrode surface (Figure 3.11). Therefore, the mass transport of H_2O_2 to the electrode surface was likely the rate-limiting step for H_2O_2 activation.

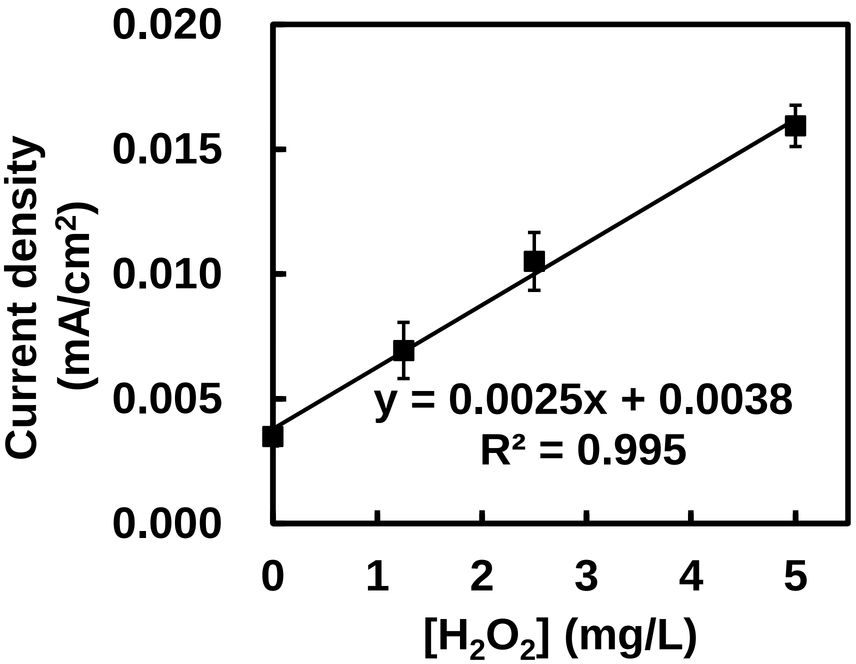

Figure 3.11 Relationship between the observed current densities and initial H_2O_2 concentration. Applied potential = +0.020V, pH = 6.

3.3.3 Reactive oxidant production

Although the activation of H_2O_2 by Fe(II) and Fe oxides has been studied for over a century (Fenton 1894), the identity of the reactive oxidants produced in these systems is still unresolved. Most evidence suggests that the homogeneous reaction of uncomplexed Fe(II) and H_2O_2 produce $^{\bullet}OH$ at low pH values and a different oxidant, most likely an Fe[IV] species, at pH values above 4 (Hug and Leupin 2003). Fe[IV] species also appears to dominate in the presence of EDTA (Rush and Koppenol 1986) and when Fe(II) is produced by photolysis of Fe(III) complexes (i.e., the photo-Fenton reaction) (Pignatello et al. 1999). For heterogeneous processes, the widely accepted mechanism involves $^{\bullet}OH$ production through reactions between H_2O_2 and surface iron species (i.e., ≡Fe(II)) (Lin and Gurol 1998). However, the identity of the reactive species generated with other heterogeneous catalysts is less certain. For example, both $^{\bullet}OH$ and an unidentified weak oxidant are formed over the acidic to near-neutral pH in a ferrihydrite-induced heterogeneous Fenton process (Chen et al. 2021). Surface ferryl (i.e., ≡ Fe[IV]) has also been proposed as the species in systems using a titanium oxide-supported iron catalyst (Kim et al. 2020).

To gain insight into the oxidants produced by H_2O_2 activation on the stainless-steel electrode, methanol (100 mM) was used as a probe to quantify the total amount of reactive oxidants (i.e., Fe[IV] and $^{\bullet}OH$), whereas 2-propanol (100 mM) was used to quantify $^{\bullet}OH$.

At +0.020 V, the yield of the main oxidation products (i.e., formaldehyde and acetone) increased as the solution pH increased from 4 to 7 and decreased as the pH further increased from 7 to 9 (Figure 3.12). The oxidant species generated at +0.020 V produced similar amounts of formaldehyde and acetone, indicating •OH was the main oxidant species. A maximum yield for •OH production of 71% was observed at pH 7, which is over an order of magnitude higher than yields observed for other Fenton systems (Chou et al. 2001, Huang et al. 2001, Huling et al. 1998, Kanel et al. 2004, Lee and Sedlak 2009, Seo et al. 2015, Valentine and Wang 1998, Xue et al. 2009). At pH 9, no reactive oxidant was formed when +0.020V was applied despite of a loss of about 20% of the H_2O_2 during the experiments.

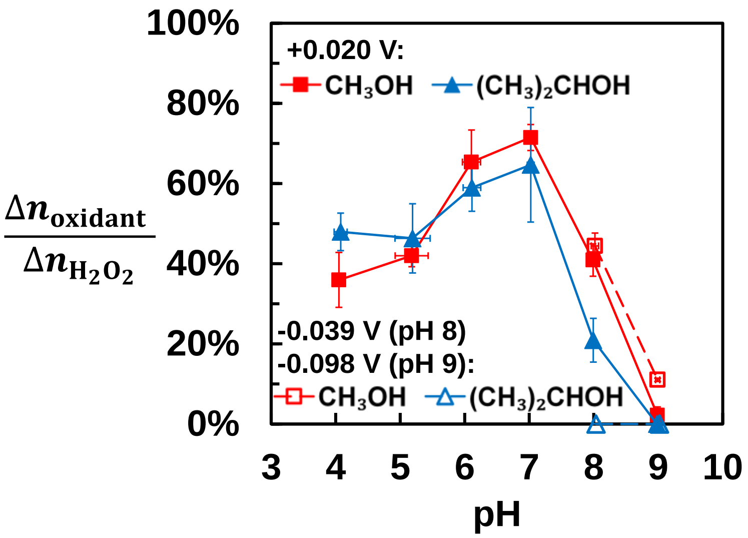

Figure 3.12 Yield of oxidants as a function of pH and applied potential. $[H_2O_2]_0 = 1.25$ mg/L, [Probe compound] = 100 mM. Error bars represent one standard deviation; error bars not shown are smaller than symbols.

After lowering the applied potential (hollow symbol in Figure 3.12), the total yield of reactive oxidants observed at pH 8 was about the same as that observed at +0.020 V and the stainless-steel generated reactive oxidants at pH 9. However, the reactive oxidant produced under these conditions were only capable of oxidizing methanol, indicating the reactive oxidant generated when H_2O_2 was activated switched from •OH to Fe[IV]. Because Fe was not detected in the aqueous phase at pH values above 7, the Fe[IV] was assumed to be a surface species (e.g., ≡Fe[IV]).

The electron utilization efficiency for producing reactive oxidants (Figure 3.13A) and for activating H_2O_2 (Figure 3.13B) followed similar trend as the yield of oxidants, with the maximum values observed at pH 7. At the optimal operating condition (i.e., pH 7 and +0.020 V), about 50% of electrons were consumed for H_2O_2 production, indicating a high electron utilization efficiency.

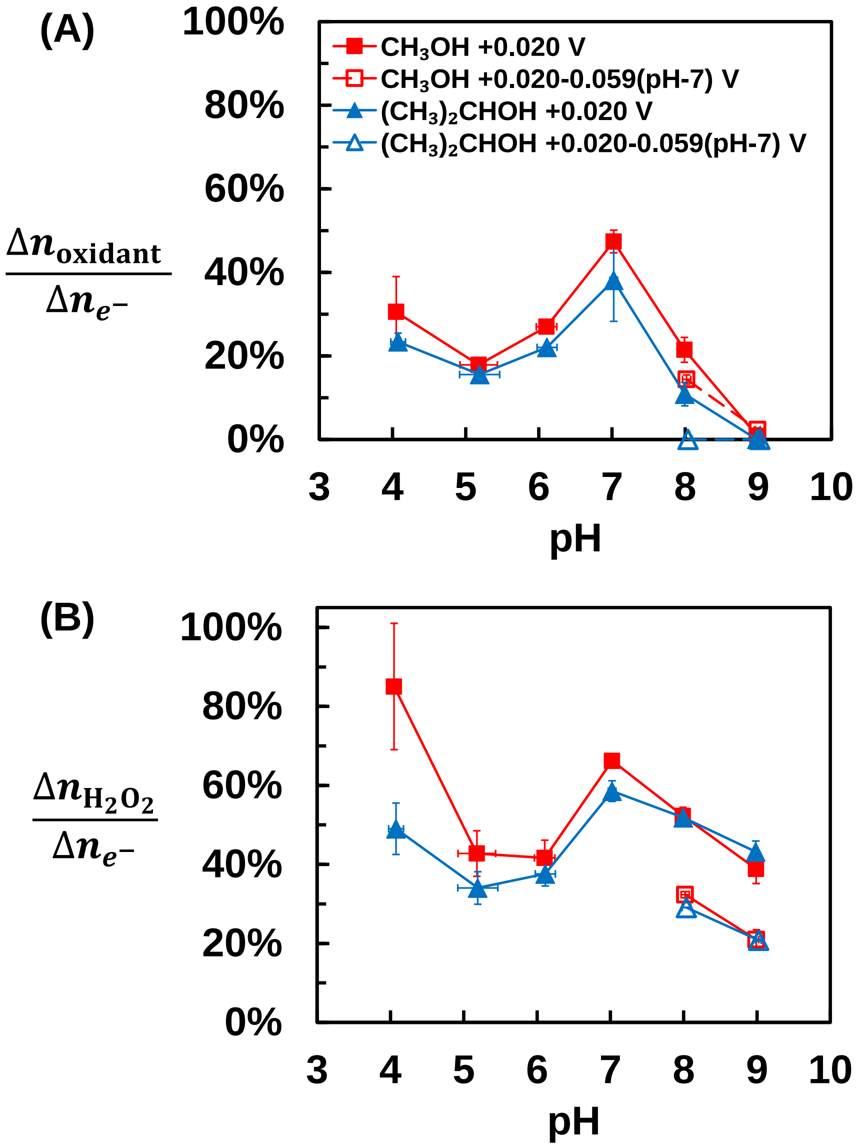

Figure 3.13 Electron utilization efficiency for (A) producing reactive oxidants and (B) for activating H_2O_2 as a function of pH and applied potential. $[H_2O_2]_0 = 1.25$ mg/L, [Probe compound] = 100 mM. Error bars represent one standard deviation; error bars not shown are smaller than symbols.

3.3.4 Metals release from stainless-steel electrode

The leaching of Fe and Cr from pre-conditioned stainless-steel electrodes decreased as the pH value increased from pH 4 to 6 at +0.020 V. No significant metal leaching was observed when the electrode was operated at pH values above 6 (Figure 3.14). Fe(II) accounted for approximately 80% of the Fe detected in solution. Almost all of the chromium released from the electrode consisted of Cr(III). The concentration of Cr(VI) was near or below the limit of detection (2 µg/L) throughout the experiment. Although negatively charged Cr(VI) species (i.e., $HCrO_4^-$) can cross the anion exchange membranes, Cr was not detected in the anode chamber. The chromium concentrations observed during these experiments were always below the USEPA maximum contaminant level (MCL) for total Cr of 100 µg/L (USEPA 2022a) and the California MCL for chromium(VI) of 10 µg/L (California Water Boards 2013). However, the Fe concentrations were above the secondary maximum contaminant level (SMCL) of 0.3 mg/L (USEPA 2022b) in experiments conducted at pH 6 and below. Other metals that are known to occur in 410 stainless-steel (e.g., Ni and Mg) were not detected in solution under any pH conditions.

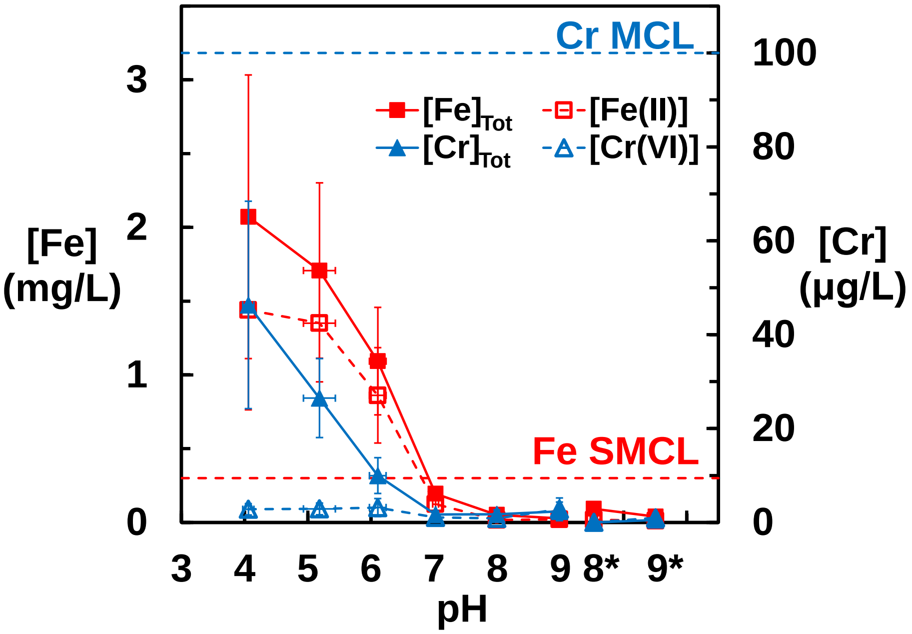

Figure 3.14 Concentrations of iron and chromium after five minutes of electrolysis at a potential of +0.020 V. *represents experiments conducted at potentials lower than +0.020 V (i.e., -0.039 V at pH 8 and -0.098 V at pH9). Error bars represent one standard deviation.

Some aspects of the leaching of metals can be understood by considering the thermodynamics of the passivation layer (Figure 3.15). At pH 4 and 5, the Fe(III)-oxides in the passivation layer should be reduced to Fe^{2+} and the Cr(III)-oxides should dissolve to produce low concentrations of aqueous Cr(III) species (i.e., Cr^{3+} or $Cr(OH)^{2+}$) at an electrode potential of +0.020 V. Additionally, as the passivation layer was reduced and dissolved, elemental Fe and Cr could be exposed to the solution, resulting in formation of Fe^{2+} and Cr(III) species, which was consistent with the anodic current observed at +0.020 V during the pre-conditioning process. At pH 6, the Fe_2O_3 could be reduced and react with Cr_2O_3 to form $FeCr_2O_4$ (eq 5 in Table 3.2), which could possibly explain the leaching of Fe and Cr at pH 6, especially because the newly formed amorphous $FeCr_2O_4$ has a higher solubility than that of the crystalline form. At pH values above 6, a passivation layer composed of $Fe_2O_{3(S)}$ and $Cr_2O_{3(S)}$ could have been formed on the surface of the stainless-steel electrode. This phase would prevent further metal leaching from stainless-steel (Nagayama and Cohen 1962).

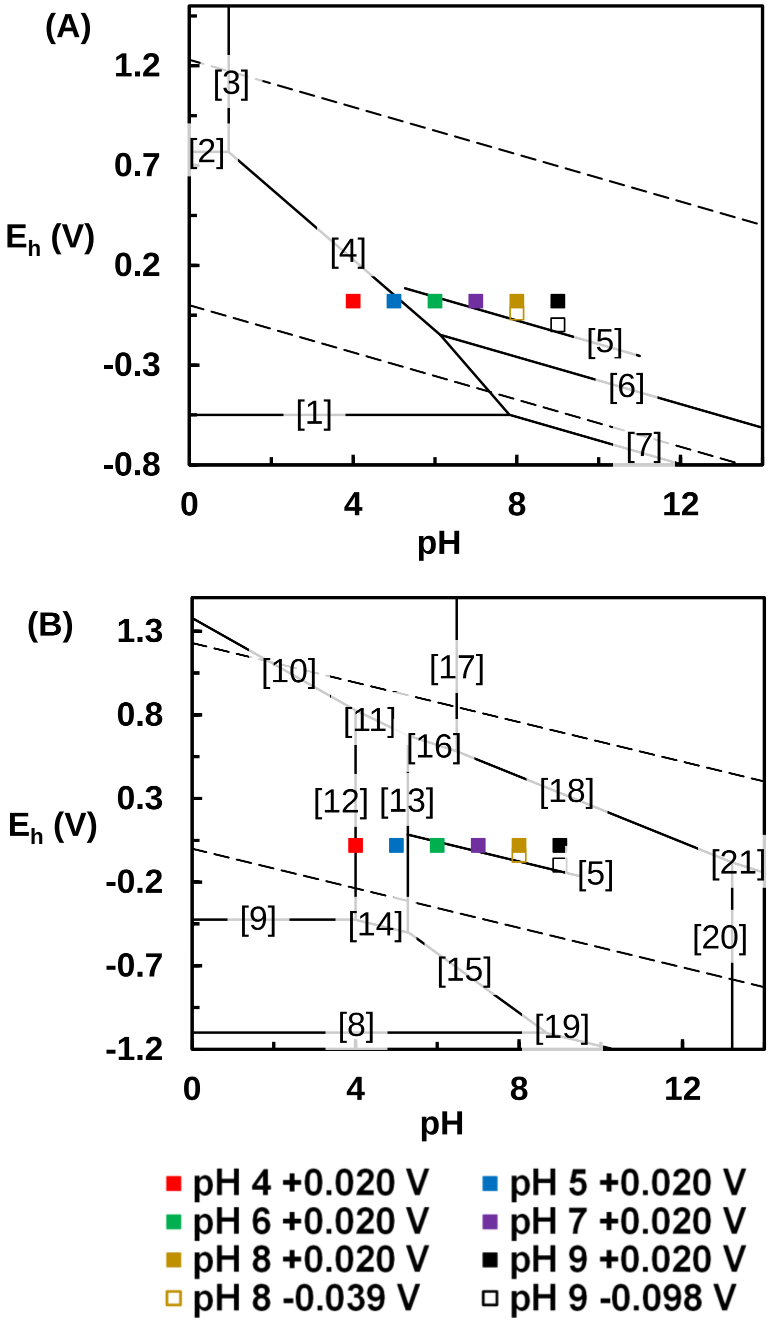

Figure 3.15 Pourbaix diagram for (A) Fe, $[Fe]_{tot}$ = 1 mg/L, (B) Cr, $[Cr]_{tot}$ = 10 µg/L. Symbols represent experimental conditions tested in this study.

Table 3.2 Reactions considered for construction of Pourbaix diagrams.

[1]	$\mathrm{Fe} \leftrightarrow \mathrm{Fe}^{2+} + 2e^-$	E° = -0.41 V
[2]	$\mathrm{Fe}^{2+} \leftrightarrow \mathrm{Fe}^{3+} + e^-$	E° = +0.77 V
[3]	$2\mathrm{Fe}^{3+} + 3\mathrm{H_2O} \leftrightarrow \mathrm{Fe_2O_3} + 6\mathrm{H}^+$	$K = 10^{3.73}$
[4]	$2\mathrm{Fe}^{2+} + 3\mathrm{H_2O} \leftrightarrow \mathrm{Fe_2O_3} + 6\mathrm{H}^+ + 2e^-$	E° = +0.66 V
[5]	$2\mathrm{FeCr_2O_4} + \mathrm{H_2O} \leftrightarrow \mathrm{Fe_2O_3} + 2\mathrm{Cr_2O_3} + 2\mathrm{H}^+ + 2e^-$	E° = +0.40 V
[6]	$2\mathrm{Fe_3O_4} + \mathrm{H_2O} \leftrightarrow 3\mathrm{Fe_2O_3} + 2\mathrm{H}^+ + 2e^-$	E° = +0.21 V
[7]	$3\mathrm{Fe} + 4\mathrm{H_2O} \leftrightarrow \mathrm{Fe_3O_4} + 8\mathrm{H}^+ + 8e^-$	E° = -0.09 V
[8]	$\mathrm{Cr} \leftrightarrow \mathrm{Cr}^{2+} + 2e^-$	E° = -0.90 V
[9]	$\mathrm{Cr}^{2+} \leftrightarrow \mathrm{Cr}^{3+} + e^-$	E° = -0.43 V
[10]	$\mathrm{Cr}^{3+} + 4\mathrm{H_2O} \leftrightarrow \mathrm{HCrO_4^-} + 3e^- + 7\mathrm{H}^+$	E° = +1.38 V
[11]	$\mathrm{CrOH}^{2+} + 3\mathrm{H_2O} \leftrightarrow \mathrm{HCrO_4^-} + 3e^- + 6\mathrm{H}^+$	E° = +1.30 V
[12]	$\mathrm{Cr}^{3+} + \mathrm{H_2O} \leftrightarrow \mathrm{CrOH}^{2+} + \mathrm{H}^+$	$K = 10^{-4.00}$
[13]	$2\mathrm{CrOH}^{2+} + \mathrm{H_2O} \leftrightarrow \mathrm{Cr_2O_3} + 4\mathrm{H}^+$	$K = 10^{-7.68}$
[14]	$\mathrm{Cr}^{2+} + \mathrm{H_2O} \leftrightarrow \mathrm{CrOH}^{2+} + \mathrm{H}^+ + e^-$	E° = -0.19 V
[15]	$2\mathrm{Cr}^{2+} + 3\mathrm{H_2O} \leftrightarrow \mathrm{Cr_2O_3} + 6\mathrm{H}^+ + 2e^-$	E° = +0.04 V
[16]	$\mathrm{Cr_2O_3} + 5\mathrm{H_2O} \leftrightarrow 2\mathrm{HCrO_4^-} + 6e^- + 8\mathrm{H}^+$	E° = 1.23 V
[17]	$\mathrm{HCrO_4^-} \leftrightarrow \mathrm{CrO_4^{2-}} + \mathrm{H}^+$	$K = 10^{-6.47}$
[18]	$\mathrm{Cr_2O_3} + 5\mathrm{H_2O} \leftrightarrow 2\mathrm{CrO_4^{2-}} + 6e^- + 10\mathrm{H}^+$	E° = 1.35 V
[19]	$2\mathrm{Cr} + 3\mathrm{H_2O} \leftrightarrow \mathrm{Cr_2O_3} + 6e^- + 6\mathrm{H}^+$	E° = -0.59 V
[20]	$\mathrm{Cr_2O_3} + 5\mathrm{H_2O} \leftrightarrow 2\mathrm{Cr(OH)_4^-} + 2\mathrm{H}^+$	$K = 10^{-39.86}$
[21]	$\mathrm{Cr(OH)_4^-} \leftrightarrow \mathrm{CrO_4^{2-}} + 3e^- + 4\mathrm{H}^+$	E° = 0.96 V

Changes in the oxidation state of Fe on the electrode surface were characterized by X-ray photoelectron spectroscopy. Samples for each operating condition were collected from at least three different locations on the electrode. Higher Fe(II) and Fe(0) contents were observed under acidic pH conditions when metal leaching was observed, which was consistent with the reduction of Fe(III)-oxides on the passivation layer coating the electrode surface (Figure 3.16). The greater heterogeneity of the electrode surface when metal leaching was observed (i.e., the wider standard deviations) was consistent with the fact that corrosion could happen at different rates at different locations (Frankel and Sridhar 2008).

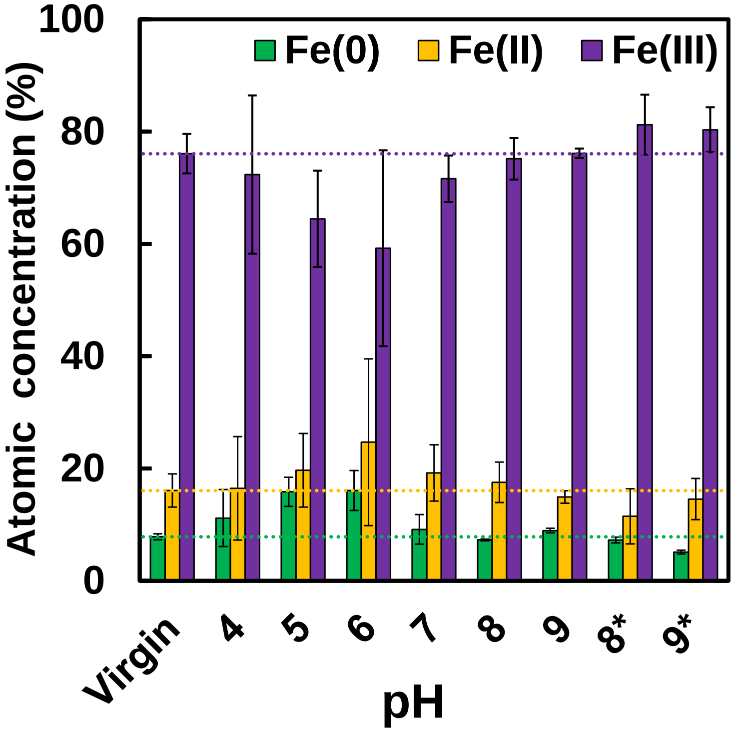

Figure 3.16 Atomic concentration of Fe in different oxidation states. Potential = +0.020 V, *represents experiments conducted at potentials lower than +0.020 V (i.e., -0.039 V at pH 8 and -0.098 V at pH9). Error bars represent one standard deviation.

Ambient-pressure soft X-ray photoelectron spectroscopy confirmed that the stainless-steel was stable in the presence of water (Figure 3.17).

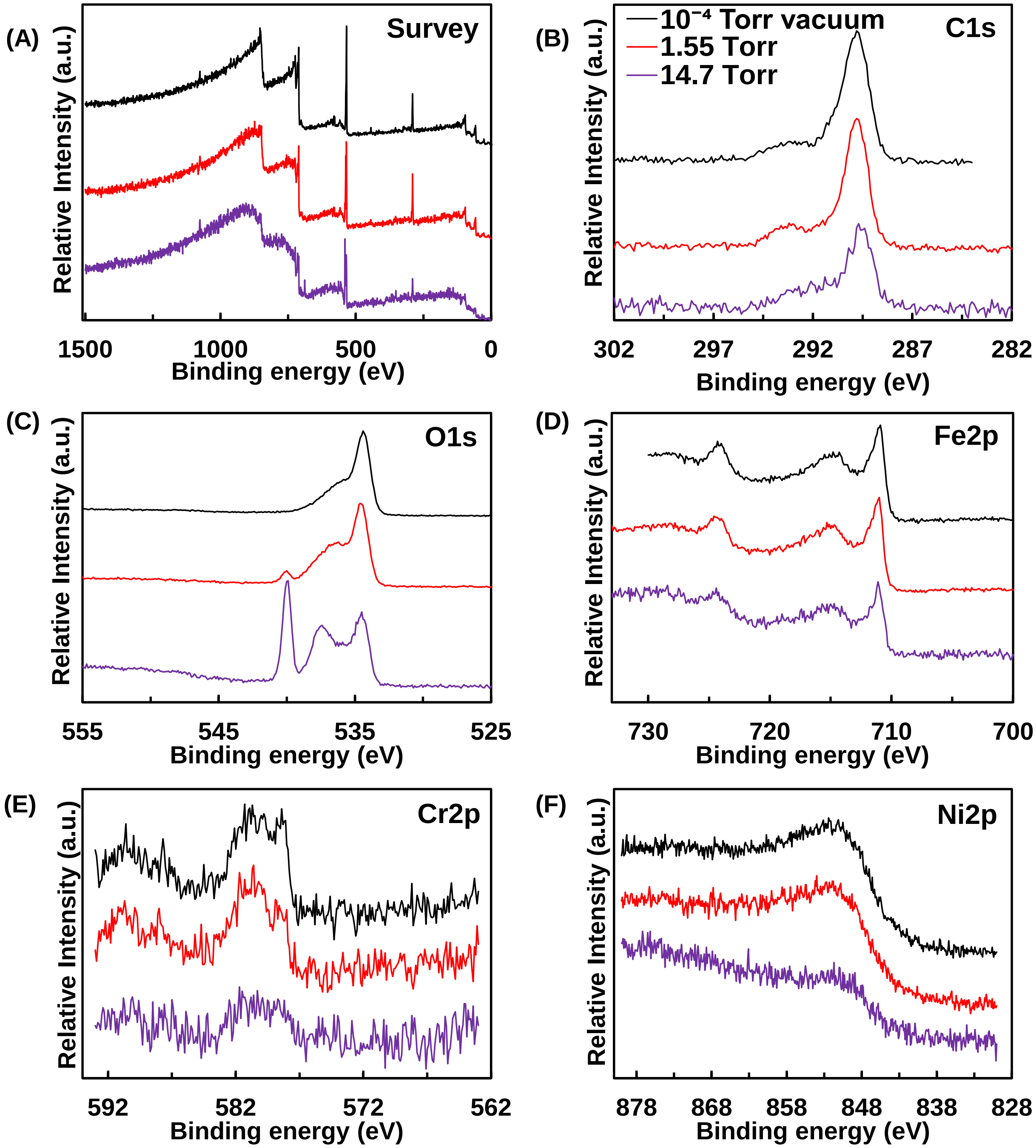

Figure 3.17 Comparison of XPS measurements at different water vapor pressure. No apparent change was observed except for O1s. The additional peaks at 537 and 540 eV for O1s were associated with water vapor and potentially physically adsorbed water, respectively.

Additionally, increasing the initial concentrations of H_2O_2 (0-5 mg/L), methanol (5-100 mM), and dissolved O_2 (anerobic versus aerobic) did not have a major impact on the leaching of Fe or Cr from stainless-steel electrodes (Figure 3.18 and 3.19). In fact, the presence of O_2 and higher concentrations of H_2O_2 slightly reduced metal leaching, possibly by enhancing the rate of oxidation of reduced Fe species (e.g., Fe(0) and Fe(II)) to form a more effective passivation layer. Therefore, the H_2O_2 activation, reactions of the oxidant species with methanol, and O_2 reduction reaction were excluded as the cause of the observed metal leaching. At an open circuit potential, the stainless-steel did not leach any metals when in contact with H_2O_2 (Figure 3.18), which further supported the conclusion that metal leaching was caused by the electrochemically driven redox reactions on the electrode surface.

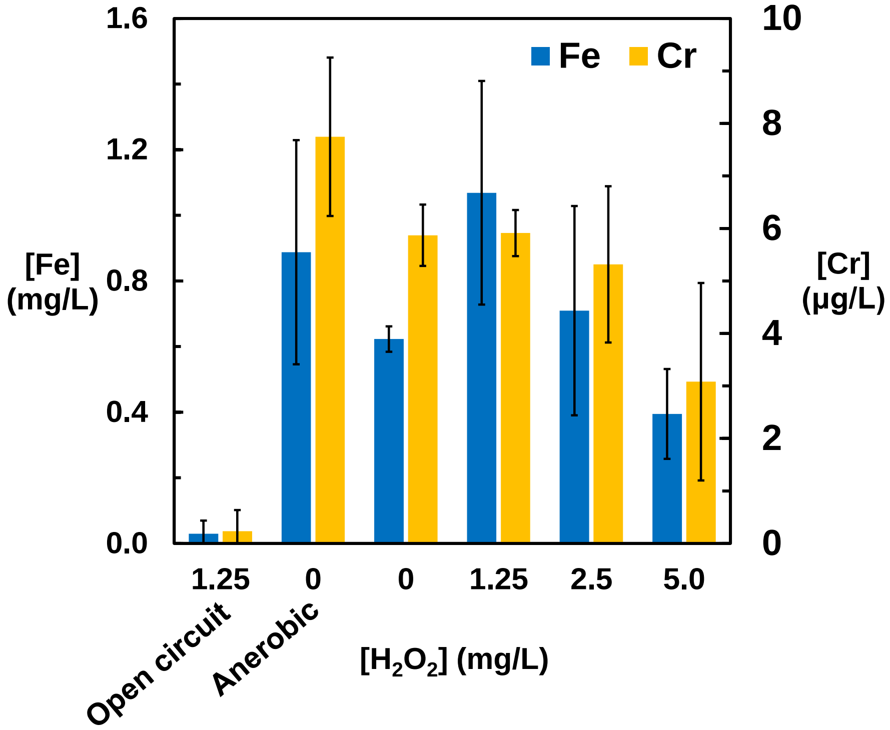

Figure 3.18 Metal concentrations after five minutes of electrolysis under various experimental conditions. Potential = +0.020 V, pH = 6. Error bars represent one standard deviation. For experiments conducted under anerobic conditions, the solution was purged with N_2 for at least 20 minutes before the experiment and was continuously purged with N_2 throughout the experiments in the sealed H-cell reactor. The flow rate of the N_2 stream was maintained at 0.5 L/min. Error bars represent one standard deviation.

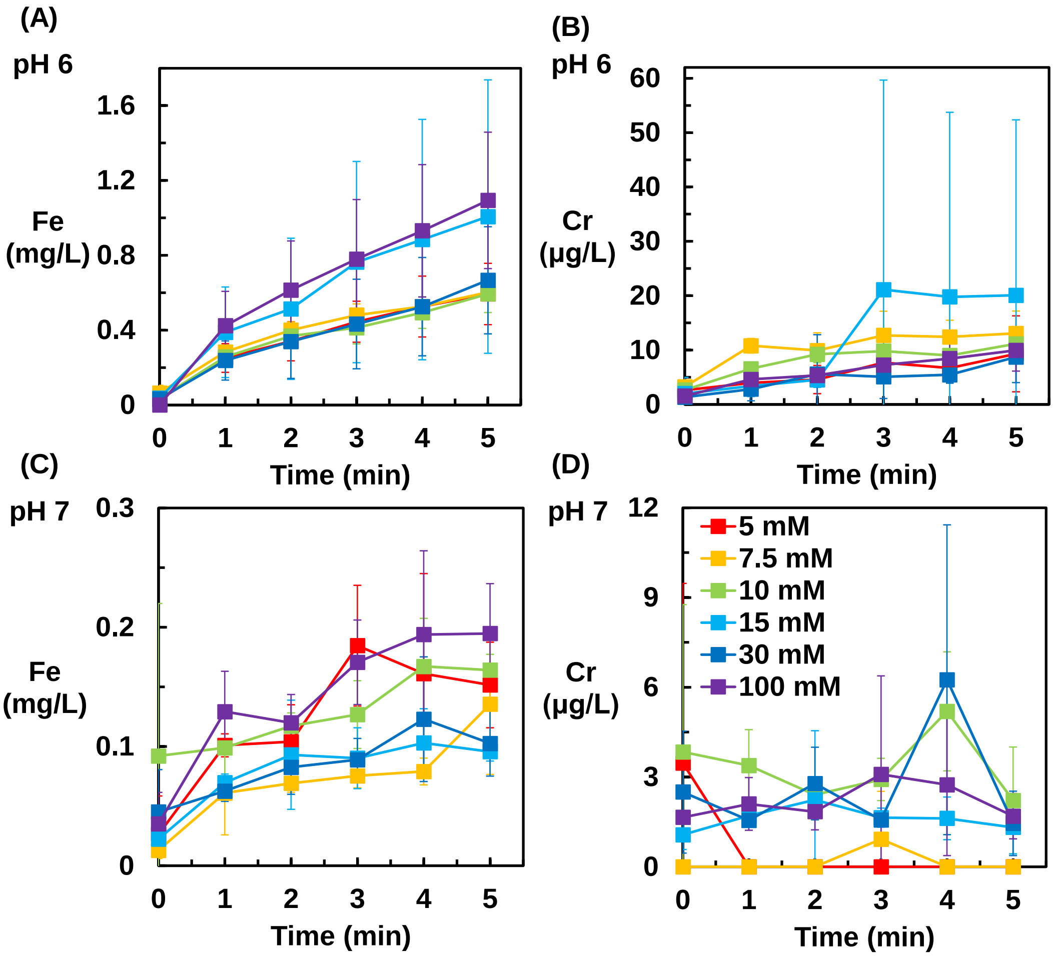

Figure 3.19 Metal concentrations after five minutes of electrolysis of electrolyte containing varying concentrations of methanol. Error bars represent one standard deviation. Potential = +0.020 V.

3.3.5 Surface scavenging of •OH

Reactions that take place at the surface that consume oxidants produced when H_2O_2 is activated can lower the efficiency of contaminant transformation (Miller and Valentine 1995, Rusevova Crincoli and Huling 2020). Different concentrations of methanol were added in the electrolyte to quantify the maximum amount of •OH produced at the surface that could be used for contaminant transformation (Figure 3.20). The observed •OH yield $(\frac{\Delta n_{\mathrm{CH_2O}}}{\Delta n_{\mathrm{H_2O_2}}})$ was used to represent the fraction of H_2O_2 that produced oxidants capable of reacting with the probe compound. The observed •OH yield depends on both •OH yield from the H_2O_2 activation process and the proportion of •OH that reacts with the probe compound (i.e., methanol). Under conditions employed in this study, •OH produced at the electrode surface could react with the probe compound (i.e., methanol), buffers, Fe^{2+}, H_2O_2, or undergo reactions at the electrode surface. Assuming that methanol and the reactions involving •OH do not affect the rate of production of •OH, the observed •OH yield can be expressed as:

$$Observed\ {}^{\bullet}OH\ yield = {}^{\bullet}OH\ yield \cdot \frac{k_{\mathrm{CH_3OH},\bullet\mathrm{OH}}[\mathrm{CH_3OH}]}{\sum k_i[i] + k_{\mathrm{surface},\bullet\mathrm{OH}}[\mathrm{Surface}]} \tag{3.5}$$

where *i* represent the species in the aqueous phase (i.e., methanol, buffer, Fe^{2+}, H_2O_2,) that react with •OH.

At the highest methanol concentrations used (i.e., 100 mM) formaldehyde yields plateaued at about 70% (i.e., the yield of •OH produced on the stainless-steel surface as depicted in Figure 3.12). As methanol concentrations decreased below 30 mM, the observed •OH yield dropped rapidly, indicating significant competition from other •OH scavenging species. At methanol concentrations above about 30 mM, methanol outcompeted all other species for •OH and the observed •OH yield approached the maximum values.

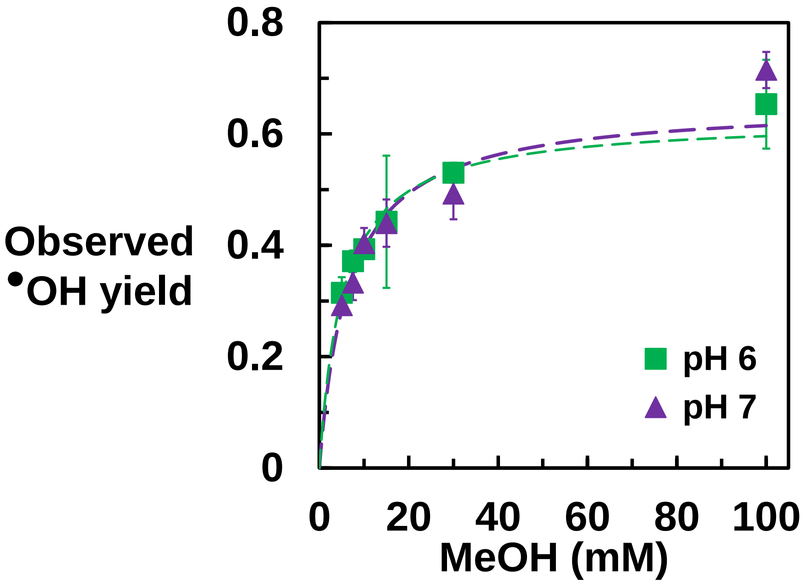

Figure 3.20 Observed •OH yield as a function of methanol concentration. Potential = +0.020 V; $[H_2O_2]_0$ = 1.25 mg/L. Dashed lines represent the predicted stoichiometric efficiency based on eq 3.5. Error bars represent one standard deviation; error bars not shown are smaller than symbols.

The reaction rate constant for the reaction between •OH and the electrode surface $k_{\mathrm{surface},\bullet\mathrm{OH}}$ was calculated by rearranging eq 3.5 into a linear form (Figure 3.21) and subtracting out contributions from H_2O_2 and the buffer to •OH scavenging. The second-order rate constants for the reactions of buffers with •OH were measured using competition kinetics as $k_{\mathrm{MES},\bullet\mathrm{OH}} = 2.1\pm0.1 \times 10^9\ \mathrm{M^{-1}\ s^{-1}}$ and $k_{\mathrm{PIPES},\bullet\mathrm{OH}} = 4.2\pm0.1\times10^9\ \mathrm{M^{-1}\ s^{-1}}$, respectively (Section A.2.1 of the Appendix). The rate constants for the reaction between the electrode surface and •OH was calculated as $6.5 \times 10^5\ \mathrm{g^{-1}\ s^{-1}}$ at pH 6 and $4.9 \times 10^5\ \mathrm{g^{-1}\ s^{-1}}$ at pH 7.

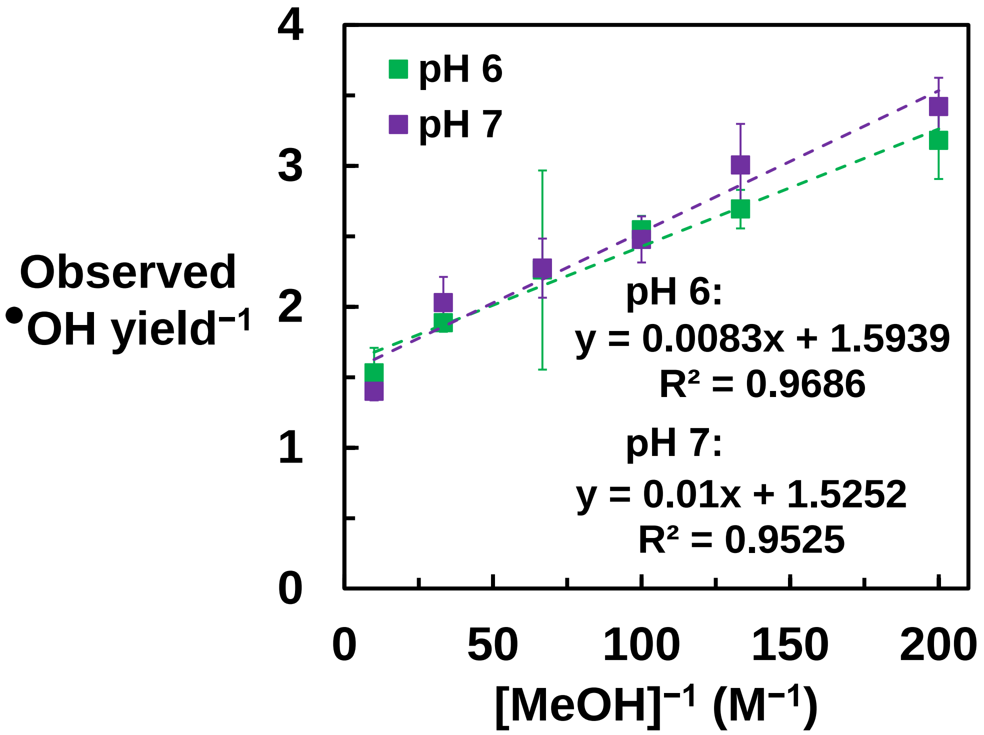

Figure 3.21 Linear relationship between inverse of observed •OH yield and inverse of concentration of methanol. Error bars represent one standard deviation.

The information obtained from these experiments was used to estimate branching ratios for •OH under representative conditions. This involved consideration of a scenario in which a 4.5 g stainless-steel electrode was used to treat 100 mL of a carbamazepine-containing solution (20 μg/L) in the presence of various concentrations of competing organic compounds. The fraction of •OH scavenged by the surface increased from about 10% to 90% as the concentrations of competing organic compounds decreased from 1000 mg-C/L to 10 mg/L (Figure 3.22). These results indicated that the performance of the stainless-steel electrode should not be affected by the presence of competing organic compounds under conditions typically encountered in natural waters (i.e., dissolved organic carbon <10 mg-C/L). Thus, only about 0.03% of the •OH that is produced from H_2O_2 activation reacts with a TrOC like carbamazepine, but variations in water quality will not affect the treatment efficacy. Due to the modest impact of other solutes (e.g., trace amounts of organic solvent) on the fate of •OH produced on the electrode surface, the stainless-steel electrode could potentially be implemented for the treatment of high-strength wastewater (e.g., industrial wastewater that containing other organic that would compete for •OH in a conventional advanced oxidation process).

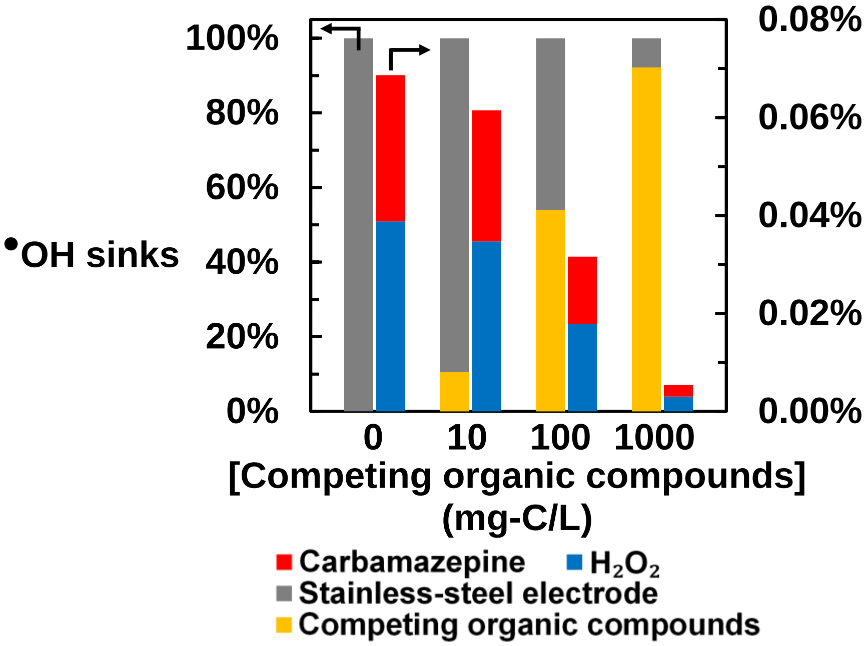

Figure 3.22 Predicted •OH branching ratios for the treatment of 20 µg/L of carbamazepine with 4.5 g of stainless-steel electrode in the presence of 1.25 mg/L of H_2O_2 and various concentrations of competing organic compounds. Carbamazepine and H_2O_2 are also shown on the right axis.

3.3.6 Possible mechanisms of H_2O_2 activation

H_2O_2 could potentially undergo three transformation pathways: (1) homogeneous Fenton processes; (2) direct electron transfer on the stainless-steel electrode; and (3) heterogeneous electro-Fenton processes (Figure 3.23). For the direct electron transfer and heterogeneous electro-Fenton pathways, any •OH produced should consist of adsorbed species (•OH_{ad}). These species may diffuse into the aqueous phase. It should be noted that the reactivity of •OH_{ad} towards organic compounds and its ability to diffuse into the aqueous phase is still unclear (Xie et al. 2022).

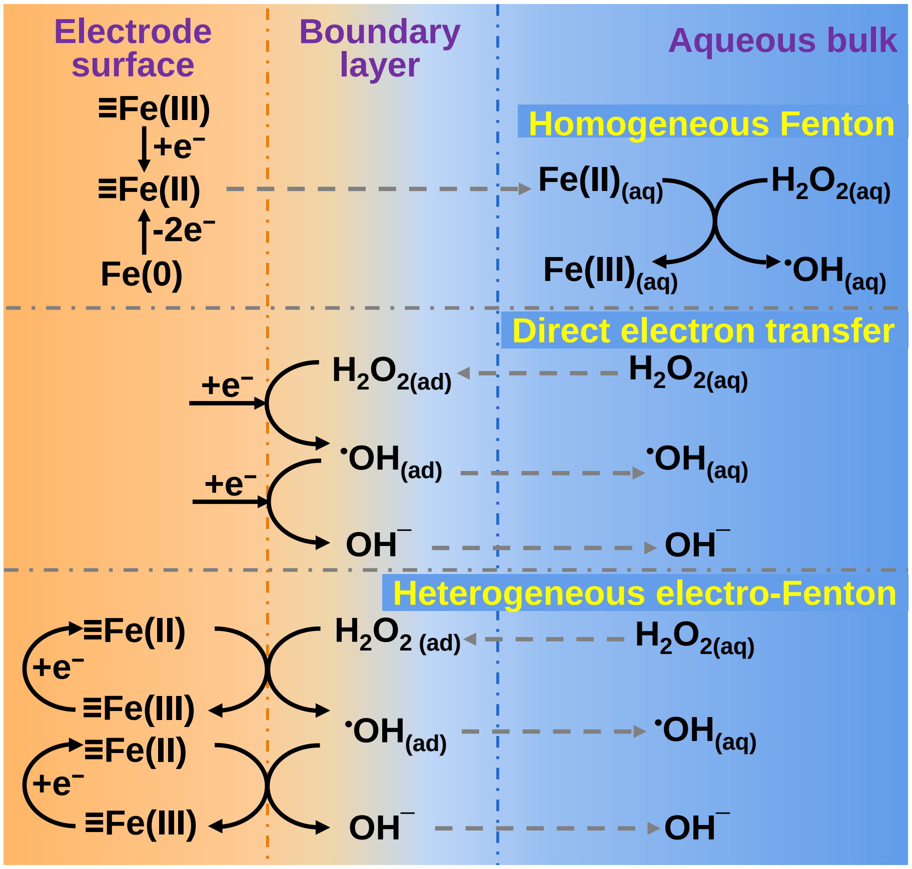

Figure 3.23 Possible mechanisms for H_2O_2 transformation.

The homogeneous pathway for H_2O_2 activation (i.e., the Fenton reaction) was evaluated at pH 4-6 using measured data on the measured concentration of dissolved Fe(II). The H_2O_2 decomposition rates from this process were estimated to be $1.4 \pm 0.7 \times 10^{-3}$ s^{-1}, $1.4 \pm 0.5 \times 10^{-3}$ s^{-1}, and $2.0 \pm 0.8 \times 10^{-3}$ s^{-1} at pH values of 4, 5, and 6 (Section A.2.3 of the Appendix). Therefore, 35%, 21% and 23% of the H_2O_2 was activated through the homogeneous Fenton pathway at pH 4, 5 and 6, respectively. At pH values above 5, this process should have produced Fe[IV] instead of $^\bullet OH$ (Bataineh et al. 2012, Hug and Leupin 2003, Lu et al. 2018). The production of $^\bullet OH$ at pH values above 5 excluded the homogeneous Fenton reaction as a mechanism for H_2O_2 activation at higher pH values.

The electrochemical reduction of H_2O_2 by direct electron transfer has been studied previously and proceeds by one-electron transfer processes at low overpotentials (e.g., *E* = +0.4 V at pH 1). H_2O_2 is first reduced to adsorbed $^\bullet OH_{ad}$. $^\bullet OH_{ad}$ is further reduced to H_2O by a second electron (Eickes et al. 2000, Flätgen et al. 1999, Honda et al. 1983, Patra and Munichandraiah 2009). Because of the similar overpotential applied on the stainless-steel electrode, it was likely that the $^\bullet OH_{ad}$ can be produced by direct electron transfer of H_2O_2. The second electron transfer to reduce $^\bullet OH_{ad}$ to H_2O can be one possible explanation of the $^\bullet OH$ scavenging by the electrode surface.

The heterogeneous electro-Fenton process can be initiated at +0.020 V and pH values below 7 by reduction of $\equiv Fe(III)$ to form $\equiv Fe(II)$. Surface $\equiv Fe(II)$ can react with H_2O_2 to produce $^{\bullet}OH_{ad}$. The formed $^{\bullet}OH_{ad}$ may react with ≡ Fe(II) on the surface, which could be another explanation for the $^{\bullet}OH$ scavenging by the electrode surface. However, at pH values above 7, the electro-Fenton pathway was unlikely to happen because ≡ Fe(III) (e.g., Fe_2O_3) was thermodynamically stable at +0.020 V.

Control experiments shown that no reaction occurred when H_2O_2 came in contact with the stainless-steel electrode in the absence of externally applied potential (Figure 3.24). Therefore, the passivation layer which contained Fe-oxides did not catalyze H_2O_2 activation through a heterogeneous Fenton process (i.e., reduction of ≡ Fe(III) to ≡ Fe(II) by H_2O_2 followed by reaction between ≡ Fe(II) and H_2O_2 to produce $^{\bullet}OH$).

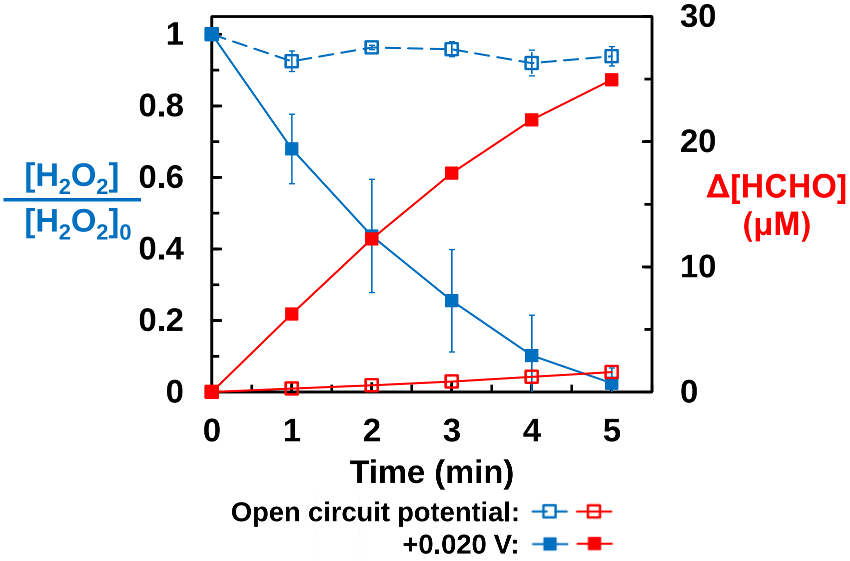

Figure 3.24 H_2O_2 decomposition and formaldehyde formation at open circuit potential and +0.020 V. Experiments conducted in buffered Na_2SO_4 electrolyte, pH = 6. $[H_2O_2]_0$ = 1.25 mg/L. Error bars represent one standard deviation.

3.3.7 Oxidation of trace organic contaminants in authentic surface water

The presence of natural organic matter and HCO_3^- poses challenges for electrochemical advanced oxidation processes because of their capacity to scavenge $^{\bullet}OH$ as well as the potential for fouling and scaling on the electrode surface (Liu et al. 2018b, Mossad and Zou 2013). Because less than 0.05% of the produced $^{\bullet}OH$ was expected to react with the TrOCs in the authentic surface water sample due to the low concentrations of contaminants (i.e., 20 μg/L), a total of 15 mg/L of H_2O_2 was added to produce sufficient $^{\bullet}OH$ (i.e., 1.25 mg/L of H_2O_2 was dosed periodically every 20 minutes throughout the treatment process).

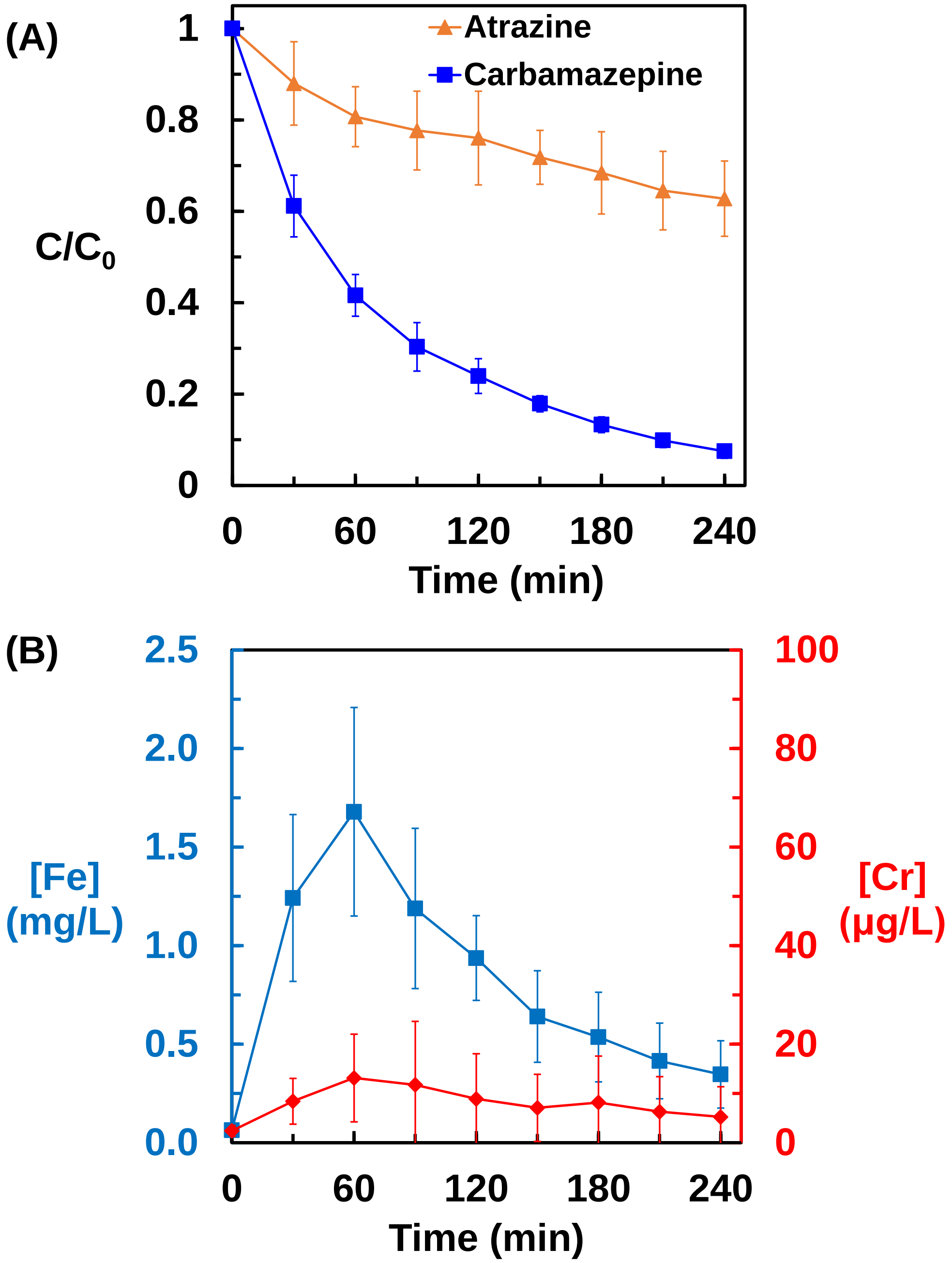

Figure 3.25 (A) concentrations of representative trace organic contaminants and (B) released Fe and Cr during the treatment of an authentic water sample. Potential = +0.020 V, 1.25 mg/L of H_2O_2 was dosed every 20 minutes. Error bars represent one standard deviation.

Over four hours of operation, more than 90% of the carbamazepine ($k_{\text{carbamazepine},\bullet\text{OH}} = 9.1 \times 10^9\ \text{M}^{-1}\ \text{s}^{-1}$) (Jasper and Sedlak 2013) and about 40% of atrazine ($k_{\text{Atrazine},\bullet\text{OH}} = 2.5 \times 10^9\ \text{M}^{-1}\ \text{s}^{-1}$) (Balci et al. 2009) were removed (Figure 3.25A). For a total dosage 15 mg/L of H_2O_2 (i.e., 0.44 mM), approximate 0.3 mM of $^\bullet$OH should have been produced on the stainless-steel electrode surface. Based on the branching ratios for carbamazepine (0.03%) and atrazine removal (0.01%), the $^\bullet$OH was expected to remove more than 90% of carbamazepine and about 30% of atrazine, which was consistent with our observations (Figure 3.25).

The maximum concentrations for Fe and Cr in the solution was observed at 60 min as 1.7 mg/L and 15 μg/L then decreased to about 0.3 mg/L and 5 μg/L at 240 min (Figure 3.25B). The decrease in Fe and Cr concentrations could have been caused by the precipitation of Fe(III)- and Cr(III)-oxide/(oxy)hydroxide at circumneutral pH conditions. The final concentration of leached Fe was near the drinking water standard and the final concentration of leached Cr in solution was below the drinking water standard (USEPA 2022a, b). Because these experiments included the one-hour pre-conditioning process, where accelerated metal leaching took place, the amounts of metals leached from a pre-conditioned electrode are expected to be below the standards when the pre-conditioned stainless-steel electrodes are used for drinking water treatment.

3.4 Environmental Implications

The low-cost stainless-steel electrode efficiently converted H_2O_2 into $^\bullet$OH at circumneutral pH conditions after an initial pre-conditioning step. The concentrations of Fe and Cr released from the surface were below primary and secondary drinking water guidelines. Despite the efficient production of $^\bullet$OH, most of the oxidant was lost to reactions on the electrode surface. Under conditions typical of drinking water (i.e., concentration of trace organic contaminant < 0.1 μM and natural organic matter < 10 mg-C/L), only about 0.03% of the $^\bullet$OH reacted with the trace organic contaminant. Due to to the dominant role of the surface as a sink for $^\bullet$OH, the presence of natural organic matter is expected to have minimal effect on the treatment performance. Under conditions of high-strength industrial wastewater, the performance of the stainless-steel surface was not expected to be affected by species that compete for $^\bullet$OH. Therefore, this system may be useful for industrial wastewater treatment.

Despite the inherent inefficiency of the stainless-steel electrode, it may still be competitive with the UV/H_2O_2 process. The equilibrium potential for oxygen evolution reaction at the counter electrode at pH 7 is +0.817 V. Therefore, under the optimal potential of +0.020 V for the stainless-steel electrode, the theoretical minimum cell voltage was around 0.8 V. Based on the electron utilization efficiency of 47% at pH 7 (Figure 3.13A), the minimum energy consumption to produce $^\bullet$OH was estimated to be 0.05 kWh/mol. For comparison, a typical low-pressure UV lamp employed for UV/H_2O_2 treatment consumes about 0.37 kWh/mol to produce photons. Considering the inefficient absorption of UV light by H_2O_2 in natural waters (i.e., more than 95% of the produced UV light is absorbed by other chromophores) (Duan and Sedlak 2021), the energy consumption for generating $^\bullet$OH by the UV/H_2O_2 process was estimated as 19 kWh/mol. Therefore, despite the loss of $^\bullet$OH on the stainless-steel surface (~90%), the energy consumption for producing $^\bullet$OH that participated in oxidation of aqueous species was estimated as 0.5 kWh/mol, which is over an order of magnitude lower than that of the UV/H_2O_2 process.

Furthermore, only about 10% of the H_2O_2 that is added to the reactor is converted to $^\bullet$OH in the UV/H_2O_2 process (Chuang et al. 2017, Zhang et al. 2019), the required

H_2O_2 dosage, as well as the energy associated with H_2O_2 production for UV/H_2O_2 process, will be about the same as a system in which $^{\bullet}OH$ is produced by electrochemical activation on stainless-steel electrodes. Therefore, the stainless-steel electrode is expected to be more energy efficient than UV/H_2O_2 process in terms of the overall energy consumption (i.e., energy for H_2O_2 production and H_2O_2 activation).

In this study, the stainless-steel electrode was operated under batch conditions. However, the porous structure and the high surface area could enhance its kinetics when used in a flow-through mode. Enhanced mass-transport of contaminants to the electrode surface could potentially lead to higher contaminant concentrations near the electrode surface, thereby reducing importance of the $^{\bullet}OH$ scavenging by the electrode surface. Additional research is needed to assess this effect of flow-through conditions as well as the long-term performance of the electrode. Research is also needed to develop reactor configurations that can operate at low ionic strength.

CHAPTER 4. Reagent-Free Electrochemical Advanced Oxidation for Distributed Water Treatment Enabled by Air-Diffusion and Stainless-Steel Electrodes

Reproduced with permission from Duan, Y., Sedlak, D. L., Reagent-Free Electrochemical Advanced Oxidation for Distributed Water Treatment Enabled by Air-Diffusion and Stainless-Steel Electrodes. In preparation.

4.1 Introduction

Growing populations, deteriorating water infrastructure, and climate change are motivating a transition from traditional centralized water supplies to a more resilient distributed approach that relies upon non-traditional water sources, including stormwater, rainwater, and groundwater from shallow aquifers as drinking water sources (Sedlak et al. 2021, Zodrow et al. 2017). New approaches for treating these water sources may be needed because they often contain trace concentration of organic contaminants that pose risks to public health (Lapworth et al. 2012, Spahr et al. 2020).

Advanced oxidation processes that convert H_2O_2 to $^{\bullet}OH$ have been used for water recycling, groundwater remediation and industrial wastewater treatment because they are capable of oxidizing most contaminants and do not produce toxic byproducts or otherwise diminish water quality (Radjenovic and Sedlak 2015, von Gunten 2018). Despite their flexibility, commercially available advanced oxidation processes are difficult to use at small-scale due to expenses associated with frequent replenishment of chemical reagents.

As an alternative to transporting chemical reagents to the end-users and storing it onsite, electrochemical H_2O_2 synthesis through oxygen reduction reactions can provide the necessary reagents for distributed treatment system (Qu and Liang 2022). Specifically, the development of air-diffusion electrodes facilitated the electrochemical synthesis process by reducing the complexity of the device and eliminating the need to bubble air or pure oxygen into the solution (Barazesh et al. 2015, Duan and Sedlak 2021). Additionally, the air-diffusion electrodes exhibit high H_2O_2 generation efficiencies by overcoming the slow mass transport of dissolved O_2 caused by its limited solubility (i.e., 8 mg/L = 0.25 mM) (Valim et al. 2013, Zhang et al. 2020b).

Electrodes have long been employed as a means of converting H_2O_2 into more reactive oxidants. Heterogeneous electro-Fenton processes are thought to oxidize trace organic contaminants (TrOCs) by converting H_2O_2 into $^{\bullet}OH$ at neutral pH conditions (Ganiyu et al. 2018). Most heterogeneous electro-Fenton processes employ a composite electrode to reduce O_2 to H_2O_2 and then convert it into $^{\bullet}OH$ by reacting with a redox active species generated on the same cathode (e.g., Fe^{II}, H*) (Ganiyu et al. 2018, Shen et al. 2020). Despite the effectiveness of these systems at the lab-scale, several drawbacks have slowed their application in distributed water treatment. Frist, because those cathodes were designed for simultaneous H_2O_2 generation and activation, they usually require complicated fabrication processes that can increase their cost (Qiu et al. 2021, Tang et al. 2020). Second, most of these systems consist of fully submerged electrodes operated in a flow-by mode (Cao et al. 2020, Liu et al. 2018a, Zhao et al. 2021), which could potentially be limited by O_2 depletion or slow mass transport of TrOC to the electrode surface. Some systems have incorporated catalysts for H_2O_2 activation onto air-diffusion electrodes (Li et al. 2022), but these electrodes could still suffer from the slow mass transport of TrOCs caused by the planar geometry of the air-diffusion electrodes. Other efforts have been made to improve the mass-transport by use of flow-through electrodes (Gao et al. 2015, Guo et al. 2021, Jiang et al. 2018a, Liu et al. 2020, Wang et al. 2020a), but these configurations often cannot generate sufficient H_2O_2 close to the catalytic site.

In addition, optimal coupling between generating H_2O_2 and activating H_2O_2 on the same electrode is often infeasible because the same potential has to be applied for electrodes responsible for both processes. The equilibrium potentials of the two reactions differ by about 500 mV (pH 7, P_{O_2} = 0.21 atm, [H_2O_2] = 1mM, and [$^\bullet$OH] = 10^{-10} M), which is a large potential difference as the H_2O_2 production rate on the air-diffusion electrode can change by a factor of 10 for only tens of mV difference in its applied potential (Lim et al. 2021, Sa et al. 2019). Furthermore, the rates of the two processes depend on the reactivity, activity and loading of the catalysts on the electrodes, which further complicates the coupling between two processes for efficient contaminants removal (Casado 2019, Wang et al. 2021, Zhang et al. 2015).

$$\mathrm{O_{2(g)}} + 2e^- + 2\mathrm{H}^+ \rightarrow \mathrm{H_2O_2} \quad E = +0.35\ \mathrm{V} \tag{4.1}$$

$$\mathrm{H_2O_2} + e^- + \mathrm{H}^+ \rightarrow {}^\bullet\mathrm{OH} + \mathrm{H_2O} \quad E = +0.80\ \mathrm{V} \tag{4.2}$$

Recently, a low-cost, commercially available material, stainless-steel scrubbing pads, has been investigated as an electrode for converting H_2O_2 to $^\bullet$OH for TrOC oxidation (Duan et al. 2022, Weng et al. 2020). Notably, the stainless-steel electrode demonstrated high yields for converting H_2O_2 into $^\bullet$OH and other species capable of transforming a recalcitrant organic compound (i.e., 1,4-dioxane) (Weng et al. 2020). The observed efficiency (i.e., ~70%) for $^\bullet$OH production was over an order of magnitude higher than that reported for heterogeneous Fenton systems (Duan et al. 2022). Although the structure of the electrode lends itself to use as a flow-through electrode, the system was only studied in a batch reactor configuration. In addition, the system was operated by externally dosing H_2O_2, which would not be suitable for distributed water treatment. Finally, the performance of the electrode was not evaluated in the presence of natural organic matter (NOM) or other solutes that could inhibit its performance, especially under low ionic strength conditions.

To better understand the potential of employing this electrode for distributed water treatment, we developed a reagent-free dual-cathode treatment process and optimized it for both the generation and activation of H_2O_2. Briefly, O_2 from air was electrochemically reduced to form H_2O_2 on an air-diffusion electrode, followed by conversion of the H_2O_2 to $^\bullet$OH on another flow-through stainless-steel electrode. The oxidation of low concentrations of two TrOCs that are relatively stable (i.e., carbamazepine and atrazine) in the dual-cathode treatment process was optimized under various applied potentials and flow conditions. The performance of the treatment system was assessed in electrolyte amended with various $^\bullet$OH scavengers and in an authentic surface water sample. The energy consumption of the dual-cathode treatment system was compared with other technologies that have been developed for removal of TrOCs in distributed systems.

4.2 Materials and Methods

4.2.1 Materials

All experiments were performed at room temperature (23 ± 2 °C) with chemicals of reagent grade or higher (Sigma-Aldrich, St. Louis, MO, and Fisher Scientific, Pittsburgh, PA). Ultrapure water from a Milli-Q system (R > 18 MΩ) was used for all experiments. H_2O_2 (30% v/v) was standardized by the $KMnO_4$ assay (Gill and Zheng 2020) and checked monthly using a Shimadzu UV-2600 UV-vis spectrophotometer at 254 nm (ε_{254nm} = 18.6 M^{-1} cm^{-1}; Morgan et al. 1988).

4.2.2 *Electrolysis*

Electrolysis experiments were conducted with a potentiostat (Gamry Instruments Inc., Warminster, PA). An Ag/AgCl electrode (3M NaCl, BASi, West Lafayette, IN) was used as the reference electrode and all potentials are reported versus a standard hydrogen electrode (SHE).

The air-diffusion electrode (4 cm × 4 cm) was fabricated by brush coating carbon black catalyst (Cabot Black Pearls 2000, Cabot, Boston, MA) onto a modified carbon fiber paper (AvCarb P75T, Fuel Cell Store, College Station, TX) with a conductive, hydrophobic support layer as previously described (Barazesh et al. 2015). A platinized titanium (Pt/Ti) electrode (dimensions: 5.1 × 7.6 cm; TWL, United States) was used as the counter electrode for the air-diffusion electrode. Two reactor cell configurations were used to investigate the performance of the air-diffusion electrode (Figure 4.1): an undivided cell ($V_{effective}$ = 60 mL) and a divided cell ($V_{effective,cathode}$ = 20 mL, $V_{effective,anode}$ = 30 mL). The inter-electrode distance for both cell configurations was around 2 cm. For the divided cell configuration, a cation exchange membrane (Ultrex CMI-7000, Membranes International Inc., Ringwood, NJ) was used to separate the cathode and anode chambers.

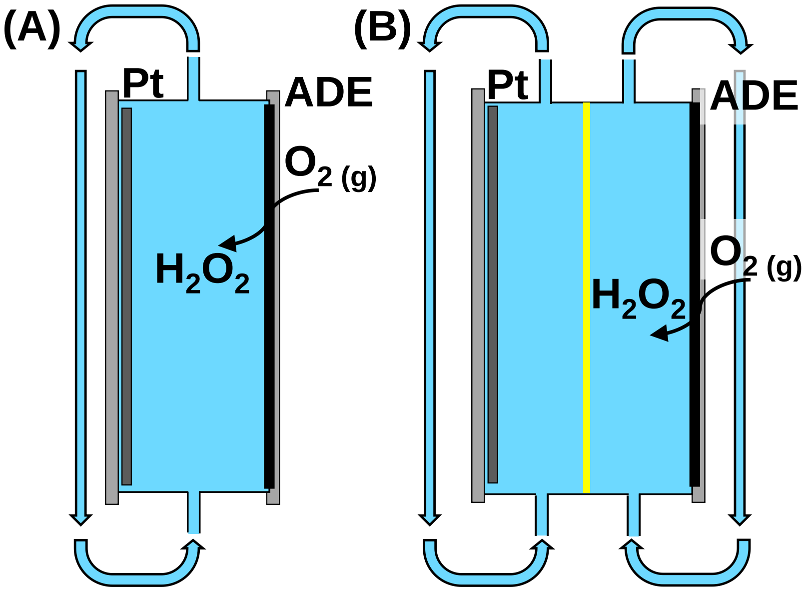

Figure 4.1 Electrochemical cell configurations for H_2O_2 generation: (A) undivided cell configuration, (B) divided cell configuration. ADE represents air-diffusion electrode.

A 20 g Scotch-Brite stainless-steel scrubber working electrode (catalogue number 214C, 3 M Company, St. Paul, MN, USA; 80 cm^2/g specific surface area) was rinsed thoroughly with ultrapure water and compressed into a flow-through reactor (Schedule 40

PVC, inner diameter = 3.5 cm, $V_{\text{effective}}$ = 80 mL, Figure 4.2). A platinum mesh counter electrode was placed about 2 mm above the stainless-steel electrode.

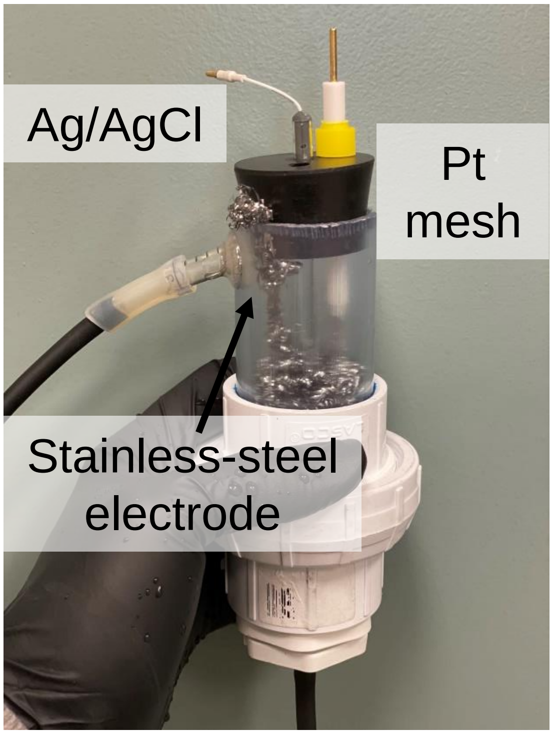

Figure 4.2 Photo of the stainless-steel electrode reactor.

The dual-cathode treatment system (Figure 4.7) was evaluated by recirculating a 200 mL of test solution between the two reactors equipped with two solution reservoirs. A peristaltic pump (Cole-Parmer, Chicago, IL) coupled with Norprene Tygon A-60-G tubing (Masterflex, Vernon Hills, IL) was used to circulate solution through the system. The treated water was first passed through the semi-divided air-diffusion electrode reactor for H_2O_2 generation followed by passing through the stainless-steel electrode.

4.2.3 Trace organic contaminants removal pathways

To deconvolute the importance of $^{\bullet}OH$ produced by the dual-cathode treatment process from transformation mechanisms, the oxidation of TrOCs was also studied in the air-diffusion electrode reactor (current = 16 mA). A 200 mL of TrOC-containing electrolyte ($[Na_2SO_4]$ = 250 mM, [TrOCs] = 20 μg/L, [PIPES] = 1 mM, pH 7) was recirculated within the reactor at a flow rate of 70 mL/min to ensure the same electrode to volume ratio and mass transport of TrOC as that of the dual-cathode treatment process. The contribution of the $^{\bullet}OH$ to the transformation of TrOC were calculated by subtracting the transformation rates obtained in separated reactors (k_{ADE} for the air-diffusion electrode reactor and k_{SSE} for the stainless-steel electrode reactor) from that of the dual-cathode system ($k_{\text{ADE+SSE}}$), eq 4.3:

$$k_{\bullet OH} = k_{ADE+SSE} - k_{ADE} - k_{SSE} \tag{4.3}$$

To provide further insights on the fate of TrOCs in the air-diffusion electrode reactor, the cathodic chamber and anodic chamber were investigated separately in a divided cell configuration. Each chamber was fed with 200 mL of TrOC-containing phosphate buffer ([TrOCs] = 20 µg/L, $[PO_4^{3-}]$ = 200 mM, pH 7). The 200 mM phosphate buffer successfully buffered the solution pH, with pH values changing by less than 0.15 pH unit over four hours of electrolysis.

The transformation pathway of the TrOCs in the two chambers of the divided air-diffusion electrode reactor was further broken down into radical reactions and direct electron transfer. Allyl alcohol has been used as a scavenger for both surface and bulk radicals in anodic processes because of its high reactivity with oxidants and its ability to interact with positively charged anode surfaces (Barazesh et al. 2016, Celdrán and González-Velasco 1981, Pastor et al. 1993a). However, allyl alcohol only selectively interacts with some cathodes, such as Pt and Pd cathodes (Arévalo et al. 2001, Pastor et al. 1991, Pastor et al. 1993b, Shukun et al. 2001, Willner et al. 1991) (e.g., it only forms a relatively weak and reversible interaction with Au cathode) (Pastor et al. 1993a). Given that no previous study had investigated the interaction between allyl alcohol and carbonaceous cathodes, it was hypothesized that both surface and aqueous radicals generated by the air-diffusion electrode would be scavenged by allyl alcohol, and that the contaminant transformation observed in its presence should be ascribed exclusively to direct electron transfer. Although this hypothesis may lead to an overestimation of direct electron transfer on the air-diffusion electrode, the ability of allyl alcohol to inhibit most of the contaminant transformation reactions suggested that direct electron transfer was of minor importance in this system.

4.2.4 Analytical methods

Samples for H_2O_2 measurement were removed from the influent and the effluent of the stainless-steel electrode. H_2O_2 was measured by a modified titanium(IV) sulfate method (Eisenberg 1943) or a modified version of the peroxidase catalyzed N,N-diethyl-p-phenylenediamine (DPD) oxidation method (Bader et al. 1988).

Samples for other analytes were removed from the effluent of the stainless-steel electrode. Samples for TrOC analysis were quenched with methanol (final concentration = 10% v/v) and analyzed in multiple reaction monitoring (MRM) mode with an Agilent 1260 series HPLC system coupled to a 6460 triple quadrupole tandem mass spectrometer (HPLC-MS/MS) as described previously (Barazesh et al. 2015).

Samples containing $^\bullet OH$ scavengers (i.e., 2-propanol and benzoic acid) and their associated $^\bullet OH$ oxidation products (i.e., para-hydroxybenzoic acid, acetone, and a unidentified acetone transformation product) were spiked with 1,10-phenanthroline (final concentration = 1 mM) to quench reactions of H_2O_2 and Fe(II) leached from the stainless-steel electrode (Duesterberg et al. 2005). The concentrations of $^\bullet OH$ scavengers and oxidation products were analyzed on an Agilent 1260 Infinity high-performance liquid chromatography (HPLC) equipped with diode array detector (Section A.3.1 of the Appendix).

Aliquots for total metals analysis were acidified immediately after sampling and quantified on an Agilent 7700 Series Inductively Coupled Plasma-Mass Spectrometer

(ICP-MS). Samples for TOC analysis were quenched by sodium thiosulfate (final concentration = 100 mM) and analyzed using a Shimadzu TOC-V analyzer.

4.3 Results and Discussion

4.3.1 Air-diffusion electrode for H_2O_2 production

Despite the fact that the air-diffusion electrode used in this study has been adapted for a point-of-use UV/H_2O_2 system and a distributed stormwater treatment system (Barazesh et al. 2015, Duan and Sedlak 2021), previous investigations focused mainly on the engineering aspect of the operation (e.g., effects of applied current density and charge dosage, maximum H_2O_2 concentration that can be generated, and optimization for energy consumption) without elucidation of the onset overpotential and current-potential relationship especially at low overpotentials. The onset overpotential is one of the most important parameters that indicates the catalytic activity of catalysts and is directly related to the voltage efficiency of the electrolysis. The current-potential relationship is important to optimization of H_2O_2 production rates to match the rate of H_2O_2 activation. Because the rate for H_2O_2 production can vary by a factor of 10 for every <100 mV change in the applied potential (Lim et al. 2021, Sa et al. 2019), efficient matching between H_2O_2 production and H_2O_2 activation could be challenging.

The onset overpotential and current-potential relationship for H_2O_2 production were evaluated in a 250 mM Na_2SO_4 electrolyte buffered with 50 mM of phosphate buffer at pH 7 using the divided cell configuration. Because H_2O_2 generation by the air-diffusion electrode is independent of the solution composition (i.e., salts and NOM) (Barazesh et al. 2015, Duan and Sedlak 2021), the observed results should represent the performance that will be encountered in drinking water treatment. A significant current response was observed for the air-diffusion electrode (i.e., > 5 mA/cm^2) whereas the carbon fiber paper produced no observable current over the whole range of potentials tested in this study. The Tafel slope under the tested potential range was 88 mV/decade (Figure 4.3), meaning that the current for oxygen reduction would increase by a factor of 10 for every 88 mV decrease in the applied potential. The onset overpotential for oxygen reduction was measured using the average current density observed during chronoamperometry experiments at each specific potential to minimize capacitive current interference (Figure 4.4A inset) (Kim et al. 2018). The low onset overpotentials (i.e., 30 mV under neutral pH conditions was comparable to the performance of state-of-the-art H_2O_2 electrochemical generation catalysts, which typically exhibit onset overpotential ranging from 10 to 150 mV (Bormann et al. 2019, Kim et al. 2018, Liang et al. 2021, Sheng et al. 2019). Because the carbon black catalyst is inexpensive ($1-2/kg) compared to prices for the raw materials of some state-of-art catalysts (e.g., NiS_2 and CoS_2 can cost more than $200/kg) and requires no further preparation or modification, it is a promising means of generating H_2O_2 in distributed treatment systems.

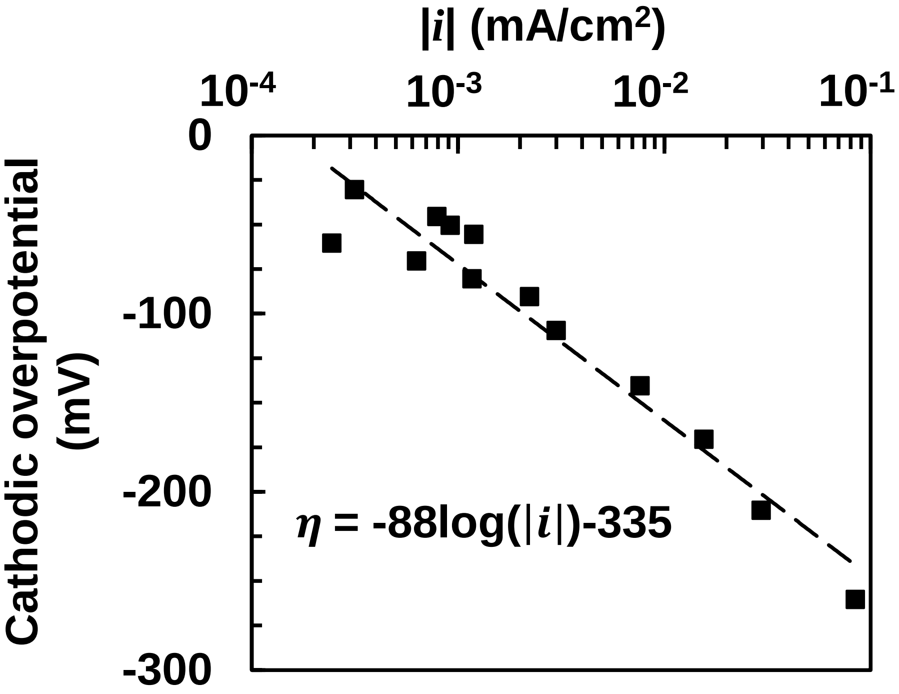

Figure 4.3 Tafel plot of the relationship between current density (i) and overpotential for O_2 reduction for the formation of H_2O_2.

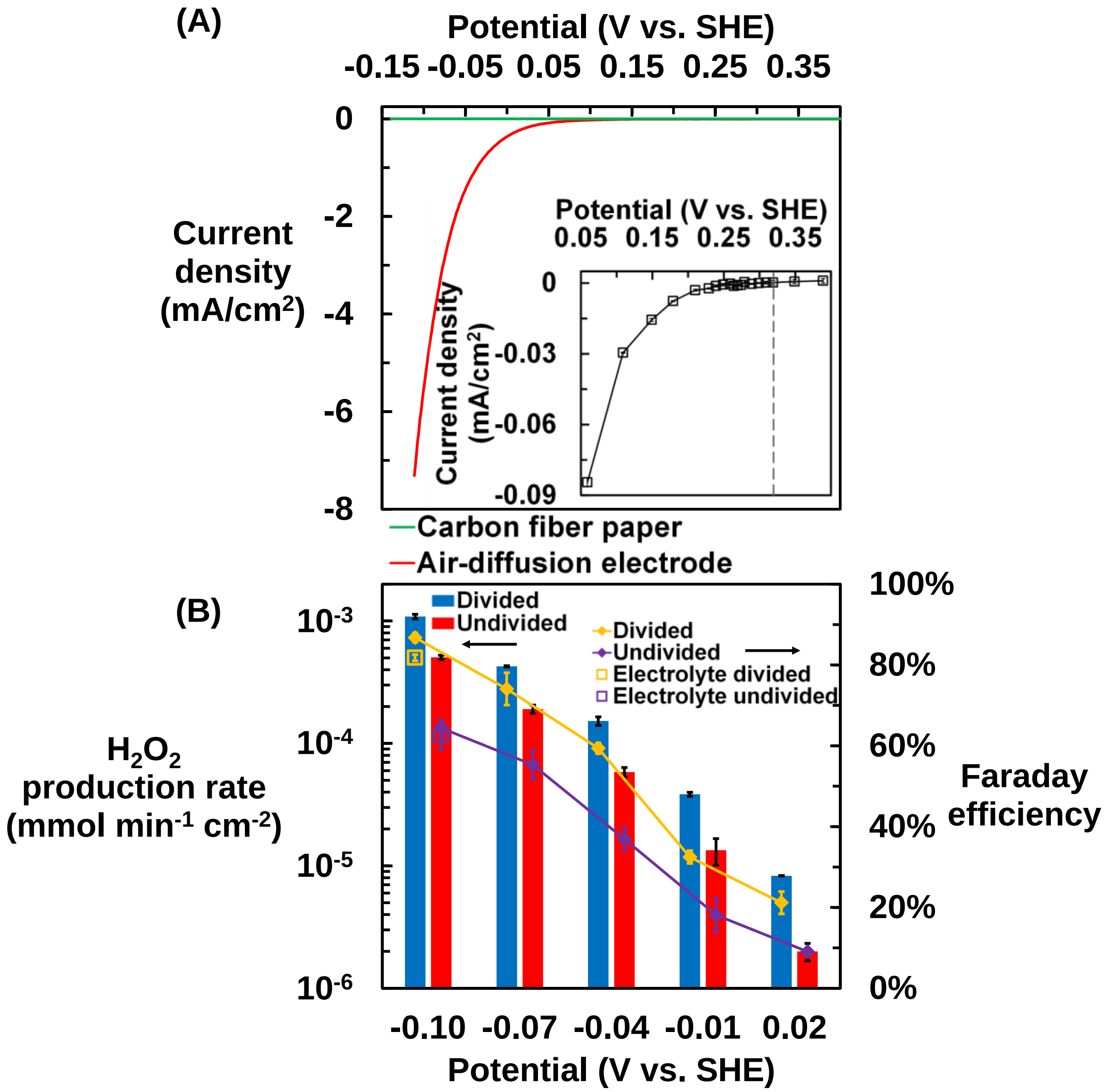

Figure 4.4 (A) Linear sweep voltammetry curves of the air-diffusion electrode and P75T carbon fiber paper substrate in 250 mM Na_2SO_4 (pH buffered at 7.0 by 50 mM phosphate buffer), potential scan rate: 2 mV s^{-1}. The inset shows the average current density observed through multiple trials using a 5 min chronoamperometry at the specified potentials in the presence of 10 mM H_2O_2. The dashed line indicates the equilibrium potential for the H_2O_2 generation reaction in the presence of 10 mM H_2O_2 at pH 7 (E = +0.32 V). (B) H_2O_2 production rate and Faraday efficiency obtained at the specified potentials with different cell configurations. Experiments conducted in real surface water amended with 250 mM of Na_2SO_4 or in 250 mM of Na_2SO_4 electrolyte.

H_2O_2 generation was assessed in two different cell configurations with applied potentials ranged from -0.10 to +0.02 V (Figure 4.4B). As the applied potential decreased from +0.02 V to -0.10 V, the H_2O_2 production rate increased by a factor of 130 and 250 for the divided cell configuration and the undivided cell configuration, respectively. The Faraday efficiency also increased from 21% to 87% for the divided configuration and from 9% to 64% for the undivided configuration. The increase in the Faraday efficiency could have been caused by the increase in the current response for the 2-electron reduction of O_2 (i.e., O_2 reduction to H_2O_2), which outcompeted other side reactions (e.g., 4-electron reduction of O_2 to H_2O, E = +0.81 V, pH = 7 and P_{O_2}= 0.21 atm). Because the air-diffusion electrode performed better in terms of H_2O_2 production rate and Faraday efficiency under a large applied overpotential, H_2O_2 generation might have benefited from applying a high current density to a small air-diffusion electrode.

Given that the self-decomposition of H_2O_2 was insignificant over the time scale of the study (Duan and Sedlak 2021), the generated H_2O_2 most likely decomposed through two anodic pathways: (i) direct anodic oxidation (eq 4.4), and (ii) reaction with HOCl produced by anodic oxidation of Cl^- (eq 4.5 and 4.6).

$$\mathrm{H_2O_2} \rightarrow \mathrm{2H^+} + \mathrm{O_2} + 2e^- \tag{4.4}$$

$$\mathrm{Cl^-} + \mathrm{H_2O} \rightarrow \mathrm{H^+} + \mathrm{HOCl} + 2e^- \tag{4.5}$$

$$\mathrm{H_2O_2} + \mathrm{HOCl} \rightarrow \mathrm{H^+} + \mathrm{Cl^-} + \mathrm{O_2} + \mathrm{H_2O} \tag{4.6}$$

Separating the cathodic chamber from the anodic chamber prevented both anodic decomposition pathways of H_2O_2 and increased the H_2O_2 production rate and Faraday efficiency by a factor of 2.8 and 1.7, respectively.

To further distinguish the effect of direct anodic oxidation from indirect anodic processes, experiments were also conducted in 250 mM of Na_2SO_4 electrolyte (Figure 4.4B, hollow square symbol). The Faraday efficiency observed in the Na_2SO_4 electrolyte was similar to that observed in the real surface water for both cell configurations, indicating the presence of drinking water-relevant level of Cl^- (e.g., 10 mg/L = 0.28 mM) resulted in minimal loss of H_2O_2.

H_2O_2 loss through the direct anodic oxidation was also assessed by its decomposition kinetics. The anodic decomposition of H_2O_2 followed first-order kinetics with a rate constant $k_{\mathrm{decomp.}}$ of 4.0×10^{-2} min^{-1} (Figure 4.5A). The Faraday efficiency loss due to the direct anodic decomposition of H_2O_2 was estimated based on the average H_2O_2 concentration over the electrolysis process (0.57 mM), Faraday constant (F, 96485 C/mol) and current (I, A):

$$Faraday\ efficiency\ loss_{\ Direct\ anodic\ oxidation} = \frac{2k_{decomp.}[\mathrm{H_2O_2}]VF}{I} \tag{4.7}$$

The anodic oxidation of H_2O_2 was estimated to cause a 20% decrease in Faraday efficiency, which further confirmed that the H_2O_2 loss was dominated by the direct oxidation pathway (Figure 4.5B).

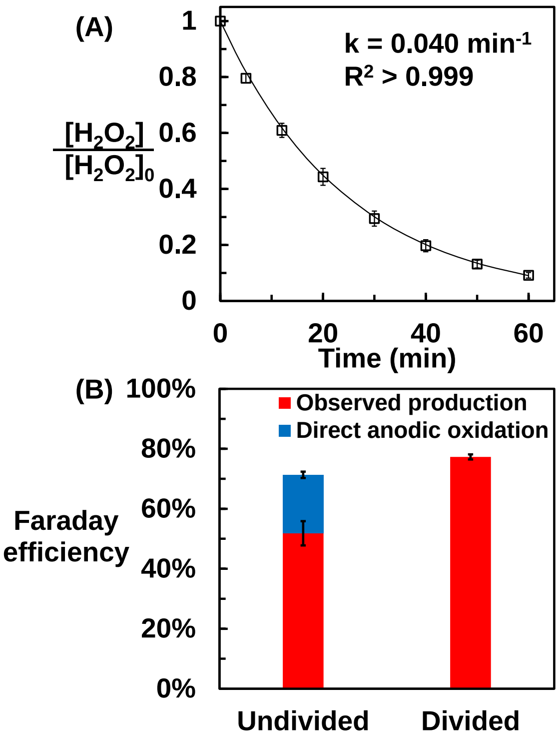

Figure 4.5 (A) Anodic decomposition of H_2O_2. Experiment was conducted in 250 mM of Na_2SO_4 electrolyte using a divided cell configuration. $[H_2O_2]_0$ = 5 mM, applied current = 20 mA. (B) Observed Faraday efficiency in Na_2SO_4-amended surface water and predicted Faraday efficiency loss due to direct anodic oxidation of H_2O_2. Applied potential = -0.07 V, average observed current = 19 ± 1 mA for the undivided cell configuration.

Although the divided cell configuration can slow H_2O_2 loss from both direct and indirect anodic processes, the divided cell causes an increase in pH of the H_2O_2-contaning catholyte (Figure 4.6).

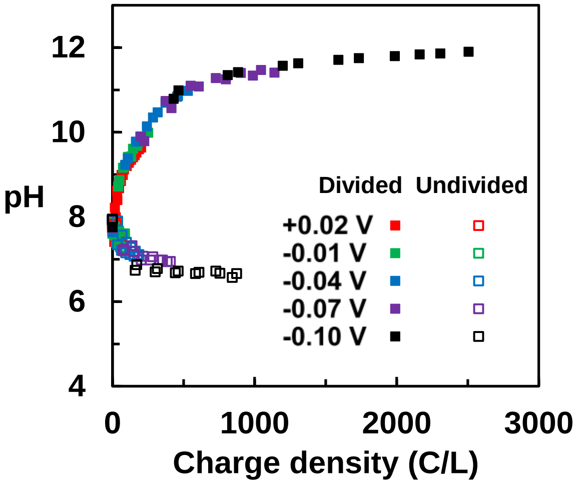

Figure 4.6 pH values observed under various applied potentials on the air-diffusion electrode with different electrochemical cell configurations. Experiment was conducted in Na_2SO_4-amended surface water.

Therefore, passing the water only through the cathode chamber in the divided cell was not suitable for generating H_2O_2 because the maximum yield for converting H_2O_2 to $^{\bullet}OH$ occurred under circumneutral pH conditions (Duan et al. 2022). Given the fact that anodically formed HOCl only played a minor role in H_2O_2 loss under drinking water condition, a semi-divided configuration was employed to minimize direct anodic oxidation of H_2O_2 and maintain a relatively constant pH by passing the water through the anode chamber prior to sending it into the cathode chamber.

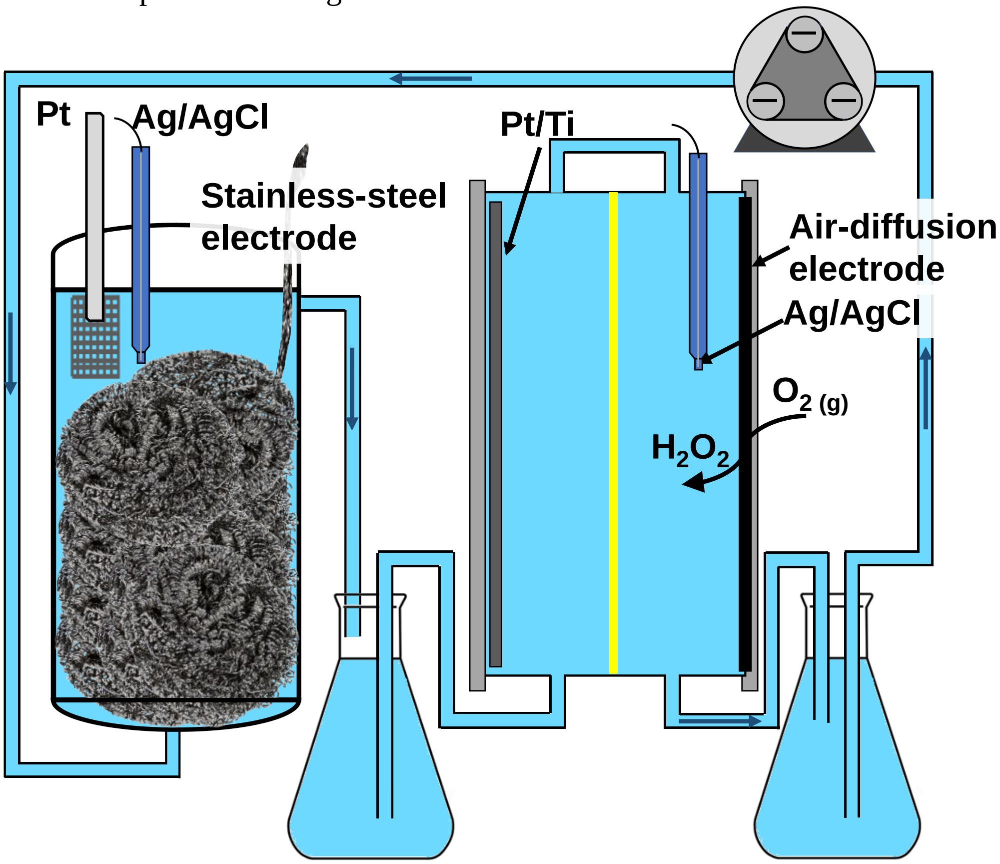

Figure 4.7 Schematic illustration of the dual-cathode treatment process. The air-diffusion electrode was separated from the Pt/Ti counter electrode by a cation exchange membrane. The stainless-steel electrode was coupled with a Pt electrode as the counter electrode in the flow-through reactor.

4.3.2 Trace organic contaminant removal by the dual-cathode treatment process

After determining the behavior of the air-diffusion electrode, we analyzed the effect of potential of the air-diffusion electrode on the rate of contaminant removal. Control experiments conducted by recirculating the electrolytes in the dual-cathode treatment system without any electric connections indicated that sorption accounted for less than 20% of the observed TrOCs loss over the four-hour experiment period (Figure 4.8). The stainless-steel electrode was operated at +0.02 V, which was the value that had identified as the optimal potential for converting H_2O_2 to $^{\bullet}OH$ (Duan et al. 2022, Weng et al. 2020). Decreasing the applied potential from +0.02 V to -0.04 V enhanced the removal of carbamazepine and atrazine by a factor of 2.7 and 1.5, respectively. Further lowering the applied potential (i.e., from -0.04 V to -0.10 V) increased the removal of the two compounds by another factor of 1.2 and 2.0, respectively (Figure 4.9A).

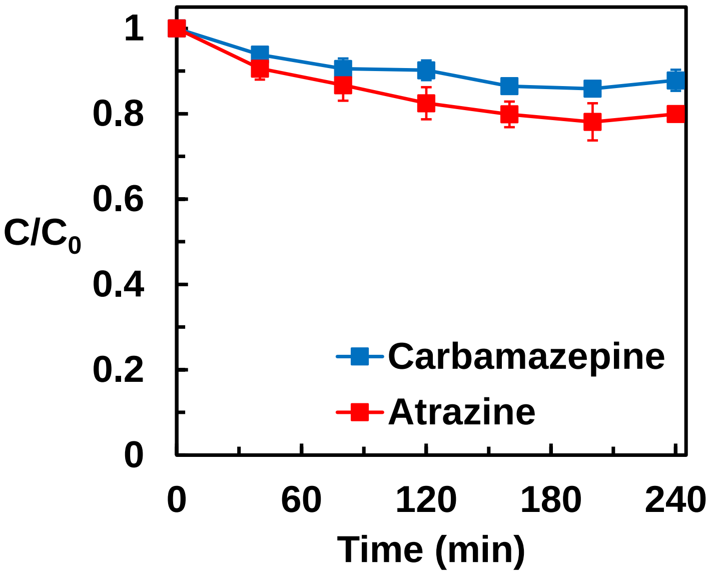

Figure 4.8 Control for TrOC sorption by the dual-cathode treatment system without any applied potential. Experimental conditions: 250 mM Na_2SO_4 buffered with 1 mM of PIPES buffer (pH 7), $[TrOCs]_0$ = 20 µg/L, recirculation rate = 70 mL/min.

A decrease in the applied potential increased the rate of production of H_2O_2. The current measured on the air-diffusion electrode increased by a factor of 6.7 for every 60 mV of potential decrease (Figure 4.9B). However, the current response on the stainless-steel electrode only increased by a factor of about 3 for every 60 mV decrease in the applied potential on the air-diffusion electrode. Based on the measured Faraday efficiency for H_2O_2 generation on the air-diffusion electrode (Figure 4.4B) and the efficiency of H_2O_2 transformation on the stainless-steel electrode, defined as the amount of H_2O_2 transformed per mole of electron consumed (62% at pH 7) (Duan et al. 2022), we determined that the optimal current ratio between the air-diffusion electrode to stainless-steel electrode to ensure complete activation of the generated H_2O_2 was 1.4, 2.1, and 5.9 for air-diffusion electrode potentials of -0.10 V, -0.04 V, and +0.02 V, respectively, whereas the observed current ratio was measured as 4.1, 1.6, and 0.9 for those potentials. As a result, the produced H_2O_2 was not all activated by the stainless-steel electrode when a large overpotential was applied (i.e., $[H_2O_2]$ = 13 mM in the effluent of stainless-steel electrode) or it was all used up when the same potential (i.e., +0.02 V) was applied on both electrodes. In other words, when +0.02 V was applied on both electrodes, poor TrOC removal was observed because H_2O_2 was depleted quickly on the stainless-steel electrode. Likewise, when too high of an overpotential was applied on the air-diffusion electrode (i.e., -0.10 V), H_2O_2 accumulated in the system. By setting the potential on the two electrodes (i.e., applying -0.04 V on the air-diffusion electrode and +0.02 V on the stainless-steel electrode) the production of H_2O_2 and its activation could be optimized.

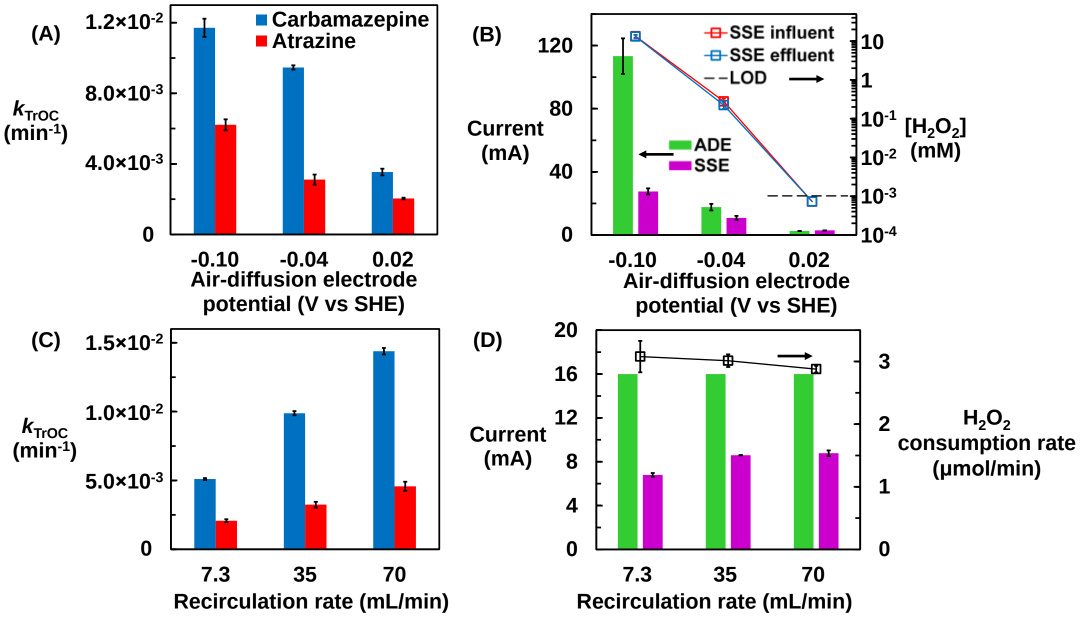

Figure 4.9 Effect of applied potential on the air-diffusion electrode on (A) rate of removal of TrOCs and (B) observed current and steady-state H_2O_2 concentration in 250 mM Na_2SO_4 buffered with 5 mM of PIPES buffer (pH 7), recirculation rate = 35 mL/min. Effect of recirculation rate on (C) rate of removal of TrOCs and (D) observed current and H_2O_2 consumption rate in 250 mM Na_2SO_4 buffered with 1 mM of PIPES buffer (pH 7), applied current on air-diffusion electrode = 16 mA, applied potential on stainless-steel electrode (SSE) = +0.02 V. $[TrOCs]_0$ = 20 μg/L for all experiments.

Additional experiments were conducted with a constant current (i.e., 16 mA) on the air-diffusion electrode (current density = 1 mA/cm^2, applied potential around -0.04 V). The system was tested at different recirculation rates to evaluate the effect of mass transfer. Increasing the recirculation rate enhanced the observed rate of TrOC removal (Figure 4.9C). However, increasing the recirculation rate, despite lowered the H_2O_2 concentration entering the stainless-steel electrode, had little effect on the current response on the stainless-steel electrode or the H_2O_2 consumption rate (Figure 4.9D). The H_2O_2 consumption rate was calculated based on the recirculation rate (Q) and reaction time (*T*):

$$H_2O_2 \text{ consumption rate} = \frac{Q}{T}\int_0^T \left([\mathrm{H_2O_2}]_{Inf} - [\mathrm{H_2O_2}]_{eff}\right)dt \qquad (4.8)$$

From these results we conclude that the enhancement in TrOC removal was caused by the enhanced mass transport of TrOCs to the electrode surface instead of enhancement of H_2O_2 activation. This implied that the active sites on the stainless-steel electrode were likely fully occupied by H_2O_2 and that H_2O_2 activation on the electrode was likely the rate-limiting step rather than mass transport of H_2O_2.

When -0.10 V was applied on the air-diffusion electrode (Figure 4.9B), the current measured on the stainless-steel electrode and the H_2O_2 consumption rate (13 ± 2 μmol/min) were both higher than expected assuming the H_2O_2 activation as the rate-limiting step. This observation suggested a switch in H_2O_2 decomposition mechanisms when a high concentration of H_2O_2 (13 mM) entered the stainless-steel electrode. The exact mechanism of H_2O_2 decomposition in the presence of high concentrations of H_2O_2 is unclear. It was not evaluated because the production of excess H_2O_2 would be disadvantageous in distributed treatment system. The ineffective use of H_2O_2 by activation in the presence of high concentrations of H_2O_2 and the slow contaminant removal observed at low flow rates indicated that the system could not be effectively scaled up as a single pass reactor that operated at a low flow rate.

Under the conditions used in the experiment depicted in Figure 4.9, approximately 0.72 mmol of H_2O_2 was transformed on the stainless-steel electrode during the four-hour experiment. At an applied current of 16 mA on the air-diffusion electrode and an assumed Faraday efficiency around 60% (Figure 4.4B at -0.04 V), the total amount of H_2O_2 generated by the air-diffusion electrode was estimated to be 0.71 mmol. At a recirculation rate of 70 mL/min, the residual H_2O_2 was approximate 0.04 mmol. These conditions suggested minimal residual H_2O_2 leaving the system and efficient activation of the stainless-steel electrodes.

4.3.3 Trace organic contaminants removal pathways

In addition to reaction with the $^\bullet OH$ generated from the H_2O_2 activation on the stainless-steel electrode, TrOCs could also be degraded by direct electron transfer and reactions with other radicals produced on the electrode surfaces (Mousset and Doudrick 2020, Qin et al. 2021, Weng et al. 2020, Xie et al. 2021, Yang et al. 2018). Due to the non-selective nature of $^\bullet OH$, distinguishing the reactions with $^\bullet OH$ from other removal pathways is essential to predicting the performance of the treatment process for removal of other TrOCs.

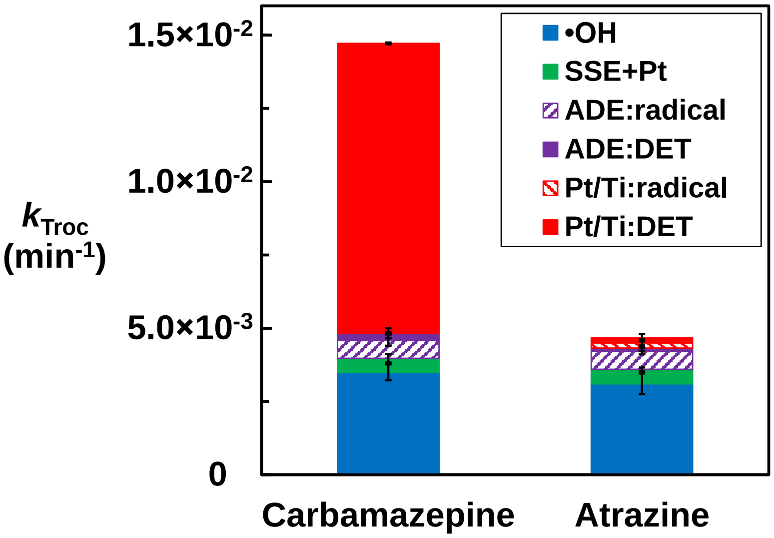

Figure 4.10 Removal pathways of carbamazepine and atrazine in the dual-cathode treatment process. Conditions: $[TrOCs]_0$ = 20 μg/L, applied current on air-diffusion electrode = 16 mA, applied potential on stainless-steel electrode = +0.02 V, recirculation rate = 70 mL/min. SSE represents stainless-steel electrode; ADE represents air-diffusion electrode; DET represents direct electron transfer.

The contributions from each removal pathway provided insight into the variations in removal rates expected for different compounds (Figure 4.10). The sum of the rate constants for each removal pathway measured separately was within 5% of that observed rate measured in the dual-cathode treatment process for both carbamazepine and atrazine. The importance of ${}^{\bullet}$OH to the removal of TrOC was assessed by subtracting the observed removal rates in individual reactor from the observed rate in the dual-cathode treatment system. The ${}^{\bullet}$OH pathway contributed to about 30% of the carbamazepine removal and 70% of atrazine removal. The contribution of ${}^{\bullet}$OH to the removal of TrOC was confirmed by quenching experiments. The inhibited TrOC removal rate upon addition of 200 mM of 2-propanol or allyl alcohol was nearly identical to the TrOC removal rate calculated based on the above-mentioned subtraction method (Figure 4.11).

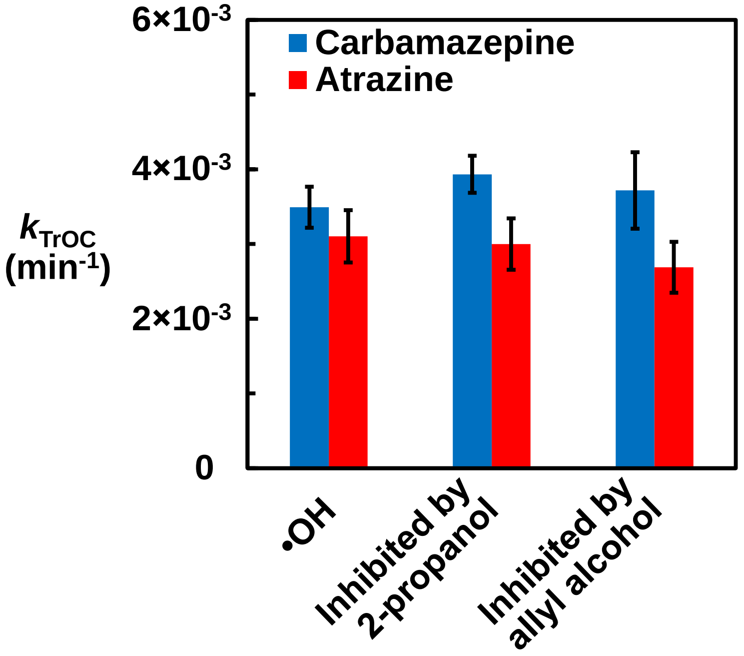

Figure 4.11 Comparison of the rate of TrOC oxidation by ${}^{\bullet}$OH calculated based on the subtraction method versus inhibited TrOC removal rate upon addition of 200 mM of 2-propanol and allyl alcohol.

In addition to the reactions with ${}^{\bullet}$OH, TrOC removal was also observed when the two reactors were operated separately (i.e., under conditions in which ${}^{\bullet}$OH formation from H_2O_2 activation did not take place). Operating the stainless-steel electrode reactor at +0.020 V resulted in removal rates that were less than 10% of those observed in the combined system, whereas operating the air-diffusion electrode reactor resulted in relatively fast removal of carbamazepine (i.e., removal rates were about 70% of the values observed in the dual-cathode treatment system) but only modest rates of removal of atrazine (i.e., removal rates for atrazine were about 20% of the rates observed in the dual-cathode treatment system). The relatively fast removal of carbamazepine was attributed to direct electron transfer by the Pt/Ti anode. The addition of 200 mM of allyl alcohol also quenched the removal of both TrOCs by the air-diffusion electrode, indicating that the air-diffusion electrode may also produces some radicals in the presence of H_2O_2 (Qin et al. 2021, Weng et al. 2020, Yang et al. 2018).

4.3.4 Performance in the presence of •OH scavengers

To gain insight into the performance of the dual-cathode treatment in natural waters, other •OH scavengers were added to the electrolyte. Benzoic acid ($pK_a = 4.20$) and 2-propanol were used to simulate the effect of a negatively charged and a neutral small molecule capable of reacting with •OH. These two •OH scavengers were chosen because their main oxidation products (i.e., para-hydroxybenzoic acid and acetone) are easily quantified.

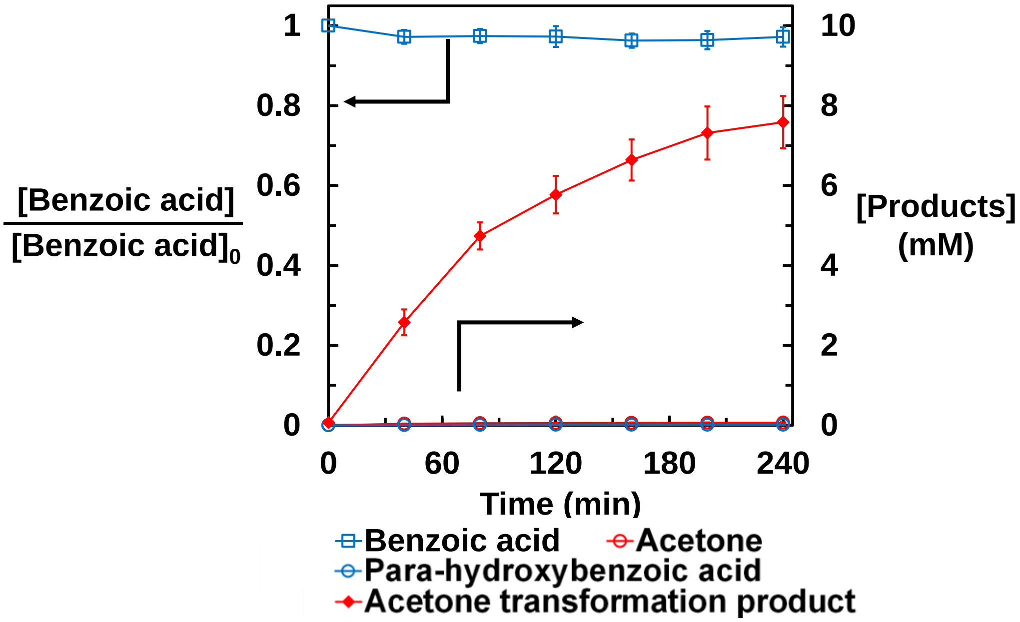

Figure 4.12 Removal of benzoic acid and production of oxidation products of 2-propanol or benzoic acid. Conditions: $[TrOC]_0$ = 20 µg/L in 250 mM Na_2SO_4 buffered with 1 mM of PIPES buffer (pH 7), $[^\bullet OH\ scavenger]_0$ = 10 mM, applied current on air-diffusion electrode = 16 mA, applied potential on stainless-steel electrode = +0.02 V, recirculation rate = 70 mL/min.

The rate of benzoic acid oxidation by •OH and the quenching effect of 2-propanol on the removal of TrOC were predicted based on steady-state concentrations of •OH ($[^\bullet OH]_{ss}$) expected under each condition (eq 4.9, *i* represents each species that reacts with •OH). The rate of •OH production was calculated based on the rate of atrazine oxidation by •OH obtained in Section 4.3.3.

$$[^\bullet \mathrm{OH}]_{SS} = \frac{Rate\ of\ \bullet OH\ production}{\sum k_{\bullet OH,i}[i]} \tag{4.9}$$

Approximately 20% of the benzoic acid was expected to be removed by •OH produced on the stainless-steel electrode over four hours of reaction. However, the benzoic acid concentration remained almost constant and only around 10 μM of para-hydroxybenzoic acid (around 0.1% of [benzoic acid]$_0$) was detected (Figure 4.12), indicating that benzoic acid oxidation was much slower than expected.

In contrast, a total of approximately 8 mM of 2-propanol was transformed based on detection of its oxidation product (i.e., acetone and an acetone transformation product, Section A.3.1 of the Appendix). The $^{\bullet}$OH generated by the dual-cathode treatment system was expected to oxidize about 2 mM of 2-propanol. The higher-than-expected transformation of 2-propanol was consistent with the anodic oxidation of 2-propanol on the Pt and Pt/Ti anode (Okanishi et al. 2016). Despite some 2-propanol was transformed by anodic oxidation, the oxidation of 2-propanol by the $^{\bullet}$OH generated from H_2O_2 activation on the stainless-steel electrode had been confirmed in a system using a divided H-type reactor that prevented the anodic oxidation (Duan et al. 2022). Therefore, the generated $^{\bullet}$OH from H_2O_2 activation on the stainless-steel could be scavenged by neutral $^{\bullet}$OH scavengers (i.e., 2-propanol).

The addition of 10 mM and 200 mM of 2-propanol should have quenched 55% and 96% of the produced $^{\bullet}$OH. The predicted quenching effect of 2-propanol on the oxidation of TrOCs was consistent with the experimental observations (Figure 4.13), further supporting the idea that $^{\bullet}$OH was scavenged by 2-propanol.

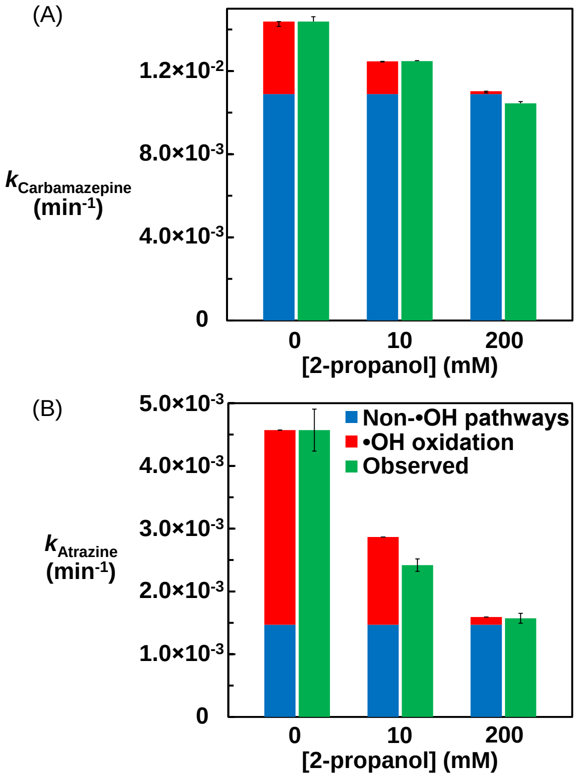

Figure 4.13 Comparison of observed versus predicted scavenging effect of 2-propanol on TrOC removal.

The difference between the transformation of 2-propanol and benzoic acid was likely caused by electrostatic repulsion between the negatively charged cathode surface and the negatively charged benzoate, which prevented the oxidation of benzoate from coming into contact with the $^{\bullet}OH$ that was produced at the electrode surface. The diffusion distance of $^{\bullet}OH$ in the aqueous phase was estimated from the Einstein-Smoluchowski equation to be around 8 nm (Section A.3.2 of the Appendix) (Schwarzenbach et al. 2016), which was about three orders of magnitude smaller than the local concentration gradients of charged species (e.g., negatively charged species like benzoate could be repelled for tens of μm from the electrode surface) (Auinger et al. 2011, Cannan et al. 2002, Lu et al. 2020, Rudd et al. 2005). Therefore, the dual-cathode treatment system may benefit from electrostatic repulsion of negatively charged $^{\bullet}OH$ scavengers such as NOM, which is the most common $^{\bullet}OH$ scavenger in drinking water treatment applications. Although the electrostatic repulsion had been applied in the field of electrified membrane to mitigate membrane fouling (Akamatsu et al. 2010, Huang et al. 2015, Zhu and Jassby 2019), it has not been reported previously in electrochemical advanced oxidation process, likely because most of those treatments focused on anodic processes.

4.3.5 Removal of trace organic contaminants from authentic surface water

The dual-cathode treatment process was also tested using an authentic surface water sample containing 5.1 mg-C/L of NOM. The observed H_2O_2 consumption rate was comparable to that observed in the pH buffered Na_2SO_4 electrolyte (e.g., about 3 μmol/min, Figure 4.14). However, the H_2O_2 concentrations flowing into the stainless-steel electrode operated in authentic surface water were higher than those observed in Na_2SO_4 electrolyte, likely due to the inhibition of H_2O_2 loss at the Pt/Ti anode by NOM.

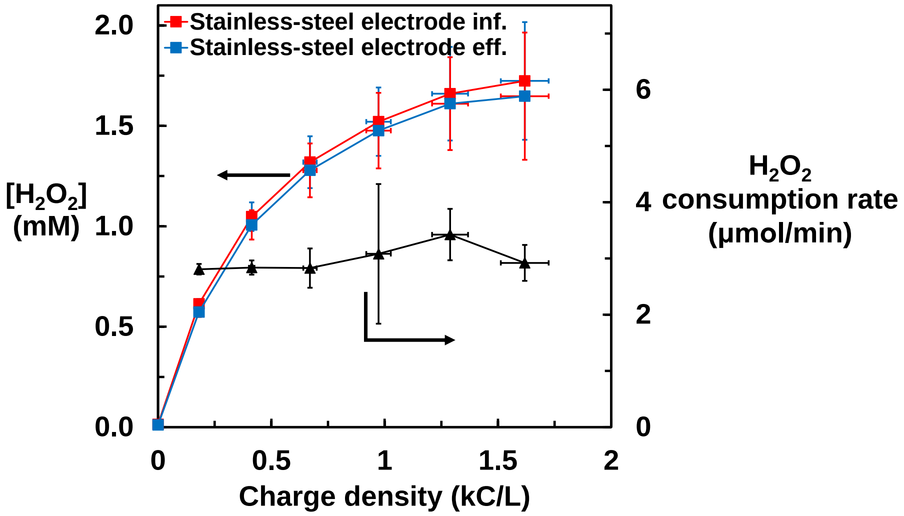

Figure 4.14 H_2O_2 concentrations and consumption rates observed when authentic water was treated. Conditions: $[TrOC]_0 = 20$ μg/L, $[TOC]_0 = 5.1$ mg-C/L, applied current on air-diffusion electrode = 16 mA, applied potential on stainless-steel electrode = +0.02 V, recirculation rate = 70 mL/min. SSE represents stainless-steel electrode.

At a charge density of around 1.6 kC/L, the dual-cathode treatment process removed more than 90% of carbamazepine and 60% of atrazine. In contrast, the total organic carbon (TOC), which mainly consists of NOM, remained unchanged throughout the treatment. Due to the non-selective nature of •OH, it is unlikely that NOM underwent oxidation without any mineralization (i.e., researchers have reported simultaneous decreases in TOC and chemical oxygen demand in advanced oxidation processes) (Ahmed et al. 2009, Ortiz-Marin et al. 2020). Therefore, it appears that the cathodically produced •OH was not scavenged by the negatively charged NOM.

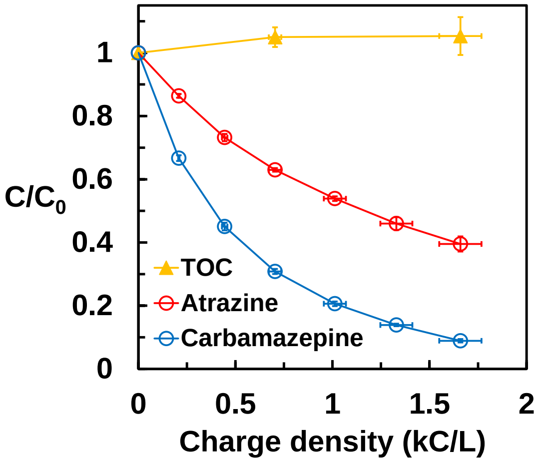

Figure 4.15 Concentrations of TrOCs and TOC observed when authentic water was treated. Conditions: $[TrOC]_0$ = 20 µg/L, $[TOC]_0$ = 5.1 mg-C/L, applied current on air-diffusion electrode = 16 mA, applied potential on stainless-steel electrode = +0.02 V, recirculation rate = 70 mL/min.

The concentrations of Fe and Cr released from the dual-cathode treatment process remained below the drinking water standards throughout the experiment (Figure 4.16) (USEPA 2022a, b).

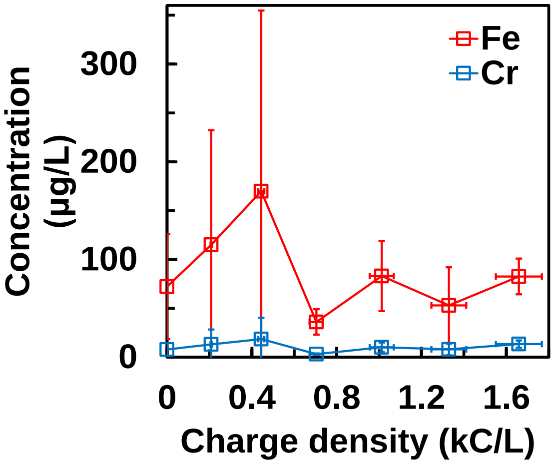

Figure 4.16 Metal released from the stainless-steel electrode when authentic water was treated. Conditions: $[TrOC]_0$ = 20 µg/L, $[TOC]_0$ = 5.1 mg-C/L, applied current on air-diffusion electrode = 16 mA, applied potential on stainless-steel electrode = +0.02 V, recirculation rate = 70 mL/min.

4.3.6 Energy consumption

One of the main challenges in the application of electrochemical techniques to drinking water is the low conductivity of the treated water, which results in a high ohmic loss between the working electrodes and counter electrodes. For source waters with low ionic strength (i.e., the secondary maximum contaminant level for drinking water corresponds to an ionic strength of about 10 mM) (Langmuir 1997, USEPA 2022b), energy consumption for electrochemical drinking water treatment can be high (Garcia-Segura et al. 2020, Ma et al. 2018, Radjenovic and Sedlak 2015). Electrical energy per order (E_{EO}) has often been used as the figure of merit in evaluations of the energy efficiency of advanced water treatment processes (Bolton et al. 2001). For the treatment of low conductivity surface water, the E_{EO} values were determined as 4.2 ± 0.3 kWh/m^3 for carbamazepine and 11.1 ± 1.4 kWh/m^3 for atrazine (Figure 4.17).

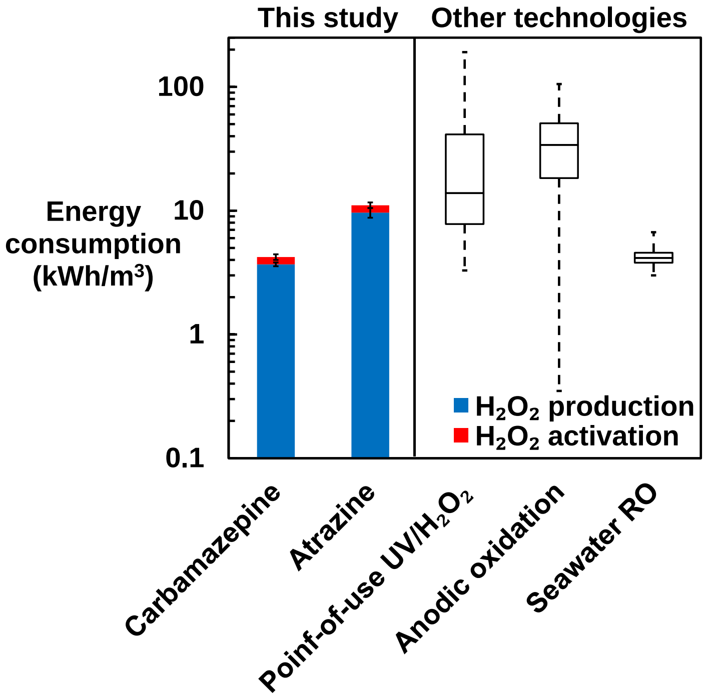

Figure 4.17 Comparison of energy consumption by the dual-cathode treatment process to other treatment technologies. The energy consumption corresponds to 90% reduction of the initial concentration of TrOCs contaminants (i.e., electrical energy per order) except for seawater RO.

The energy consumption of the dual-cathode treatment process was comparable to other distributed water treatment technologies and seawater desalination by reverse osmosis (RO) (Kim et al. 2019, Miklos et al. 2018). The energy cost associated with externally-supplied H_2O_2 was calculated followed a method proposed by Pisarenko, et al. (2012) (Section A.3.3 of the Appendix). Although further optimization could improve the energy efficiency of the dual-cathode treatment process, the data observed during the treatment of authentic surface water suggests that this technology may be advantageous relative to other approaches. Assuming a person only needs 10 L/d of clean drinking water, the energy consumption would be only 0.1 kWh/capita/day.

4.4 Environmental implications

Considering the ease of the fabrication of the air-diffusion electrode and the low cost of the stainless-steel electrode, the dual-cathode treatment process described in this study shows considerable promise for distributed water treatment. To achieve 90% removal of atrazine, a compound that was mostly removed through the reaction with $^{\bullet}OH$, the bench-scale prototype was estimated to be capable of producing around 20 mL/h of clean water under realistic water conditions. For a typical household containing three persons, approximate 23 L/day of water would be needed for hydration and food preparation (World Health Organization 2017). Therefore, the prototype needs be scaled up by about a factor of about 50 for realistic applications. Because higher Faraday efficiency was observed at low applied potentials, the H_2O_2 generation process could be easily scaled up by applying a higher current density on the air-diffusion electrode. The stainless-steel electrode also could be scaled up by compressing the material into a treatment module. Because of the inefficient H_2O_2 utilization in the presence of a high concentration of H_2O_2 in the stainless-steel electrode, the scaled-up reactor might require multiple points for dosing the H_2O_2 to avoid localized high H_2O_2 concentrations within the stainless-steel electrode reactor (Figure 4.18).

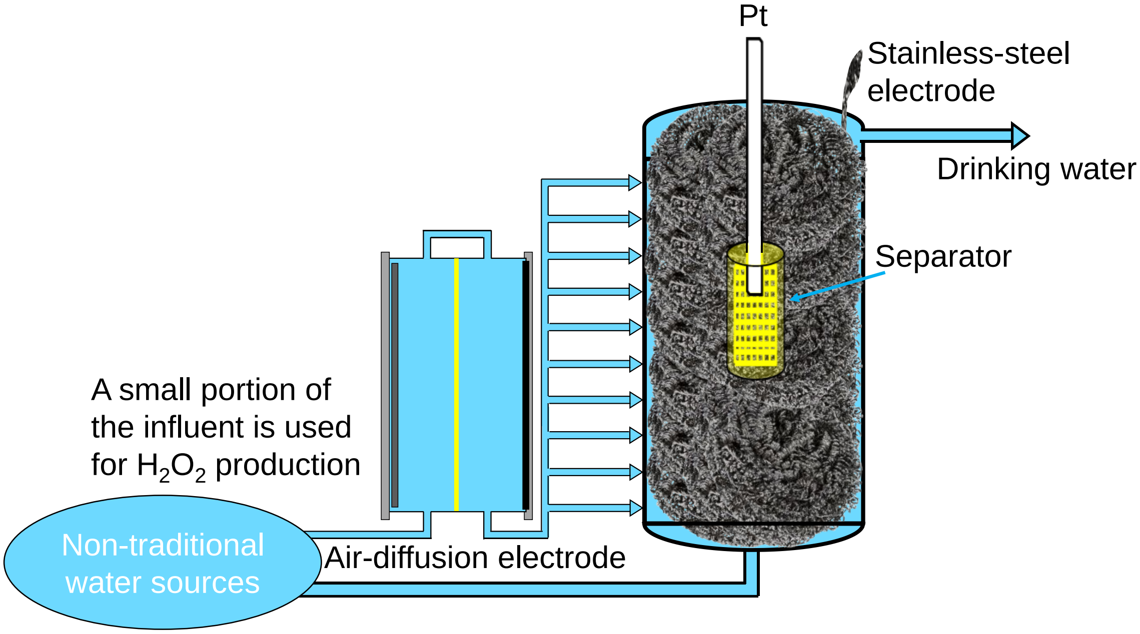

Figure 4.18 Schematic of a dual-cathode treatment system with multiple points for dosing H_2O_2.

Sufficient longevity of the electrodes is another important factor for successful operation under field conditions. The air-diffusion electrode in this study demonstrated good performance for H_2O_2 generation after about 70 hours of operation, with a Faraday efficiency of 95 ±2 % and a H_2O_2 production rate of 3×10^{-3} mmol min^{-1} cm^{-2} (Figure 4.19). Results from a previous study demonstrated stable performance of the air-diffusion electrode over 50 days, with an applied current density of 1.5 mA/cm^2 (Barazesh et al. 2015). However, inorganic fouling and flooding can damage the air-diffusion electrode after extended use (Barazesh et al. 2015, Duan and Sedlak 2021), leading to failure of the air-diffusion electrode. The stainless-steel electrode was used to treat the authentic surface water sample for over 12 hours and with no decrease in $^{\bullet}OH$ production (Figure 4.20). However, testing over a longer time scale with water of different composition is needed to ensure the effectiveness of the treatment system. Finally, the mechanisms of failure and associated mitigating strategies for both electrode merits further research.

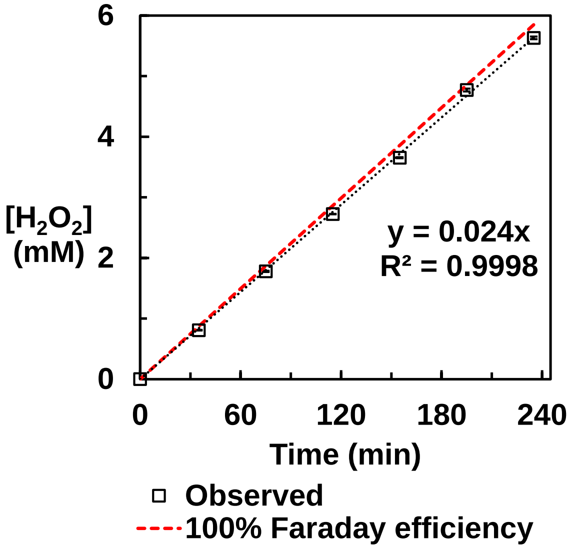

Figure 4.19 H_2O_2 generation in 250 mM Na_2SO_4 buffered with 1 mM of PIPES buffer (pH 7), $[TrOCs]_0$ = 20 µg/L using the divided cell configuration. Applied current on air-diffusion electrode = 16 mA, recirculation rate = 70 mL/min. The air-diffusion electrode had been operated for about 70 hours at 16 mA prior to the test.

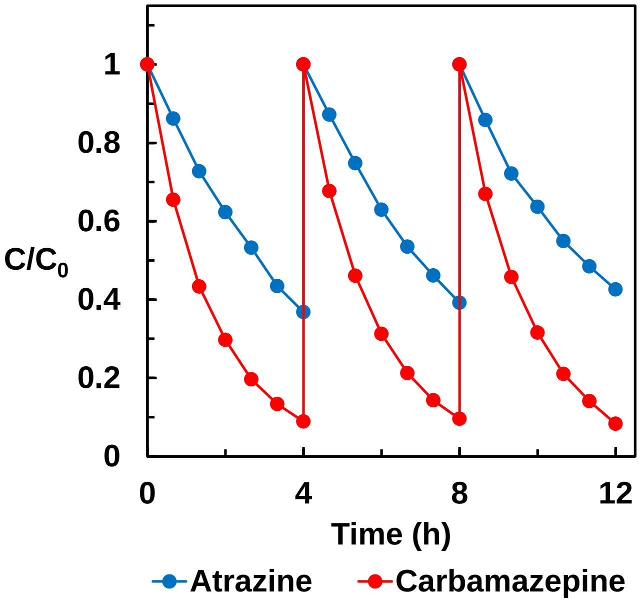

Figure 4.20 Degradation of TrOCs over three cycles of operation. Applied current on air-diffusion electrode = 16 mA, applied potential on stainless-steel electrode = 0.02 V. Experiments conducted in real surface water, [TrOCs]$_0$ = 20 μg/L, recirculation rate = 70 mL/min.

CHAPTER 5. Conclusions

5.1 Summary

Climate change, urbanization, and chemical contaminants are posing new challenges to humanity and the environment. Much of our existing water infrastructure was built decades ago and is not well suited for current conditions. This mismatch results in water scarcity and exposure of humans and wildlife to toxic chemicals (National Academies of Sciences, Engineering, and Medicine 2019). Distributed treatment systems have the potential to address some of these challenges by exploitation of non-traditional water sources. However, implementation of distributed treatment technologies is often limited by the need for frequent replenishment of chemical reagents and a lack of cost-effective methods to generate species that react with recalcitrant contaminants. Innovative treatment methods are needed for the transition from the traditional centralized water system to a more resilient distributed water system.

The primary goals of my doctoral research were to develop treatment technologies suitable for distributed water treatment. The following sections summarize the important findings, implications, and future research directions.

5.1.1 An electrochemical advanced oxidation process for the treatment of urban stormwater

In Chapter 2, an electrochemical advanced oxidation system (UV/H_2O_2) that is compatible with high-capacity stormwater recharge systems (e.g., drywells) was developed. The system employed an air-diffusion cathode to generate a H_2O_2 stock solution (i.e., typically around 600 mM) prior to the storm event. The H_2O_2 stock solution was then metered into stormwater and converted into $^{\bullet}OH$ by an ultraviolet lamp. The energy consumption for H_2O_2 generation was optimized by adjusting the applied current density and adding an inert salt (e.g., Na_2SO_4) to a concentrated solution that could be generated prior to the arrival of a storm. H_2O_2 in the stock solution was unstable. By mixing the basic H_2O_2 containing catholyte and the acidic anolyte, the stability increased, enabling generation of the H_2O_2 stock solution up to three days prior to the storm event with loss of less than 20% of the H_2O_2. Lab-scale experiments and a kinetic model were used to assess the feasibility of deploying the full-scale advanced oxidation system. System performance decreased at elevated concentrations of dissolved organic carbon in stormwater, due to enhanced light reflection and backscattering at the water-air interface in the UV reactor, competition for UV light absorption with H_2O_2 and the tendency of organic matter to act as a $^{\bullet}OH$ scavenger. Nonetheless, the system can be incorporated into drywells to remove greater than 90% of trace organic contaminants under typical operating conditions. The electrical energy per order of the system is estimated to range from 0.5 to 2 kWh/m^3, depending on the dissolved organic carbon concentration.

5.1.2 Factors affecting the yield of hydroxyl radical by electrochemical activation of H_2O_2 on stainless-steel electrodes

The research described in Chapter 3 investigated the reaction mechanism and oxidation yields produced by a low-cost stainless-steel electrode, which has the potential to be employed in lieu of UV lamps for using H_2O_2 to oxidize contaminants in distributed water treatment systems. To assess system performance, the stainless-steel electrodes were operated at different pH values and applied potentials, with methanol and 2-propanol serving as probe compounds for oxidants behaving in a manner similar to Fe[IV] and •OH, respectively. H_2O_2 transformation rates were highest under circumneutral pH conditions. At +0.020 V, the stainless-steel electrode generated •OH from H_2O_2 with a yield that was over an order of magnitude higher than that reported for other systems that employ iron oxides as catalysts under circumneutral pH conditions. Increasing the applied overpotential at pH 8 and 9 resulted in production of more Fe[IV]. Significant metal leaching was only observed under acidic pH conditions (i.e., at pH <5), with the release of up to about 2 mg/L of Fe and 50 μg/L of Cr(III) as the thickness of the passivation layer decreased and elemental Fe and Cr were oxidized. Despite the high yield of •OH, the majority of the •OH was scavenged by the electrode surface under conditions similar to those expected in drinking water sources. Although the stainless-steel electrode oxidized trace organic contaminants, the loss of •OH to the electrode surface decreased the performance of the system for the removal of TrOCs.

5.1.3 Reagent-free electrochemical advanced oxidation for distributed water treatment enabled by air-diffusion and stainless-steel electrodes

The research described in Chapter 4 described a reagent-free electrochemical advanced oxidation process that coupled an air-diffusion electrode with a stainless-steel electrode. Separating the H_2O_2 generation and activation steps enabled the optimization of each process. The optimal condition for H_2O_2 production and trace organic contaminants transformation were optimized employed a potential of -0.04 V for the air-diffusion electrode and +0.02 V for the stainless-steel electrode. The treatment performance improved when the recirculation rate increased, likely due to enhanced mass transport of trace organic contaminants to the stainless-steel electrode. The system was unable to oxidize benzoate, suggesting that electrostatic repulsion minimizes the scavenging effect of negatively charged •OH scavengers. Similarly, the treatment process selectively removed trace organic contaminants in the presence of natural organic matter in an authentic surface water sample, indicating the ability of the system to transform organic contaminants will not be impacted by the presence of negatively charged polymers like natural organic matter. The proposed treatment system consumed about 10 kWh/m^3, which is comparable to that of anodic oxidation and point-of-use UV/H_2O_2 processes.

5.2 Future research

Scaling up the production of H_2O_2 by the air-diffusion electrode can be achieved by increasing the applied current density or increasing the electrode size. In Chapter 2, we evaluated the feasibility of increasing the applied current density. However, for field-scale application, engineering designs that increase the electrode area may be more effective. Because the air-diffusion electrode must be installed between water and the atmosphere, scaling up the air-diffusion electrode in parallel plate reactors by simply increasing the area is infeasible due to constrains on the system footprint. Additionally, the cross-electrode hydraulic pressure increases as the size of the electrode increases, a factor that could cause water to leak through the pores on the electrodes. As an alternative, spiral reactor module is a promising configuration to scale up the H_2O_2 generation process (Figure 5.1).

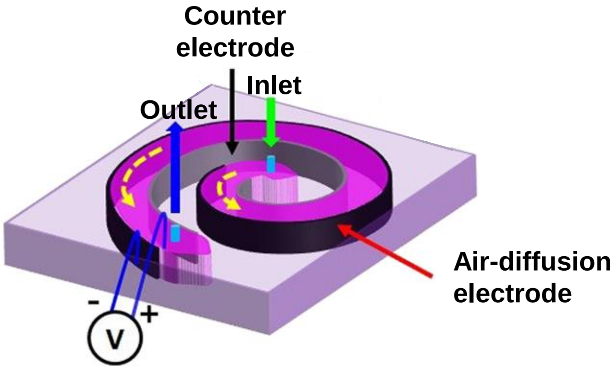

Figure 5.1 Schematic of a spiral reactor for scaling up the H_2O_2 production. Image modified from (Arun et al. 2019).

The longevity of the electrodes is another important factor to ensure the effective operation of a distributed electrochemical treatment system. Despite previous results indicating stable long-term performance of the air-diffusion electrode at a low current density (e.g., < 30 A/m^2) and low charge density (e.g., < 400 C/L) (Barazesh et al. 2015), preliminary results showed that the performance of the air-diffusion electrode decreased significantly after 24 hours of operation when operated under high current density (i.e., 200 A/cm^2) and high charge density (i.e., 125 kC/L) (Figure 5.2A). Preliminary results indicated the decreased performance was related to the decrease in the hydrophobicity of the electrode. In the presence of natural organic matter, a more significant decrease in the performance was observed, likely due to organic fouling on the electrode, which blocked the active sites (Figure 5.2B).

For the stainless-steel electrode, its lifetime may be affected by the corrosion of the electrode surface and other factors such as fouling and scaling. Therefore, additional research is needed to create standard protocols to assess the long-term performance of electrodes and to assess the mechanisms of electrode failure.

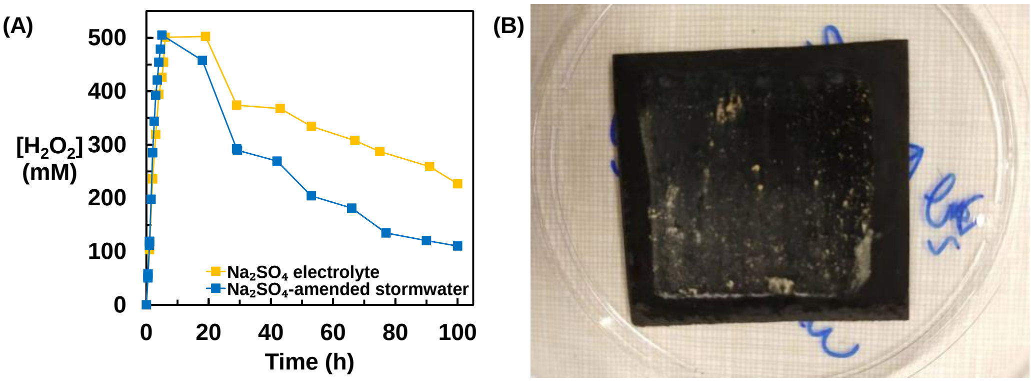

Figure 5.2 (A) Long-term performance of the air-diffusion electrode operated in a flow-through mode. The stormwater contained 10 mg-C/L of humic acid. Current density = 200 A/cm^2, applied charge density = 125 kC/L. (B) Image of the liquid-facing side of the air-diffusion electrode after operation in Na_2SO_4-amended stormwater for 100 hours.

Transitioning from the conventional centralized treatment systems to distributed systems will not be feasible unless water quality and safety can be ensured. Unlike centralized systems, where engineers can monitor water quality for millions of users by collecting samples at a few locations, distributed water systems require monitoring and remote control for each individual treatment module. As discussed in Chapter 2, the performance of the advanced oxidation process could be predicted from parameters such as H_2O_2 concentration, UV fluence, total organic carbon concentration, and hydraulic residence time. These parameters can be measured or estimated with sensors that monitor water quality parameters (e.g., conductivity, light absorption) and operational parameters related to the treatment process (e.g., electrolysis time, current density). Therefore, developing control algorithms that are capable of control the system operation based on off-the-shelf sensors and telemetry (i.e., a cell phone relay) merits further research (Figure 5.3).

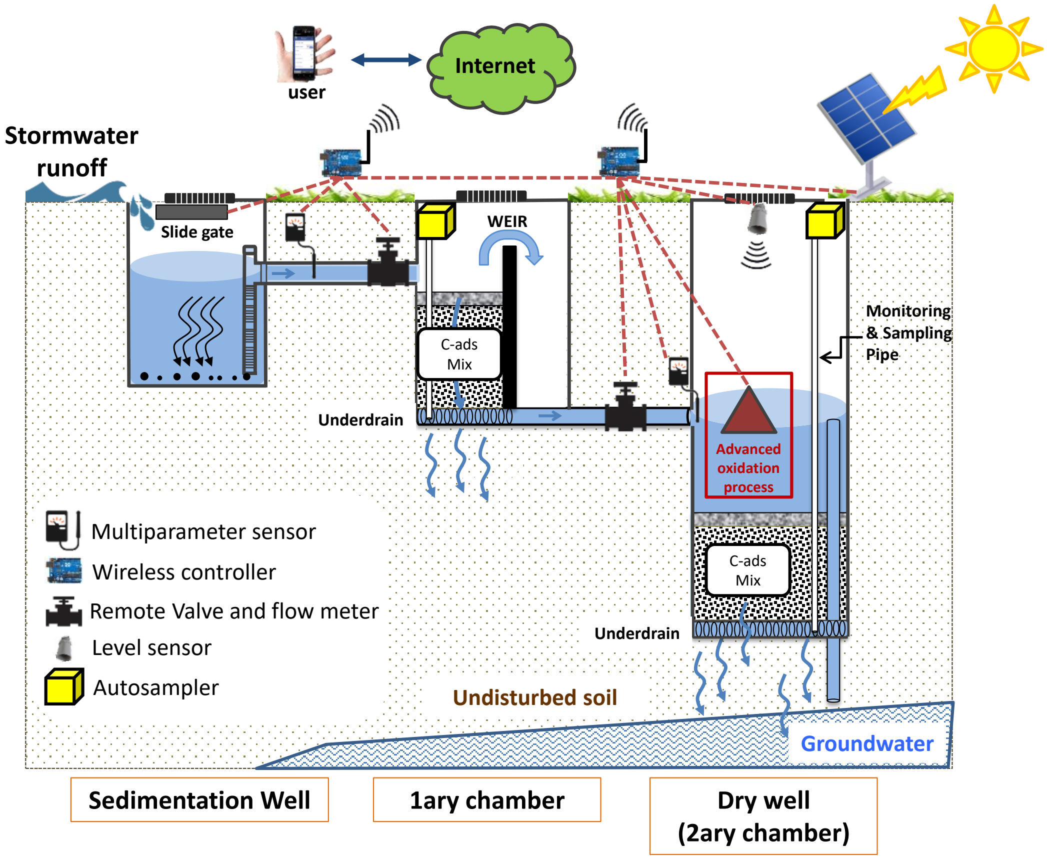

Figure 5.3 Schematic of an automated stormwater advanced oxidation process enabled by wireless controllers and sensors.

References

Abdekhodaie, M., Cheng, J. and Wu, X. (2015) Effect of formulation factors on the bioactivity of glucose oxidase encapsulated chitosan–alginate microspheres: In vitro investigation and mathematical model prediction. Chemical Engineering Science 125, 4-12.

Abdullah, G.H. and Xing, Y. (2017) Hydrogen Peroxide Generation in Divided-Cell Trickle Bed Electrochemical Reactor. Industrial & Engineering Chemistry Research 56(39), 11058-11064.

Abel, E. (1952) Über die Selbstzersetzung von Wasserstoffsuperoxyd. Monatshefte für Chemie und verwandte Teile anderer Wissenschaften 83(2), 422-439.

Acero, J.L., Stemmler, K. and von Gunten, U. (2000) Degradation Kinetics of Atrazine and Its Degradation Products with Ozone and OH Radicals: A Predictive Tool for Drinking Water Treatment. Environmental Science & Technology 34(4), 591-597.

Ahmed, B., Mohamed, H., Limem, E. and Nasr, B. (2009) Degradation and Mineralization of Organic Pollutants Contained in Actual Pulp and Paper Mill Wastewaters by a UV/H2O2 Process. Industrial & Engineering Chemistry Research 48(7), 3370-3379.

Aiken, G.R., Hsu-Kim, H. and Ryan, J.N. (2011) Influence of Dissolved Organic Matter on the Environmental Fate of Metals, Nanoparticles, and Colloids. Environmental Science & Technology 45(8), 3196-3201.

Akamatsu, K., Lu, W., Sugawara, T. and Nakao, S.-i. (2010) Development of a novel fouling suppression system in membrane bioreactors using an intermittent electric field. Water Research 44(3), 825-830.

American Society of Civil Engineers (2021) 2021 Report Card for America's Infrastructure.

Appiani, E., Page, S.E. and McNeill, K. (2014) On the Use of Hydroxyl Radical Kinetics to Assess the Number-Average Molecular Weight of Dissolved Organic Matter. Environmental Science & Technology 48(20), 11794-11802.

Aregahegn, K.Z., Shemesh, D., Gerber, R.B. and Finlayson-Pitts, B.J. (2017) Photochemistry of Thin Solid Films of the Neonicotinoid Imidacloprid on Surfaces. Environmental Science & Technology 51(5), 2660-2668.

Arévalo, M.C., Rodríguez, J.L. and Pastor, E. (2001) Elucidation of the reaction pathways of allyl alcohol at polycrystalline palladium electrodes. Journal of Electroanalytical Chemistry 505(1), 62-71.

Armbrust, K.L. (2000) Pesticide hydroxyl radical rate constants: Measurements and estimates of their importance in aquatic environments. Environmental Toxicology and Chemistry 19(9), 2175-2180.

Arun, R.K., Anjali, Sardar, M., Singh, P., Jha, B.M. and Chanda, N. (2019) A spiral shaped regenerative microfluidic fuel cell with Ni-C based porous electrodes. International Journal of Energy Research 43(14), 8834-8840.

Ashoori, N., Teixido, M., Spahr, S., LeFevre, G.H., Sedlak, D.L. and Luthy, R.G. (2019) Evaluation of pilot-scale biochar-amended woodchip bioreactors to remove nitrate, metals, and trace organic contaminants from urban stormwater runoff. Water Research 154, 1-11.

Asmus, K., Möckel, H. and Henglein, A. (1973) Pulse radiolytic study of the site of hydroxyl radical attack on aliphatic alcohols in aqueous solution. The Journal of Physical Chemistry 77(10), 1218-1221.

Auinger, M., Katsounaros, I., Meier, J.C., Klemm, S.O., Biedermann, P.U., Topalov, A.A., Rohwerder, M. and Mayrhofer, K.J.J. (2011) Near-surface ion distribution and buffer effects during electrochemical reactions. Physical Chemistry Chemical Physics 13(36), 16384-16394.

Axnanda, S., Crumlin, E.J., Mao, B., Rani, S., Chang, R., Karlsson, P.G., Edwards, M.O., Lundqvist, M., Moberg, R. and Ross, P. (2015) Using “tender” X-ray ambient pressure X-ray photoelectron spectroscopy as a direct probe of solid-liquid interface. Scientific reports 5(1), 1-12.

Azizi, O., Hubler, D., Schrader, G., Farrell, J. and Chaplin, B.P. (2011) Mechanism of Perchlorate Formation on Boron-Doped Diamond Film Anodes. Environmental Science & Technology 45(24), 10582-10590.

Bader, H., Sturzenegger, V. and Hoigné, J. (1988) Photometric method for the determination of low concentrations of hydrogen peroxide by the peroxidase catalyzed oxidation of N,N-diethyl-p-phenylenediamine (DPD). Water Research 22(9), 1109-1115.

Baeza, C. and Knappe, D.R.U. (2011) Transformation kinetics of biochemically active compounds in low-pressure UV Photolysis and UV/H2O2 advanced oxidation processes. Water Research 45(15), 4531-4543.

Balci, B., Oturan, N., Cherrier, R. and Oturan, M.A. (2009) Degradation of atrazine in aqueous medium by electrocatalytically generated hydroxyl radicals. A kinetic and mechanistic study. Water Research 43(7), 1924-1934.

Barazesh, J.M., Hennebel, T., Jasper, J.T. and Sedlak, D.L. (2015) Modular Advanced Oxidation Process Enabled by Cathodic Hydrogen Peroxide Production. Environmental Science & Technology 49(12), 7391-7399.

Barazesh, J.M., Prasse, C. and Sedlak, D.L. (2016) Electrochemical Transformation of Trace Organic Contaminants in the Presence of Halide and Carbonate Ions. Environmental Science & Technology 50(18), 10143-10152.

Barnes, R.T., Gallagher, M.E., Masiello, C.A., Liu, Z. and Dugan, B. (2014) Biochar-induced changes in soil hydraulic conductivity and dissolved nutrient fluxes constrained by laboratory experiments. PloS one 9(9), e108340.

Baskar, A.V., Bolan, N., Hoang, S.A., Sooriyakumar, P., Kumar, M., Singh, L., Jasemizad, T., Padhye, L.P., Singh, G., Vinu, A., Sarkar, B., Kirkham, M.B., Rinklebe, J., Wang, S., Wang, H., Balasubramanian, R. and Siddique, K.H.M. (2022) Recovery, regeneration and sustainable management of spent adsorbents from wastewater treatment streams: A review. Science of The Total Environment 822, 153555.

Bataineh, H., Pestovsky, O. and Bakac, A. (2012) pH-induced mechanistic changeover from hydroxyl radicals to iron(iv) in the Fenton reaction. Chemical Science 3(5), 1594-1599.

Baxendale, J. and Wilson, J. (1957) The photolysis of hydrogen peroxide at high light intensities. Transactions of the Faraday Society 53, 344-356.

Benitez, F.J., Acero, J.L., Real, F.J. and Roman, S. (2004) Oxidation of MCPA and 2,4-d by UV Radiation, Ozone, and the Combinations UV/H2O2 and O3/H2O2. Journal of Environmental Science and Health, Part B 39(3), 393-409.

Benitez, F.J., Real, F.J., Acero, J.L. and Garcia, C. (2006) Photochemical oxidation processes for the elimination of phenyl-urea herbicides in waters. Journal of Hazardous Materials 138(2), 278-287.

Benjamin, M.M. (2014) Water chemistry, Waveland Press.

Bergmann, M.E.H. and Rollin, J. (2007) Product and by-product formation in laboratory studies on disinfection electrolysis of water using boron-doped diamond anodes. Catalysis Today 124(3), 198-203.

Bettman, N. (2020) Assessment of an Advanced Oxidation System for the Generation of Oxidative Species and Effectiveness of Treating Synthetic and Real Stormwater, Master's Thesis, Department of Civil Geological and Environmental Engineering, University of Saskatchewan, Saskatoon.

Boehm, A.B., Bell, C.D., Fitzgerald, N.J.M., Gallo, E., Higgins, C.P., Hogue, T.S., Luthy, R.G., Portmann, A.C., Ulrich, B.A. and Wolfand, J.M. (2020) Biochar-augmented biofilters to improve pollutant removal from stormwater – can they improve receiving water quality? Environmental Science: Water Research & Technology 6(6), 1520-1537.

Bolton, J.R., Bircher, K.G., Tumas, W. and Tolman, C.A. (2001) Figures-of-merit for the technical development and application of advanced oxidation technologies for both electric-and solar-driven systems (IUPAC Technical Report). Pure and Applied Chemistry 73(4), 627-637.

Bolton, J.R. and Linden, K.G. (2003) Standardization of methods for fluence (UV dose) determination in bench-scale UV experiments. Journal of environmental engineering 129(3), 209-215.

Bormann, S., van Schie, M.M.C.H., De Almeida, T.P., Zhang, W., Stöckl, M., Ulber, R., Hollmann, F. and Holtmann, D. (2019) H2O2 Production at Low Overpotentials for Electroenzymatic Halogenation Reactions. ChemSusChem 12(21), 4759-4763.

Bossmann, S.H., Oliveros, E., Göb, S., Siegwart, S., Dahlen, E.P., Payawan, L., Straub, M., Wörner, M. and Braun, A.M. (1998) New Evidence against Hydroxyl Radicals as Reactive Intermediates in the Thermal and Photochemically Enhanced Fenton Reactions. The Journal of Physical Chemistry A 102(28), 5542-5550.

Brillas, E., Sirés, I. and Oturan, M.A. (2009) Electro-Fenton Process and Related Electrochemical Technologies Based on Fenton’s Reaction Chemistry. Chemical Reviews 109(12), 6570-6631.

Buxton, G.V., Greenstock, C.L., Helman, W.P. and Ross, A.B. (1988) Critical review of rate constants for reactions of hydrated electrons, hydrogen atoms and hydroxyl radicals (· OH/· O− in aqueous solution. Journal of physical and chemical reference data 17(2), 513-886.

California Water Boards, State Water Resources Control Board (2013) Chromium-6 Drinking Water MCL.

Cannan, S., Douglas Macklam, I. and Unwin, P.R. (2002) Three-dimensional imaging of proton gradients at microelectrode surfaces using confocal laser scanning microscopy. Electrochemistry Communications 4(11), 886-892.

Canonica, S., Meunier, L. and Von Gunten, U. (2008) Phototransformation of selected pharmaceuticals during UV treatment of drinking water. Water Research 42(1-2), 121-128.

Cao, P., Quan, X., Zhao, K., Chen, S., Yu, H. and Su, Y. (2020) High-Efficiency Electrocatalysis of Molecular Oxygen toward Hydroxyl Radicals Enabled by an Atomically Dispersed Iron Catalyst. Environmental Science & Technology 54(19), 12662-12672.

Carlesi Jara, C. and Fino, D. (2010) Cost optimization of the current density for electroxidation wastewater processes. Chemical Engineering Journal 160(2), 497-502.

Casado, J. (2019) Towards industrial implementation of Electro-Fenton and derived technologies for wastewater treatment: A review. Journal of Environmental Chemical Engineering 7(1), 102823.

Cater, S.R., Stefan, M.I., Bolton, J.R. and Safarzadeh-Amiri, A. (2000) UV/H2O2 Treatment of Methyl tert-Butyl Ether in Contaminated Waters. Environmental Science & Technology 34(4), 659-662.

Celdrán, R. and González-Velasco, J.J. (1981) Oxidation mechanism of allyl alcohol on an Au-electrode in basic solutions. Electrochimica Acta 26(4), 525-533.

Chaplin, B.P. (2014) Critical review of electrochemical advanced oxidation processes for water treatment applications. Environmental Science: Processes & Impacts 16(6), 1182-1203.

Chaplin, B.P. (2019) The Prospect of Electrochemical Technologies Advancing Worldwide Water Treatment. Accounts of Chemical Research 52(3), 596-604.

Charbonnet, J.A., Duan, Y. and Sedlak, D.L. (2020) The use of manganese oxide-coated sand for the removal of trace metal ions from stormwater. Environmental Science: Water Research & Technology 6(3), 593-603.

Charbonnet, J.A., Duan, Y., van Genuchten, C.M. and Sedlak, D.L. (2018) Chemical Regeneration of Manganese Oxide-Coated Sand for Oxidation of Organic Stormwater Contaminants. Environmental Science & Technology 52(18), 10728-10736.

Charbonnet, J.A., Duan, Y., van Genuchten, C.M. and Sedlak, D.L. (2021) Regenerated Manganese-Oxide Coated Sands: The Role of Mineral Phase in Organic Contaminant Reactivity. Environmental Science & Technology 55(8), 5282-5290.

Chen, Y., Miller, C.J. and Waite, T.D. (2021) pH Dependence of Hydroxyl Radical, Ferryl, and/or Ferric Peroxo Species Generation in the Heterogeneous Fenton Process. Environmental Science & Technology.

Chen, Z., Chen, S., Siahrostami, S., Chakthranont, P., Hahn, C., Nordlund, D., Dimosthenis, S., Nørskov, J.K., Bao, Z. and Jaramillo, T.F. (2017) Development of a reactor with carbon catalysts for modular-scale, low-cost electrochemical generation of H2O2. Reaction Chemistry & Engineering 2(2), 239-245.

Chou, S., Huang, C. and Huang, Y.-H. (2001) Heterogeneous and Homogeneous Catalytic Oxidation by Supported γ-FeOOH in a Fluidized-Bed Reactor: Kinetic Approach. Environmental Science & Technology 35(6), 1247-1251.

Chuang, Y.-H., Chen, S., Chinn, C.J. and Mitch, W.A. (2017) Comparing the UV/Monochloramine and UV/Free Chlorine Advanced Oxidation Processes (AOPs) to the UV/Hydrogen Peroxide AOP Under Scenarios Relevant to Potable Reuse. Environmental Science & Technology 51(23), 13859-13868.

City of Portland Bureau of Environmental Services (2008) Decision Making Framework for Groundwater Protectiveness Demonstrations: Underground Injection Control System Evaluation and Response. Posted at: <http://www.portlandoregon.gov/bes/48213>.

Clarke, G.L., Ewing, G.C. and Lorenzen, C.J. (1970) Spectra of Backscattered Light from the Sea Obtained from Aircraft as a Measure of Chlorophyll Concentration. Science 167(3921), 1119-1121.

Collén, J. and Pedersén, M. (1996) Production, scavenging and toxicity of hydrogen peroxide in the green seaweed Ulva rigida. European Journal of Phycology 31(3), 265-271.

Crittenden, J.C., Hu, S., Hand, D.W. and Green, S.A. (1999) A kinetic model for H2O2/UV process in a completely mixed batch reactor. Water Research 33(10), 2315-2328.

Cuerda-Correa, E.M., Alexandre-Franco, M.F. and Fernández-González, C. (2020) Advanced Oxidation Processes for the Removal of Antibiotics from Water. An Overview. Water 12(1), 102.

de Souza, R.M., Seibert, D., Quesada, H.B., de Jesus Bassetti, F., Fagundes-Klen, M.R. and Bergamasco, R. (2020) Occurrence, impacts and general aspects of pesticides in surface water: A review. Process Safety and Environmental Protection 135, 22-37.

Draganić, Z.D., Negron-Mendoza, A., Sehested, K., Vujošević, S.I., Navarro-Gonzales, R., Albarran-Sanchez, M. and Draganić, I.G. (1991) Radiolysis of aqueous solutions of ammonium bicarbonate over a large dose range. International Journal of Radiation Applications and Instrumentation. Part C. Radiation Physics and Chemistry 38(3), 317-321.

Duan, Y., Jiang, W. and Sedlak, D.L. (2022) Factors Affecting the Yield of Hydroxyl Radical by Electrochemical Activation of H_2O_2 on Stainless Steel Electrodes (In preparation).

Duan, Y. and Sedlak, D.L. (2021) An electrochemical advanced oxidation process for the treatment of urban stormwater. Water Research X 13, 100127.

Duesterberg, C.K., Cooper, W.J. and Waite, T.D. (2005) Fenton-mediated oxidation in the presence and absence of oxygen. Environmental Science & Technology 39(13), 5052-5058.

Duke, F.R. and Haas, T.W. (1961) The homogeneous base-catalyzed decomposition of hydrogen peroxide1. The Journal of Physical Chemistry 65(2), 304-306.

East Bay Municipal Utility District (2019) 2019 Annual Water Quality Report.

Edwards, E.C., Harter, T., Fogg, G.E., Washburn, B. and Hamad, H. (2016) Assessing the effectiveness of drywells as tools for stormwater management and aquifer recharge and their groundwater contamination potential. Journal of Hydrology 539, 539-553.

Eickes, C., Weil, K.G. and Doblhofer, K. (2000) Faradaic impedance studies of the autocatalytic reduction of H2O2 on Ag electrodes in HClO4. Physical Chemistry Chemical Physics 2(24), 5691-5697.

Eisenberg, G. (1943) Colorimetric Determination of Hydrogen Peroxide. Industrial & Engineering Chemistry Analytical Edition 15(5), 327-328.

Elliot, A.J. and Buxton, G.V. (1992) Temperature dependence of the reactions OH+ O–2 and OH+ HO 2 in water up to 200° C. Journal of the Chemical Society, Faraday Transactions 88(17), 2465-2470.

Eriksen, T., Lind, J. and Merenyi, G. (1985) On the acid-base equilibrium of the carbonate radical. Radiation Physics and Chemistry (1977) 26(2), 197-199.

Ezeh, A., Oyebode, O., Satterthwaite, D., Chen, Y.F., Ndugwa, R., Sartori, J., Mberu, B., Melendez-Torres, G.J., Haregu, T., Watson, S.I., Caiaffa, W., Capon, A. and Lilford, R.J. (2017) The history, geography, and sociology of slums and the health problems of people who live in slums. Lancet 389(10068), 547-558.

Fast, S.A., Gude, V.G., Truax, D.D., Martin, J. and Magbanua, B.S. (2017) A Critical Evaluation of Advanced Oxidation Processes for Emerging Contaminants Removal. Environmental Processes 4(1), 283-302.

Feigenbrugel, V., Le Calvé, S. and Mirabel, P. (2006) Molar absorptivities of 2,4-D, cymoxanil, fenpropidin, isoproturon and pyrimethanil in aqueous solution in the near-UV. Spectrochimica Acta Part A: Molecular and Biomolecular Spectroscopy 63(1), 103-110.

Feng, W., McCarthy, D.T., Wang, Z., Zhang, X. and Deletic, A. (2018) Stormwater disinfection using electrochemical oxidation: A feasibility investigation. Water Research 140, 301-310.

Fenton, H.J.H. (1894) LXXIII.—Oxidation of tartaric acid in presence of iron. Journal of the Chemical Society, Transactions 65, 899-910.

Flätgen, G., Wasle, S., Lübke, M., Eickes, C., Radhakrishnan, G., Doblhofer, K. and Ertl, G. (1999) Autocatalytic mechanism of H2O2 reduction on Ag electrodes in acidic electrolyte: experiments and simulations. Electrochimica Acta 44(25), 4499-4506.

Flörke, M., Schneider, C. and McDonald, R.I. (2018) Water competition between cities and agriculture driven by climate change and urban growth. Nature Sustainability 1(1), 51-58.

Foller, P., Allen, R., Vora, R., Bombard, R. and DeMarinis, M. (1991) The use of gas diffusion electrodes in the on-site generation of oxidants and reductants.

Frankel, G.S. and Sridhar, N. (2008) Understanding localized corrosion. Materials Today 11(10), 38-44.

Gadgil, A. (2008) Safe and Affordable Drinking Water for Developing Countries. AIP Conference Proceedings 1044(1), 176-191.

Gadgil, A. and Garud, V. (1998) UV water disinfector, U.S. Patent No. 5,780,860. Washington, DC: U.S. Patent and Trademark Office.

Galbács, Z.M. and Csányi, L.J. (1983) Alkali-induced decomposition of hydrogen peroxide. Journal of the Chemical Society, Dalton Transactions (11), 2353-2357.

Ganiyu, S.O., Zhou, M. and Martínez-Huitle, C.A. (2018) Heterogeneous electro-Fenton and photoelectro-Fenton processes: A critical review of fundamental principles and application for water/wastewater treatment. Applied Catalysis B: Environmental 235, 103-129.

Gao, G., Zhang, Q., Hao, Z. and Vecitis, C.D. (2015) Carbon Nanotube Membrane Stack for Flow-through Sequential Regenerative Electro-Fenton. Environmental Science & Technology 49(4), 2375-2383.

Garcia-Segura, S., Nienhauser, A.B., Fajardo, A.S., Bansal, R., Conrad, C.L., Fortner, J.D., Marcos-Hernández, M., Rogers, T., Villagran, D., Wong, M.S. and Westerhoff, P. (2020) Disparities between experimental and environmental conditions: Research steps toward making electrochemical water treatment a reality. Current Opinion in Electrochemistry 22, 9-16.

Giggy, C., Winkler, H. (Ed.) (1993) Das perox-pure™ Verfahren zur Entfernung organischer Schadstoffe aus Wasser (The perox-pure™ process for the elimination of organic water pollutants).

Gill, T.M. and Zheng, X. (2020) Comparing Methods for Quantifying Electrochemically Accumulated H2O2. Chemistry of Materials 32(15), 6285-6294.

Glaze, W.H., Lay, Y. and Kang, J.-W. (1995) Advanced oxidation processes. A kinetic model for the oxidation of 1, 2-dibromo-3-chloropropane in water by the combination of hydrogen peroxide and UV radiation. Industrial & Engineering Chemistry Research 34(7), 2314-2323.

González-Davila, M., Santana-Casiano, J.M. and Millero, F.J. (2005) Oxidation of iron (II) nanomolar with H2O2 in seawater. Geochimica et Cosmochimica Acta 69(1), 83-93.

Good, N.E., Winget, G.D., Winter, W., Connolly, T.N., Izawa, S. and Singh, R.M.M. (1966) Hydrogen Ion Buffers for Biological Research*. Biochemistry 5(2), 467-477.

Grebel, J.E., Charbonnet, J.A. and Sedlak, D.L. (2016) Oxidation of organic contaminants by manganese oxide geomedia for passive urban stormwater treatment systems. Water research 88, 481-491.

Grebel, J.E., Mohanty, S.K., Torkelson, A.A., Boehm, A.B., Higgins, C.P., Maxwell, R.M., Nelson, K.L. and Sedlak, D.L. (2013) Engineered Infiltration Systems for Urban Stormwater Reclamation. Environmental Engineering Science 30(8), 437-454.

Gros, P. and Bergel, A. (1995) Improved model of a polypyrrole glucose oxidase modified electrode. Journal of Electroanalytical Chemistry 386(1-2), 65-73.

Grüniger, H., Möbius, D. and Meyer, H. (1983) Enhanced light reflection by dye monolayers at the air–water interface. The Journal of Chemical Physics 79(8), 3701-3710.

Guo, D., Liu, Y., Ji, H., Wang, C.-C., Chen, B., Shen, C., Li, F., Wang, Y., Lu, P. and Liu, W. (2021) Silicate-Enhanced Heterogeneous Flow-Through Electro-Fenton System Using Iron Oxides under Nanoconfinement. Environmental Science & Technology 55(6), 4045-4053.

Haber, F. and Weiss, J. (1934) The catalytic decomposition of hydrogen peroxide by iron salts. Proceedings of the Royal Society of London. Series A-Mathematical and Physical Sciences 147(861), 332-351.

Hering, J.G., Waite, T.D., Luthy, R.G., Drewes, J.E. and Sedlak, D.L. (2013) A Changing Framework for Urban Water Systems. Environmental Science & Technology 47(19), 10721-10726.

Hessler, D., Gorenflo, V. and Frimmel, F. (1993) Degradation of Aqueous Atrazine and Metazachlor Solutions by UV and UV/H2O2—Influence of pH and Herbicide Concentration Abbau von Atrazin und Metazachlor in wäßriger Lösung durch UV und UV/H2O2—Einfluß von pH und Herbizid‐Konzentration. Acta hydrochimica et hydrobiologica 21(4), 209-214.

Hirvonen, A., Tuhkanen, T., Ettala, M., Korhonen, S. and Kalliokoski, P. (1998) Evaluation of a Field-Scale UV/H2O2-Oxidation System for the Purification of Groundwater Contaminated with PCE. Environmental Technology 19(8), 821-828.

Hodges, B.C., Cates, E.L. and Kim, J.-H. (2018) Challenges and prospects of advanced oxidation water treatment processes using catalytic nanomaterials. Nature Nanotechnology 13(8), 642-650.

Honda, M., Kodera, T. and Kita, H. (1983) On the electrochemical behavior of H2O2 AT Ag in alkaline solution. Electrochimica Acta 28(5), 727-733.

Hu, J., Wang, S., Yu, J., Nie, W., Sun, J. and Wang, S. (2021) Duet Fe3C and FeNx Sites for H2O2 Generation and Activation toward Enhanced Electro-Fenton Performance in Wastewater Treatment. Environmental Science & Technology 55(2), 1260-1269.

Huang, H.-H., Lu, M.-C. and Chen, J.-N. (2001) Catalytic Decomposition of Hydrogen Peroxide and 2-chlorophenol with iron oxides. Water Research 35(9), 2291-2299.

Huang, J., Wang, Z., Zhang, J., Zhang, X., Ma, J. and Wu, Z. (2015) A novel composite conductive microfiltration membrane and its anti-fouling performance with an external electric field in membrane bioreactors. Scientific reports 5(1), 9268.

Hug, S.J. and Leupin, O. (2003) Iron-Catalyzed Oxidation of Arsenic(III) by Oxygen and by Hydrogen Peroxide: pH-Dependent Formation of Oxidants in the Fenton Reaction. Environmental Science & Technology 37(12), 2734-2742.

Huie, R.E. and Clifton, C.L. (1990) Temperature dependence of the rate constants for reactions of the sulfate radical, SO4-, with anions. Journal of Physical Chemistry 94(23), 8561-8567.

Huling, S.G., Arnold, R.G., Sierka, R.A. and Miller, M.R. (1998) Measurement of Hydroxyl Radical Activity in a Soil Slurry Using the Spin Trap α-(4-Pyridyl-1-oxide)- N-tert-butylnitrone. Environmental Science & Technology 32(21), 3436-3441.

Hunt, W.F., Traver, R.G., Davis, A.P., Emerson, C.H., Collins, K.A. and Stagge, J.H. (2010) Low impact development practices: designing to infiltrate in urban environments. Effects of urbanization on groundwater: an engineering case-based approach for sustainable development, 308-343.

Ianni, J.C. (2003) Computational fluid and solid mechanics 2003, pp. 1368-1372, Elsevier.

Ike, I.A., Karanfil, T., Cho, J. and Hur, J. (2019) Oxidation byproducts from the degradation of dissolved organic matter by advanced oxidation processes – A critical review. Water Research 164, 114929.

Iwasaki, T., Masuda, Y., Ogihara, H. and Yamanaka, I. (2018) Direct Synthesis of Pure H2O2 Aqueous Solution by CoTPP/Ketjen-Black Electrocatalyst and the Fuel Cell Reactor. Electrocatalysis 9(2), 236-242.

Jacobsen, F., Holcman, J. and Sehested, K. (1998) Reactions of the ferryl ion with some compounds found in cloud water. International Journal of Chemical Kinetics 30(3), 215-221.

Jasper, J.T., Jones, Z.L., Sharp, J.O. and Sedlak, D.L. (2014) Biotransformation of Trace Organic Contaminants in Open-Water Unit Process Treatment Wetlands. Environmental Science & Technology 48(9), 5136-5144.

Jasper, J.T. and Sedlak, D.L. (2013) Phototransformation of Wastewater-Derived Trace Organic Contaminants in Open-Water Unit Process Treatment Wetlands. Environmental Science & Technology 47(19), 10781-10790.

Jayson, G., Parsons, B. and Swallow, A.J. (1973) Some simple, highly reactive, inorganic chlorine derivatives in aqueous solution. Their formation using pulses of radiation and their role in the mechanism of the Fricke dosimeter. Journal of the Chemical Society, Faraday Transactions 1: Physical Chemistry in Condensed Phases 69, 1597-1607.

Jiang, W.-L., Xia, X., Han, J.-L., Ding, Y.-C., Haider, M.R. and Wang, A.-J. (2018a) Graphene Modified Electro-Fenton Catalytic Membrane for in Situ Degradation of Antibiotic Florfenicol. Environmental Science & Technology 52(17), 9972-9982.

Jiang, Y., Ni, P., Chen, C., Lu, Y., Yang, P., Kong, B., Fisher, A. and Wang, X. (2018b) Selective Electrochemical H2O2 Production through Two‐Electron Oxygen Electrochemistry. Advanced Energy Materials 8(31), 1801909.

Jirkovský, J., Faure, V. and Boule, P. (1997) Photolysis of Diuron. Pesticide Science 50(1), 42-52.

Jurgens, B.C., Burow, K.R., Dalgish, B.A. and Shelton, J.L. (2008) Hydrogeology, water chemistry, and factors affecting the transport of contaminants in the zone of contribution of a public-supply well in Modesto, eastern San Joaquin Valley, California, U. S. Geological Survey.

Kabir, M.I., Daly, E. and Maggi, F. (2014) A review of ion and metal pollutants in urban green water infrastructures. Science of The Total Environment 470-471, 695-706.

Kah, M., Oliver, D. and Kookana, R. (2021) Sequestration and potential release of PFAS from spent engineered sorbents. Science of The Total Environment 765, 142770.

Kakarla, P.K. and Watts, R.J. (1997) Depth of Fenton-like oxidation in remediation of surface soil. Journal of environmental engineering 123(1), 11-17.

Kanakaraju, D., Glass, B.D. and Oelgemöller, M. (2018) Advanced oxidation process-mediated removal of pharmaceuticals from water: A review. Journal of Environmental Management 219, 189-207.

Kanel, S.R., Neppolian, B., Jung, H. and Choi, H. (2004) Comparative removal of polycyclic aromatic hydrocarbons using iron oxide and hydrogen peroxide in soil slurries. Environmental Engineering Science 21(6), 741-751.

Kapałka, A., Fóti, G. and Comninellis, C. (2009) The importance of electrode material in environmental electrochemistry: Formation and reactivity of free hydroxyl radicals on boron-doped diamond electrodes. Electrochimica Acta 54(7), 2018-2023.

Katsoyiannis, I.A., Canonica, S. and von Gunten, U. (2011) Efficiency and energy requirements for the transformation of organic micropollutants by ozone, O3/H2O2 and UV/H2O2. Water Research 45(13), 3811-3822.

Keenan, C.R. and Sedlak, D.L. (2008) Factors affecting the yield of oxidants from the reaction of nanoparticulate zero-valent iron and oxygen. Environmental Science & Technology 42(4), 1262-1267.

Kerkez, B., Gruden, C., Lewis, M., Montestruque, L., Quigley, M., Wong, B., Bedig, A., Kertesz, R., Braun, T., Cadwalader, O., Poresky, A. and Pak, C. (2016) Smarter Stormwater Systems. Environmental Science & Technology 50(14), 7267-7273.

Kim, H.-H., Lee, H., Lee, D., Ko, Y.-J., Woo, H., Lee, J., Lee, C. and Pham, A.L.-T. (2020) Activation of Hydrogen Peroxide by a Titanium Oxide-Supported Iron Catalyst: Evidence for Surface Fe(IV) and Its Selectivity. Environmental Science & Technology 54(23), 15424-15432.

Kim, H.W., Ross, M.B., Kornienko, N., Zhang, L., Guo, J., Yang, P. and McCloskey, B.D. (2018) Efficient hydrogen peroxide generation using reduced graphene oxide-based oxygen reduction electrocatalysts. Nature Catalysis 1(4), 282-290.

Kim, J., Park, K., Yang, D.R. and Hong, S. (2019) A comprehensive review of energy consumption of seawater reverse osmosis desalination plants. Applied Energy 254, 113652.

King, D.W. and Farlow, R. (2000) Role of carbonate speciation on the oxidation of Fe(II) by H2O2. Marine Chemistry 70(1), 201-209.

King, J.F., Szczuka, A., Zhang, Z. and Mitch, W.A. (2020) Efficacy of ozone for removal of pesticides, metals and indicator virus from reverse osmosis concentrates generated during potable reuse of municipal wastewaters. Water Research 176, 115744.

Ko, K.B., Lee, J.Y., Yoon, Y.H., Moon, T.H., Ahn, Y.H., Park, C.G., Min, K.S. and Park, J.H. (2009) Effects of nitrate on the UV photolysis of H2O2 for 2,4-dichlorophenol degradation in treated effluents. Desalination and Water Treatment 2(1-3), 6-11.

Kopinke, F.-D. (2020) Comment to the article "Hydroxyl radical scavenging by solid mineral surfaces in oxidative treatment systems: Rate constants and implications" published by K. Rusevova Crincoli and S. G. Huling in Water Research 169, 2020, 115240. Water Research 186, 116308.

Koubek, E. (1977) Oxidation of refractory organics in aqueous waste streams by hydrogen peroxide and ultraviolet light, U.S. Patent No. 4,012,321. Washington, DC: U.S. Patent and Trademark Office.

Kozarac, Z., Risovic, D., Frka, S. and Mobius, D. (2005) Reflection of light from the air/water interface covered with sea-surface microlayers. Marine Chemistry 96(1-2), 99-113.

Kwan, W.P. and Voelker, B.M. (2002) Decomposition of Hydrogen Peroxide and Organic Compounds in the Presence of Dissolved Iron and Ferrihydrite. Environmental Science & Technology 36(7), 1467-1476.

Langmuir, D. (1997) Aqueous environmental. Geochemistry Prentice Hall: Upper Saddle River, NJ 600.

Lanzarini-Lopes, M., Garcia-Segura, S., Hristovski, K. and Westerhoff, P. (2017) Electrical energy per order and current efficiency for electrochemical oxidation of p-chlorobenzoic acid with boron-doped diamond anode. Chemosphere 188, 304-311.

Lapworth, D.J., Baran, N., Stuart, M.E. and Ward, R.S. (2012) Emerging organic contaminants in groundwater: A review of sources, fate and occurrence. Environmental Pollution 163, 287-303.

Larsen, T.A., Hoffmann, S., Lüthi, C., Truffer, B. and Maurer, M. (2016) Emerging solutions to the water challenges of an urbanizing world. Science 352(6288), 928-933.

Lee, C. and Sedlak, D.L. (2009) A novel homogeneous Fenton-like system with Fe(III)–phosphotungstate for oxidation of organic compounds at neutral pH values. Journal of Molecular Catalysis A: Chemical 311(1), 1-6.

Lee, E., Shon, H.K. and Cho, J. (2014) Role of wetland organic matters as photosensitizer for degradation of micropollutants and metabolites. Journal of Hazardous Materials 276, 1-9.

Leigh, N.G. and Lee, H. (2019) Sustainable and Resilient Urban Water Systems: The Role of Decentralization and Planning. Sustainability 11(3), 918.

Lhotský, O., Krákorová, E., Mašín, P., Žebrák, R., Linhartová, L., Křesinová, Z., Kašlík, J., Steinová, J., Rødsand, T., Filipová, A., Petrů, K., Kroupová, K. and Cajthaml, T. (2017) Pharmaceuticals, benzene, toluene and chlorobenzene removal from contaminated groundwater by combined UV/H2O2 photo-oxidation and aeration. Water Research 120, 245-255.

Li, H., Wen, P., Itanze, D.S., Hood, Z.D., Adhikari, S., Lu, C., Ma, X., Dun, C., Jiang, L., Carroll, D.L., Qiu, Y. and Geyer, S.M. (2020) Scalable neutral H2O2 electrosynthesis by platinum diphosphide nanocrystals by regulating oxygen reduction reaction pathways. Nature Communications 11(1), 3928.

Li, L. (2000) The advances and characteristics of high-power diode laser materials processing. Optics and Lasers in Engineering 34(4), 231-253.

Li, W., Bonakdarpour, A., Gyenge, E. and Wilkinson, D.P. (2013) Drinking Water Purification by Electrosynthesis of Hydrogen Peroxide in a Power-Producing PEM Fuel Cell. ChemSusChem 6(11), 2137-2143.

Li, W., Shen, Z., Tian, T., Liu, R. and Qiu, J. (2012) Temporal variation of heavy metal pollution in urban stormwater runoff. Frontiers of Environmental Science & Engineering 6(5), 692-700.

Li, Y., Miller, C.J., Wu, L. and Waite, T.D. (2022) Hydroxyl Radical Production via a Reaction of Electrochemically Generated Hydrogen Peroxide and Atomic Hydrogen: An Effective Process for Contaminant Oxidation? Environmental Science & Technology 56(9), 5820-5829.

Liang, J., Wang, Y., Liu, Q., Luo, Y., Li, T., Zhao, H., Lu, S., Zhang, F., Asiri, A.M., Liu, F., Ma, D. and Sun, X. (2021) Electrocatalytic hydrogen peroxide production in acidic media enabled by NiS2 nanosheets. Journal of Materials Chemistry A 9(10), 6117-6122.

Lim, J.S., Kim, J.H., Woo, J., Baek, D.S., Ihm, K., Shin, T.J., Sa, Y.J. and Joo, S.H. (2021) Designing highly active nanoporous carbon H2O2 production electrocatalysts through active site identification. Chem 7(11), 3114-3130.

Lin, S.-S. and Gurol, M.D. (1998) Catalytic Decomposition of Hydrogen Peroxide on Iron Oxide: Kinetics, Mechanism, and Implications. Environmental Science & Technology 32(10), 1417-1423.

Lindemann, J. (1999) Evaluation of Urban Runoff Infiltration and Impact to Groundwater Quality in Park Ridge, Wisconsin, Master's Thesis, College of Natural Resources, University of Wisconsin Stevens Point, Wisconsin.

Linden, K.G., Hull, N. and Speight, V. (2019) Thinking Outside the Treatment Plant: UV for Water Distribution System Disinfection. Accounts of Chemical Research 52(5), 1226-1233.

Liu, F., Liu, Y., Yao, Q., Wang, Y., Fang, X., Shen, C., Li, F., Huang, M., Wang, Z., Sand, W. and Xie, J. (2020) Supported Atomically-Precise Gold Nanoclusters for Enhanced Flow-through Electro-Fenton. Environmental Science & Technology 54(9), 5913-5921.

Liu, K., Yu, J.C.-C., Dong, H., Wu, J.C.S. and Hoffmann, M.R. (2018a) Degradation and Mineralization of Carbamazepine Using an Electro-Fenton Reaction Catalyzed by Magnetite Nanoparticles Fixed on an Electrocatalytic Carbon Fiber Textile Cathode. Environmental Science & Technology 52(21), 12667-12674.

Liu, X., Whitacre, J.F. and Mauter, M.S. (2018b) Mechanisms of Humic Acid Fouling on Capacitive and Insertion Electrodes for Electrochemical Desalination. Environmental Science & Technology 52(21), 12633-12641.

Lu, H.-F., Chen, H.-F., Kao, C.-L., Chao, I. and Chen, H.-Y. (2018) A computational study of the Fenton reaction in different pH ranges. Physical Chemistry Chemical Physics 20(35), 22890-22901.

Lu, X., Zhu, C., Wu, Z., Xuan, J., Francisco, J.S. and Wang, H. (2020) In Situ Observation of the pH Gradient near the Gas Diffusion Electrode of CO2 Reduction in Alkaline Electrolyte. Journal of the American Chemical Society 142(36), 15438-15444.

Luo, H., Li, C., Wu, C. and Dong, X. (2015) In situ electrosynthesis of hydrogen peroxide with an improved gas diffusion cathode by rolling carbon black and PTFE. RSC Advances 5(80), 65227-65235.

Luo, Y., Guo, W., Ngo, H.H., Nghiem, L.D., Hai, F.I., Zhang, J., Liang, S. and Wang, X.C. (2014) A review on the occurrence of micropollutants in the aquatic environment and their fate and removal during wastewater treatment. Science of The Total Environment 473-474, 619-641.

Luthy, R.G., Sharvelle, S. and Dillon, P. (2019) Urban Stormwater to Enhance Water Supply. Environmental Science & Technology 53(10), 5534-5542.

Ma, P., Ma, H., Galia, A., Sabatino, S. and Scialdone, O. (2019) Reduction of oxygen to H2O2 at carbon felt cathode in undivided cells. Effect of the ratio between the anode and the cathode surfaces and of other operative parameters. Separation and Purification Technology 208, 116-122.

Ma, P., Ma, H., Sabatino, S., Galia, A. and Scialdone, O. (2018) Electrochemical treatment of real wastewater. Part 1: Effluents with low conductivity. Chemical Engineering Journal 336, 133-140.

Mandal, P.C., Bardhan, D.K., Sarkar, S. and Bhattacharyya, S.N. (1991) Oxidation of nickel (II) ethylenediaminetetraacetate by carbonate radical. Journal of the Chemical Society, Dalton Transactions (6), 1457-1461.

Marin, M.L., Lhiaubet-Vallet, V., Santos-Juanes, L., Soler, J., Gomis, J., Arques, A., Amat, A.M. and Miranda, M.A. (2011) A photophysical approach to investigate the photooxidation mechanism of pesticides: Hydroxyl radical versus electron transfer. Applied Catalysis B: Environmental 103(1), 48-53.

Masson-Delmotte, V., Zhai, P., Pirani, A., Connors, S.L., Péan, C., Berger, S., Caud, N., Chen, Y., Goldfarb, L. and Gomis, M. (2021) Climate change 2021: the physical science basis. Contribution of working group I to the sixth assessment report of the intergovernmental panel on climate change, 2.

Mazellier, P., Leroy, E., De Laat, J. and Legube, B. (2003) Degradation of carbendazim by UV/H 2 O 2 investigated by kinetic modelling. Environmental Chemistry Letters 1(1), 68-72.

Mazellier, P., Leroy, É. and Legube, B. (2002) Photochemical behavior of the fungicide carbendazim in dilute aqueous solution. Journal of Photochemistry and Photobiology A: Chemistry 153(1), 221-227.

McElroy, A.C., Hyman, M.R. and Knappe, D.R.U. (2019) 1,4-Dioxane in drinking water: emerging for 40 years and still unregulated. Current Opinion in Environmental Science & Health 7, 117-125.

McKee, D. (1969) Catalytic decomposition of hydrogen peroxide by metals and alloys of the platinum group. Journal of Catalysis 14(4), 355-364.

Mikkonen, A., Yläranta, K., Tiirola, M., Dutra, L.A.L., Salmi, P., Romantschuk, M., Copley, S., Ikäheimo, J. and Sinkkonen, A. (2018) Successful aerobic bioremediation of groundwater contaminated with higher chlorinated phenols by indigenous degrader bacteria. Water Research 138, 118-128.

Miklos, D.B., Remy, C., Jekel, M., Linden, K.G., Drewes, J.E. and Hubner, U. (2018) Evaluation of advanced oxidation processes for water and wastewater treatment - A critical review. Water Research 139, 118-131.

Miller, C.M. and Valentine, R.L. (1995) Hydrogen peroxide decomposition and quinoline degradation in the presence of aquifer material. Water Research 29(10), 2353-2359.

Minnesota Stormwater Steering Committee (2005) The Minnesota stormwater manual, Minnesota Pollution Control Agency.

Moreira, F.C., Boaventura, R.A., Brillas, E. and Vilar, V.J. (2017) Electrochemical advanced oxidation processes: a review on their application to synthetic and real wastewaters. Applied Catalysis B: Environmental 202, 217-261.

Morgan, M.S., Van Trieste, P.F., Garlick, S.M., Mahon, M.J. and Smith, A.L. (1988) Ultraviolet molar absorptivities of aqueous hydrogen peroxide and hydroperoxyl ion. Analytica chimica acta 215, 325-329.

Mossad, M. and Zou, L. (2013) Study of fouling and scaling in capacitive deionisation by using dissolved organic and inorganic salts. Journal of Hazardous Materials 244, 387-393.

Mousset, E. and Doudrick, K. (2020) A review of electrochemical reduction processes to treat oxidized contaminants in water. Current Opinion in Electrochemistry 22, 221-227.

Mousset, E., Loh, W.H., Lim, W.S., Jarry, L., Wang, Z. and Lefebvre, O. (2021) Cost comparison of advanced oxidation processes for wastewater treatment using accumulated oxygen-equivalent criteria. Water Research 200, 117234.

Mullapudi, A., Wong, B.P. and Kerkez, B. (2017) Emerging investigators series: building a theory for smart stormwater systems. Environmental Science: Water Research & Technology 3(1), 66-77.

Müller, J. (1998) Comparison of combined oxidation processes in a lab-scale continuous-flow plant, Dissertation. TU Berlin, Berlin.

Nagayama, M.-i. and Cohen, M. (1962) The Anodic Oxidation of Iron in a Neutral Solution. Journal of The Electrochemical Society 109(9), 781.

National Academies of Sciences, Engineering and Medicine (2019) Environmental Engineering for the 21st Century: Addressing Grand Challenges, The National Academies Press, Washington, DC.

Netto, L.E., Chae, H.Z., Kang, S.-W., Rhee, S.G. and Stadtman, E.R. (1996) Removal of hydrogen peroxide by thiol-specific antioxidant enzyme (TSA) is involved with its antioxidant properties TSA possesses thiol peroxidase activity. Journal of Biological Chemistry 271(26), 15315-15321.

Nick, K., Schöler, H., Mark, G., Söylemez, T., Akhlaq, M., Schuchmann, H. and Von Sonntag, C. (1992) Degradation of some triazine herbicides by UV radiation such as used in the UV disinfection of drinking water. Aqua- Journal of Water Supply: Research and Technology 41(2), 82-87.

Nicoll, W. and Smith, A. (1955) Stability of dilute alkaline solutions of hydrogen peroxide. Industrial & Engineering Chemistry 47(12), 2548-2554.

Nidheesh, P.V., Couras, C., Karim, A.V. and Nadais, H. (2022) A review of integrated advanced oxidation processes and biological processes for organic pollutant removal. Chemical Engineering Communications 209(3), 390-432.

Nidheesh, P.V., Zhou, M. and Oturan, M.A. (2018) An overview on the removal of synthetic dyes from water by electrochemical advanced oxidation processes. Chemosphere 197, 210-227.

Okanishi, T., Katayama, Y., Ito, R., Muroyama, H., Matsui, T. and Eguchi, K. (2016) Electrochemical oxidation of 2-propanol over platinum and palladium electrodes in alkaline media studied by in situ attenuated total reflection infrared spectroscopy. Physical Chemistry Chemical Physics 18(15), 10109-10115.

Olasehinde, E.F., Hasan, N., Omogbehin, S.A., Kondo, H. and Sakugawa, H. (2013) Hydroxyl radical mediated degradation of diuron in river water. The Journal of American Science 9(4), 29-34.

Oloman, C. and Watkinson, A. (1979) Hydrogen peroxide production in trickle-bed electrochemical reactors. Journal of applied electrochemistry 9(1), 117-123.

Onstein, P., Stefan, M.I. and Bolton, J.R. (1999) Competition Kinetics Method for the Determination of Rate Constants for the Reaction of Hydroxyl Radicals with Organic Pollutants Using the UV/H~ 2O~ 2 Advanced Oxidation Technology: The Rate Constants for the tert-Butyl Formate Ester and 2, 4-Dinitrophenol. Journal of Advanced Oxidation Technologies 4, 231-236.

Ortiz-Marin, A.D., Amabilis-Sosa, L.E., Bandala, E.R., Guillén-Garcés, R.A., Treviño-Quintanilla, L.G., Roé-Sosa, A. and Moeller-Chávez, G.E. (2020) Using sequentially coupled UV/H2O2-biologic systems to treat industrial wastewater with high carbon and nitrogen contents. Process Safety and Environmental Protection 137, 192-199.

Panizza, M. and Cerisola, G. (2008) Electrochemical generation of H2O2 in low ionic strength media on gas diffusion cathode fed with air. Electrochimica Acta 54(2), 876-878.

Park, S., Lee, H., Shin, S.-H., Kim, N., Shin, D. and Bae, B. (2018) Increasing the Durability of Polymer Electrolyte Membranes Using Organic Additives. ACS Omega 3(9), 11262-11269.

Pastor, E., Arévalo, M.C., González, S. and Arvia, A.J. (1991) The electroformation and the anodic stripping characteristics of adsorbed residues formed on platinum electrodes from acid solutions containing different alcohols. Electrochimica Acta 36(13), 2003-2013.

Pastor, E., Schmidt, V.M., Iwasita, T., Arévalo, M.C., González, S. and Arvia, A.J. (1993a) The reactivity of primary C3-alcohols on gold electrodes in acid media. A comparative study based on dems data. Electrochimica Acta 38(10), 1337-1344.

Pastor, E., Wasmus, S., Iwasita, T., Arévalo, M.C., González, S. and Arvia, A.J. (1993b) DEMS and in-situ FTIR investigations of C3 primary alcohols on platinum electrodes in acid solutions.: Part II. Allyl alcohol. Journal of Electroanalytical Chemistry 353(1), 81-100.

Patra, S. and Munichandraiah, N. (2009) Electrochemical reduction of hydrogen peroxide on stainless steel. Journal of Chemical Sciences 121(5), 675.

Peller, J.R., Mezyk, S.P. and Cooper, W.J. (2009) Bisphenol A reactions with hydroxyl radicals: diverse pathways determined between deionized water and tertiary treated wastewater solutions. Research on Chemical Intermediates 35(1), 21-34.

Peng, Q., Zhao, H., Qian, L., Wang, Y. and Zhao, G. (2015) Design of a neutral photo-electro-Fenton system with 3D-ordered macroporous Fe2O3/carbon aerogel cathode: high activity and low energy consumption. Applied Catalysis B: Environmental 174, 157-166.

Pereira, V.J., Linden, K.G. and Weinberg, H.S. (2007a) Evaluation of UV irradiation for photolytic and oxidative degradation of pharmaceutical compounds in water. Water Research 41(19), 4413-4423.

Pereira, V.J., Weinberg, H.S., Linden, K.G. and Singer, P.C. (2007b) UV Degradation Kinetics and Modeling of Pharmaceutical Compounds in Laboratory Grade and Surface Water via Direct and Indirect Photolysis at 254 nm. Environmental Science & Technology 41(5), 1682-1688.

Pérez, J.F., Galia, A., Rodrigo, M.A., Llanos, J., Sabatino, S., Sáez, C., Schiavo, B. and Scialdone, O. (2017) Effect of pressure on the electrochemical generation of hydrogen peroxide in undivided cells on carbon felt electrodes. Electrochimica Acta 248, 169-177.

Peter-Varbanets, M., Zurbrügg, C., Swartz, C. and Pronk, W. (2009) Decentralized systems for potable water and the potential of membrane technology. Water Research 43(2), 245-265.

Petigara, B.R., Blough, N.V. and Mignerey, A.C. (2002) Mechanisms of Hydrogen Peroxide Decomposition in Soils. Environmental Science & Technology 36(4), 639-645.

Pham, A.L.-T., Doyle, F.M. and Sedlak, D.L. (2012a) Kinetics and efficiency of H2O2 activation by iron-containing minerals and aquifer materials. Water Research 46(19), 6454-6462.

Pham, A.L.-T., Lee, C., Doyle, F.M. and Sedlak, D.L. (2009) A Silica-Supported Iron Oxide Catalyst Capable of Activating Hydrogen Peroxide at Neutral pH Values. Environmental Science & Technology 43(23), 8930-8935.

Pham, A.L.-T., Sedlak, D.L. and Doyle, F.M. (2012b) Dissolution of mesoporous silica supports in aqueous solutions: Implications for mesoporous silica-based water treatment processes. Applied Catalysis B: Environmental 126, 258-264.

Pignatello, J.J., Liu, D. and Huston, P. (1999) Evidence for an additional oxidant in the photoassisted Fenton reaction. Environmental Science & Technology 33(11), 1832-1839.

Pignatello, J.J., Oliveros, E. and MacKay, A. (2006) Advanced Oxidation Processes for Organic Contaminant Destruction Based on the Fenton Reaction and Related Chemistry. Critical Reviews in Environmental Science and Technology 36(1), 1-84.

Pisarenko, A.N., Stanford, B.D., Yan, D., Gerrity, D. and Snyder, S.A. (2012) Effects of ozone and ozone/peroxide on trace organic contaminants and NDMA in drinking water and water reuse applications. Water Research 46(2), 316-326.

Prince George's County, Maryland (1999) Low-Impact Development Design Strategies An Integrated Design Approach Low-Impact Development: An Integrated Design Approach. Department of Environmental Resources: Largo, MD, USA.

Qin, X., Zhao, K., Quan, X., Cao, P., Chen, S. and Yu, H. (2021) Highly efficient metal-free electro-Fenton degradation of organic contaminants on a bifunctional catalyst. Journal of Hazardous Materials 416, 125859.

Qiu, S., Wang, Y., Wan, J., Ma, Y., Yan, Z. and Yang, S. (2021) Enhanced electro-Fenton catalytic performance with in-situ grown Ce/Fe@NPC-GF as self-standing cathode: Fabrication, influence factors and mechanism. Chemosphere 273, 130269.

Qu, C. and Liang, D.-w. (2022) Novel electrochemical advanced oxidation processes with H2O2 generation cathode for water treatment: A review. Journal of Environmental Chemical Engineering 10(3), 107896.

Radjenovic, J. and Sedlak, D.L. (2015) Challenges and Opportunities for Electrochemical Processes as Next-Generation Technologies for the Treatment of Contaminated Water. Environmental Science & Technology 49(19), 11292-11302.

Ray, J.R., Shabtai, I.A., Teixidó, M., Mishael, Y.G. and Sedlak, D.L. (2019) Polymer-clay composite geomedia for sorptive removal of trace organic compounds and metals in urban stormwater. Water Research 157, 454-462.

Regnery, J., Gerba, C.P., Dickenson, E.R.V. and Drewes, J.E. (2017) The importance of key attenuation factors for microbial and chemical contaminants during managed aquifer recharge: A review. Critical Reviews in Environmental Science and Technology 47(15), 1409-1452.

Rippy, M.A., Deletic, A., Black, J., Aryal, R., Lampard, J.-L., Tang, J.Y.-M., McCarthy, D., Kolotelo, P., Sidhu, J. and Gernjak, W. (2017) Pesticide occurrence and spatio-temporal variability in urban run-off across Australia. Water Research 115, 245-255.

Ritchie, H. and Roser, M. (2021) Clean water and sanitation. Our World in Data.

Romero, A., Santos, A., Vicente, F., Rodriguez, S. and Lafuente, A.L. (2009) In situ oxidation remediation technologies: kinetic of hydrogen peroxide decomposition on soil organic matter. Journal of Hazardous Materials 170(2-3), 627-632.

Rose, A.L. and Waite, T.D. (2003) Predicting iron speciation in coastal waters from the kinetics of sunlight-mediated iron redox cycling. Aquatic Sciences 65(4), 375-383.

Rozas, O., Vidal, C., Baeza, C., Jardim, W.F., Rossner, A. and Mansilla, H.D. (2016) Organic micropollutants (OMPs) in natural waters: Oxidation by UV/H2O2 treatment and toxicity assessment. Water Research 98, 109-118.

Rudd, N.C., Cannan, S., Bitziou, E., Ciani, I., Whitworth, A.L. and Unwin, P.R. (2005) Fluorescence Confocal Laser Scanning Microscopy as a Probe of pH Gradients in Electrode Reactions and Surface Activity. Analytical Chemistry 77(19), 6205-6217.

Rusevova Crincoli, K. and Huling, S.G. (2020) Hydroxyl radical scavenging by solid mineral surfaces in oxidative treatment systems: Rate constants and implications. Water Research 169, 115240.

Rush, J.D. and Koppenol, W.H. (1986) Oxidizing intermediates in the reaction of ferrous EDTA with hydrogen peroxide. Reactions with organic molecules and ferrocytochrome c. Journal of Biological Chemistry 261(15), 6730-6733.

Sa, Y.J., Kim, J.H. and Joo, S.H. (2019) Active Edge-Site-Rich Carbon Nanocatalysts with Enhanced Electron Transfer for Efficient Electrochemical Hydrogen Peroxide Production. Angewandte Chemie International Edition 58(4), 1100-1105.

Safarzadeh-Amiri, A. (2001) O3/H2O2 treatment of methyl-tert-butyl ether (MTBE) in contaminated waters. Water Research 35(15), 3706-3714.

Sanches, S., Barreto Crespo, M.T. and Pereira, V.J. (2010) Drinking water treatment of priority pesticides using low pressure UV photolysis and advanced oxidation processes. Water Research 44(6), 1809-1818.

Schwarzenbach, R.P., Gschwend, P.M. and Imboden, D.M. (2016) Environmental organic chemistry, John Wiley & Sons.

Sedlak, D., Mauter, M., Macknick, J., Stokes-Draut, J., Fiske, P., Agarwal, D., Borch, T., Breckenridge, R., Cath, T. and Chellam, S. (2021) National Alliance for Water Innovation (NAWI) Master Technology Roadmap, National Renewable Energy Lab.(NREL), Golden, CO (United States).

Sehested, K., Rasmussen, O.L. and Fricke, H. (1968) Rate constants of OH with HO2, O2-, and H2O2+ from hydrogen peroxide formation in pulse-irradiated oxygenated water. The Journal of Physical Chemistry 72(2), 626-631.

Semitsoglou-Tsiapou, S., Templeton, M.R., Graham, N.J.D., Hernández Leal, L., Martijn, B.J., Royce, A. and Kruithof, J.C. (2016) Low pressure UV/H2O2 treatment for the degradation of the pesticides metaldehyde, clopyralid and mecoprop – Kinetics and reaction product formation. Water Research 91, 285-294.

Seo, J., Lee, H.-J., Lee, H., Kim, H.-E., Lee, J.-Y., Kim, H.S. and Lee, C. (2015) Enhanced production of reactive oxidants by Fenton-like reactions in the presence of carbon materials. Chemical Engineering Journal 273, 502-508.

Shemer, H. and Linden, K.G. (2006) Degradation and by-product formation of diazinon in water during UV and UV/H2O2 treatment. Journal of Hazardous Materials 136(3), 553-559.

Shen, X., Xiao, F., Zhao, H., Chen, Y., Fang, C., Xiao, R., Chu, W. and Zhao, G. (2020) In Situ-Formed PdFe Nanoalloy and Carbon Defects in Cathode for Synergic Reduction–

Oxidation of Chlorinated Pollutants in Electro-Fenton Process. Environmental Science & Technology 54(7), 4564-4572.

Sheng, H., Hermes, E.D., Yang, X., Ying, D., Janes, A.N., Li, W., Schmidt, J.R. and Jin, S. (2019) Electrocatalytic Production of H2O2 by Selective Oxygen Reduction Using Earth-Abundant Cobalt Pyrite (CoS2). ACS Catalysis 9(9), 8433-8442.

Shimabuku, K.K., Kearns, J.P., Martinez, J.E., Mahoney, R.B., Moreno-Vasquez, L. and Summers, R.S. (2016) Biochar sorbents for sulfamethoxazole removal from surface water, stormwater, and wastewater effluent. Water Research 96, 236-245.

Shukun, H., Youqun, S., Jindong, Z. and Jian, S. (2001) Mechanism of Electroreduction of Allyl Alcohol at Platinized Platinum Electrode in Acidic Aqueous Solution. The Journal of Organic Chemistry 66(13), 4487-4493.

Song, W., Ravindran, V. and Pirbazari, M. (2008) Process optimization using a kinetic model for the ultraviolet radiation-hydrogen peroxide decomposition of natural and synthetic organic compounds in groundwater. Chemical Engineering Science 63(12), 3249-3270.

Spahr, S., Teixidó, M., Sedlak, D.L. and Luthy, R.G. (2020) Hydrophilic trace organic contaminants in urban stormwater: occurrence, toxicological relevance, and the need to enhance green stormwater infrastructure. Environmental Science: Water Research & Technology 6(1), 15-44.

Špalek, O., Balej, J. and Paseka, I. (1982) Kinetics of the decomposition of hydrogen peroxide in alkaline solutions. Journal of the Chemical Society, Faraday Transactions 1: Physical Chemistry in Condensed Phases 78(8), 2349-2359.

Stacy, G.L., et al., and R G. Eilers*. (1994) CAV-OX CAVITATION OXIDIATION PROCESS - MAGNUM WATER TECHNOLOGY, INC. - APPLICATIONS ANALYSIS REPORT. EPA/540/AR-93/520 (NTIS PB94-189438).

Stang, C. and Harnisch, F. (2016) The dilemma of supporting electrolytes for electroorganic synthesis: a case study on Kolbe electrolysis. ChemSusChem 9(1), 50-60.

Sun, P., Tyree, C. and Huang, C.-H. (2016) Inactivation of Escherichia coli, Bacteriophage MS2, and Bacillus Spores under UV/H2O2 and UV/Peroxydisulfate Advanced Disinfection Conditions. Environmental Science & Technology 50(8), 4448-4458.

Taha, M., Gupta, B.S., Khoiroh, I. and Lee, M.-J. (2011) Interactions of Biological Buffers with Macromolecules: The Ubiquitous “Smart” Polymer PNIPAM and the Biological Buffers MES, MOPS, and MOPSO. Macromolecules 44(21), 8575-8589.

Tang, Q., Li, B., Ma, W., Gao, H., Zhou, H., Yang, C., Gao, Y. and Wang, D. (2020) Fabrication of a double-layer membrane cathode based on modified carbon nanotubes for the sequential electro-Fenton oxidation of p-nitrophenol. Environmental Science and Pollution Research 27(15), 18773-18783.

Tixier, C., Singer, H.P., Oellers, S. and Müller, S.R. (2003) Occurrence and Fate of Carbamazepine, Clofibric Acid, Diclofenac, Ibuprofen, Ketoprofen, and Naproxen in Surface Waters. Environmental Science & Technology 37(6), 1061-1068.

Toor, R. and Mohseni, M. (2007) UV-H2O2 based AOP and its integration with biological activated carbon treatment for DBP reduction in drinking water. Chemosphere 66(11), 2087-2095.

Torrent Resources MaxWell®IV DRAINAGE SYSTEM Product Information and Design Features. http://www.torrentresources.com/.

Trellu, C., Oturan, N., Keita, F.K., Fourdrin, C., Pechaud, Y. and Oturan, M.A. (2018) Regeneration of Activated Carbon Fiber by the Electro-Fenton Process. Environmental Science & Technology 52(13), 7450-7457.

U.S. Energy Information Administration (2020) Table 5.6.A. Average Price of Electricity to Ultimate Customers by End-Use Sector. URL:https://www.eia.gov/electricity/monthly/epm_table_grapher.php?t=epmt_5_6_a.

U.S. Environmental Protection Agency (2017) Technical Fact Sheet – 1,2,3-Trichloropropane (TCP). Environmental Protection Agency. Available from: https://www.epa.gov/fedfac/technical-fact-sheet-123-trichloropropane-tcp (accessed 23 May 2022).

Ulrich, B.A., Im, E.A., Werner, D. and Higgins, C.P. (2015) Biochar and Activated Carbon for Enhanced Trace Organic Contaminant Retention in Stormwater Infiltration Systems. Environmental Science & Technology 49(10), 6222-6230.

Unicef (2017) Progress on drinking water, sanitation and hygiene.

US Environmental Protection Agency (1992) Method 7196A: Chromium, hexavalent (colorimetric).

USEPA (2022a) National primary drinking water regulations.

USEPA (2022b) Secondary Drinking Water Standards: Guidance for Nuisance Chemicals.

USEPA, J. (2003) Ultraviolet disinfection guidance manual, EPA-815-D-03-007.

Vafaei Molamahmood, H., Geng, W., Wei, Y., Miao, J., Yu, S., Shahi, A., Chen, C. and Long, M. (2022) Catalyzed H2O2 decomposition over iron oxides and oxyhydroxides: Insights from oxygen production and organic degradation. Chemosphere 291, 133037.

Vahid, B. and Khataee, A. (2013) Photoassisted electrochemical recirculation system with boron-doped diamond anode and carbon nanotubes containing cathode for degradation of a model azo dye. Electrochimica Acta 88, 614-620.

Valentine, R.L. and Wang, H.C.A. (1998) Iron Oxide Surface Catalyzed Oxidation of Quinoline by Hydrogen Peroxide. Journal of environmental engineering 124(1), 31-38.

Valim, R.B., Reis, R.M., Castro, P.S., Lima, A.S., Rocha, R.S., Bertotti, M. and Lanza, M.R.V. (2013) Electrogeneration of hydrogen peroxide in gas diffusion electrodes modified with tert-butyl-anthraquinone on carbon black support. Carbon 61, 236-244.

Viollier, E., Inglett, P.W., Hunter, K., Roychoudhury, A.N. and Van Cappellen, P. (2000) The ferrozine method revisited: Fe(II)/Fe(III) determination in natural waters. Applied Geochemistry 15(6), 785-790.

Vogna, D., Marotta, R., Andreozzi, R., Napolitano, A. and d'Ischia, M. (2004) Kinetic and chemical assessment of the UV/H2O2 treatment of antiepileptic drug carbamazepine. Chemosphere 54(4), 497-505.

von Gunten, U. (2018) Oxidation processes in water treatment: are we on track? Environmental Science & Technology 52(9), 5062-5075.

Walling, C. (1975) Fenton's reagent revisited. Accounts of Chemical Research 8(4), 125-131.

Walling, C. and Goosen, A. (1973) Mechanism of the ferric ion catalyzed decomposition of hydrogen peroxide. Effect of organic substrates. Journal of the American Chemical Society 95(9), 2987-2991.

Wang, C., Gu, Y., Wu, S., Yu, H., Chen, S., Su, Y., Guo, Y., Wang, X., Chen, H., Kang, W. and Quan, X. (2020a) Construction of a Microchannel Electrochemical Reactor with a Monolithic Porous-Carbon Cathode for Adsorption and Degradation of Organic Pollutants in Several Minutes of Retention Time. Environmental Science & Technology 54(3), 1920-1928.

Wang, F., van Halem, D. and van der Hoek, J.P. (2016) The fate of H2O2 during managed aquifer recharge: A residual from advanced oxidation processes for drinking water production. Chemosphere 148, 263-269.

Wang, J., Li, S., Qin, Q. and Peng, C. (2021) Sustainable and feasible reagent-free electro-Fenton via sequential dual-cathode electrocatalysis. Proceedings of the National Academy of Sciences 118(34), e2108573118.

Wang, Y., Shi, R., Shang, L., Waterhouse, G.I.N., Zhao, J., Zhang, Q., Gu, L. and Zhang, T. (2020b) High-Efficiency Oxygen Reduction to Hydrogen Peroxide Catalyzed by Nickel Single-Atom Catalysts with Tetradentate N2O2 Coordination in a Three-Phase Flow Cell. Angewandte Chemie International Edition 59(31), 13057-13062.

Watts, M.J., Hofmann, R. and Rcdsenfeldt, E.J. (2012) Low-pressure UV/Cl2 for advanced oxidation of taste and odor. Journal AWWA 104(1), E58-E65.

Watts, R.J., Foget, M.K., Kong, S.-H. and Teel, A.L. (1999) Hydrogen peroxide decomposition in model subsurface systems. Journal of Hazardous Materials 69(2), 229-243.

Weinstein, J. and Bielski, B.H. (1979) Kinetics of the interaction of perhydroxyl and superoxide radicals with hydrogen peroxide. The Haber-Weiss reaction. Journal of the American Chemical Society 101(1), 58-62.

Weishaar, J.L., Aiken, G.R., Bergamaschi, B.A., Fram, M.S., Fujii, R. and Mopper, K. (2003) Evaluation of Specific Ultraviolet Absorbance as an Indicator of the Chemical Composition and Reactivity of Dissolved Organic Carbon. Environmental Science & Technology 37(20), 4702-4708.

Weng, C., Chuang, Y.-H., Davey, B. and Mitch, W.A. (2020) Reductive Electrochemical Activation of Hydrogen Peroxide as an Advanced Oxidation Process for Treatment of Reverse Osmosis Permeate during Potable Reuse. Environmental Science & Technology 54(19), 12593-12601.

Whatcom County, Washington (2021) Stormwater Facilities Inspection and Maintenance Handbook. Whatcom County Public Works Stormwater Division.

Willner, I., Rosen, M. and Eichen, Y. (1991) Characterization of the Hydrogenation Process of Allyl Alcohol at a Pt Electrode Using a Double Galvanostatic Pulse Technique. Journal of The Electrochemical Society 138(2), 434-439.

Wols, B.A. and Hofman-Caris, C.H.M. (2012) Review of photochemical reaction constants of organic micropollutants required for UV advanced oxidation processes in water. Water Research 46(9), 2815-2827.

Wong, C.C. and Chu, W. (2003) The direct photolysis and photocatalytic degradation of alachlor at different TiO2 and UV sources. Chemosphere 50(8), 981-987.

World Bank Group (2017) Populations Estimates and Projections. Available at https://datacatalog.worldbank.org.

World Health Organization (2017) Guidelines for drinking-water quality, 4th edition, incorporating the 1st addendum, ISBN: 978-92-4-154995-0.

Wu, C., Shemer, H. and Linden, K.G. (2007) Photodegradation of Metolachlor Applying UV and UV/H2O2. Journal of Agricultural and Food Chemistry 55(10), 4059-4065.

Wu, J., Cao, M., Tong, D., Finkelstein, Z. and Hoek, E.M.V. (2021a) A critical review of point-of-use drinking water treatment in the United States. npj Clean Water 4(1), 40.

Wu, Z., Yang, L., Tang, Y., Qiang, Z. and Li, M. (2021b) Dimethoate degradation by VUV/UV process: Kinetics, mechanism and economic feasibility. Chemosphere 273, 129724.

Xia, C., Xia, Y., Zhu, P., Fan, L. and Wang, H. (2019) Direct electrosynthesis of pure aqueous H2O2 solutions up to 20% by weight using a solid electrolyte. Science 366(6462), 226-231.

Xie, J., Ma, J., Zhang, C. and Waite, T.D. (2021) Direct electron transfer (DET) processes in a flow anode system–Energy-efficient electrochemical oxidation of phenol. Water Research 203, 117547.

Xie, J., Zhang, C. and Waite, T.D. (2022) Hydroxyl radicals in anodic oxidation systems: generation, identification and quantification. Water Research 217, 118425.

Xue, X., Hanna, K. and Deng, N. (2009) Fenton-like oxidation of Rhodamine B in the presence of two types of iron (II, III) oxide. Journal of Hazardous Materials 166(1), 407-414.

Yamanaka, I., Hashimoto, T., Ichihashi, R. and Otsuka, K. (2008) Direct synthesis of H2O2 acid solutions on carbon cathode prepared from activated carbon and vapor-growing-carbon-fiber by a H2/O2 fuel cell. Electrochimica Acta 53(14), 4824-4832.

Yamanaka, I. and Murayama, T. (2008) Neutral H2O2 Synthesis by Electrolysis of Water and O2. Angewandte Chemie International Edition 47(10), 1900-1902.

Yamanaka, I., Onizawa, T., Suzuki, H., Hanaizumi, N. and Otsuka, K. (2006) Electrocatalysis of heat-treated Mn–porphyrin/carbon cathode for synthesis of H2O2 acid solutions by H2/O2 fuel cell method. Chemistry letters 35(12), 1330-1331.

Yang, W., Zhou, M. and Liang, L. (2018) Highly efficient in-situ metal-free electrochemical advanced oxidation process using graphite felt modified with N-doped graphene. Chemical Engineering Journal 338, 700-708.

Yang, Y. (2020) Recent advances in the electrochemical oxidation water treatment: Spotlight on byproduct control. Frontiers of Environmental Science & Engineering 14(5), 85.

Yang, Y. and Hoffmann, M.R. (2016) Synthesis and Stabilization of Blue-Black TiO2 Nanotube Arrays for Electrochemical Oxidant Generation and Wastewater Treatment. Environmental Science & Technology 50(21), 11888-11894.

Ying, G.-G., Toze, S., Hanna, J., Yu, X.-Y., Dillon, P.J. and Kookana, R.S. (2008) Decay of endocrine-disrupting chemicals in aerobic and anoxic groundwater. Water Research 42(4), 1133-1141.

Yu, Q., Kandegedara, A., Xu, Y. and Rorabacher, D.B. (1997) Avoiding Interferences from Good's Buffers: A Contiguous Series of Noncomplexing Tertiary Amine Buffers Covering the Entire Range of pH 3–11. Analytical Biochemistry 253(1), 50-56.

Zeng, H., Zhang, G., Ji, Q., Liu, H., Hua, X., Xia, H., Sillanpää, M. and Qu, J. (2020) pH-Independent Production of Hydroxyl Radical from Atomic H*-Mediated Electrocatalytic H2O2 Reduction: A Green Fenton Process without Byproducts. Environmental Science & Technology 54(22), 14725-14731.

Zhang, K., Bach, P.M., Mathios, J., Dotto, C.B.S. and Deletic, A. (2020a) Quantifying the benefits of stormwater harvesting for pollution mitigation. Water Research 171, 115395.

Zhang, Q., Zhou, M., Ren, G., Li, Y., Li, Y. and Du, X. (2020b) Highly efficient electrosynthesis of hydrogen peroxide on a superhydrophobic three-phase interface by natural air diffusion. Nature Communications 11(1), 1731.

Zhang, Y., Wang, Y. and Angelidaki, I. (2015) Alternate switching between microbial fuel cell and microbial electrolysis cell operation as a new method to control H2O2 level in Bioelectro-Fenton system. Journal of Power Sources 291, 108-116.

Zhang, Z., Chuang, Y.-H., Huang, N. and Mitch, W.A. (2019) Predicting the Contribution of Chloramines to Contaminant Decay during Ultraviolet/Hydrogen Peroxide Advanced Oxidation Process Treatment for Potable Reuse. Environmental Science & Technology 53(8), 4416-4425.

Zhao, G. and Chasteen, N.D. (2006) Oxidation of Good's buffers by hydrogen peroxide. Analytical Biochemistry 349(2), 262-267.

Zhao, H., Qian, L., Guan, X., Wu, D. and Zhao, G. (2016) Continuous bulk FeCuC aerogel with ultradispersed metal nanoparticles: an efficient 3D heterogeneous electro-Fenton cathode over a wide range of pH 3–9. Environmental Science & Technology 50(10), 5225-5233.

Zhao, H., Wang, Y., Wang, Y., Cao, T. and Zhao, G. (2012) Electro-Fenton oxidation of pesticides with a novel Fe3O4@ Fe2O3/activated carbon aerogel cathode: High activity, wide pH range and catalytic mechanism. Applied Catalysis B: Environmental 125, 120-127.

Zhao, K., Quan, X., Su, Y., Qin, X., Chen, S. and Yu, H. (2021) Enhanced Chlorinated Pollutant Degradation by the Synergistic Effect between Dechlorination and Hydroxyl Radical Oxidation on a Bimetallic Single-Atom Catalyst. Environmental Science & Technology 55(20), 14194-14203.

Zheng, Z., Zhang, K., Toe, C.Y., Amal, R., Zhang, X., McCarthy, D.T. and Deletic, A. (2021) Stormwater herbicides removal with a solar-driven advanced oxidation process: A feasibility investigation. Water Research 190, 116783.

Zhu, X. and Jassby, D. (2019) Electroactive Membranes for Water Treatment: Enhanced Treatment Functionalities, Energy Considerations, and Future Challenges. Accounts of Chemical Research 52(5), 1177-1186.

Zodrow, K.R., Li, Q., Buono, R.M., Chen, W., Daigger, G., Dueñas-Osorio, L., Elimelech, M., Huang, X., Jiang, G., Kim, J.-H., Logan, B.E., Sedlak, D.L., Westerhoff, P. and Alvarez, P.J.J. (2017) Advanced Materials, Technologies, and Complex Systems Analyses: Emerging Opportunities to Enhance Urban Water Security. Environmental Science & Technology 51(18), 10274-10281.

Appendix

A.1 An electrochemical advanced oxidation process for the treatment of urban stormwater

A.1.1 Determination of the photon fluence rate

Photon fluence rates at 254 nm (i.e., the main wavelength of energy for the low-pressure Hg lamp used in the reactor) were determined using 100 µg/L of atrazine ($\mathcal{E}_{254}$ = 3860 M^{-1} cm^{-1}, Φ_{254} = 0.046 mol Ei^{-1}) as a chemical actinometer (Bolton and Linden 2003, Canonica et al. 2008). The photon fluence rates were characterized for all simulated stormwater compositions tested in the AOP experiments ([humic acid] = 0-5 mg-C/L). The simulated stormwater was amended with 5 mM of phosphate buffer to maintain a pH value of 7. The actinometry experiments were conducted in batch mode by circulating the solution between the UV reactor and a solution reservoir as described in Section 2.2.5. The fluence was calculated from the phototransformation rate of atrazine:

$$-\frac{d[C]}{dt} = [\frac{W_\lambda}{Z}\,(1\text{-}10^{-\alpha_\lambda Z})\,\frac{\mathcal{E}_\lambda \Phi_\lambda}{\alpha_\lambda}][C] \tag{A.1}$$

This yields a first-order direct photolysis rate constant, *k*:

$$k = \frac{W_\lambda}{Z}\,(1\text{-}10^{-\alpha_\lambda Z})\,\frac{\mathcal{E}_\lambda \Phi_\lambda}{\alpha_\lambda} \tag{A.2}$$

where: W_λ −Fluence $[\frac{\mathrm{mE_i}}{\mathrm{cm^2 s}}]$
Z−Pathlength [cm]
$\mathcal{E}_\lambda$ −Molar attenuation coefficient $[\mathrm{M^{-1}cm^{-1}}]$
α_λ − Beam attenuation coefficient $[\mathrm{cm^{-1}}] = \sum(\mathcal{E}_\lambda C_i)$
Φ_λ − Quantum yield

The light pathlength was estimated by dividing the water stream cross-sectional area in the reactor (80 cm^2) by the width of the air-water interface (30 cm).

By plotting the natural logarithm of atrazine removal with time (Figure A.1), the observed photolysis rate constants, $k_{observed}$ (Table A.1) were obtained and used to calculate the observed fluence value, $W_{254,\ observed}$ (Table A.2) using:

$$W_\lambda = \frac{kZ\alpha_\lambda}{(1-10^{-\alpha_\lambda Z})\mathcal{E}_\lambda \Phi_\lambda} \tag{A.3}$$

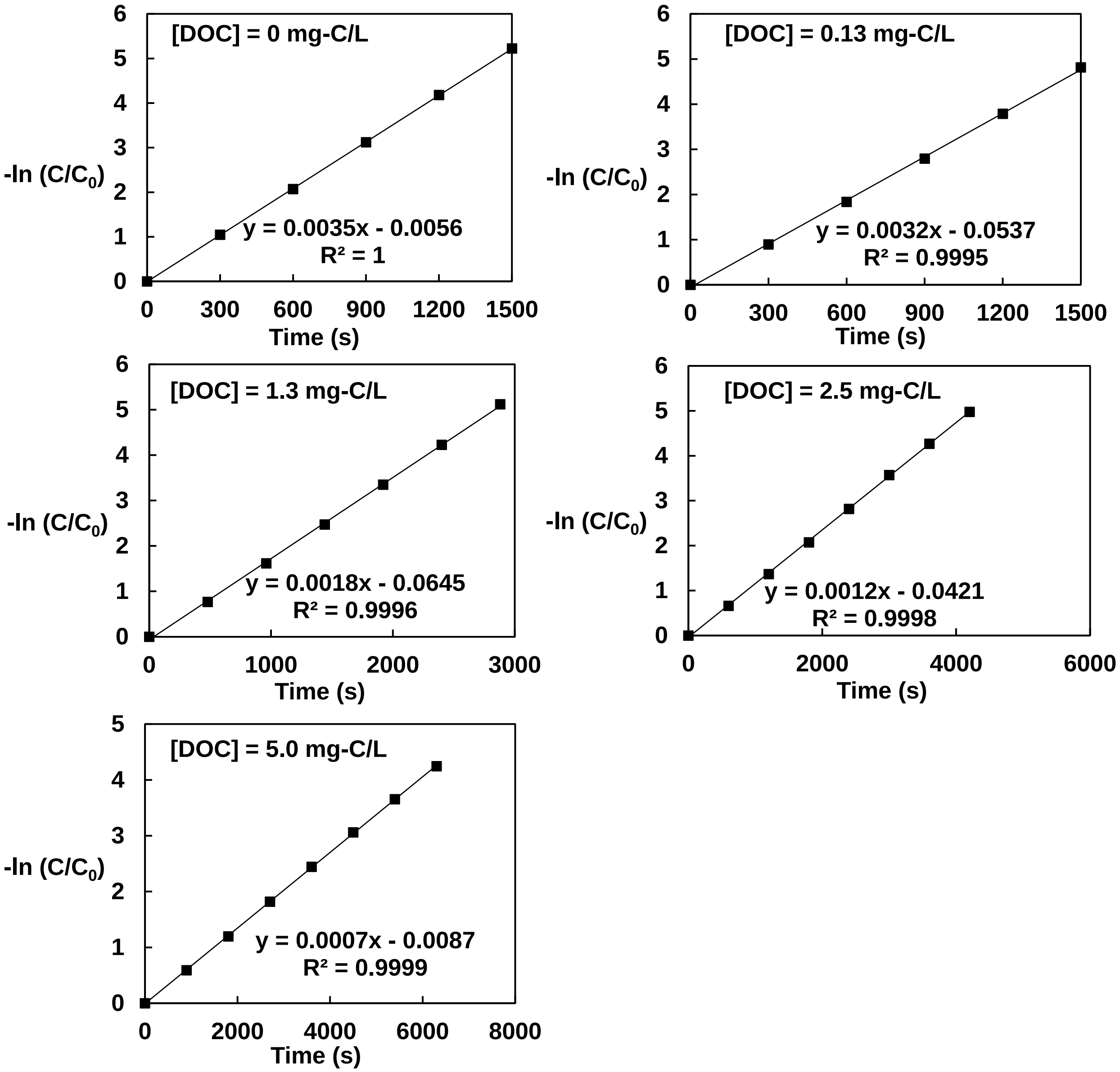

Figure A.1 Natural logarithm of normalized atrazine concentration versus time. $[\text{Atrazine}]_0$ = 100 μg/L in simulated stormwater with 5 mM phosphate buffer (pH = 7) amended with different concentrations of humic acid.

Mass balance was applied to deconvolute the effect of water recirculation on determination of the photolysis rate constants (k_{real}) and photon fluence rates ($W_{254,\ real}$). The solution reservoir was assumed to act as a continuous stirred-tank reactor with no reaction; The UV reactor was simplified as a plug-flow reactor without dispersion.

Within one hydraulic residence time of the UV reactor (HRT_{UV}), the effluent concentration of atrazine was not related to the feed water but depended only on the time of exposure to UV light, which was determined by the reaction time, and the initial atrazine concentration. After one HRT_{UV}, the water fed from the solution reservoir started to flow out of the UV reactor, and water that flowing through the UV reactor was exposed to UV light for one HRT_{UV} of duration. Therefore, the effluent concentration of the UV reactor, C_1, can be expressed as:

$$C_1(t) = \begin{cases} C_0\, exp(-k_{real}t) & t \leq HRT_{UV} \\ C_2(t)\, exp(-k_{real}HRT_{UV}) & t > HRT_{UV} \end{cases} \qquad \text{(A.4)}$$

For the concentration inside the solution reservoir, C:

$$V_1 \frac{dC}{dt} = QC_1 - QC_2 = QC_1 - QC \qquad \text{(A.5)}$$

Initial condition: $C = C_0$

where C_0, C_1, C_2, are initial atrazine concentration, atrazine concentration in the effluent and influent of the UV reactor. V_1 and V_2 are the volume of the solution reservoir and UV reactor, respectively.

The k_{real} value is determined as the value that led to the minimal sum of squared residuals of the C/C_0 values after one HRT_{UV} (Table A.1). The results were plotted in Figure A.2. The $W_{254,\ real}$ was calculated based on eq A.3 (Table A.2).

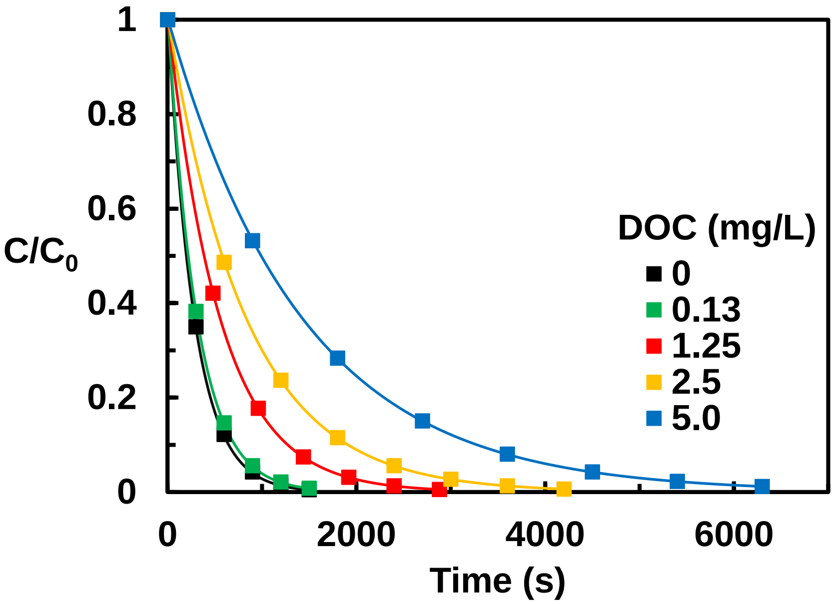

Figure A.2 Graphically determination of k_{real} value from the actinometry experiments. Symbols and lines are assigned to results calculated based on $k_{observed}$ and k_{real}, respectively.

Table A.1 Atrazine photolysis rate constants.

[Humic acid] (mg-C/L)	0	0.13	1.3	2.5	5.0
$k_{observed}$ (s^{-1})	3.5×10^{-3}	3.2×10^{-3}	1.8×10^{-3}	1.2×10^{-3}	7.0×10^{-4}
k_{real} (s^{-1})	7.4×10^{-3}	6.7×10^{-3}	3.7×10^{-3}	2.5×10^{-3}	1.4×10^{-3}

Table A.2 Photon fluence rates for simulated stormwater amended with different concentrations of humic acid (0-5 mg-C/L).

[Humic acid] (mg-C/L)	0	0.13	1.3	2.5	5.0
$W_{254,\ observed}$ (mEi/cm^2/s)	8.6×10^{-6}	8.1×10^{-6}	6.0×10^{-6}	5.3×10^{-6}	4.8×10^{-6}
$W_{254,\ real}$ (mEi/cm^2/s)	1.8×10^{-5}	1.7×10^{-5}	1.2×10^{-5}	1.1×10^{-5}	9.7×10^{-6}

A.2 Factors affecting the yield of hydroxyl radical by electrochemical activation of H_2O_2 on stainless-steel electrodes

A.2.1 Reaction rate constants for $^{\bullet}$OH with organic buffer compounds

Second-order rate constants for the reaction of $^{\bullet}$OH with MES and PIPES were measured using competition kinetics (Onstein et al. 1999). Briefly, individual test compounds (MES or PIPES, 1.0 μM) was irradiated in a customized brown glass bottle ($V_{effective}$ = 600 mL), using a 9 W low-pressure Hg UV-C lamp (arc length = 12.5 cm, Anyray, US). The solutions contained 0.5 μM carbamazepine as a reference compound $k_{\mathrm{carbamazepine},\bullet\mathrm{OH}} = 9.1 \times 10^9\ M^{-1}\ s^{-1}$ (Jasper and Sedlak 2013), along with H_2O_2 as a photosensitizer (10 μM). Carbamazepine was chosen as a reference compound because it exhibits low rate of direct photolysis (Pereira et al. 2007a).

Solution pH was buffered with 100 μM phosphate buffer at 6.0 for the MES experiment and 7.0 for the PIPES experiment, respectively. The pH changed by < 0.2 units through the photolysis experiments. Details of the analytical method and the rate constants determination are described in Section A.2.2 of the appendix. Because the reaction between the test compounds and H_2O_2 are slow (Zhao and Chasteen 2006) and no H_2O_2 consumption was observed when test compounds were added to H_2O_2-contaning solution, the direct oxidation of the test compounds by H_2O_2 was negligible over the time scale of this study.

Control experiments for direct transformation of the test compounds and carbamazepine were conducted under similar experimental conditions in the absence of H_2O_2. The pseudo 1st-order rate constants for direct photolysis of carbamazepine and test compounds in the absence of H_2O_2 were less than 10% of the values observed in the presence of H_2O_2 (Figure A.3). Due to the low molar absorptivity of MES and PIPES (Good et al. 1966, Taha et al. 2011), the contribution of direct photolysis to the overall phototransformation in the presence of H_2O_2 was neglected because the presence of H_2O_2 was expected to further slowdown direct photolysis reactions due to competition for photons. Assuming that losses of the test compounds and carbamazepine were due only to reaction with $^{\bullet}$OH and direct photolysis, the following equation could be used to estimate the rate of reaction of a buffer compound with $^{\bullet}$OH ($k_{\text{Buffer},\bullet\text{OH}}$):

$$ln[\frac{[Compound]_t}{[Compound]_0}] = \frac{k_{Compound,\bullet OH}}{k_{carbamazepine,\bullet OH}} ln[\frac{[Carbamazepine]_t}{[Carbamazepine]_0}] \qquad (A.6)$$

A.2.2 Analytical methods for detection of MES and PIPES

100 µL of methanol and 10 µL of isotopically labeled internal standard was added to 1 mL of (diluted) samples right after sampling to quench any possible $^{\bullet}$OH reactions that could consume buffers and carbamazepine. Additionally, 100 µL of 1 N H_2SO_4 was added to all MES-containing samples to obtain a good chromatography.

MES and carbamazepine were separated using a 150 x 3 mm Synergi™ 4 µm Hydro-RP 80 Å column, eluted with at 0.4 mL min^{-1} methanol and 0.1% acetic acid in water with the following gradient: 0 minutes, 0% methanol; 2 minutes, 0% methanol; 8 minutes, 60% methanol; 11 minutes, 95% methanol; 12 minutes, 95% methanol; 12.1 minutes, 0% methanol; 18 minutes, 0% methanol.

Pipes and carbamazepine were separated using a 4.6 mm X 150 mm Waters™ Symmetry C18 100Å, 3.5 µm column, eluted with at 0.4 mL min^{-1} methanol and 0.1% acetic acid in water with the following gradient: 0 minutes, 10% methanol; 3 minutes, 10% methanol; 11 minutes, 95% methanol; 12 minutes, 95% methanol; 15 minutes, 10% methanol; 23 minutes, 10% methanol.

Buffer compounds and carbamazepine were quantified in multiple reaction monitoring (MRM) mode with an Agilent 1260 series HPLC system coupled to a 6460 triple quadrupole tandem mass spectrometer (HPLC-MS/MS) using electrospray ionization (ESI) with a 7-200 ms dwell time and a gas temperature of 350° C, a gas flow rate of 9 L/min at 45 psi, and a capillary voltage of 3600 V. Compound-specific parameters are given in Table A.3.

Table A.3 Compound-specific mass spectroscopy parameters.

Compound	Precursor ion (amu)	Product ion (amu)	Fragmentor voltage (V)	Collision energy (V)	Ionization mode
Carbamazepine	237	194 179	120 120	15 35	Positive
Carbamazepine-d10	247	204	120	20	Positive
MES	196	196	92	0	Positive
PIPES	303	303	92	0	Positive

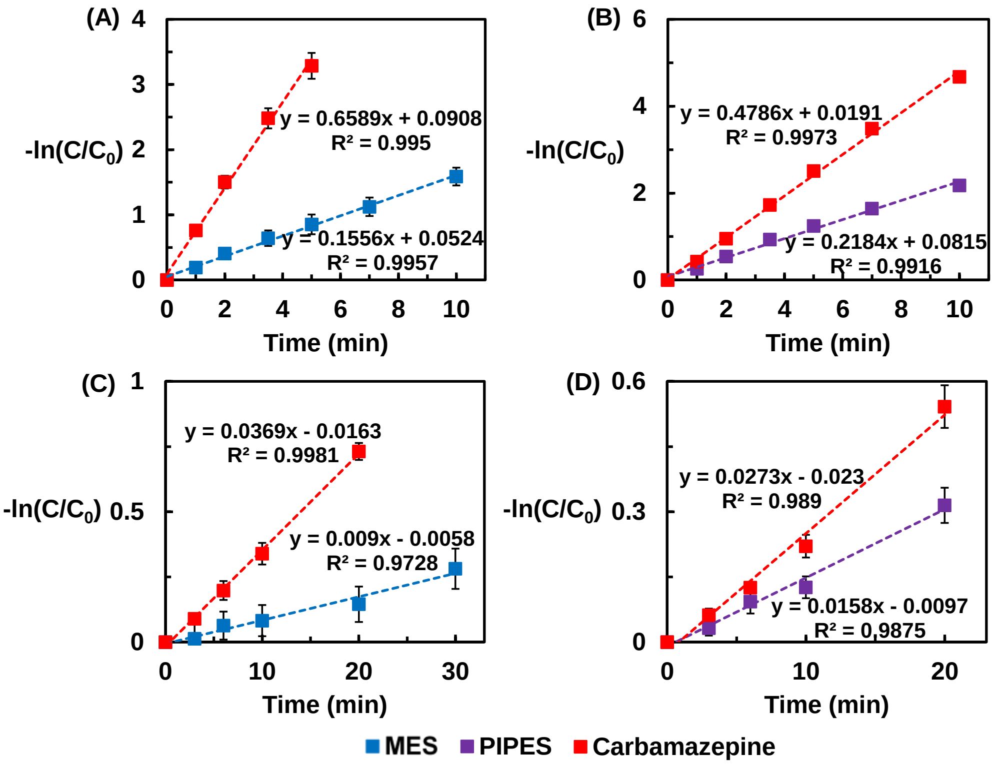

Figure A.3 Natural logarithm of normalized concentration versus time for carbamazepine and (A) MES in the presence of H_2O_2 at pH 6, (B) PIPES in the presence of H_2O_2 at pH 7, (C) MES in the absence of H_2O_2 at pH 6, and (D) PIPES in the absence of H_2O_2 at pH 7. [Test compound]$_{init.}$ = 1.0 µM, [CBZ]$_{init.}$ = 0.5 µM, [H_2O_2]$_{init.}$ = 10 µM, [Phosphate buffer] = 100 µM. Error bars represent one standard deviation.

A.2.3 Prediction of reaction rate between H_2O_2 and Fe(II)

The rate of H_2O_2 transformation through the reaction with Fe(II)$_{(aq)}$ calculated by:

$$k_{H_2O_2} = (k_{Fe^{2+}}\alpha_{Fe^{2+}} + k_{FeOH^+}\alpha_{FeOH^+} + k_{Fe(OH)_2^\circ}\alpha_{Fe(OH)_2^\circ})[\mathrm{Fe(II)}] \qquad (A.7)$$

where, $k_{\mathrm{Fe}^{2+}}$ = 76 $M^{-1}s^{-1}$, k_{FeOH^+} = 6.3×10^6 s^{-1} $M^{-1}s^{-1}$, and $k_{\mathrm{Fe(OH)}_2^\circ}$= 7.9×10^9 $M^{-1}s^{-1}$ (González-Davila et al. 2005, King and Farlow 2000, Walling 1975), and α_i is the fraction of Fe(II) that exist in the form *i* and calculated based on:

$$\mathrm{Fe^{2+} + OH^- = FeOH^+} \qquad Log\beta_1 = 4.50 \qquad (A.8)$$

$$\mathrm{Fe^{2+} + 2OH^- = Fe(OH)_0^\circ} \qquad Log\beta_2 = 7.43 \qquad (A.9)$$

A.3 Factors affecting the yield of hydroxyl radical by electrochemical activation of H_2O_2 on stainless-steel electrodes

A.3.1 Detection of $^{\bullet}OH$ scavengers and the associated oxidation products

An aliquot of 1,10-phenanthroline (final concentration = 1 mM) was added to samples to quench the possible reaction between H_2O_2 and Fe(II).(Duesterberg et al. 2005) Benzoate- and para-hydroxybenzoate-containing samples were acidified with 1 M H_2SO_4 (10% v/v) and the concentrations were determined by HPLC with an isocratic elution of 30% methanol and 70% formic acid water (0.1% v/v) using a 150 × 3 mm Synergi™ 4 µm Hydro-RP 80 Å column at a flow rate of 0.4 mL/min. Benzoate was quantified at 275 nm and para-hydroxybenzoate was quantified at 255 nm.

Acetone, the oxidation product of 2-propanol, was derivatized using 2,4-dinitrophenylhydrazine (DNPH) and determined by HPLC at wavelength of 365 nm with an isocratic elution of 70% acetonitrile and 30% formic acid water (0.1% v/v) using a Symmetry C18 Column, 100Å, 5 µm, 4.6 mm × 150 mm column at a flow rate of 1 mL/min.

For experiments conducted in the presence of 2-propanol, one additional peak besides acetone was observed (Figure A.4B). The additional peak (retention time = 2.9 min) was confirmed as the peak of acetone transformation product by an experiment with 10 mM acetone-amended electrolyte (Figure A.4C). The acetone transformation product was not quantifiable due to a lack of chemical standard.

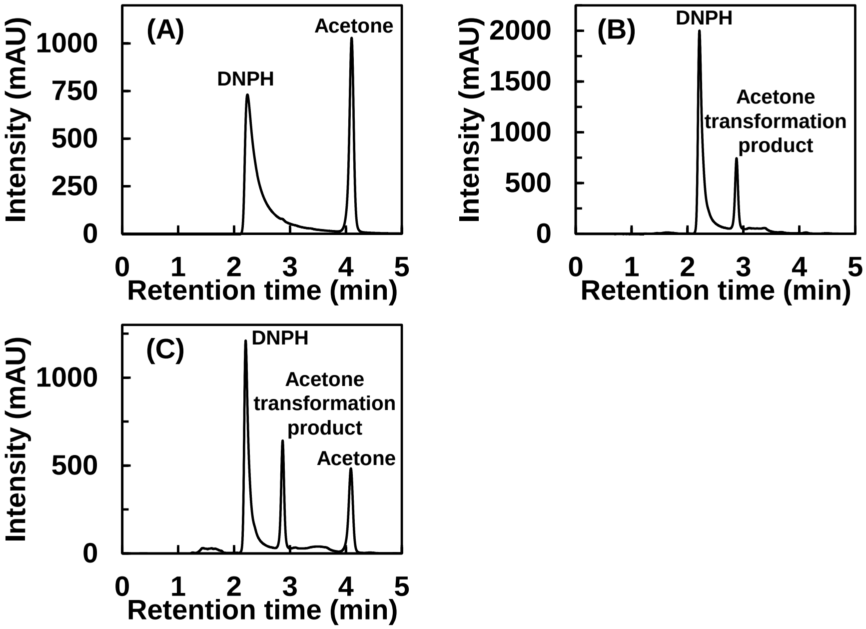

Figure A.4 Example chromatogram of (A) DNPH method for acetone detection, (B) 10×diluted sample for the treatment of electrolyte containing 10 mM of 2-propanol at 120 min, (C) 10×diluted sample for the treatment of 250 mM Na_2SO_4 electrolyte containing 10 mM of acetone at 120 min, the electrolyte was buffered by 1 mM of PIPES buffer (pH 7). Applied current on air-diffusion electrode = 16 mA, applied potential on stainless-steel electrode = 0.02 V, recirculation rate = 70 mL/min.

A linear relationship was found between the peak area of the acetone transformation product and the amount of acetone that was transformed in an experiment conducted with a Na_2SO_4 electrolyte that containing 10 mM of acetone (Figure A.5A). Control experiments indicated no acetone contamination from laboratory air (data not shown). The amount of acetone that underwent transformation was calculated by subtracting the evaporation loss (Figure A.5B) from the total observed loss of acetone.

The amount of acetone that underwent further transformation in the experiment depicted in Figure 4.12 was quantified using the peak area of the transformation product based on the linear relationship.

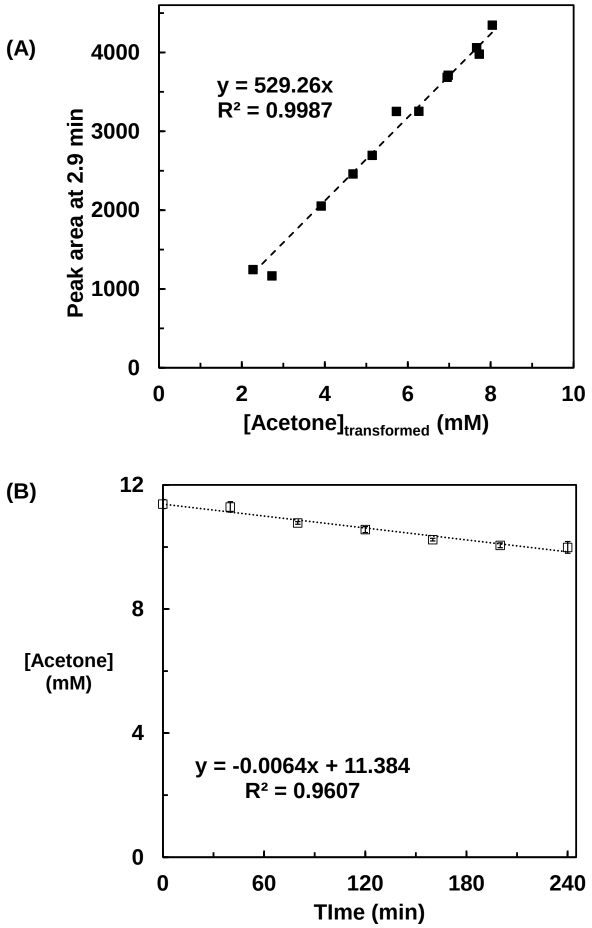

Figure A.5 (A) Linear relation between the peak area of the acetone transformation product and the concentration of acetone that was transformed. Experimental condition: 250 mM Na_2SO_4 buffered with 1 mM of PIPES buffer (pH 7), $[acetone]_0$ = 10 mM. Applied current on air-diffusion electrode = 16 mA, applied potential on stainless-steel electrode = 0.02 V, recirculation rate = 70 mL/min. (B) Evaporation control for acetone in water, $[acetone]_0$ = 10 mM.

A.3.2 Estimation of the diffusion distance of $^\bullet$OH

The diffusion distance of $^\bullet$OH in aqueous phase was estimated from the Einstein-Smoluchowski equation, eq A.7:

$$L \sim \sqrt{2Dt} \tag{A.10}$$

where L is the characteristic distance, D is the diffusion coefficient for $^{\bullet}$OH radical, 2×10^{-9} m^2 s^{-1} (Kopinke 2020), and *t* is the diffusion time, calculated as the half-life of $^{\bullet}$OH radical:

$$t = \frac{ln2}{k_{decomp.}} \qquad \text{(A 11)}$$

$$k_{dcomp.} = \sum k_{\bullet OH,i}[i] \tag{A.12}$$

where $k_{\bullet OH,i}$ represents the rate constants of species *i* (carbamazepine, atrazine, H_2O_2, PIPES and benzoate) with $^{\bullet}$OH.

A.3.3 Energy consumption of point-of-use UV/H_2O_2 process

Table A.4 E_{EO} values for UV/H_2O_2 processes at household scales.

Reference	Water type	Contaminants	Log removal	[H_2O_2] (mg/L)	E_{EO} UV (kWh/m^3)	E_{EO} H_2O_2 (kWh/m^3)	E_{EO} (kWh/m^3)
(Stacy 1994)	Groundwater	TCE=1675 µg/L	3.0	23	5.4	8.5	13.8
		Benzene=252 µg/L	3.0	23	5.4	8.5	13.8
		TCE=1675 µg/L	2.7	48	7.5	19.4	26.9
		Benzene=252 µg/L	2.7	48	7.5	19.4	26.9
		TCE=1675 µg/L	2.5	48	16.2	20.8	37.0
		Benzene=252 µg/L	2.7	48	15.1	19.4	34.6
(Safarzadeh-Amiri 2001)	Groundwater	MTBE=100 mg/L	4.0	500	10.7	135.6	146.3
			4.0	500	5.1	135.6	140.7
			4.0	650	15.0	176.2	191.2
			4.0	650	8.0	176.2	184.2
(Hirvonen et al. 1998)	Groundwater	PCE=200 µg/L	2.0	27	0.5	14.6	15.1
(Müller 1998)	Groundwater	CHC	2.0	100	1.0	54.2	55.2
	Groundwater	PAH	1.3	800	6.1	666.9	673.0
	Groundwater	Atrazine	0.5	2	0.2	3.1	3.3
(Giggy 1993)	Groundwater	4-methylphenol=476 µg/L	1.5	60	2.4	42.7	45.1
(Toor and Mohseni 2007)	Surface water	DBP	0.2	23		102.2	>102.18
(Müller 1998)	Drinking water	Atrazine	1.0	10	1.7	10.8	12.5
(Giggy 1993)	Industrial effluent	DMSO=1500 mg/L, Acyrlnitrile=48 mg/L	1.7	540	15.4	344.7	360.1
(Cater et al. 2000)	Toronto municipal drinking water	MTBE = 100 µg/L	1.7	30	0.2	19.2	19.3
		MTBE = 1000 µg/L	2.8	30	0.3	11.5	11.8
		MTBE = 10000 µg/L	3.2	30	1.4	10.1	11.5
		MTBE = 100000 µg/L	0.6	30	7.5	57.4	64.9

Table A.4 Continued.

Reference	Water type	Contaminants	Log removal	$[H_2O_2]$ (mg/L)	E_{EO} UV (kWh/m^3)	E_{EO} H_2O_2 (kWh/m^3)	E_{EO} (kWh/m^3)
(Katsoyiannis et al. 2011)	Dübendorf wastewater effluent	pCBA	1.0	7	0.6	7.4	7.9
			1.0	34	0.7	36.9	37.6
			1.0	170	1.8	184.4	186.2
	Lake Zürich water	SMX = 0.5 µM	1.0	7	0.4	7.4	7.8
			1.0	7	0.2	7.4	7.5
			1.0	7	0.1	7.4	7.5
		pCBA= 0.5 µM	1.0	7	0.8	7.4	8.1
			1.0	7	0.2	7.4	7.6
			1.0	7	0.2	7.4	7.5
		ATR= 0.5 µM	1.0	7	1.0	7.4	8.4
			1.0	7	0.3	7.4	7.7
			1.0	7	0.2	7.4	7.6
		NDMA= 0.5 µM	1.0	7	1.6	7.4	9.0
			1.0	7	0.4	7.4	7.8
			1.0	7	0.3	7.4	7.7